Diffraction-limited spectropolarimetry of quiet-Sun magnetic fields

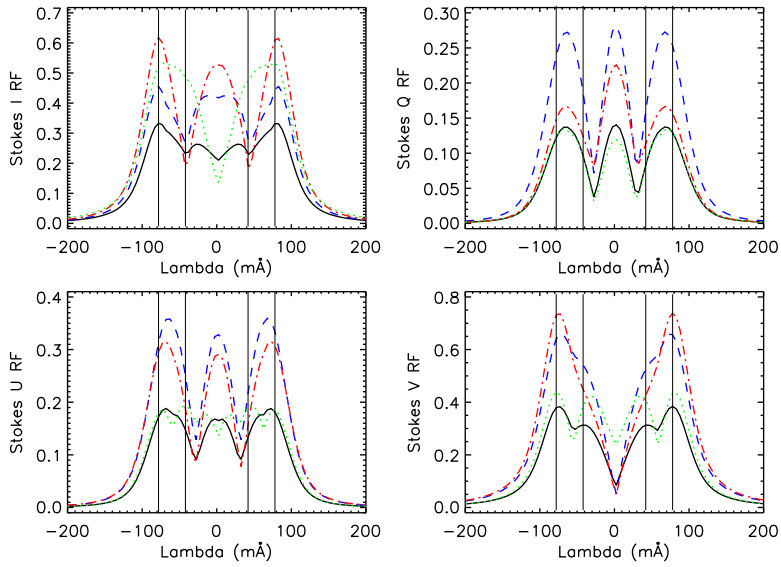

David Orozco Suárez

INSTITUTO Đ ASTROFÍSICA Đ ANDALUCÍA

Consejo Superior de Investigaciones Científicas

Editor: Editorial de la Universidad de Granada
Autor: David Orozco Suárez
D.L.: GR.1867-2008
ISBN: 978-84-691-5694-0

Some of the figures included in this document have been previously published in The Astrophysical Journal, Astronomy & Astrophysics and Publications of the Astronomical Society of Japan

DEPARTAMENTO DE FÍSICA APLICADA

Universidad de Granada

Diffraction-limited spectropolarimetry of quiet-Sun magnetic fields

Memoria que presenta
D. David Orozco Suárez
para optar al grado de
Doctor en Astrofísica.

Dr. D. Jose Carlos del Toro Iniesta Dr. D. Luis R. Bellot Rubio

INSTITUTO Đ ASTROFÍSICA Đ ANDALUCÍA

Consejo Superior de Investigaciones Científicas
16 de Septiembre de 2008

A mi familia y a Susi

Resumen

Esta tesis presenta en primer lugar la deducción analítica y estudio detallado de las llamadas funciones de respuesta (FR) de las líneas espectrales que se forman en la fotosfera solar con la aproximación Milne-Eddington (ME) a la ecuación de transporte radiativo (ETR). Éstas nos permiten estudiar los cambios que ocurren en las líneas espectrales cuando perturbamos algunos de los parámetros del modelo ME. También nos permiten seleccionar, de forma efectiva, tanto el número de longitudes de onda como sus respectivas posiciones para ser observadas con magnetógrafos vectoriales. A partir de las FR discutimos la capacidad de las líneas espectrales visibles para el diagnóstico espectropolarimétrico y, más en concreto, para la distinción precisa entre campos magnéticos débiles y fuertes. También demostramos que la intensidad del campo y el factor de llenado magnético pueden separarse y encontramos una estimación de los límites de detectabilidad de los distintos parámetros de la atmósfera modelo.

A continuación, desarrollamos un código de inversión de la ETR en su aproximación ME. El código permite analizar los perfiles de Stokes que emergen de la fotosfera solar, obteniendose así las propiedades magnéticas y dinámicas del plasma fotosférico.

Los parámetros físicos de las atmósferas que dan lugar a los perfiles reales varian con la altura, por lo que que los perfiles observados contienen información sobre la estructura vertical de la atmósfera. La aproximación ME se caracteriza por tratar los diferentes parámetros del modelo como constantes a lo largo de la fotosfera solar. Por esta razón, presentamos un estudio detallado de las capacidades y limitaciones del código ME para el análisis de perfiles reales. Para ello disponemos de simulaciones magnetohidrodinámicas de la fotosfera solar que nos proporcionan los modelos de atmósfera necesarios para generar los perfiles. Éstos son después utilizados para realizar un análisis en profundidad de los errores asociados a la aproximación ME en el análisis.

También hacemos uso de las simulaciones magnetohidrodinámicas para simular datos observacionales del espectropolarímetro del satelite *Hinode*. Realizamos un análisis detallado de los efectos que tiene sobre los perfiles simulados, la difracción del telescopio, y el pixelado de la CCD y el ruido fotónico. También analizamos en detalle si somos capaces de obtener los parámetros atmosféricos del modelo mediante inversiones ME. Encontramos que el código ME produce resultados satisfactorios siempre y cuando tengamos en cuenta una contaminación por luz difusa local. Ésta nos permite corregir los efectos de la difracción

del telescopio sobre los perfiles de polarización.

También analizamos observaciones de primera luz del satélite japonés *Hinode*. En particular, presentamos los resultados de la inversión ME de perfiles de Stokes pertenecientes a una región del Sol en calma tomados con el espectropolarímetro de *Hinode*. La región observada contiene dos líneas de Hierro neutro a 630.15 y 630.25 nm. A partir de estas inversiones determinamos las funciones de densidad de probabilidad de la intensidad y de la inclinación del campo magnético, así como la del factor de luz difusa. Éstas indican que el Sol en calma está mayormente poblado por campos magnéticos del orden de cientos de Gauss y preferentemente horizontales. Este análisis nos ha permitido contribuir a resolver el magnetismo del Sol en calma. En el análisis hemos hecho especial hincapié en la unicidad de los modelos proporcionados por la inversión.

También mostramos y describimos una nueva forma de emergencia de flujo magnético a través de celdas convectivas en el Sol en calma. Para ello disponemos de series temporales de datos espectropolarimétricos tomadas por el satélite japonés *Hinode*. Haciendo uso de las propiedades intrínsecas de los parámetros de Stokes estudiamos la evolución temporal de estructuras de campo magnético. En el análisis preliminar de los datos encontramos señales magnéticas unipolares que emergen en los gránulos. No hallamos indicios de señales de polarización lineal, lo que sugiere que las líneas de campo emergentes tienen orientación vertical. Finalmente discutimos posibles mecanismos físicos que podrían dar lugar a este tipo de fenómeno.

Para terminar, hemos simulado datos observacionales del instrumento IMaX que volará a bordo del globo estratosférico *Sunrise*. Uno de los objetivos es analizar la idoneidad de las líneas candidatas a ser observadas por IMaX para obtener el campo magnético y la velocidad a partir de sus perfiles de Stokes. También analizamos el efecto que produce la difracción del telescopio y el pixelado de la CCD. Prestamos especial interés en como afecta el interferometro Fabry Pérot de IMaX a los perfiles de Stokes. IMaX tomará un máximo de cinco muestras de longitudes de onda a lo largo de una línea espectral fotosférica, por lo que uno de los objetivos es analizar la precisión con la que somos capaces de determinar el campo magnético y la velocidad a partir de inversiones ME de perfiles muestreados en cinco puntos a lo largo de la línea.

Contents

1

Introduction

1.1 Quiet-Sun magnetism and diagnostic techniques

The standard way to learn about the physical properties of the solar plasma[1] is through its radiation. The photosphere, chromosphere, corona and heliosphere are the parts of the Sun that can be directly observable while the Sun's interior is not measurable: the photons carrying information about its physical properties are confined. The first ones escaping[2] from the Sun define the solar surface, corresponding to the layer at which the optical depth τ is unity. For visible wavelengths it is defined at $\lambda = 5000$Å and is known as the photosphere.

The photosphere extends between the bottom of the solar surface and the temperature minimum, with a total thickness of about 500 km and a effective temperature of 5777 K (see Fig. 1.1). The photosphere is the simplest layer of the Sun. It is very well explained in local thermodynamic equilibrium, i.e., the radiation that emerge from it (source function) is equal to the Planck function at any wavelength; the temperature of the plasma decreases as we go outwards; and the number density of the particular species of atoms and the population of atomic levels can be simply derived by solving the Saha and Boltzmann

[1] the Sun is a ball of ionized gas (plasma) that rotates, auto-gravitates and is in hydrostatic equilibrium, irradiating light in every directions. For a complete introduction to solar plasmas refer to Foucal (1990) and Stix (2004).

[2] The density of the plasma diminishes rapidly as we move toward higher layers. At the same time the mean free path of the photons became large enough for not being anymore absorbed by the solar plasma

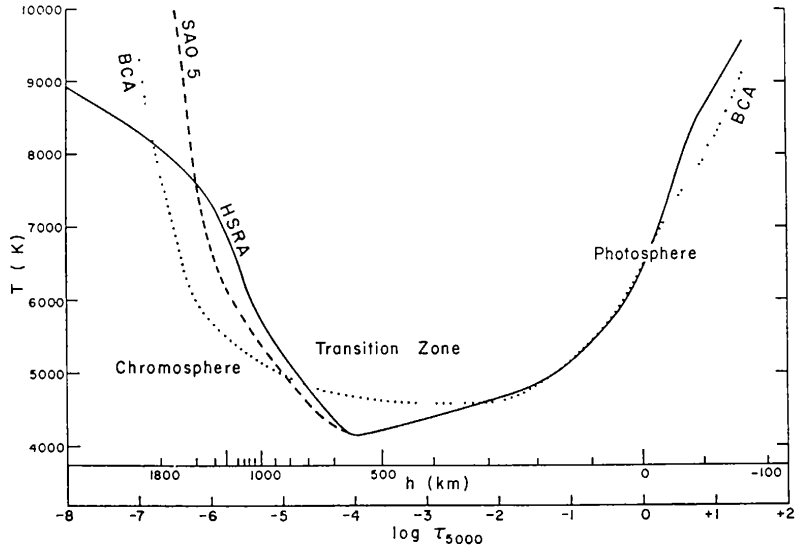

FIGURE 1.1:— Variation of temperature with optical depth at 5000 Å for three model solar atmospheres: the Harvard-Smithsonian Reference Atmosphere (HSRA), the Bilderberg Continuum Atmosphere (BCA; Gingerich & de Jager, 1968), and a revision of the BCA model (SAO 5;). The physical depth scale h (km) is the height above $\tau_{5000} = 1$ for the HSRA model. Notice that a temperature minimum zone is reached only at $\tau_{5000} = 10^{-4}$. Taken from Gingerich et al. (1970).

equations.

In the photosphere we can easily identify a number of main features: granules, sunspots and faculae (see Fig. 1.2). Some of these features are known as active regions. The rest of the solar surface is non-active.

We know that the magnetic field is the root of active regions. At the level of the photosphere they are the visible effects of the solar dynamo. For instance, sunspots are concentrations of very intense magnetic lines that emerge from the convection zone. Non-active regions do also contain a large, unknown amount of magnetic flux and covers most of the solar surface area, $\sim 90\%$ (Howard & Stenflo 1972). Nowadays, scientists are far from providing satisfactory explanations to many of the magnetic phenomena that can be seen in the photosphere despite the advance on theoretical aspects and the improvements in the quality of solar polarimeters.

A major source of debate of current solar physics is in the magnetic nature of the quiet solar regions. The activity of the quiet Sun represent a challenging problem for current instrumentation and for theoreticians because it occurs at very small scales, produce very small magnetic fluxes and higher Reynold

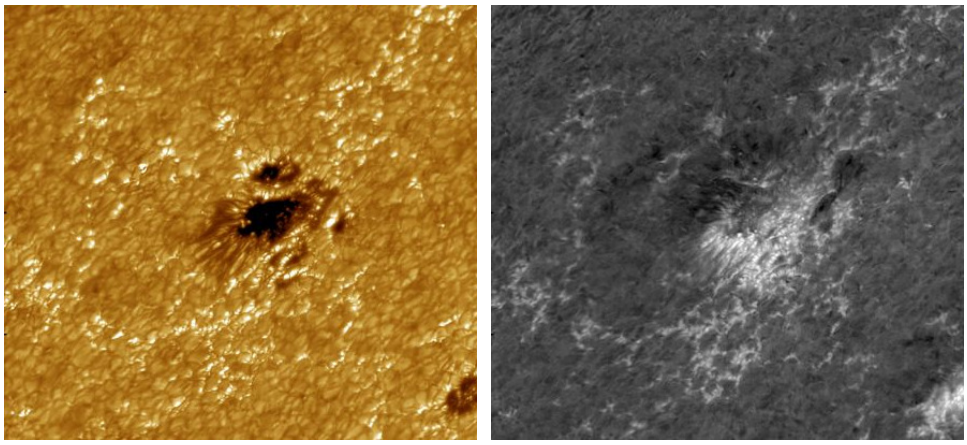

FIGURE 1.2:— Continuum ($\sim$ 430 nm) and circular polarization (Stokes V) images obtained with the Swedish Solar Telescope (SST) on La Palma, left and right respectively. The filtergram has been taken in the region of a Zeeman sensitive photospheric spectral line. White corresponds to magnetic fields of positive polarity. Gray regions indicate the presence of weak polarimetric signals. The image has been taken at an heliocentric angle of 45°. The images show an active region, including a sunspot, faculae and granulation. The sunspot has spatial dimensions comparable to Earth diameter. The granulation covers the full field of view except the sunspot, where granulation is inhibited. Brighter features corresponds to the upper parts of granular cells corresponding with upwelling plasma. The darker parts of the granulation are correlated with downward, more denser plasmas. The brightest structures, of 150 km size, indicate strong concentration of magnetic fields.

numbers. Therefore, their analysis demand from very high spatial resolution observations, temporal cadences and very high polarimetric sensitivities. The quiet Sun is divided into two regions (Zwaan 1987), the network and the Inter-Network (IN). The network fields outline the regions where the magnetic field lines are advected by the supergranular[3] flow, and are composed of intense flux tubes. The IN corresponds to the solar region at the interior of supergranular cells. The first signs of the presence of magnetic fields on IN regions were obtained by Livingston & Harvey (1971) and Smithson (1975).

Keller et al. (1994) carried out the first polarimetric observations of IN regions in the visible. They obtained that the IN have magnetic fields below kG and set an upper limit to the field strength of 500 G. Subsequent studies of the IN magnetic fields have benefited from instrumental advances in solar spectropolarimetry and have contributed to understand the origin of the quiet-Sun IN magnetism. However, there is still a major debate and controversy on the

[3]granular and supergranular structures are visible in MDI Dopplergrams. These to structures dominate the Quiet sun (Fig. 1.3).

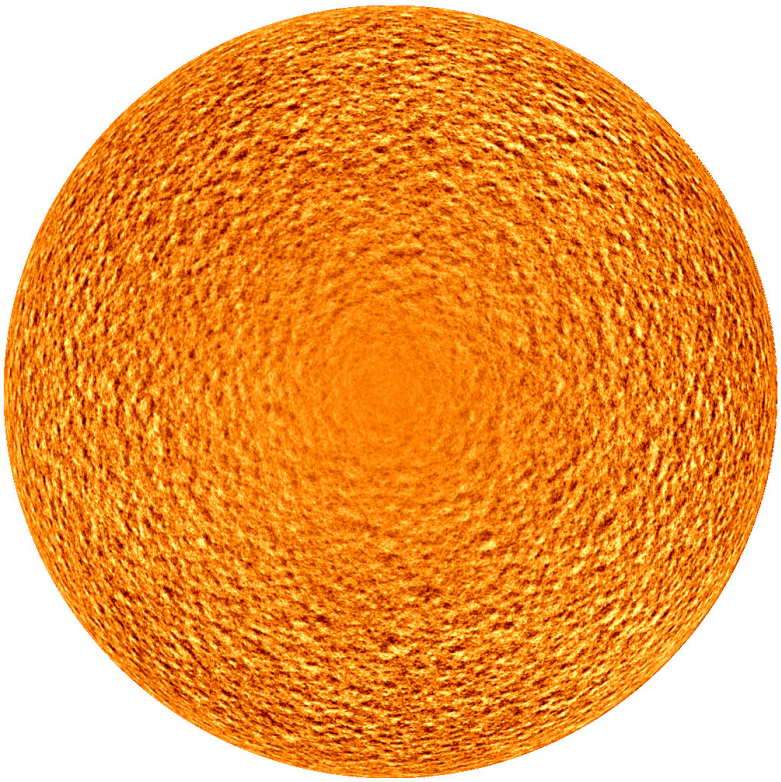

FIGURE 1.3:— Average of 30 minutes of a series of *SOHO*/MDI Dopplergrams obtained on 13 January 1996. The color scale is such that dark is motion towards the observer and bright is motion away from the observer. The supergranulation pattern is clearly visible. The central part shows no pattern since the line-of-sight does not "see" the horizontal motion of the plasma, but that parallel toward *SOHO*. The supergranulation was first studied by Leighton et al. (1962) and covers the whole Sun at the photosphere. It works as the normal granulation (the material rises at the center and moves outwards to finally subduct at the network edges) but at larger spatial scales.

intrinsic field strength values and magnetic fluxes in these regions. The reason is that depending on the targeted spectral lines and the diagnostic method the average field strengths and fluxes vary from hundred to kilo Gauss and from few ($\sim 7-9$, e.g., Khomenko 2006) to tens of Gauss ($\sim 30-60$; Trujillo Bueno et al. 2004.).

Major studies of the IN magnetism consisted in: first, the analysis of spectropolarimetric data taken at different spectral regions, and secondly the numerical simulation of magnetic, convective flows using magnetohydrodynamic. The former have provided contradictory results to the IN magnetism by using

the Zeeman and Hanle effects and different spectral regions, the visible and the infrared. The latter, is able to reproduce the convective flow at the photosphere with weak fields. Particular simulations of a local dynamo have predicted that the turbulent convective flow is able to concentrate, hence intensify, magnetic fields in the granulation (Cattaneo 1999; Cattaneo et al. 2003).

There is no meter able to probe the photospheric plasma and to provide us with its physical properties. To derive its magnetic properties we need to interpret the spectropolarimetric measurements. To this end we utilize diagnosis methods, mainly based on the radiative transfer equation. All new discoveries of solar physics have been linked to the knowledge of the radiative transfer in stellar atmospheres (e.g., del Toro Iniesta 2003, Landi degl'Innocenti & Landolfi 2004) and to the development of new instrumentation. Both have been providing new outputs to understand the Sun's magnetism.

The problem of interpreting solar measurements started more than a century ago. In 1908, George E. Hale pointed out to the difficulties of interpreting the complex phenomena recorded by spectroheliograph plates of the hydrogen lines. His work ended suggesting the possible existence of magnetic fields in the Sun.

The goal of this thesis is to learn if we are able to obtain reliable physical quantities from the analysis of current and future spectropolarimetric observations of the quiet Sun at very high spatial resolution. This analysis includes the study and development of diagnostic techniques for extracting information from polarimetric measurements, the application of these techniques to infer physical condition from quiet Sun measurements, and their use to provide feed-back on the design of new and state-of-the-art solar instrumentation.

1.2 Motivation

Our knowledge of the properties of magnetic field structures is still very limited because of current spatial resolutions which make the polarization signals weak and contaminated by noise. Therefore, for a better understanding of the physical phenomena taking place in the solar photosphere, we need from spectropolarimetric measurements at very high spatial resolutions or the order of, or better than ~ 100 km and high polarimetric efficiencies. At present, many new instruments are being built to achieve such spatial resolution. The latter is being improved by boarding the instruments into satellites, therefore eliminating the Earth atmosphere contamination. Among the planned instruments we have the Helioseismic and Magnetic Imager (HMI; Scherrer & SDO/HMI Team 2002) aboard the *Solar Dynamics Observatory*, NASA, and the Polari-

metric and Helioseismic Imager (PHI; Marsch et al. 2005), *Solar Orbiter*, ESA.

A promising instrument is the Imaging Magnetograph eXperiment (IMaX; Martínez Pillet et al. 2004), planned instrument for the *Sunrise* balloon (Gandorfer et al. 2006) mission. *Sunrise* is a one-meter telescope that will be able to provide spatial resolutions of the order of 80 km (at 520 nm) of the solar photosphere. A stratospheric balloon will be responsible of carrying *Sunrise* to heights of 40 km, getting rid from most of the Earth atmosphere.

An instrument currently providing nearly diffraction-limited observations of the solar photosphere is the spectropolarimeter (Lites et al. 2001) of the Solar Optical Telescope aboard *Hinode* (Kosugi et al. 2007; Tsuneta el al. 2008), which is already providing nearly diffraction-limited observations of the solar photosphere.

The high spatial resolution spectropolarimetric measurements have to be translated into the proper physical quantities. These quantities, i.e. the atmospheric parameters describing the model atmospheres from with the polarimetric measurements have been taken, have to be retrieved with suitable methods.

Therefore, in this thesis we explore the diagnostic potential of current and future high spatial spectropolarimetric measurements of the solar photosphere. The atmospheric parameters

1.3 Overview

In what follows we give a brief outline of the structure of this thesis:

- Chapter 2 is just a mere introduction to radiative transfer and the measurement of light, including a brief explanation about how current polarimeters work. We also introduce to the Milne-Eddington (ME) approximation of the radiative transfer equation.

- Chapter 3 constitutes a great proportion of the present thesis. In this, we introduce the concept of Response Functions (RFs) in ME atmospheres. The analysis of the ME RFs provides information regarding the different sensitivities of spectral lines to perturbations on the model parameters. They also are of interest to the design of vector magnetographs. The analytical expression of these RFs are explicitly written in Appendix A. Part of the Chapter has been published in *Astronomy & Astrophysics* (Orozco Suárez and del Toro Iniesta 2007).

- A brief introduction to inversion methods based on the radiative transfer equation and a description of the MILOS (MILne-Eddington inversion of

pOlarized Spectra) and SIR (Stokes Inversion based on Response Functions) codes are the topics of Chapter 4.

- In this Chapter we aim at understanding the relationship between the physical parameters describing the solar photosphere, the measurements (the Stokes profiles) and the physical quantities obtained after the application of Milne-Eddington inversions to the spectra. Explicitly we measure the uncertainties of the model parameters inferred from ME inversions when applied to real observations in the absence of noise and of any additional source of error. We also describe basic properties of the magnetohydrodynamic simulations utilized to simulate the Stokes profiles of the present study.

- In Chapter 6 we simulate high-spatial resolution observations taken with the spectropolarimeter attached to the solar optical telescope aboard the *Hinode* satellite and analyze the performance of ME inversions for quiet Sun measurements. We also make a detailed description of the effects of diffraction on the Stokes profiles. Various of the main results have been published in the *Astrophysical Journal letters* (Orozco Suárez, Bellot Rubio & del Toro Iniesta 2007).

- A detailed analysis of internetwork quiet Sun observations taken with the spectropolarimeter of the *Hinode* is carried out in Chapter 7. We determine the distribution of the magnetic fields and of their inclinations on internetwork regions as well as the contribution of stray-light to the observations. The physical quantities are obtained using ME inversions. We also analyze the robustness of the results. Results from this chapter have been publish in the *Astrophysical Journal letters* and the *Publications of the Astronomical Society of Japan* (Orozco Suárez, Bellot Rubio, del Toro Iniesta, et al. 2007a,b).

- In Chapter 8 we make use of the ability of the *Hinode* spectropolarimeter to continuously raster a small portion of the QS in order to obtain maps with relatively high temporal cadence. This allows the study of the evolution of small-scale magnetic features. In particular, we analyze the evolution of apparently *vertical* magnetic flux concentrations over granular convection cells, We discuss on their physical properties and derive intrinsic characteristics. Results from this chapter have been publish in *Astronomy & Astrophysics* (Orozco Suárez, Bellot Rubio, del Toro Iniesta, & Tsuneta, 2008).

- The capabilities of future state-of-the-art instrumentation are analyzed in Chapter 9. In particular we focus our attention in IMaX and PHI, planned instruments for the Sunrise stratospheric balloon and the ESA/NASA Solar Orbiter mission. We analyze how the observables are affected by the use of vector magnetographs, through the effect of the limited wavelength sampling and position of wavelength points, to the retrieval of the model parameters and their uncertainties. We provide feedback to the design of vector magnetographs and explore the limitations when inferring physical quantities from their measurements.

- An summary of the addressed topics as well as general remarks and future plans are outlined in Chapter 10

2

Radiative transfer and the measurement of light

Introductions to the measurement of light, to vector, filter-based magnetographs, and to radiative transfer are presented in this Chapter. We will also introduce one of the approximations for solving the radiative transfer equation: the *Milne-Eddington* approximation, which will be widely used in this thesis. For an extended introduction to all these issues and their applications refer to, e.g., del Toro Iniesta (2003).

2.1 The measurement of light

A light beam that propagates through an isotropic medium can be interpreted as the superposition of plane electromagnetic waves, each described by its associated electric field vector, which is contained in the plane perpendicular to the direction of propagation of the beam.

If the light beam propagates along the Z-axis, then

$$E_x(t) = A_x(t)\,\mathrm{e}^{-i[\omega t - \delta_x(t)]}, \tag{2.1}$$

$$E_y(t) = A_y(t)\,\mathrm{e}^{-i[\omega t - \delta_y(t)]}, \tag{2.2}$$

where $\delta_x(t)$ and $\delta_y(t)$ represent the phase shift of each of the x and y components, $A_x(t)$ and $A_y(t)$ their amplitudes and ω the frequency.

Giving values to these four parameters, we can describe any electromagnetic wave. The convenient form to describe the polarization properties of any electromagnetic wave is by a set of four parameters, called the Stokes parameters. The Stokes parameters that represent an arbitrarily polarized beam are:

$$\begin{aligned} I = &\quad k(\langle|E_x(t)|^2\rangle + \langle|E_y(t)|^2\rangle) &&= \quad k\langle A_x^2 + A_y^2\rangle, \\ Q = &\quad k(\langle|E_x(t)|^2\rangle - \langle|E_y(t)|^2\rangle) &&= \quad k\langle A_x^2 - A_y^2\rangle, \\ U = &\quad k(\langle E_x(t)^* E_y(t)\rangle + \langle E_y(t) E_x(t)^*\rangle) &&= \quad 2k\langle A_x A_y \cos\delta\rangle, \\ V = &\quad ik(\langle E_x(t)^* E_y(t)\rangle - \langle E_y(t) E_x(t)^*\rangle) &&= \quad 2k\langle A_x A_y \sin\delta\rangle, \end{aligned} \tag{2.3}$$

where * means complex conjugate, k is a constant, $\delta(t) = \delta_x(t) - \delta_y(t)$ is the phase difference of the x and y components of the electric field and $\langle\,\rangle$ stands for time average. Thus, $\mathbf{I} = (I, Q, U, V)^\dagger$ is called the Stokes vector, where $\dagger$ means transposition. The quantities defined above are real and *measurable* and must follow the relationship: $I^2 \geq Q^2 + U^2 + V^2$. When equality occurs, the light beam is said to be totally polarized. When $Q = U = V = 0$, light is called natural or totally unpolarized. In any other case, light is said to be partially polarized. Since no confusion is possible, we hereafter omit the argument (t) on the amplitudes and phase shifts as in the right-most terms of Eq. (2.3).

To analyze the polarization of a light beam we need some optical devices. Among them, linear polarizers and retarders are the most common ones. A linear retarder is an optical device capable of introducing a phase difference, the so-called retardance, between the two perpendicular components of the electric field associated to the beam. Therefore, the linear retarder does not alter the total intensity, I. The device is characterized by two fundamental optical axes, namely the fast and the slow axes. The retardance phase shift angle depends on different optical and geometrical properties of the medium light is travelling through. As an example, let us consider a retarder whose fast axis is aligned with the X-axis of the reference coordinate system. If E_x and E_y represent the input light beam and E'_x and E'_y the output beam, a retardance plate will introduce a phase difference δ in one of the components, say y, as follows:

$$E'_x = E_x \quad ; \quad E'_y = E_y \mathrm{e}^{i\delta}. \tag{2.4}$$

A linear polarizer is an optical device from which the emergent light is completely linearly polarized at angle θ, regardless of the state of polarization of the incident light. This angle characterizes its fundamental, or transmission, axis along which the transmission of light is maximum. The electric field aligned to the axis propagates naturally through it; the orthogonal component of the

field is completely absorbed though. The only non-null component of the output beam is along the θ axis and given by

$$E_\theta = E_x \cos\theta + E_y \sin\theta. \tag{2.5}$$

An example of a double linear polarizer is the so-colled *beam splitter*. It is capable of separating any input light beam into two independent beams with orthogonal polarization states.

As an example, let us suppose a retarder wave plate whose fast axis is oriented along the X-axis followed by a linear polarizer whose fundamental axis form an angle θ with the X-axis. The first optical device introduces a retardance on the phase of the y component of the electric field, δ. Then, the light beam crosses the linear polarizer, which allows only the θ component of the electric field to be transmitted. Thus, the output beam is given by:

$$E_\theta = E_x \cos\theta + E_y \mathrm{e}^{i\delta} \sin\theta. \tag{2.6}$$

In the detector, only the time-averaged square modulus of the beam electric field is measured:

$$I_{\mathrm{meas}} = \langle E_\theta^* E_\theta \rangle, \tag{2.7}$$

where * means complex conjugate. Now, according to Eq. (2.3), and assuming $k = 1$ (which is in practice irrelevant), we have

$$\begin{aligned} \langle E_x(t) E_x^*(t) \rangle &= \tfrac{1}{2}(I + Q), \\ \langle E_y(t) E_y^*(t) \rangle &= \tfrac{1}{2}(I - Q), \\ \langle E_x(t) E_y^*(t) \rangle &= \tfrac{1}{2}(U + \mathrm{i}V), \\ \langle E_x^*(t) E_y(t) \rangle &= \tfrac{1}{2}(U - \mathrm{i}V). \end{aligned} \tag{2.8}$$

From these equations, the measured light beam intensity can be cast in terms of the various Stokes parameters as

$$I_{\mathrm{meas}}(\theta, \delta) = \frac{1}{2}(I + Q\cos 2\theta + U \sin 2\theta \cos\delta + V \sin 2\theta \sin\delta)\,. \tag{2.9}$$

This equation provides the possibility of measuring the polarization of light by means of different optical devices and setups, just by giving specific values to θ and δ. Specifically,

$$\begin{aligned} I &= I_{\mathrm{meas}}(0,0) + I_{\mathrm{meas}}(\pi/2, 0), \\ Q &= I_{\mathrm{meas}}(0,0) - I_{\mathrm{meas}}(\pi/2, 0), \\ U &= I_{\mathrm{meas}}(\pi/4, 0) - I_{\mathrm{meas}}(3\pi/4, 0), \\ V &= I_{\mathrm{meas}}(\pi/4, \pi/2) - I_{\mathrm{meas}}(3\pi/4, \pi/2). \end{aligned} \tag{2.10}$$

Hence, I is the total intensity, Q is the difference between the intensities of linear components at 0°and 90°, U is the difference between the intensities of linear components at 45°and 135°, and V is the difference between clockwise and counterclockwise circulary polarized light. In what follows we are introducing a particular optical configuration, namely, that adopted for the IMaX instrument.

2.2 Brief introduction to IMaX

The most suitable instruments to analyze the rapid changes that occur on the magnetic and dynamic properties of solar plasmas in two dimensions are the filter-based magnetographs (Zirin 1995). We shall exemplify the previous section by means of a particular vector magnetograph: the Imaging Magnetograph eXperiment (IMaX; Martínez Pillet et al. 2004) is a vector polarimeter capable of observing a photospheric spectral line in five wavelength samples in less than one minute. It has been designed in order to obtain maps of the magnetic field vector and the flow velocity of a given zone of the solar surface. It is one of the post-focus instruments of the SUNRISE balloon mission (Gandorfer et al. 2006) and will provide invaluable information about the magnetism and the dynamics of the solar photospheric plasmas. It will achieve unprecedented spatial and temporal resolution with high polarimetric sensitivity. To this end, IMaX is made up of two fundamental optical parts: one for the polarimetric modulation of light and another for the spectral analysis. The latter is done by means of a Fabry-Pérot interferometer (étalon) based on $LiNbO_3$ in an incoming collimated system. The étalon is a narrow-band, tunable filter which allows the selection of the different wavelength samples. The system has a narrow-band pre-filter of 10 Å, as well. The polarimetric modulation is carried out using two liquid crystal variable retarders (ROCLIs)[1] and a beam splitter for the linear polarization analysis. This optical configuration allows us to measure the Stokes vector, $\mathbf{I} = (I, Q, U, V)^\dagger$, at five wavelength samples in less than one minute. In the following subsections we analyze the optical parts of the instrument.

2.2.1 Polarimetric analysis

Equipped with two ROCLIs and a linear polarizer, this instrument (as any other with equivalent optical configuration) will allow to measure the full Stokes

[1]We shall use the Spanish abreviation (Retardadores Ópticos de Cristal Líquido) rather than the English LCVRs.

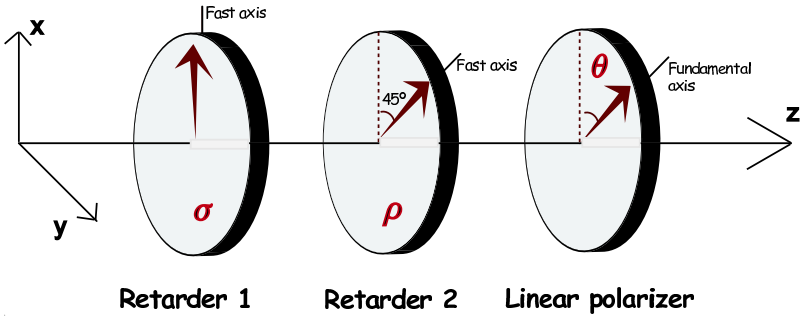

FIGURE 2.1:— Optical scheme for the IMaX polarization analysis.

vector. Figure 2.1 sketches an optical bench with these three devices. The fast axis of the first retarder is vertical while that for the second retarder forms an angle of 45º with the vertical direction. They introduce retardances of σ and ρ, respectively. At the exit of the two retarders there is a linear polarizer whose fundamental axis forms an angle θ with the vertical direction.

Following the same reasoning as in the previous section, we find that at the exit of the optical system the mean intensity is:

$$\begin{aligned} I_{\rm meas} &= \frac{1}{2}(I + Q\cos 2\theta\cos\sigma + U(\cos 2\theta\sin\sigma\sin\rho + \sin 2\theta\cos\rho) + \\ &\quad + V(\sin 2\theta\sin\rho - \cos 2\theta\sin\sigma\cos\rho)\,. \end{aligned} \tag{2.11}$$

If the linear polarizer is a *beam splitter*, then at the exit we have two perpendicular light beams with orthogonal polarizations. Moreover, if the fundamental axis of the *beam splitter* is aligned with the vertical direction, hence parallel to the fast axis of the first retarder, then θ is 0º and 90º, respectively, for the two output beams. Finally, these output beams are measured by two different detectors. The measured intensities are nothing but linear combinations of the four Stokes parameters:

$$\begin{aligned} I_{\rm meas,1} &= \frac{1}{2}(I + Q\cos\sigma + U\sin\sigma\sin\rho - V\sin\sigma\cos\rho)\,, \\ I_{\rm meas,2} &= \frac{1}{2}(I - Q\cos\sigma - U\sin\sigma\sin\rho + V\sin\sigma\cos\rho)\,. \end{aligned} \tag{2.12}$$

To measure the four Stokes vector at least four different intensity modulations, I_i, are needed. This is achieved through changing the σ and ρ values by simply modifying the applied voltages to the ROCLIs. Thus, assume that the

following modulated measurements are recorded by the detectors:

$$\begin{aligned} I_1 &= I + \frac{1}{\sqrt{3}}Q + \frac{1}{\sqrt{3}}U + \frac{1}{\sqrt{3}}V, \\ I_2 &= I + \frac{1}{\sqrt{3}}Q - \frac{1}{\sqrt{3}}U - \frac{1}{\sqrt{3}}V, \\ I_3 &= I - \frac{1}{\sqrt{3}}Q - \frac{1}{\sqrt{3}}U + \frac{1}{\sqrt{3}}V, \\ I_4 &= I - \frac{1}{\sqrt{3}}Q + \frac{1}{\sqrt{3}}U - \frac{1}{\sqrt{3}}V. \end{aligned} \tag{2.13}$$

The four Stokes parameters are then derived from the four modulation states as

$$\begin{aligned} I &= \frac{1}{4}I_1 + \frac{1}{4}I_2 + \frac{1}{4}I_3 + \frac{1}{4}I_4, \\ Q &= \frac{\sqrt{3}}{4}I_1 + \frac{\sqrt{3}}{4}I_2 - \frac{\sqrt{3}}{4}I_3 - \frac{\sqrt{3}}{4}I_4, \\ U &= \frac{\sqrt{3}}{4}I_1 - \frac{\sqrt{3}}{4}I_2 - \frac{\sqrt{3}}{4}I_3 + \frac{\sqrt{3}}{4}I_4, \\ V &= \frac{\sqrt{3}}{4}I_1 - \frac{\sqrt{3}}{4}I_2 + \frac{\sqrt{3}}{4}I_3 - \frac{\sqrt{3}}{4}I_4. \end{aligned} \tag{2.14}$$

The σ and ρ parameters are suitably determined in order to maximize the efficiencies of the polarimeter (see del Toro Iniesta & Collados 2000). In fact, two independent determinations of $\mathbf{I}$ according to Eq. (2.13) are carried out, one with each of the two cameras of the instrument. This double determination helps increase the final signal to the noise (S/N) ratios of the observations.

2.2.2 Spectral modulation: Fabry-Pérot interferometers

In order to obtain 2D maps of the solar photosphere and at different wavelengths we need an optical device capable of sampling different wavelength points through a determined spectral region or line. The chosen device for IMaX is a Fabry-Pérot interferometer. Such an interferometer is an optical instrument which uses multiple-beam interference. It is made up of two plane-parallel plates with a medium in between of a given refractive index. The light beam suffers multiple reflections within the two plates. As a consequence, the optical system has maximum transmission at some wavelengths. The distance between the two plane-parallel plates (and even the angle of attack) can be modified at will, thus changing the wavelength at which the transmission is maximum. As a result, this optical device allows the selection of different

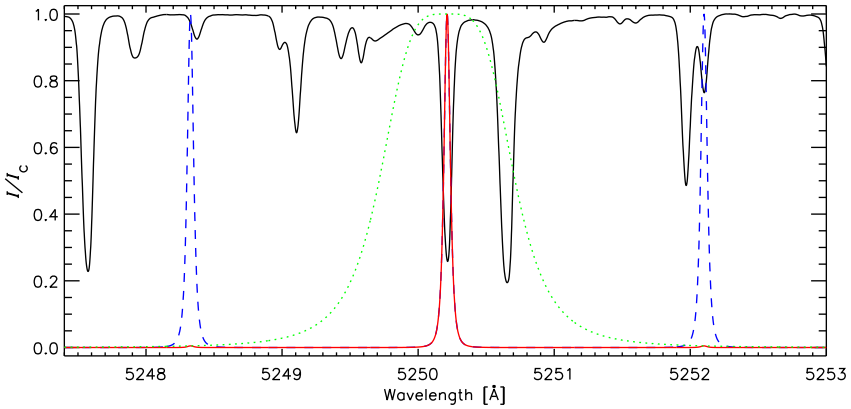

FIGURE 2.2:— FTS spectral atlas (black) around the 525.0 nm spectral region. Over-plotted is the IMaX transmission filter: the blue, dashed line represents the secondary transmission peaks of the Fabry-Pérot (not to scale) while the red, solid one shows the mean transmission peak. The green dotted line stands for the spectral shape of the pre-filter.

wavelength samples in a straightforward way, so a spectral line can be scanned. For further reading on how these optical systems work see e.g. Kentischer et al. (1998) and references therein. Fabry-Pérot interferometry is the most suitable way for simultaneous high-resolution imaging and spectroscopy.

The main transmission profile of a Fabry-Pérot is approximately given by a Lorentzian function. The full-width-at-half-maximum (FWHM) of this function characterizes the spectral resolution of the Fabry-Pérot. When more than a Fabry-Pérot is employed, the FWHM can be decreased, therefore increasing the spectral resolution of the instrument. The IMaX solution is a double passage through the same étalon. It is also important to reduce the amplitude of the secondary transmission peaks (Lorentzians as well) of the etalon. To this end, the system is also equipped with an interference pre-filter which opens a narrow spectral window. In Fig. 2.2 we represent the transmission function of the Fabry-Pérot over-plotted with a spectral region of ~ 6 Å from the NSO Fourier Transform Spectrometer atlas (Kurucz et al. 1984) centered at 525.0 nm. The dashed line represents the secondary peaks of the transmission filter while the dotted line the pre-filter. The amplitude of the secondary peaks is strongly reduced by the interference filter, thus minimizing their effect. Note that these secondary peaks should lie on continuum windows whereby minimizing (if not avoiding) spurious polarization signals since the continuum polarization level is smaller than the noise level of $10^{-3}I_c$. In the case illustrated in Fig. 2.2, the secondary peak locations coincide with various spectral lines. This should be

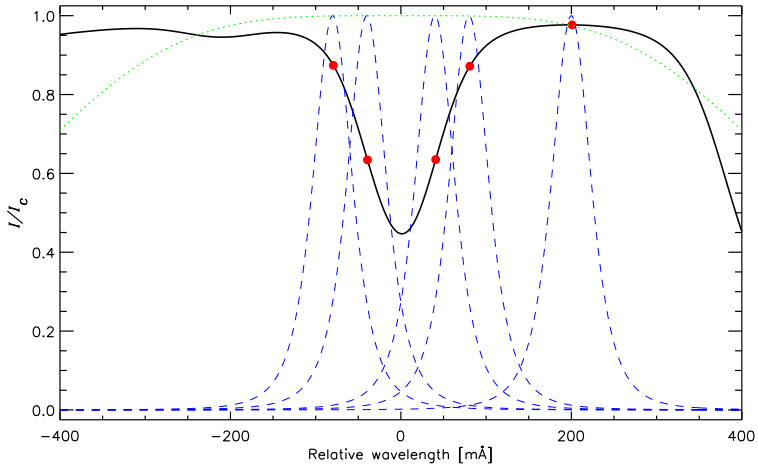

FIGURE 2.3:— Possible observed wavelength samples for the IMaX magnetograph. Wavelength samples are at [-80,-40,40,80,200] mÅ from the reference wavelength of the Fe I 525.06 nm spectral line. The green, dotted line stands for the pre-filter and the dashed ones for the Fabry-Pérot profile at the various sample wavelengths.

avoided whenever possible.

Typical setups for Fabry-Pérot interferometers are collimated or telecentric mountings. For a number of reasons, the selected configuration for IMaX is collimated. This setup generates a wavelength blue shift across the field of view (FOV), but it provides a better spectral resolution and image quality than the telecentric configuration (Kentischer et al. 1998).

The polarimetric modulation analysis and the spectral analysis have to be performed in such a way that the whole process takes the shorter duration possible. Measurements should be carried out in a time shorter than the characteristic variation of solar structures. This is the main reason for limiting the number of wavelength samples that are measured. IMaX will observe five wavelength samples (four within the line plus one in the nearby continuum). To reach a S/N= $10^{-3}I_c$ in the continuum, a given set of measurements (e.g. five wavelengths times four polarization states) should be repeated a number of times, and the resulting images accumulated. Figure 2.3 illustrates how the Fabry-Pérot interferometer will scan the Fe I 525.02 nm spectral line. The green, dotted line illustrates the pre-filter transmission. The blue, dashed lines show the Fabry-Pérot transmission curve tuned to the various wavelength samples. The final transmission is given by the product of the two functions. In this example we have taken the wavelength samples at [-80,-40,40,80,200] mÅ

from the reference wavelength of the line. One of the questions we will be tackling in this thesis (Chapter 9) is whether it is possible (and to which extent) to infer the magnetic field vector and the flow velocity from a spectral line that has been scanned at only a few wavelength points.

2.3 Radiative transfer

In this section we discuss the basic concepts for the radiative transfer through magnetized atmospheres and introduce one of its multiple representations: the Milne-Eddington approximation.

The radiative transfer equation (hereafter referred to as RTE) for polarized light in a plane-parallel atmosphere reads

$$\frac{d\mathbf{I}}{d\tau} = \mathbf{K}(\mathbf{I} - \mathbf{S}), \tag{2.15}$$

where $\mathbf{I} = (I, Q, U, V)^\dagger$ stands for the Stokes vector which gives a full description of the polarization state of light, τ for the continuum optical depth at a reference wavelength, $\mathbf{K}$ for the 4x4 propagation matrix, $\mathbf{S}$ for the source function vector, and $\dagger$ means the transpose. All the medium properties relevant to line formation are contained in $\mathbf{K}$ and $\mathbf{S}$. In local thermodynamic equilibrium conditions (LTE) conditions, $\mathbf{S} = (B_\lambda(T), 0, 0, 0)^\dagger$, where $B_\lambda(T)$ is the Planck function at the local temperature T.

The propagation matrix $\mathbf{K}$ of the RTE can be cast in the form (e.g. del Toro Iniesta, 2003):

$$\mathbf{K} = \begin{pmatrix} \eta_I & \eta_Q & \eta_U & \eta_V \\ \eta_Q & \eta_I & \rho_V & -\rho_U \\ \eta_U & -\rho_V & \eta_I & \rho_Q \\ \eta_V & \rho_U & -\rho_Q & \eta_I \end{pmatrix}, \tag{2.16}$$

where

$$
\begin{aligned}
\eta_I &= 1 + \frac{\eta_0}{2}\left[\phi_p \sin^2\gamma + \frac{\phi_b+\phi_r}{2}(1+\cos^2\gamma)\right], \\
\eta_Q &= \frac{\eta_0}{2}\left[\phi_p - \frac{\phi_b+\phi_r}{2}\right]\sin^2\gamma\cos 2\chi, \\
\eta_U &= \frac{\eta_0}{2}\left[\phi_p - \frac{\phi_b+\phi_r}{2}\right]\sin^2\gamma\sin 2\chi, \\
\eta_V &= \frac{\eta_0}{2}\left[\phi_r - \phi_b\right]\cos\gamma, \\
\rho_Q &= \frac{\eta_0}{2}\left[\psi_p - \frac{\psi_b+\psi_r}{2}\right]\sin^2\gamma\cos 2\chi, \\
\rho_U &= \frac{\eta_0}{2}\left[\psi_p - \frac{\psi_b+\psi_r}{2}\right]\sin^2\gamma\sin 2\chi, \\
\rho_V &= \frac{\eta_0}{2}\left[\psi_r - \psi_b\right]\cos\gamma,
\end{aligned}
\tag{2.17}
$$

and $\phi_{p,b,r}$ and $\psi_{p,b,r}$ are the absorption and dispersion profiles, the p, b, r indices stand for the π and σ components of a Zeeman multiplet, and η_0 is the ratio between the line and continuum absorption coefficients.

$\phi_{p,b,r}$ and $\psi_{p,b,r}$ can be written as a sum of as many absorption and dispersion profiles as the number of p, b, r components as follows:

$$
\begin{aligned}
\phi_j &= \sum_{M_l - M_u = j} S_{M_l M_u, j} \frac{1}{\sqrt{\pi}} H(a, \upsilon), \\
\psi_j &= 2 \sum_{M_l - M_u = j} S_{M_l M_u, j} \frac{1}{\sqrt{\pi}} F(a, \upsilon),
\end{aligned}
\tag{2.18}
$$

$S_{M_l M_u, j}$ being the strength of each component with $j = -1, 0, 1$ corresponding to b, p and r. υ stands for the wavelength shift in Doppler units:

$$
\upsilon = \frac{\lambda - \lambda_0}{\Delta\lambda_{\rm D}} + \frac{\Delta\lambda_{\rm B}}{\Delta\lambda_{\rm D}} - \frac{\lambda_0 \upsilon_{\rm LOS}}{c\Delta\lambda_{\rm D}}. \tag{2.19}
$$

$H(a, \upsilon)$ and $F(a, \upsilon)$ are the Voigt and Faraday-Voigt functions:

$$
H(a, \upsilon) = \frac{a}{\pi} \int_{-\infty}^{\infty} e^{-y^2} \frac{1}{(\upsilon - y)^2 + a^2} dy, \tag{2.20}
$$

$$
F(a, \upsilon) = \frac{1}{\pi} \int_{-\infty}^{\infty} e^{-y^2} \frac{\upsilon - y}{(\upsilon - y)^2 + a^2} dy. \tag{2.21}
$$

The wavelength shift of the different Zeeman components with respect to the original position is given by

$$\Delta\lambda_{\rm B} = \frac{e\lambda_0^2 B}{4\pi mc^2}(g_l M_l - g_u M_u), \tag{2.22}$$

where l and u stand for the lower and upper levels of the line transition, g for the level Landé factor, and M for the magnetic level quantum number; e and m are the electron charge and mass, and c is the speed of light.

2.3.1 The Milne-Eddington approximation

In a Milne-Eddington (ME) model atmosphere, an analytical solution is found for the RTE (see, e.g. Unno 1956; Rachkovsky 1962, 1967; Landolfi & Landi Degl'Innocenti 1982). In such an atmosphere, all the atmospheric quantities are constant with depth except for the source function that varies linearly:

$$\mathbf{S} = \mathbf{S}_0 + \mathbf{S}_1\tau = (S_0 + S_1\tau)(1,0,0,0)^\dagger. \tag{2.23}$$

The propagation matrix is also constant with depth. Following, for instance, the notation in del Toro Iniesta (2003), such an analytical solution reads

$$\begin{aligned} I &= S_0 + \Delta^{-1}[\eta_I(\eta_I^2 + \rho_Q^2 + \rho_U^2 + \rho_V^2)]\, S_1, \\ Q &= -\Delta^{-1}[\eta_I^2\eta_Q + \eta_I(\eta_V\rho_U - \eta_U\rho_V) + \rho_Q\Pi]\, S_1, \\ U &= -\Delta^{-1}[\eta_I^2\eta_U + \eta_I(\eta_Q\rho_V - \eta_V\rho_Q) + \rho_U\Pi]\, S_1, \\ V &= -\Delta^{-1}[\eta_I^2\eta_V + \eta_I(\eta_U\rho_Q - \eta_Q\rho_U) + \rho_V\Pi]\, S_1, \end{aligned} \tag{2.24}$$

with

$$\Delta = \eta_I^2(\eta_I^2 - \eta_Q^2 - \eta_U^2 - \eta_V^2 + \rho_Q^2 + \rho_U^2 + \rho_V^2) - \Pi^2, \tag{2.25}$$

where

$$\Pi = \eta_Q\rho_Q + \eta_U\rho_U + \eta_V\rho_V. \tag{2.26}$$

It can easily be seen that η_I, η_Q, η_U, η_V, ρ_Q, ρ_U, and ρ_V, and hence the solution depend on just nine parameters, namely, on (B, γ, χ), the three components of the vector magnetic field, on S_0, S_1, the two parameters describing the source function, on η_0, the line-to-continuum absorption coefficient ratio, on $\Delta\lambda_{\rm D}$, the Doppler width of the line, on the damping parameter a, and on the line-of-sight velocity, $v_{\rm LOS}$.

3

ME Response Functions and their practical applications

In this chapter we aim at introducing analytical response functions and their main properties as an important diagnostic tool that help understand Stokes profile formation physics and the meaning of well-known behaviors of standard inversion codes of the radiative transfer equation often used to measure solar magnetic fields. We also show that response functions are helpful in selecting sample wavelengths optimized for specific parameter diagnostics and to estimate the minimum values for the model parameters that can be discriminated from noise.

3.1 Introduction

The adventure of diagnosing the solar atmosphere from spectropolarimetric observations is one of the most challenging subjects of solar physics nowadays. Both the theoretical understanding of the physical processes taking place in the photosphere and the design of new instrumentation that improve our capabilities of getting more and better information from the Sun can benefit from a thorough study of the radiative transfer equation (RTE) which is, in fact, the only tool we have to describe the problem mathematically. Approximations of a variety of types have been devised so far to tackle the tasks depending on both the observational and the *post-facto* computational capabilities. Very remarkably, the Milne-Eddington (ME) approximation has provided for long a

good means for gaining insight into the physical processes taking place in line formation and inferring accurate values of several physical parameters of the solar atmosphere. Its specific analytical character is its most powerful feature that implies a remarkable practical usefulness.

A physical analysis of the sensitivities of spectral lines in terms of analytic mathematical functions is still missing in the literature and certainly promises to provide an insight on how the solar parameters influence the shape of the observed Stokes profiles of these spectral lines and explanations for several (at least, if not all) trade-offs and other well-known behaviors of inversion codes currently used for the inference of such solar atmospheric parameters. Here we introduce the *analytic* response functions (RFs) of Stokes profiles as formed in ME model atmospheres and thoroughly discuss their main properties.

Weighting functions for unpolarized light (Mein 1971) were the precursors of RFs, extended to polarized light by Landi Degl'Innocenti & Landi Degl'Innocenti (1977). As explained by Ruiz Cobo & del Toro Iniesta (1994; see also del Toro Iniesta 2003), RFs provide the sensitivities of Stokes profiles to the various atmospheric quantities playing a role in line formation. Since all these quantities are constant with depth in a ME atmosphere, ME RFs are simply partial derivatives of the analytic solution of the RTE with respect to the model parameters. This feature enables us to deduce analytic formulae for the sensitivities (they are explicitly written in Appendix A) and to study their characteristics and properties. Such properties are shown to be useful in practice for understanding the behavior of spectral lines as well as for helping in line and sample selection when designing new instruments.

In this chapter we firstly introduce the concept of response functions in a Milne-Eddington atmosphere and present their analytical formulation. We then use a simple ME model atmosphere to discuss on the main qualitative properties of the RFs through a sample spectral line (Sec. 3.2). The usefulness of the RFs for selecting the wavelength samples and number of wavelength points to be observed by vector magnetographs are discussed on Sec. 3.3. Their ability to estimate minimum detectable values of various model parameters is discussed on Sec. 3.4. Finally, we summarize the main conclusions in Sec. 3.5.

3.2 The response functions in a Milne Eddington atmosphere

3.2.1 Milne-Eddington response functions

According to Ruiz Cobo & del Toro Iniesta (1994) (see also del Toro Iniesta & Ruiz Cobo 1996; del Toro Iniesta 2003) the sensitivity of the Stokes profiles to perturbations of the atmospheric physical quantities is given by the response functions (RFs). These response functions can be written as:

$$\mathbf{R}_i(\tau_c) \equiv \mathbf{O}(0,\tau_c)\left[\mathbf{K}(\tau_c)\frac{\partial \mathbf{S}}{\partial x_i} - \frac{\partial \mathbf{K}}{\partial x_i}[\mathbf{I}(\tau_c) - \mathbf{S}(\tau_c)]\right], \tag{3.1}$$

with $\mathbf{O}(0,\tau_c)$ being the evolution operator from τ_c to the surface, $\mathbf{K}$ the propagation matrix and $\mathbf{S}$ the source function vector.

Fortunately, in the specific case of constant quantities (model parameters) with depth, as is the case of a ME atmosphere, such RFs are the partial derivatives of the Stokes vector with respect to the corresponding model parameter:

$$\mathbf{R}_x(\lambda) = \frac{\partial \mathbf{I}(\lambda)}{\partial x}, \tag{3.2}$$

where x represents any of the model parameters.

Therefore, by simply taking derivatives of the analytical solution (2.24), the sensitivities of the Stokes profiles to perturbations of the ME model parameters can be found (see Appendix A for explicit formulae). Note that these sensitivities are the only tools we have to evaluate our ability for determining the various quantities: should the $\mathbf{I}$ Stokes vector not vary after a perturbation of a parameter, x, we would be unable to infer it from the observations (it would not be a proper model parameter, indeed).

3.2.2 Line sensitivities: the shape of RFs

Equations (2.24) and (3.2) provide all the necessary means for studying the behavior of the ME Stokes profiles. Fortunately, the shapes of RFs do not vary dramatically either from model to model or from line to line. In fact, the RFs look homologous to each other. This property allows us to choose a single line to illustrate the practical usefulness of our functions. Let us take the Fe I line at 525.064 nm as an example. We selected this line because it was one of the candidates lines to be used by the IMaX magnetograph (Martínez Pillet et al. 2004) and some of the results may have implications either for the design or for the analysis of the data to be obtained with this magnetograph. The

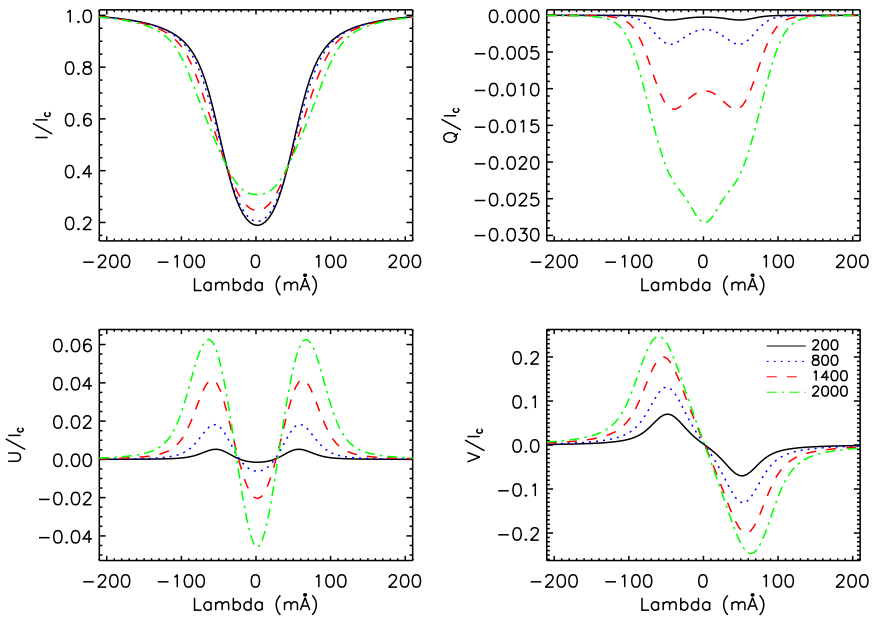

FIGURE 3.1:— Stokes I, Q, U and V, for the Fe I line at 525.06 nm, with a magnetic inclination and azimuth of 45 degrees. Different lines stand for different magnetic field strength values. The Stokes parameters are normalized to the local continuum.

line has an effective Landé factor of 1.5 and is often considered to be quite insensitive to temperature perturbations (e.g., Stenflo et al. 1984). A single model is also enough for our purposes. To construct it we have used the NSO Fourier Transform Spectrometer atlas as a reference spectrum and then the line has been fit with success (yielding errors smaller than a 2%; see Chapter 4 for further details about the inversion procedure). The resulting model parameters are: $S_0 = 0.02$, $S_1 = 1$, $\eta_0 = 7.2$, $a = 0.3$, $\Delta\lambda_D = 30$ mÅ and a macroturbulent velocity, $v_{\rm mac} = 0.37$ km/s. Unless otherwise stated, all the numerical examples that follow in this Chapter refer to this line and this model. Several magnetic field strengths (200, 800, 1400 and 2000 G) have been used to synthesize the Stokes profiles and their RFs, assuming a constant field inclination and azimuth of 45°.

Fig. 3.1 shows the synthesized Stokes profiles. It can be seen how, as the magnetic field increases, the Stokes V lobes increase but their peaks do not separate much because the strong field regime has not been reached for this line with these strengths. In Fig. 3.2, we find a graphical illustration of the analytical RFs of the four Stokes parameters to magnetic field strength per-

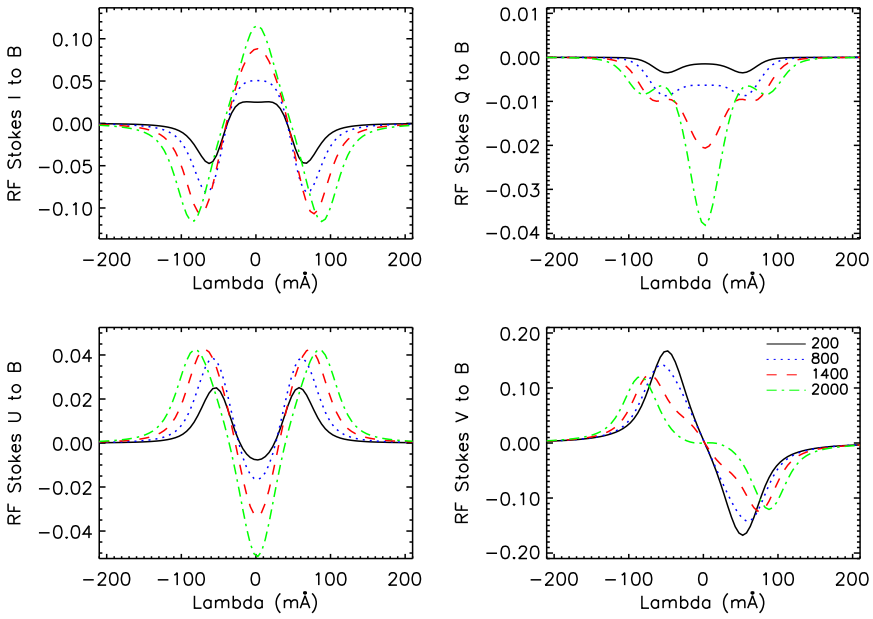

FIGURE 3.2:— Analytical ME RFs of Stokes I, Q, U and V to magnetic field strength for the Fe I line at 525.06 nm, with a magnetic inclination and azimuth of 45°. Different lines stand for different magnetic field strength values. Units are 10^{-3} G^{-1}.

turbations. By simply looking at these RFs, different properties can be drawn. Note that both the Stokes profiles and the RFs present wavelength symmetry properties, as expected from a ME model atmosphere. The RFs to the magnetic field strength preserve the Stokes profile symmetries whilst velocity RFs display opposite parity (see Fig. 3.3).

As can be seen in Fig. 3.2, the most evident property is that the response of the line is wavelength dependent. Different wavelength positions have different sensitivities. Within a single Stokes profile different wavelength samples react differently to the same perturbation. Some of the samples, in fact, are insensitive. For instance, in this numerical example the Stokes V zero-crossing point remains the same independently of B and, hence, the response is zero at this wavelength. All the RFs show peaks corresponding to different maxima and minima. Note that these extrema pinpoint where the Stokes profiles are more sensitive to perturbations of the physical quantity: the bigger the peak, the larger the sensitivity.

Remarkably, although Stokes I, Q and U are more sensitive to B perturbations when the strength is higher, the Stokes V profile sensitivity to field

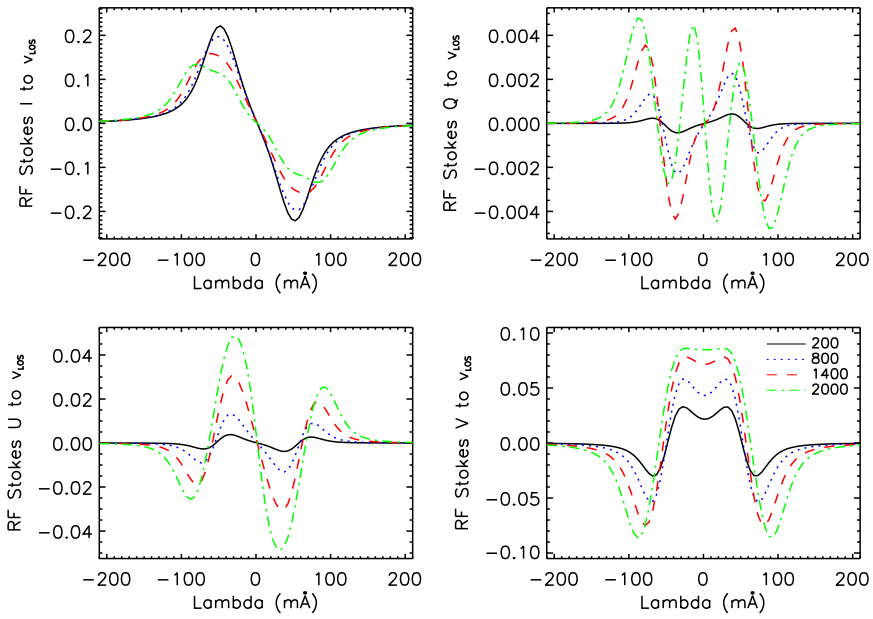

FIGURE 3.3:— Analytical ME RFs of Stokes I, Q, U and V to LOS velocity for the Fe I line at 525.06 nm, with a magnetic inclination and azimuth of 45 degrees. Different lines stand for different magnetic field strength values. Units are $[\mathrm{km/s}]^{-1}$.

strength perturbations is maximum for the weak fields and decreases while increasing the field strength. This effect can easily be understood: in the weak field regime, Stokes V is proportional to B and any change of B is translated directly to an increase (or a decrease) of the V signal; when the field increases, however, a competition between increasing the profile and peak separation becomes important; finally, at a given B value peaks will no longer increase but just separate from each other. This behavior of Stokes profiles is known for long but a glance to the Stokes V panel of Fig. 3.2 illustrates it in a very clear way. Moreover, the significant sensitivity of Stokes V in the weak field regime provides a solid argument to understanding the reasonably accurate inversion results for weak magnetic fields obtained in numerical experiments by Westendorp Plaza et al. (1998).

Fig. 3.3 shows the Stokes RFs to LOS velocity. The first clear feature in this figure is that neither the sizes nor the shapes depend on the LOS velocity. The latter only shifts the RFs as it does with the profiles. The RF size is larger for Stokes I and V than for Stokes Q and U, simply because of the corresponding size of the profiles. Since Stokes I and V are larger than Stokes Q and U in

this example, most information on velocities is carried by I and V. The LOS velocity can always be well determined because the loss of sensitivity to $v_{\rm LOS}$ perturbations of the Stokes I profile is compensated by that of the V profile.

The Stokes I RF to LOS velocity perturbations decreases with B while the Stokes Q, U, and V RFs increase. This result is mostly due to the different shape ratios of the various profiles. According to Cabrera Solana, Bellot Rubio, and del Toro Iniesta (2005), the spectral line sensitivity to the LOS velocity is mostly determined by the ratio between the width and the depth of the line. It is clear that the larger the field strength, the wider and shallower the Stokes I profile. Therefore, its sensitivity to $v_{\rm LOS}$ perturbations decreases with increasing B. Each lobe of Stokes V, however, first becomes bigger and then narrower and steeper at the central wavelength as B increases. Hence its larger sensitivity to $v_{\rm LOS}$ for stronger field strengths.

The relative maxima of the RFs to LOS velocity perturbations correspond to wavelength positions where the inflection points of the Stokes profiles are located and independently of the model atmosphere and spectral line. For instance, the minimum of Stokes I and the peaks of Stokes V correspond to zeros on the corresponding RFs to LOS velocity, therefore regions where the Stokes profiles do not change while LOS velocity does.

The extrema of the RFs to B and to $v_{\rm LOS}$ perturbations do not coincide with those of the corresponding profiles. This fact can be clearly seen in, e.g., the bottom right panels of Figs. 3.2 and 3.3. Therefore, the extrema of the Stokes profiles are not carrying, in principle, more information on given parameters than any other particular wavelength sample. Another very interesting feature is that, for a given spectral line, the RFs differ from each other. RFs to magnetic field strength perturbations do not resemble those to LOS velocity perturbations (compare Figs. 3.2 and 3.3). For instance, their maximum sensitivities (RF peaks) are placed at different wavelengths. These differences among RFs help disentangle the influences on spectral line formation of the various model quantities and, allow inversion algorithms based on RFs (e.g., SIR by Ruiz Cobo & del Toro Iniesta 1992) to get accurate results: if a given Stokes profile is useless at a particular wavelength sample, other profile or wavelength sample provides the required information. RF differences can also be seen for the other ME parameters except for $\Delta\lambda_{\rm D}$, η_0 and a. The RFs to these thermodynamic parameter perturbations are very similar to each other as can be seen in Fig. 3.4. A small perturbation of any of these three parameters produces a modification in the Stokes profiles that is very similar to the changes produced by small perturbations of the other two. These similarities between the $\Delta\lambda_{\rm D}$, η_0 and a RFs explain the trade-offs often observed in ME inversions among them. Fortunately, their RFs are different enough from those

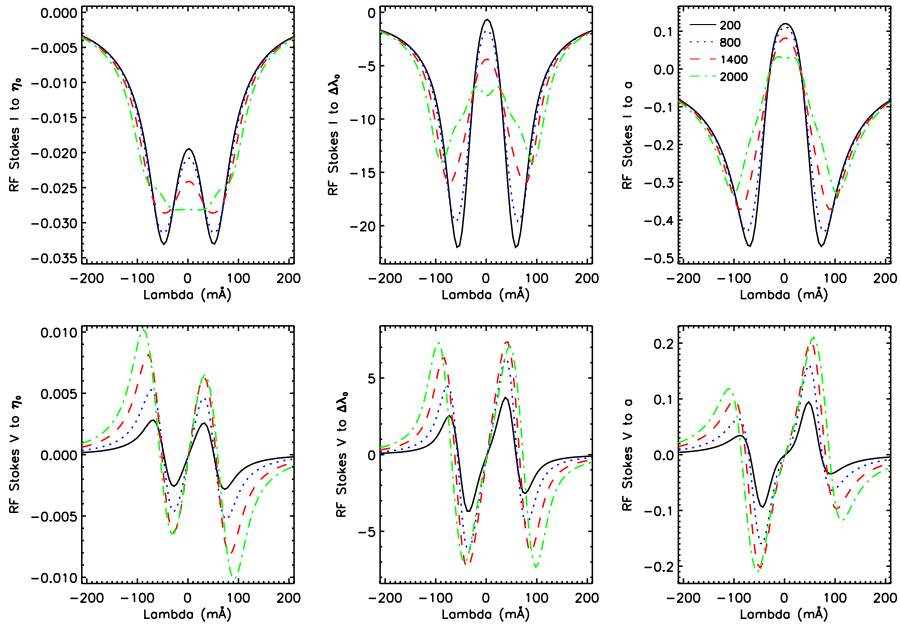

FIGURE 3.4:— Analytical ME RFs of Stokes I (upper panels) and V (bottom panels) to η_0, to $\Delta\lambda_D$ and to a (left, middle and right panels respectively), for the Fe I line at 525.06 nm, with a magnetic inclination and azimuth of 45 degrees. Different lines stand for different magnetic field strength values. Units are none for the left and right panels since η_0 and a are dimensionless. Units for the middle panels are Å^{-1}. Note the similarities among the different RFs.

of the other model parameters as for them to be accurately retrieved (see, e.g., Westendorp Plaza et al. 1998). In other words, we can say that the ME model atmosphere, although providing a probably too simplistic scenario for the line formation which may not give full account of thermodynamic properties, allows fairly accurate inferences of constant magnetic field vector $\mathbf{B}$, $v_{\rm LOS}$, S_0 and S_1.

Remarkably, the RFs to magnetic field inclination and azimuth perturbations do not depend on the derivatives of the absorption and dispersion profiles; thus, the shapes of the RFs are very similar to the corresponding Stokes profiles (see Fig. 3.5). Of course, only Stokes Q and U respond to azimuth perturbations. The larger the field strength, the larger the sensitivity of the Stokes profiles to γ and χ perturbations. This is again an explanation of a well known fact: we measure γ and χ better when B is strong.

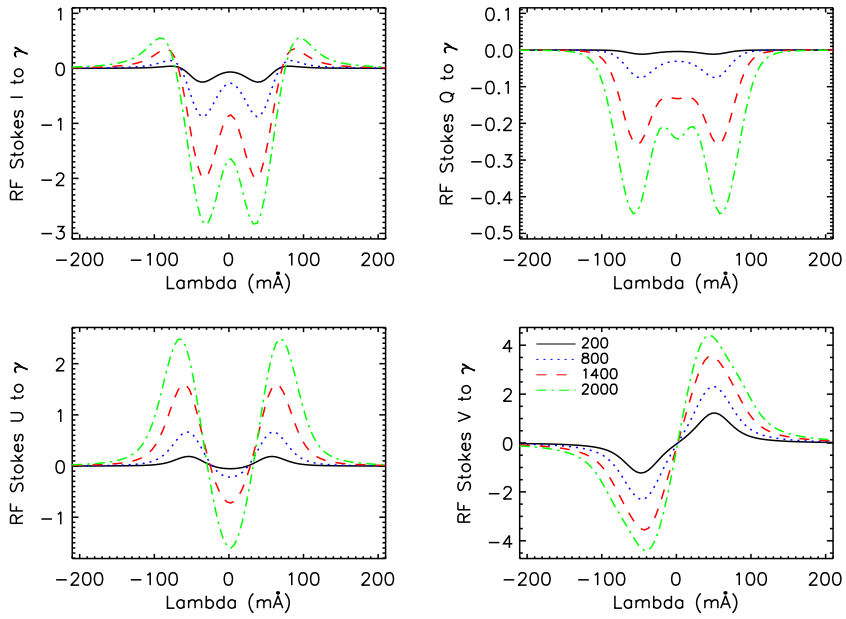

FIGURE 3.5:— Analytical ME RFs of Stokes I, Q, U and V to magnetic field inclination, γ, for the Fe I line at 525.06 nm, with a magnetic inclination and azimuth of 45 degrees. Different lines stand for different magnetic field strength values. Units are in 10^{-3} [degrees]$^{-1}$.

3.2.3 Relative response functions

So far we have only discussed about "absolute" RFs, i.e., functions with dimensions; e.g., the RF to B is measured in G^{-1}, that to $v_{\rm LOS}$ perturbation is measured in (km s^{-1})$^{-1}$ and so on: RFs give modifications of the profile per unit perturbation of the parameter. To compare them to one another, relative RFs should be used (Ruiz Cobo & del Toro Iniesta 1994; del Toro Iniesta & Ruiz Cobo 1996). These ME relative responses are obtained by multiplying the standard, absolute RFs by the corresponding model parameter. Relative RFs tell us how much sensitive is one model parameter compared with the others. For instance, the relative RF to $\Delta\lambda_{\rm D}$ is much larger than that to η_0 and that to a (in particular three times as large as the RFs to η_0 and twenty times larger than those to a for Stokes I, in our sample ME atmosphere). This means that a small relative perturbation of $\Delta\lambda_{\rm D}$ changes the Stokes profiles much more than the same relative perturbation of η_0 or a. Consequently, $\Delta\lambda_{\rm D}$ should be better determined by ME inversion codes.

3.2.4 Two-component model atmospheres

Model atmospheres with two or more components are commonly used in the analysis of observations. Any two-component model atmosphere is based on the assumption that within the resolution element two different atmospheres coexist, namely, one magnetic atmosphere filling a surface fraction f, and one non-magnetic atmosphere filling the remaining $(1-f)$ fraction. f is called the magnetic filling factor. If $\mathbf{I}_{\rm m}$ stands for the Stokes profile vector emerging from the magnetic region and $\mathbf{I}_{\rm nm}$ for that of the non-magnetized atmosphere, the observed Stokes vector can be written as $\mathbf{I} = (1-f)\mathbf{I}_{\rm nm} + f\mathbf{I}_{\rm m}$.

Thus, according to Eq. (3.2), the RFs to f perturbations are given by $\mathbf{I}_{\rm m} - \mathbf{I}_{\rm nm}$. Hence, the largest the difference between the magnetic and the non-magnetic atmospheres, the biggest the sensitivity to f. But this is once more a known fact: since most of the differences is the polarization signal itself, $Q_{\rm m}$, $U_{\rm m}$, $V_{\rm m}$, when this signal is strong we can easily discern it from the non-magnetic signal.

3.2.5 The influence of smearing

Spectral line smearing by macroturbulence is a well known effect that needs be taken into account in the analysis of most observations except, perhaps, in those with very high spatial resolution (Asplund et al. 2000). Besides macroturbulence, instruments have finite-width profiles that produce smearing of the observed Stokes profiles which become wider and with smaller peaks. This smearing reduces the information on physical parameters carried by the spectral line through convolution: $\mathbf{I}_{\rm obs} = \mathbf{I} * F(\lambda)$, where * stands for the convolution symbol and the scalar smearing profile, $F(\lambda)$, is convolved with all the four Stokes parameters.

This loss of information through smearing is also translated into a loss of sensitivity of spectral lines to the atmospheric quantities. In fact, since the derivative of a convolution is equal to the convolution of the derivative of one of the functions with the second one, response functions become smeared as well:

$$\mathbf{R}_{{\rm obs},x} = \mathbf{R}_x * F(\lambda). \tag{3.3}$$

Figure 3.6 shows the effect of RF smearing. The convolved RFs are smoother and significant information is lost.

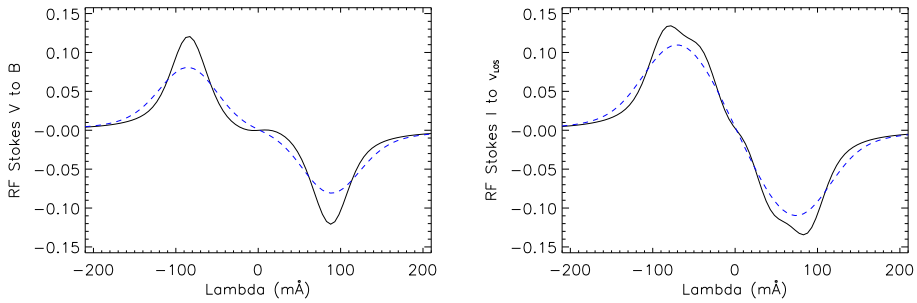

FIGURE 3.6:— Analytical ME RFs of Stokes V to the magnetic field strength (left panel) and of Stokes I to the LOS velocity (right panel) for the Fe I line at 525.06 nm, with a magnetic field strength of 2000 G and field inclination and azimuth of 45 degrees. The dashed lines correspond to the RFs convolved with a Gaussian smearing profile of 60 mÅ of full width at half maximum (FWHM). Solid lines correspond to the original RFs. Units are in 10^{-3} G^{-1} (left) and [km/s]$^{-1}$ (right).

3.3 Detectable dissimilarities between weak and strong fields

Consider two ME atmospheres whose thermodynamic parameters are the same. Let us take for instance those coming from a fit to the FTS, quiet Sun spectrum of the Fe I line at 630.25 nm. Two different atmospheres will be built by assuming a different magnetic field strength: 200 and 1500 G. The magnetic inclination and azimuth, γ and ϕ, are taken equal to 45° for both model atmospheres. The specific values have nothing to do with the qualitative results and, in fact, are pretended to be representative of the general problem. From these two atmospheres different Stokes profiles emerge as can be seen in Fig. 3.7. Solid and dotted lines correspond to the weak and strong field cases, respectively. The shapes of the profiles are clearly dissimilar and the Zeeman splitting is more conspicuous for the strong-field profiles. A filling factor unity is assumed in both cases. The differences are so significant that distinguishing between the two cases is fairly easy. Inversion techniques should have no problem in inferring either of the two models.

It can be argued that a filling factor $f = 0.133$ in the strong-field case would be equivalent to the weak-field atmosphere because the magnetic flux is the same in the two models. Nevertheless, as can also be seen in Fig. 3.7, the differences can be as large as 1% in Stokes Q, as 2% in Stokes U, and as 8–10% in Stokes I and V. Hence, the differences are between one to two orders of magnitude larger than the typical noise ($10^{-3}I_c$) achievable by modern

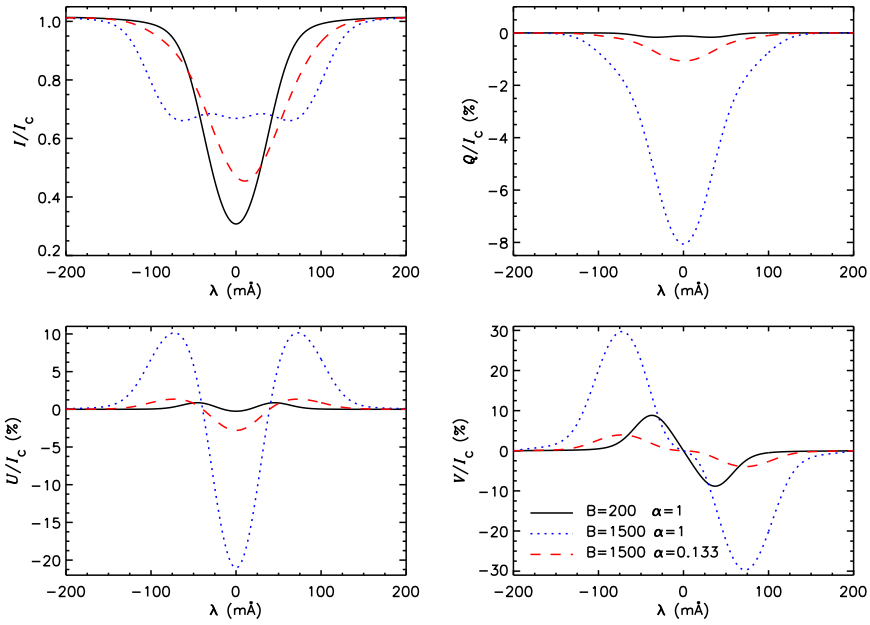

FIGURE 3.7:— Emergent ME Stokes profiles from three different atmospheres with the same thermodynamic parameters. Differences lie on their magnetic field strength and filling factor. Check line coding in the figure inset (right, bottom panel).

spectropolarimeters and are thus discernible by current inversion codes. Of course, our conclusion depends on the validity of the scenario as the belief on the better accuracy for the flux determination lies in the proportionality between magnetic flux and Stokes V. This proportionality is true in a very narrow range of values or the field strength, however. We know, indeed, that strict proportionality only takes place while second-order effects are negligible; but the mere existence of linear polarization breaks this condition: Stokes Q and U are of second order (Landi degl'Innocenti 1992). This means that wherever we measure linear polarization, the proportionality is not exact and second-order effects are enough for the accuracy of inferences as soon as they are bigger than the noise. Eventual mistakes (e.g., disproportionally large field strengths with extremely small filling factors) obtained with actual inversion codes cannot then be ascribed to intrinsic difficulties based on radiative transfer theory but to specific numerical and/or programming problems.

The more important feature from the measurement point of view, however, is the sensitivities of the profiles as shown in Sect. 3.2.2. The different RFs represent weak- and strong-field models (with field strengths varying from 200

to 2000 G). A spectral line responds differently in each model to a given perturbation of the atmospheric parameters. Also, the various wavelengths react differently to the same perturbation in the two field regimes. This is the key feature for inversion codes to discriminate between the two models.

The relative accuracies of inferences in the two field regimes lie on their relative sensitivity or RF values. Contrary to common beliefs, such differences in sensitivity are less than one order of magnitude in terms of the continuum intensity. This means that small factors equal the maximum RF values of each model: that is, 3 G can be as significant in one of the models as 1 G is in the other. The maximum sensitivity is even larger for Stokes Q and V in the weak model than in the strong model. Moreover, it is not only the maximum sensitivity what matters but the effect of the whole profile. Indeed, inferences in the weak-field case can eventually be more accurate as we are going to see in the next section. The point we want to stress in here is the fact that the neat shape differences of the RFs ease the tasks of inversion codes in disentangling strong from weak magnetic fields. This is a similar situation to that giving rise to a discrimination between the magnetic and dynamic parameters from the thermodynamic parameters in ME inversions (Sect. 3.2.2; Orozco Suárez, & del Toro Iniesta 2007).

The fact that filling factor and magnetic field strength influence differently the Stokes profiles can also be assessed with RFs. As shown in Fig. 3.8, in the weak field model the sensitivity of Stokes V (the same occurs for Stokes Q and U) to f perturbations has exactly the same shape than the sensitivity to B perturbations. This is so because V scales with both f and B. (Both RFs have a V-shaped profile.) This is not the case, however, for Stokes I: the RFs of Stokes I to f and B are very different. Since the observed spectrum is a linear combination of the magnetic and non-magnetic atmospheres, as shown in Sect. 3.2.2, the RF to f perturbations is simply the difference between the magnetic and non-magnetic Stokes profiles and hence has a V-like shape. Therefore, in Stokes I the reliability of the two-case separation is rooted. The intensity cannot be fitted by modifying one of the two parameters regardless of the other.

3.4 The usefulness of the RFs for designing instruments

Modern vector magnetographs are not restricted to one or two wavelength samples as the classical ones. Instruments like IMaX are devised to measure up to five wavelengths: one in the continuum and four across the line profile.

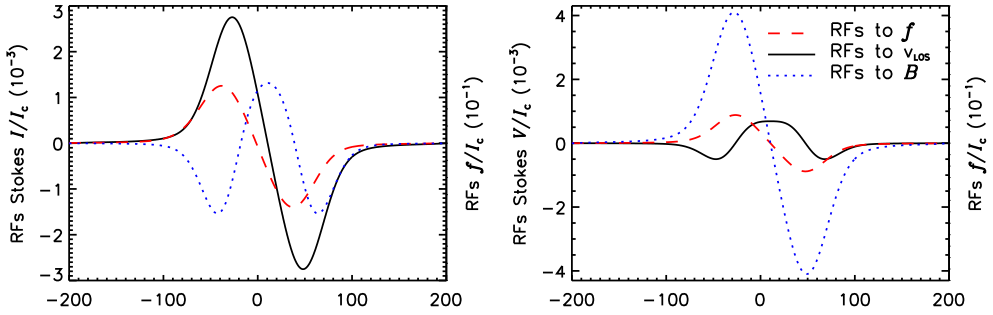

FIGURE 3.8:— Stokes I (*left*) and V (*right*) RFs to $v_{\rm LOS}$(solid, black lines), to B (dotted, blue lines), and to f (dashed, red lines) in the weak-field case ($B = 200$ G). Perturbations of 10 m s^{-1}for $v_{\rm LOS}$, of 10 G for B, and of 0.1 for f have been assumed.

The choices of the spectral line, of the number of samples and of the precise wavelength for each of them are important issues that arise during the design phase of the instrument. This section is aimed at illustrating how RFs can help make such decisions relevant to the instrument development.

Finding a suitable spectral line is crucial and can be achieved through RFs on the simple phenomenological model by Cabrera Solana et al. (2005) that allows establishing a ranking of sensitivities to the different atmospheric parameters among the various lines considered. The IMaX Fe I line at 525.064 nm[1] line can be seen in Fig. 3.9. Data for this line have been included in the original figure by Cabrera Solana et al. (2005), where it is identified as one of the most sensitive of the set to velocity perturbations. It has a medium sensitivity to magnetic field strength perturbations in both the strong and the weak field regimes. However, it is not very sensitive to temperature (not shown) and, hence, a good candidate for inferences in the various solar structures avoiding thermodynamical trade-offs. The Helioseismic and Magnetic Imager (HMI; Scherrer & SDO/HMI Team 2002) and the Polarimetric and Helioseismic Imager (PHI, a proposal for the Visible-light Imager and Magnetograph; Marsch et al. 2005), two planned instruments for the *Solar Dynamics Observatory*, NASA, and the *Solar Orbiter*, ESA, missions respectively, will use the Fe I line at 617.334 nm. This spectral line is very well ranked in Fig. 3.9 for inferences of both magnetic field strengths and LOS velocities.

A minimum number of wavelength samples is obtained by roughly doubling the free parameters of the model: since a ME model is made up with just ten

[1]This line was the principal candidate to be observed with the IMaX instrument. By the time of this thesis, the line has been changed to its neighbor Fe I line at 525.02 nm. The analysis in this section is straightforwardly applicable to other lines.

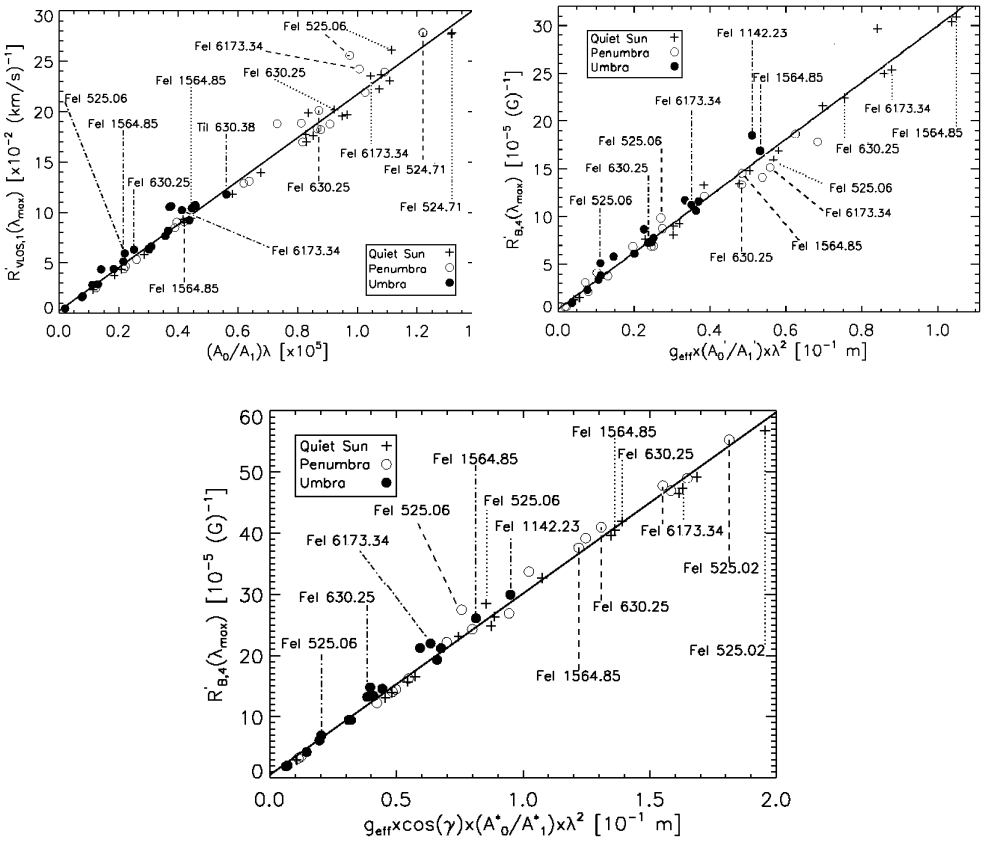

FIGURE 3.9:— *Upper left*: Maximum value of the integrated RF to $v_{\rm LOS}$ for different lines as a function of the shape ratio multiplied by the central wavelength of the transition (see Cabrera Solana et al. 2005). *Upper right*: Maximum values of the integrated RF to B for the same set of lines with $g_{\rm eff}\neq 0$, as a function of the shape ratio multiplied by the squared central wavelength (strong field regime). *Bottom panel*: Maximum values of the integrated RF to B (weak field regime). The sensitivities have been evaluated in the quiet Sun (crosses), penumbral (circles) and hot umbral (filled circles) model atmospheres. Dotted, dashed, and dash-dotted lines mark specific transitions in the quiet sun, penumbral, and umbral models, respectively.

parameters, a minimum of twenty observables (five wavelength times the four Stokes parameters) is needed. This is the choice for all the three instruments mentioned above. Unfortunately, no purely objective means exist to select the wavelengths for the samples. Nevertheless, RFs are a powerful tool that help selecting those wavelengths that better suit our purposes. If one is interested, for instance, on just the magnetic field strength and neglect the other physical quantities, choosing those wavelengths where the RFs to B reach local maxima

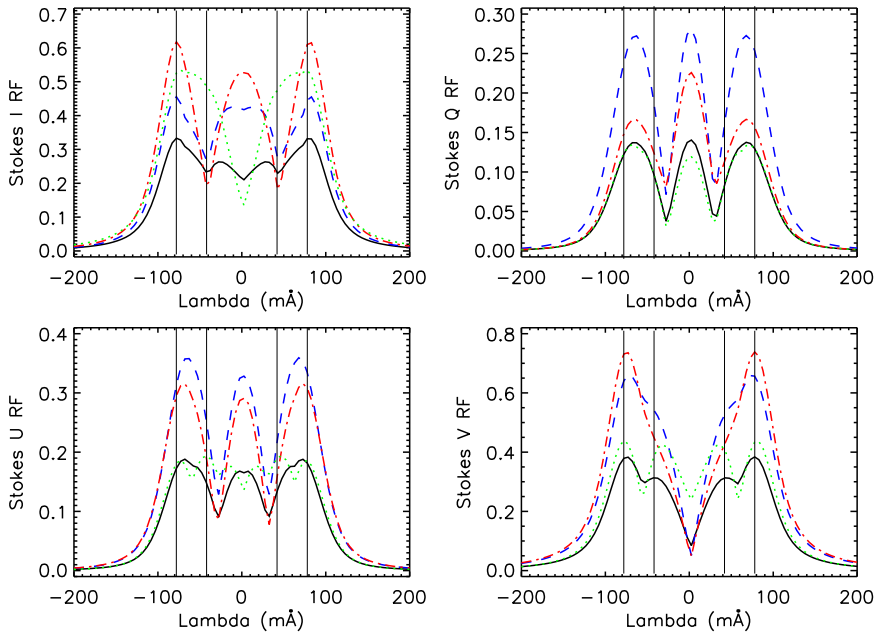

FIGURE 3.10:— Four different linear combinations of the Stokes vector RFs for the IMaX line. The plotted curves correspond to $\beta_{1,2,3,4} = 1, 1, 1, 1$ (solid, black lines), $\beta_{1,2,3,4} = 2, 2, 2, 0.5$ (dashed, blue lines), $\beta_{1,2,3,4} = 3, 1, 1, 0.5$ (dashed-dotted, red lines), and $\beta_{1,2,3,4} = 0.5, 1, 1, 3$ (dotted, green lines). The light-grey, vertical lines indicate a possible choice for wavelength sampling ($\pm 42, 78$ mÅ).

would be advisable. If the interest lies on several physical quantities at the same time (e.g. on the three components of the magnetic field and on the LOS velocity) we suggest the use of a linear combination of regular RFs weighted according to the specific interests. In fact, since RFs can be positive or negative, we propose the use of absolute-valued RFs. Hence, we suggest to consider

$$\mathcal{R}_j = \sum_i \beta_i \, |R_{j,i}|, \tag{3.4}$$

where j runs from 1 through 4, corresponding to the four Stokes parameters, and index i accounts for the physical parameters. Since the set of weights β_i can be tailored at will, there is no single choice for samples but an examination of $\mathcal{R}$ provides important hints for the selection. As an example, Fig. 3.10 shows different such linear combinations for the IMaX line case. If index i runs from 1 through 4 standing for B, γ, χ, and $v_{\rm LOS}$, respectively, the plotted curves correspond to $\beta_{1,2,3,4} = 1, 1, 1, 1$ (solid, black lines), $\beta_{1,2,3,4} = 2, 2, 2, 0.5$ (dashed, blue lines), $\beta_{1,2,3,4} = 3, 1, 1, 0.5$ (dashed-dotted, red lines), and $\beta_{1,2,3,4} = 0.5, 1, 1, 3$

(dotted, green lines). The vertical lines indicate a possible choice for wavelength sampling ($\pm 42, 78$ mÅ), selected mostly from the properties of the Stokes I and V RFs since these two parameters usually exhibit the largest signals in solar atmospheres. While the most external samples seem to be quite optimum, some other good choices for the inner wavelengths are possible and up to the user.

3.4.1 Noise and inference accuracy

Stokes profiles are affected by the noise intrinsic to the observational process. Should the polarimetric signal be buried by noise, any algorithm one could devise to determine atmospheric quantities would dramatically fail. Therefore, our abilities for inferring accurate solar parameters depend significantly on the signal-to-noise ratio of the observations.

Response functions can help in quantifying this effect. In fact, since RFs simply provide the modification of the Stokes profiles after a perturbation of the physical quantities, if that modification is smaller than the noise level it will be effectively undetectable. In other words, the size of RFs to perturbations of a given quantity sets a threshold for the detection of a unit of such a quantity: for instance, according to Fig. 3.2, 1 G will only be detectable by a single wavelength sample if noise is below $1.5{\cdot}10^{-4}$ (continuum intensity is at 1); within the linear approximation[2], 10 G will be detectable with a noise below $1.5{\cdot}10^{-3}$ and so on.

In any case, what matters is the whole profile (or the whole set of samples). Single sample determinations will certainly be less accurate. In what follows we are providing an estimate on how noise influences the accuracy in the parameter inferences.

Assume that all inaccuracies in the m physical parameters contribute in a similar amount to the final noise. (In reality, our assumption is that noise imparts equally distributed inaccuracies to the m searched-for parameters.) In such a case, the variance of the j wavelength sample in the i-th Stokes parameter[3] can be written as

$$\sigma_{i,j}^2 = m f^2 (R_{i,j}^x)^2 \sigma_x^2, \tag{3.5}$$

where f stands for the magnetic filling factor, $R_{i,j}^x$ is the RF of Stokes i at wavelength j to perturbations of the x model parameter, and σ_x^2 is the variance of that parameter. Summing up for all Stokes parameters and wavelengths,

[2] RFs come in fact from a linear perturbation analysis of the radiative transfer equation

[3] Index i runs from 1 through 4, corresponding to Stokes I, Q, U, and V, respectively.

Eq. (3.5) becomes

$$\sum_{i=1}^{4}\sum_{j=1}^{n_\lambda}\sigma_{i,j}^2 = mf^2\sigma_x^2\sum_{i=1}^{4}\sum_{j=1}^{n_\lambda}(R_{i,j}^x)^2, \tag{3.6}$$

where n_λ is the total number of wavelength samples.

According to del Toro Iniesta & Collados (2000), if all the modulated measurements (n_p) needed to derive the Stokes parameters have the same variance, σ^2, due, for instance, to photon noise, then

$$\sigma_{i,j}^2 = \frac{1}{n_p}\frac{\sigma^2}{\epsilon_i^2}, \forall j = 1,\ldots,n_\lambda, \tag{3.7}$$

where ϵ_i is the polarimetric efficiency of the i-th Stokes parameter.

After Eq. (3.7), the inaccuracy of the x parameter can finally be cast as

$$\sigma_x = \frac{\sqrt{n_\lambda\sum_{i=1}^{4}(1/\epsilon_i^2)}\,\sigma}{f\sqrt{n_p m}\sqrt{\sum_{i=1}^{4}\sum_{j=1}^{n_\lambda}(R_{i,j}^x)^2}}. \tag{3.8}$$

The above formula gives an estimate for the noise-induced, i.e. random, effects and no systematic errors are included. It illustrates very well how the noise on the (modulated) polarization measurement influences directly the accuracy in any inferred parameter. Obviously, the better the polarimetric efficiencies of the instrument, the smaller the inaccuracies. That is also the case for RFs: the larger the RFs (the sensitivity) the smaller σ_x.

Finally, notice that this representation holds when dealing with Stokes profiles that can be satisfactorily represented with ME models. In any other case, it simply represents the *minimum* confidence limits.

3.4.2 Practical examples

As a practical example, let us consider the proposed wavelengths on Sec. 3.4, i.e., four wavelength samples across the line plus one in the continuum (-78, -42, 42, 78 and 300 mÅ). Let us assume an instrumental filter of FWHM 60 mÅ (as for IMaX) described by a Gaussian function and a noise level $\sigma = 10^{-3}I_c$. By appropriately substituting the values of the RFs on Eq. (3.8), and assuming $m = 9$ and $f = 1$, we can evaluate the minimum detectable values for the model parameters. For instance, Fig. 3.11 illustrates the results of such a numerical

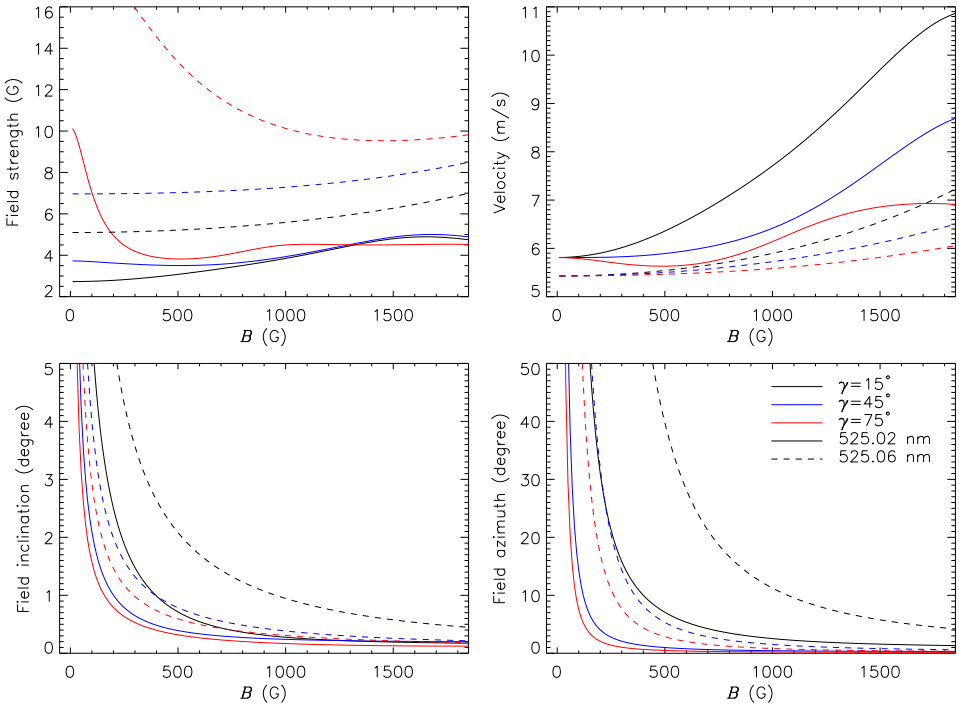

FIGURE 3.11:— Minimum detectable magnetic field strength, field inclination and azimuth, and LOS velocity as a function of the magnetic field strength. Different line shapes stand for two different spectral lines.

experiment, for the magnetic field strength, its inclination and azimuth and for the LOS velocity as a function of the magnetic field strength. Different colors stand for three different configurations of the magnetic field vector. The solid and dashed lines stand for the two Fe I lines of the 525.0 nm spectral region. For both lines, the ME model parameter characterizing them have been obtained by fitting the FTS spectral atlas.

The figure indicates that spectropolarimetic observations on these lines yield errors that are of the order of 4 to 10 G for the magnetic field strength and 5.5 to 10 m s^{-1} for the LOS velocity, depending on the spectral line and on the magnetic field configuration. These values are in agreement with the minimum uncertainties for the MDI and HMI measurements. Also, the results show the dissimilar sensitivities of the two lines to magnetic fields and velocity perturbations.

For instance, the 525.02 nm spectral line has larger sensitivity to the magnetic field vector than the 525.06 nm spectral line and provides more accurate

magnetic field strength, inclination and azimuth inferences. In both lines, the uncertainties on the field strength increase for weaker fields. This increase is larger for the 525.06 nm spectral line. The same holds for the magnetic field inclination and its azimuth. Contrary, the 525.06 nm spectral line has larger sensitivity to velocity perturbations, as shown in Fig. 3.11 (upper right panel). The uncertainties for the LOS velocity increase for larger field strengths.

The overall increase in the v_{LOS} inaccuracies with the field strength is because lines become broader as the strength grows. It is not so easy to understand the slight but appreciable increase of σ_B with B; the behavior of the inclination and filling factors are supposed to be more natural: determinations are better when B is big. Nevertheless, as we advanced in the previous section, it is the effect of all the four Stokes profiles that is relevant to the final inference; arguments based on just one Stokes parameter may fail.

In the test, f has been set to unity. Therefore these calculations apply to very high spatial resolution observations, where the magnetic field occupies the whole resolution element. It is finally noteworthy how the accuracy in each parameter is inversely proportional to the magnetic filling factor, according to Eq. (3.8). Hence, the ordinate scale of the figure should be multiplied by 10 if $f = 0.1$. In such a case, and even in the eventual assumption that our estimates are wrong by a 100%, the expected inaccuracies support the fact that strong and weak fields can be distinguished when observed with modern instruments and interpreted with modern inversion techniques. We also caution that this analysis is valid as long as statistical errors are concerned. We have not included any systhematic error, apart from those associated to the limited wavelength sampling and spectral purity.

In any case, Eq. (3.8) allows us to test the sensitivities of spectral lines to various physical quantities perturbations and helps evaluate how these sensitivities vary when using different instrument approaches to record them. For instance, it helps in determining the effects of the instrumental filter width in the inferences. To illustrate it we resort to the HMI and PHI instruments. Both will observe the 617.3 nm spectral line at 6 wavelength positions across the line, say at -78, -42, 0, 42, 78 and 300 mÅ from the line center. We can solve Eq. (3.8) for this spectral line and check the dependencies of the inferences on the instrument configuration. Let us take three different instrumental filter widths and bulk velocities. f is set to unity. Then, Eq. (3.8) provides us with the minimum detectable magnetic field strengths and LOS velocities as a function of the magnetic field strength (Fig. 3.12).

At a glance, it is noticeable that the various curves show significant periodic variations. These are explained by the fact that we are sampling the spectral line at only few wavelength positions. The maximum sensitivities of

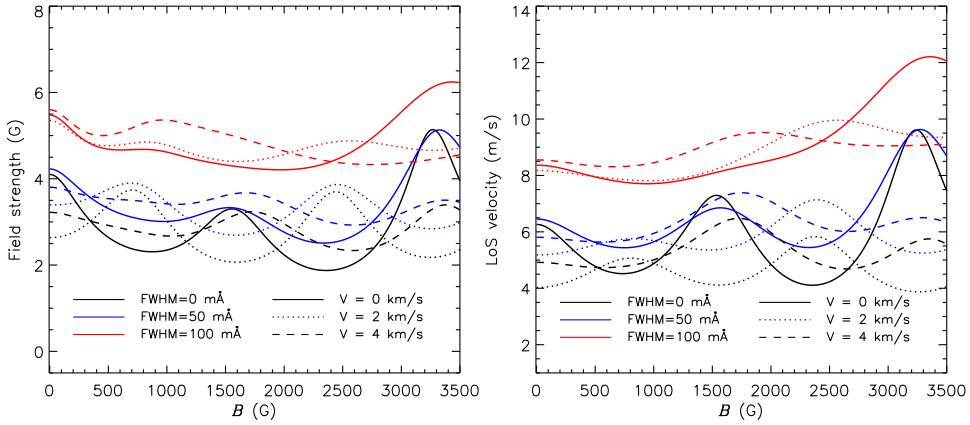

FIGURE 3.12:— Minimum detectable magnetic field strength and LOS velocity as a function of the magnetic field strength. Different line shapes stand for three different velocity shifts of the plasma and colors stands for different smearing filter widths.

the different model parameters pinpoint wavelengths (see e.g., Fig. 3.10) whose location change with the magnetic field strength and velocity. Notice that the curves representing different bulk velocities have essentially the same shape. Notice as well that the broader the filter the smoother the different curves. As we mentioned in Sect. 3.2.5, the instrumental filter affects the RFs through convolution; therefore we expect RFs smaller in amplitude and broader.

3.5 Conclusions

Many interesting features of analytic response functions have been discussed in this Chapter by considering the specific case of a ME model atmosphere. Since an analytic solution for the radiative transfer equation is available for this atmosphere, the sensitivities of spectral lines, as described by RFs, can also be cast in analytical form by simply taking partial derivatives of such a solution with respect to the model parameters. The analytic ME solution has been thoroughly used in the past for getting insight in the radiative transfer physics and as a purely practical diagnostic tool through ME inversion codes. Likewise, we have shown that the analytic, ME RFs are useful to better understand spectral line formation and the behavior of Stokes profiles in different formation conditions and also to get practical recipes that can help in selecting spectral lines for given purposes, in selecting wavelength samples, etc.

A summary of the various results obtained follows:

1. Response functions look homologous to each other, hence enabling qualitative, general discussions by considering a single spectral line in a specific model atmosphere. Here, we have targeted the Fe I line at 525.06 nm in a ME model representative of the quiet Sun thermodynamics (as observed by FTS) and with various vector magnetic fields and LOS velocities.

2. Very notably, the sensitivities of spectral lines to the various parameters depend on wavelength: some samples are better suited to diagnose one given parameter or another; some wavelengths are even insensitive to given parameters. The RF extrema show trivially those wavelengths were sensitivity is maximum.

3. As expected in ME conditions where no gradient of LOS velocity is present, RFs display clear wavelength symmetry properties. Noteworthy, the RFs to magnetic field strength perturbations show similar parity as the Stokes profiles while the RFs to LOS velocity perturbations are of opposite parity.

4. Stokes V sensitivities to B perturbations are significant for very weak field strengths. This fact explains the reasonably accurate results of ME inversions in this strength regime.

5. The shape of the RFs to LOS velocity perturbations does not depend on $v_{\rm LOS}$ except for the Doppler shift. Variations of sensitivity of the Stokes I and V profiles are compensated: when information on $v_{\rm LOS}$ decreases on Stokes I it increases on Stokes V, so that $v_{\rm LOS}$ remains well inferred in any circumstance.

6. We understand the trade-offs often found in the inversion codes among ME thermodynamic parameters: their corresponding RFs are very similar to each other. Fortunately, they are neatly different from the other RFs and can accurately infer vector magnetic fields and LOS velocities. Among the thermodynamic parameters, the relative sensitivity to $\Delta\lambda_D$ perturbations is larger than that to η_0 and a, hence enabling better inferences.

7. The magnetic filling factor f is better determined if there are significant differences between magnetic and non-magnetic atmospheres. When B is large this result is quite natural; when B is small, this result explains that differences in the thermodynamics of both atmospheres can help in inferring f properly.

8. Response functions can also be used to select spectral lines for given purposes or for given measurements. Moreover, a suitable combination of RFs provide quantitative arguments for wavelength sample choice.

9. It is possible to analytically evaluate the minimum detectable values for each of the model parameters by suitably re-writing the variances. The results provided us with *a-priory* estimations of affordable errors for different model parameters and with useful hints to select a suitable spectral line, given the design of the instrument.

4

The inference of physical quantities: inversion methods

This Chapter aims at introducing one of the available techniques to extract the atmospheric parameters encoded in polarized spectra: the inversion methods of the RTE. In particular, we discuss the capabilities and disadvantages of inversion codes based on the Levenberg-Marquardt algorithm, with especial interest on those based on the Milne-Eddington solution to the RTE.

4.1 Introduction

The fundamental goal in solar physics is the derivation of the physical variables that characterize the processes taking place on the solar atmosphere. Extracting the information about the magnetic, dynamic and thermal properties of the media from the observed Stokes profiles is not a straightforward task, though. The data do not only contain information about the plasma properties, but are also affected by the way we measure them. Therefore, in the selection of specific diagnostics to infer the desired information, we have to make sure that the observables are able to disentangle the searched-for physical variables from all the effects that degrade the data.

Fortunately, the Stokes profiles that emerge from the solar atmosphere and that we measure are well described by the RTE for polarized light. This equation shows us how the Stokes profiles depend on the physical conditions of the atmosphere, i.e., on the prevailing thermodynamic equilibrium, on the temper-

ature, on the electronic pressure, on the plasma velocity, on the magnetic field strength, inclination and azimuth, and on the abundance and other atomic parameters of the various chemical species. They depend on the vertical stratification of these physical parameters as well.

To infer the different physical quantities, with special interest on the magnetic field vector and plasma velocity, a variety of techniques have been developed in the past, most of them based on different approximations for the RTE and exploiting the various properties exhibited by the spectral lines sensitive to the magnetic field. Among them, the line ratio technique of the Stokes V profiles, and developed by Stenflo (1973), the center-of-gravity technique (Semel 1967; del Toro Iniesta et al. 1990) or the weak-field approximation (Jefferies & Mickey 1991). These techniques have been reviewed by, e.g., Solanki (1992).

Besides these techniques, the most widely used methods for the analysis of spectropolarimetric observations are based on the inversion of the Stokes profiles. All inversion algorithms obey the same principle, namely, the attempt to retrieve the different model parameters through comparison of the observed Stokes profiles with synthesized ones.

We can classify them in two groups: those that use iterative mathematical (fitting) algorithms and the rest. The first ones are usually based on the minimization of a merit function. This quantity gives information about the goodness of the fit and can be used by any iterative algorithm to find the best profiles that fit the observations. For instance, iterative methods based on the minimization of a merit function are the genetic algorithms (Charbonneau 1995). These have been successfully applied to observations of the He I triplet line at 1083.0 nm (Lagg et al. 2004). Well known are those based on non-linear, least-squared algorithms. Starting from an initial model atmosphere, i.e., from an initial set of the physical parameters, they are able to modify the model until the observations are reproduced. All is done by means of analytical or numerical solutions of the RTE. The first inversion method based on this approach was proposed by Auer et al. (1977). Since then, many inversion codes have been developed. Among them, SIR (Stokes Inversion based on Response functions; Ruiz Cobo & del Toro Iniesta 1992), SPINOR (Frutiger 2000), and those based on the ME approximation for the RTE (e.g. Skumanich and Lites 1987; Lites and Skumanich 1990 and Orozco Suárez & del Toro Iniesta 2007 [see Sect. 4.4.2]).

Among the techniques that do not use iterative methods we shall highlight those based on look-up tables. For instance, the Principal components analysis (PCA) method described by Rees et al. (2000), see also López Ariste & Casini (2002), or the techniques based on Artificial Neural Networks (ANNs, Carrol and Staude 2001; Socas Navarro 2003,2005; Carroll and Kopf 2008). These

techniques are less accurate but faster. This feature is of special interest for ongoing (and planned) instruments which are delivering (and are expected to deliver) huge amounts of data and hence require large amounts of computing time. Finally, Bayesian techniques have also successfully applied to the inversion of Stokes profiles (Asensio Ramos et al. 2007). The reader is referred to Bellot Rubio (2006) for a recent review.

In the next sections we will be discussing the non-linear, least-squares inversion problem and in particular the Levenberg-Marquardt algorithm. We will also introduce the two codes that will be employed throughout this thesis and perform some numerical tests. Finally we will summarize the main conclusions.

4.2 The inversion problem

By contrast to the so-called direct method problem in which model parameters are modified manually until synthetic profiles match the observations, we usually understand by the inversion problem that of obtaining the relevant model parameters through automatic minimization of the squared differences between synthetic and observed Stokes profiles. Hence, all inversion codes are based on the minimization of a merit function $\chi^2(\mathbf{x})$, given by

$$\chi^2(\mathbf{x}) = \frac{1}{\nu} \sum_{i=1}^{4} \sum_{j=1}^{M} \frac{\left[I_i^{\rm obs}(\lambda_j) - I_i^{\rm syn}(\mathbf{x}, \lambda_j) \right]^2}{\sigma_i^2} w_i^2, \tag{4.1}$$

where i refers to the four Stokes parameters, $j = 1 \ldots M$ represents the wavelength samples, σ_i the uncertainties of the observations, w_i is an arbitrary weight that can be assigned to the different Stokes profiles, $\mathbf{x}$ is a vector containing the N model parameters, and $\nu = 4M - N$ is the number of degrees of freedom. $I_i^{\rm obs}(\lambda_j)$ and $I_i^{\rm syn}(\mathbf{x}, \lambda_j)$ stand for the observed and synthetic Stokes profiles respectively.

To obtain the model parameters $\mathbf{x}$, we have to find the absolute minimum of the $\chi^2(\mathbf{x})$ function. This is not a trivial task since the $\chi^2(\mathbf{x})$ is a non-linear function in a N-dimensional space. In the case of a ME atmosphere N is, at least, nine. In addition, the $\chi^2(\mathbf{x})$ function may have several local minima, which increases dramatically the complexity of the problem. In the next section we briefly introduce one of the most efficient method to minimize a merit function.

4.2.1 The Levenberg-Marquardt algorithm

The Levenberg-Marquardt (LM) algorithm is an iterative technique aimed at finding out the absolute minimum of a given merit function. It was first proposed by Levenberg (1944) and later modified by Marquardt (1963). The method is a combination of the Gauss-Newton method and the steepest descent method. When the solution if far from the local minimum the algorithm behaves like the steepest descent method, more robust but poor in the final convergence. When the solution is close to the local minimum then the Gauss-Newton method is favored. The last is based on the Taylor expansion of the merit function and has quadratic final convergence. Therefore it possesses the advantages of the two methods, improving the general convergence. For the sake of completeness, we briefly describe the basics of the LM algorithm. The detailed analysis of the algorithm and its practical applications is beyond the scope of this section. For a more comprehensive treatment, refer to Press et al. (1992).

Suposse that a merit function $\chi^2(\mathbf{x}) : \mathbb{R}^n \to \mathbb{R}$ is being minimized, i.e., that we are looking for a vector $\mathbf{x} \in \mathbb{R}^n$ that minimizes $\chi^2(\mathbf{x})$. Then, the algorithm is based on the solution of

$$\nabla\chi^2(\mathbf{x}) + \mathbf{H}'\delta\mathbf{x} = 0, \tag{4.2}$$

where the $\delta\mathbf{x}$ stand for the direction on the N-dimansional space. $\nabla\chi^2(\mathbf{x}) = \dfrac{\partial\chi^2(\mathbf{x})}{\partial x_k}$ stands for the Jacobian of the merit function, i.e., the gradient. $\mathbf{H}' = \mathbf{H}(\mathbb{1} + \lambda)$ is referred to as the modified Hessian matrix $\mathbf{H}$. Here, $\mathbb{1}$ is the identity matrix and λ is the so called Marquardt damping parameter. Notice that λ affects only the diagonal elements of $\mathbf{H}$. This improves the numerical computational properties and the stability of the algorithm. The elements of $\mathbf{H}$ contain the derivatives of the merit function with respect to $\mathbf{x}$ approximated by the product of first derivatives:

$$H_{kl} = \frac{\partial\chi^2(\mathbf{x})}{\partial x_k}\frac{\partial\chi^2(\mathbf{x})}{\partial x_l}. \tag{4.3}$$

The iterative LM algorithm can be described as follows

1- Set the initial guess model, $\mathbf{x} = \mathbf{x}_0$, and damping parameter $\lambda = \lambda_0$,

2- solve Equation (4.2) for $\delta\mathbf{x}$,

3- set $\mathbf{x} = \mathbf{x} + \delta\mathbf{x}$,

4- update λ according to the new χ^2,

5- repeat from 2 through 4 until one of the stopping criteria have been reached.

Of interest is the evaluation of the inverse of the modified Hessian matrix $\mathbf{H}'$. It is symmetric and positive semidefinite. Then, $\mathbf{H}' = \mathbf{v}^\dagger \Sigma \mathbf{u}$ is its singular value decomposition, where μ_k are the eigenvalues (diagonal elements of Σ), and $\mathbf{v}_k$ the eigenvectors. † indicates transposition. Then the solution of Eq. (4.2) can be cast as

$$\delta\mathbf{x} = -\mathbf{H}'^{-1}\nabla\chi^2(\mathbf{x}) = -\sum_{k=1}^{n} \frac{\mathbf{u}_k^\dagger \nabla\chi^2(\mathbf{x})}{\mu_k}\mathbf{v}_k, \tag{4.4}$$

where n is the number of free parameters.

A critical step on the LM algorithm is the updating of the λ parameter. Marquardt proposed that given λ_0, when in an iteration step $\chi^2(\mathbf{x}+\delta\mathbf{x}) < \chi^2(\mathbf{x})$ then $\lambda = \lambda/10$, the Gauss-Newton method is favored, or else $\lambda = \lambda \times 10$, so the steepest descent method is favored, meaning that we are far from the solution. Therefore, the damping term ensures the convergence of the algorithm when the parameter space is highly non-linear, avoiding singularities on the $\mathbf{H}'$ matrix.

4.2.2 The MILne-Eddington inversion of pOlarized Spectra: MILOS

The MILOS inversion code has been developed along this thesis. It is capable of fitting a given set of Stokes profiles under the Milne-Eddington (Sec. 2.3.1) approximation. The inversion code uses the LM iterative scheme that has been described in the previous section. The code defines the merit function as in Eq. (4.1). Thus, the derivatives of the merit function can be cast as

$$\frac{\partial\chi^2(\mathbf{x})}{\partial x_k} = -\frac{2}{\nu}\sum_{i=1}^{4}\sum_{j=1}^{M} \frac{\left[I_i^{\rm obs}(\lambda_j) - I_i^{\rm syn}(\mathbf{x},\lambda_j)\right]}{\sigma_i^2} w_i^2 R_i^x(\lambda_j), \tag{4.5}$$

where $R_i^x(\lambda_j)$ is the corresponding RF with respect to x_k, j stands for the wavelength samples and i for the Stokes parameter. The elements of the Hessian matrix can be written as

$$H_{kl} \simeq -\frac{2}{\nu}\sum_{i=1}^{4}\sum_{j=1}^{M} R_i^{x_k}(\lambda_j) R_i^{x_l}(\lambda_j)\frac{w_i^2}{\sigma_i^2}. \tag{4.6}$$

Eq. (4.5) and (4.6) show that the jacobian and the Hessian depend on RFs, implying that the LM iterative algorithm uses the properties of RFs (see Chap. 3) to find the direction $\delta\mathbf{x}$. In a ME model atmosphere, these RFs can be evaluated analytically; this improves the computational times.

The nine free parameters are: the thermodynamic parameters, S_0, S_1, η_0, $\Delta\lambda_{\rm D}$ and a, the magnetic field vector, B, γ, χ, and the plasma velocity, $v_{\rm LOS}$.

Fundamentals of operation

Running the inversion code is straightforward: one has to provide a set of observed Stokes profiles and an initial guess model atmosphere. Then, the code solves the RTE within the ME approximation, computes the corresponding RFs and iteratively updates the model until it finds the best fit. The user has also to provide the initial λ_0 parameter and the intrinsic noise σ of the observations.

The user can account for the finite spectral resolution of the instrument by giving the full width at half maximum of an assumed Gaussian function with which the synthesized Stokes profiles are then convoluted.

It also accounts for the effects of scattered/stray light by the instrument. One should model the appropriate Stokes I profile to account for stray light and then give it to the inversion code. As a stray light profile, an averaged Stokes I coming from the surrounding, non-magnetized regions is typically used. The code then fits the stray-light factor α, and the final emergent Stokes spectrum is given by $\mathbf{I} = \alpha\mathbf{I}_{\rm stray} + (1-\alpha)\mathbf{I}_{\rm m}$, where $\mathbf{I}_{\rm m}$ stands for the magnetic component and $\mathbf{I}_{\rm stray}$ for the stray-light component. When stray light is accounted for the number of free parameters increases to ten ($N = 9 + 1$). Notice that the stray light may be interpreted as a non-magnetized component. In this case, the fill fraction of the magentic component is given by $f = (1 - \alpha)$.

An extra broadening of the spectral lines by macroturbulent velocity, $v_{\rm mac}$, can be included as well. In this case, each Stokes parameter is convolved with a Gaussian function

$$f_{\rm mac}(\lambda) = \frac{1}{\sqrt{2\pi}\sigma}\exp^{-\frac{1}{2}\left(\frac{\lambda-\lambda_0}{\sigma}\right)^2}, \tag{4.7}$$

where $\sigma = \dfrac{\lambda_0 v_{\rm mac}}{c}$, λ_0 is the central wavelength of the transition and c is the speed of light. This increases the free parameters by one as well.

As shown in Eq. (4.1) one can also set the different weights for the different Stokes profiles and wavelength samples, for instance, in order to give more importance to the linear polarizations signals in detriment of the circular polarization signal.

The code stops once any of the two criteria hold

$$\chi^2(\mathbf{x}) < \epsilon_1, \tag{4.8}$$

$$k \geq k_{\max}, \tag{4.9}$$

where k stands for the number of iterations and ϵ_1 is a constant.

Evaluating Eq. (4.4) by means of the SVD algorithm, allows additional control over each iteration step. This helps as well to tackle singularities of the Hessian matrix. For instance, by simply truncating the number of eigenvalues μ_k used to evaluate Eq. (4.4), we can control the effect of noise on $\delta\mathbf{x}$. This is known as the Tikhonov SVD (Press et al. 1992).

Initialization and convergence tests

To initialize the LM algorithm, one has to provide an initial guess model and λ_0. There exist no specific rule to assign values to these parameters. In practice, depending on the initial guess model we have to set the λ_0 parameter: should the guess model be close to the final solution, the λ_0 would be smaller than unity, therefore favoring the Gauss-Newton method. In case the guess model is far from the best solution, λ_0 should be grater than unity to favor the steepest descent method. In addition to this, the final solution has to be found in, at least, a nine-dimensional parameter space. This increases the possibility of the code being settled in a secondary minimum instead on an absolute one.

This behavior of the LM algorithm settling in local minima (in the ME fitting scenario) have been reported before (e.g. Socas-Navarro et al. 2001) and have yielded to adopt different criteria in order to circumvent the limitations of the inversion. For instance, one can generate a set of n random initial model atmospheres an then run the corresponding n inversions, the solution will be that which gives better convergence (smaller $\chi^2(\mathbf{x})$). This way of tackling the problem is however extremely slow.

Other strategy may be based on adopting the solution from the fit of a neighbor pixel as the initial guess model. Although, being much faster than the previous, it may also fail, introduce non-desired dependences on the final solution, and errors can propagate easily. This can happen as well when using approximate solutions to the RTE to initialize the inversion.

There are codes that use genetic algorithms to fit the Stokes profiles. Then, the retrieved model is used to initialize an LM iterative scheme for a more robust final convergence (hybrid codes, e.g. ASP code, Skumanich and Lites 1987). The results indicate great final convergence, although at the expense of a big computational time. Other hybrid codes exists, for instance, based

on efficient numerical methods for global optimization as the DIRECT method (Jones et al. 1993) used to initialize an inversion code for the He I 1083 nm spectral line (see Asensio Ramos et al. 2007).

But, why does the LM occasionally fail? There are only two reasons, namely, that the merit function has no well-defined global minimum or that the updating strategy for the model atmosphere or for the damping parameter is not well suited to the problem. Let us discuss both reasons separately.

If two or more model atmospheres produce equally good fits (i.e., equally low values of χ^2), then either the observational noise is such that hides the true minimum or the underlying model assumptions are ambiguous, or both. That the noise hampers the measurements is out of the question. However, the physical constraints behind the model can be such that, for instance, the number of free parameters are too high for the information available from the observables. For example, Martínez Gonzalez et al. (2006) have shown that the Fe I pair of lines at 630 nm is not able to provide a single solution for a scenario in which two atmospheres variable with depth, one magnetic and another non-magnetic, fill each spatial resolution element. On the other hand, the well-known trade-off between the η_0, $\Delta\lambda_D$, and a parameters of ME inversions (see Westendorp Plaza et al. 1998; Orozco Suárez, Bellot Rubio & del Toro Iniesta 2007; Chapter 2 of this thesis) produces that several sets of such three parameters may give fits with the same quality without changing the magnetic and velocity parameters. In other words, the navigation of the algorithm through the parameter space is difficult and ambiguous.

Let us suppose that the model fully explain the observations, i.e., that a clear global minimum exists. To reach it the usual strategy is to increase or decrease the λ parameter by a factor ten, depending on the divergence or not of the algorithm. If the code settles in a local minimum, the damping parameter has to be large enough in order to favor bigger $\delta\mathbf{x}$ steps and overcome that local minimum. Sometimes however, the updating strategy is such that the "damping" is unable to get rid of the local minimum.

To illustrate the problem, in Fig. 4.1 (left panel) we represent the evolution of the λ and the χ^2 values for a particular inversion, started with a $\lambda_0 = 1$ and not too close, neither too far from the final solution. We can see how χ^2 decreases very fast at the beginning, and then stabilizes. We also see how, while the fit improves (smaller χ^2), the λ parameter decreases until a certain value at which it starts oscillating. *The inversion code has been trapped on a local minimum.* The example fit is shown in the right panel from Fig. 4.1. In this case the final solution is very close to the absolute minimum. We notice that this can happen at any iteration, depending on the shape of the N-parameter space.

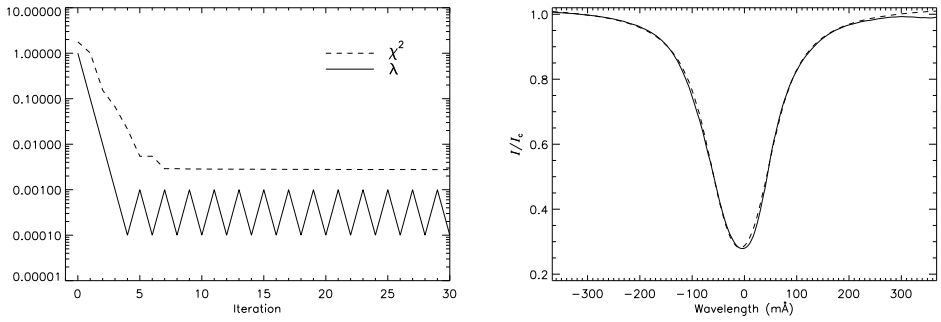

FIGURE 4.1:— Left: evolution of the damping parameter, λ, and the best χ^2 with the iteration steps. Units are dimensionless. Right: example fit (dashed) to the Fe I line at 525.06 nm (solid), and used to calculate the evolution of the merit function and the damping parameter.

Therefore, to overcome this convergence limitations an efficient updating strategy for the damping parameter is needed, as well as a proper initial λ_0 value. Different damping strategies can enormously improve LM convergence speeds. Our experience using the MILOS code tells that a small percent ($\sim$3%) of the inversions with real data fail to converge (using the Marquardt damping strategy). The general convergence of the algorithm improves when allowing only $\delta\mathbf{x}$ relative variations smaller than a fixed percentage, but this strategy has slower final convergence. An example for a different updating strategy of the damping parameter can be found in (Borrero et al. 2008).

Hereafter and unless otherwise stated, we set $\lambda_0 = 10$, along this thesis regardless of the initial guess model. In cases where we detect that the inversion has failed to converge, we just remove this result from the analysis.

4.2.3 SIR

Developed by Ruiz Cobo and del Toro Iniesta (1992), SIR (Stokes Inversion based on Response Functions) represents one of the most standardized inversion techniques that have been successfully applied to Stokes spectra. It is based on the solution of the RTE under local thermodynamic equilibrium (LTE) and in plane-parallel atmospheres. It takes into account the depth dependence of all important physical parameters for the formation of spectral lines. The code uses the LM algorithm to modify the initial model atmosphere which is dependent on the optical depth. Unlike the ME case, RFs are evaluated numerically since the evolution operator has not an analytical expression in general (see, e.g., del Toro Iniesta 2003). We will not analyze in detail the guts of the SIR inversion

code (see the original paper or del Toro Iniesta 2003, for details) but we shall pay attention to one of its peculiarities.

SIR deals with the full stratification of the various model parameters. If the atmosphere is sampled at m different optical depths, the number of free parameters would increase by a factor m. In practice it is useless to modify the whole stratification as it would lead the code to fail. Therefore, SIR evaluates the perturbations to the different model quantities at selected optical depths, called nodes, in such a way that the whole stratification is taken into account. For instance, if one assumes a single node for a given physical quantity, the whole atmosphere will be modified by a constant in that quantity; if two nodes are selected instead, the atmosphere will be perturbed linearly throughout; the perturbation will be parabolic if the number of nodes is three, and so on. This approach reduces the dimensionality of the problem, and strengthen its abilities to disentangle model parameters from one another.

4.3 Reliability of the inversion code

In this section we test the robustness of the inversion code. To this end we have generated a reference basis of Milne-Eddington Stokes profiles for the Fe I 525.06 nm line using the MELANIE code developed by Héctor Socas Navarro at the High Altitude Observatory (HAO). This code has been widely used for the analysis of solar observations and is based on the ASP code (Skumanich & Lites 1987; Lites & Skumanich 1990). Then we have inverted the full profiles with the MILOS code. The inversion results allow us to check the reliability of the code and provide the uncertainties on the model parameters due to the intrinsic noise (statistical errors of the ME inversion).

The reference basis consists of a set of synthesized Stokes profiles emerging from 10 000 ME model atmospheres with a *uniform random distribution* of vector magnetic fields (B from 0 to 2500 G, inclination and azimuth from 0 to 180°) and LOS velocities (between -4 and 4 km s^{-1}). The remaining model parameters have been determined by fitting the FTS atlas (Kurucz et al. 1984). The fits of the lines have yielded errors smaller than 2%. Importantly, we have added noise to all profiles at the level of 10^{-3}. The wavelength sampling has been 0.1 pm, with a total of 100 samples across the spectral line.

The inversion of the profiles has been carried out under the following initial conditions: the initial damping parameter have been set to $\lambda_0 = 10$, the maximum number of iterations $k = 300$, the ϵ_1 parameter, which controls when the inversion has converged has been set small enough to allow the inversion code to perform the 300 iterations. Finally, the initial model parameters were:

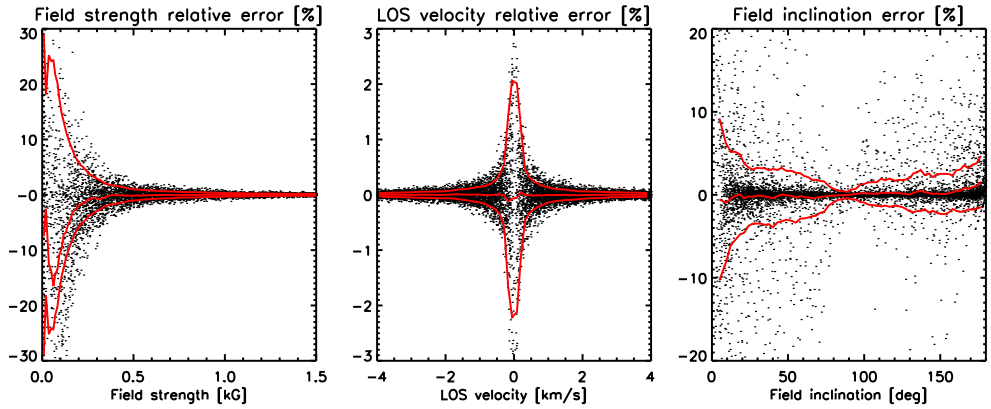

FIGURE 4.2:— Relative errors for the magnetic field strength, field inclination and LOS velocity from the full profile inversion with noise added at the level of 10^{-3}. The solid lines stand for the mean and rms values.

$S_0 = 0.2$, $S_1 = 0.8$, $\eta_0 = 6.5$, $B = 200$ G, $\gamma = 20°$, $\chi = 20°$, $\Delta\lambda_D = 30$ mÅ, $v_{LOS} = 0.25$ km s^{-1} and $a = 0.03$. In the inversion we determine all the 9 free parameters. The weights on the χ^2 have been set to unity, and $\sigma = 10^{-3}$ to account for the noise introduced on the simulated profiles.

Figure 4.2 shows the rms values of the relative errors on the magnetic field strength, field inclination and LOS velocity (left, right and middle panels, respectively).

Note that the retrieved errors are very small, being for the magnetic field strength, smaller than 2% for fields larger than ∼500 G, or smaller than 0.1% for the LOS velocity. This errors are solely due to photon noise. The results for the inclination are noisier. Also, the rest of model parameters are determined with high accuracy (not shown). Additional test results from the inversion of the full Stokes profiles in the absence of noise retrieve negligible errors. All results together demonstrate the reliability of the inversion code.

5

ME inferences of solar magnetic fields: a performance analysis based on MHD simulations

The solar atmosphere is complexly featuring rapid changes in its physical conditions both horizontally and vertically. As a result, the determination of the existing physical quantities can be an arduous task depending on how intricate the atmosphere is. In this Chapter we are interested in examining the applicability of ME inversions to high spatial resolution observations of the quiet Sun. We particularly study how appropriate the ME approximation is to infer model parameters from realistic data, with the aim of understanding the connection between the ME model parameters and the real stratifications of the atmospheric parameters. To this end, we use magnetoconvection simulations of the solar surface to synthesize Stokes profiles and then we invert the profiles with the ME approximation. We perform an empirical analysis of the heights of formation of ME measurements and analyze quantitatively the errors due to the ME approximation. We also comment on the quality of the best-fit ME profiles and their relationship with the particular model stratifications.

5.1 Introduction

Stokes profiles contain information about the physical properties of the solar atmosphere. In general, the information encoded on the shape of the lines is

not confined to single atmospheric layers, but to a broad range of heights. In a crude way the extraction of such information directly from the observables is limited and difficult. The measurement of the Stokes profiles in combination with the method of analysis introduce uncertainties in the physical quantities retrieved from the observations. The former includes errors due to detector photon noise and instrumental effects, e.g., the limited spectral resolution and wavelength sampling, the finite angular resolution, etc. The latter contains the uncertainties due to the simplifications and approximations of the physical model used to explain the observed profiles.

In this Chapter, we want to analyze real Stokes profiles with the ME approximation. This approximation do not account for vertical stratifications on the atmospheric quantities (see Chapter 2) which make it unfruitful to successfully reproduce the physical conditions of the solar atmosphere as soon as its physical properties (temperature, density, magnetic field, etc.) change through the photosphere. When the "observations" are synthetic ME Stokes profiles, the ME model is fully compatible and lead to uncertainties that are solely due to the intrinsic noise and, in a smaller extent, to the convergence of the algorithm, provided the spectral resolution and wavelength sampling is optimum. Uncertainties caused by noise are known as statistical errors. They can be evaluated by means of numerical tests or, more efficiently, by using ME Response Functions (see Chapter 3). What does it happen when we analyze realistic Stokes profiles (with no noise) with the ME approximation? Which are the intrinsic errors of such an analysis? This is, in all purposes, the aim of the present Chapter.

A pioneering study of the capabilities and limitations of ME inversion codes[1] was carried out by Westendorp Plaza et al. (1998) using the Fe I spectral lines at 630.15 and 630.25 nm. They made a quantitative comparison between results obtained with SIR and the ASP ME code, all using synthetic Stokes profiles describing different solar scenarios. The conclusion of their work was that the ME inversion provides accurate average values for the "real" stratifications of the physical quantities.

More recently, Khomenko, Collados, & Solanki (2004) have analyzed whether it is possible to determine the magnetic field stratification from SIR inversions of Stokes profiles synthesized from MHD simulations. They have shown that the inversion is able to recover the magnetic stratifications for fields as weak as 50 G, using the Stokes profiles of the Fe I at 630 nm in the absence of noise. This work complements the results of Westendorp Plaza et al. (1998). Also with the

[1]The analysis of Stokes profiles with the ME approximation entail the use of inversion codes to determine the ME model parameters

help of MHD simulations Khomenko, & Collados (2004) have evaluated the diagnostic potential of different spectral lines for magnetic field measurements by means of the line ratio technique. The results were not very satisfactory for the pair of Fe I lines at 630 nm. They have shown that errors are large, making the line ratio technique useless. They also pointed out the importance of accounting for atmospheric gradients in the model atmospheres to infer the field strength from these two lines accurately. Note that the information about atmospheric gradients is contained in the line asymmetries: *the ME model cannot reproduce Stokes profile asymmetries*.

In this Chapter we carry out a complete analysis of the capabilities and limitations of ME inversion codes for the analysis of real observations: first, we take a set of state-of-the-art magneto hydrodynamic simulations to describe the solar photosphere as realistically as possible (Sect. 5.2). Then, the Stokes I, Q, U and V profiles are synthesized from the model atmospheres provided by the simulations (Sect. 5.3). The SIR code is used to synthesize the corresponding Stokes vector. We then apply the ME inversion to the profiles in the absence of noise and instrumental effects. For the inversions, we use the MILOS code. A direct comparison of the retrieved atmospheric parameters with real ones is use to determine the uncertainties due to the ME approximation (Sect. 5.4). The lines used for the analysis are the two Fe I lines at 630.2 nm. As mentioned before, in this study we neglect any source of errors due to the use of solar instrumentation (including photon noise). In Chapters 6 and 9 we fully simulate measurements made by real instruments.

5.2 Magnetohydrodynamic simulations

To describe the Sun's photosphere we use the radiative MHD simulations of (Vögler et al. 2003, 2005; Vögler 2003). They were performed with the MURaM[2] code which solves the 3D time-dependent MHD equations for a compressible and partially ionized plasma, taking into account non-grey radiative energy transport and opacity binning.

The code has been used to evaluate the diagnostic potential of different spectral lines and to compare them with real observations (Khomenko et al. 2004a,b; 2005a,b; Shelyag et al. 2007), to study facular brightening (Keller et al. 2004) and to investigate the relationship between G-bang bright points and magnetic flux concentrations (Schüssler et al. 2003; Shelyag et al. 2004). More recently the code has been used to simulate high-spatial resolution spectropolarimetric observations of space-borne instruments and to analyze the diagnostic poten-

[2] MPS/University of Chicago RAdiative MHD

TABLE 5.1:— Physical parameters provided by the simulation runs.

VARIABLE	UNITS	DESCRIPTION
ρ	g cm^{-3}	Density
$\rho_{m_{x,y,z}}$	g cm^{-2} s^{-1}	Momentum density components
e_{tot}	g cm^{-1} s^{-2}	Total energy density
$B_{x,y,z}$	G/$\sqrt{4\pi}$	Magnetic field components
T	K	Temperature
P_g	g cm^{-2} s^{-2}	Gas pressure

tial of visible lines for internetwork field determinations (Orozco Suárez et al. 2007). It has also been used to simulate small solar pores (Cameron et al. 2007), the emergence of magnetic flux tubes from the upper convection zone to the photosphere (Cheung 2006; Cheung et al. 2007), umbral dots (Schüssler & Vögler 2006) and also to study the origin of the strong horizontal internetwork magnetic fields in the quiet solar photosphere as revealed by the *Hinode* spectropolarimeter to which the local near-surface dynamo action seem to contribute signicantly (Schüssler & Vögler 2008). Finally, the code has been used to analyze the image contrast of the solar granulation as seen by the *Hinode* spectropolarimeter (Danilovich et al. 2008).

To develop our work we employ two snapshots from simulation runs representing a very quiet, unipolar internetwork region and a weak plage region with an average magnetic field, $\langle B \rangle$, of 10 and 50 G, respectively. We also use a sequence of 5 minutes with a cadence of 10 seconds (which makes a total of 30 snapshots) of a mixed polarity simulation run representing a strong network region of (unsigned) $\langle B \rangle = 140$ G. To generate the snapshots the code was initialized with an homogeneous vertical magnetic field of 200 G and continued until $\langle B \rangle$ at $\tau = 1$[3] had decayed to a level of about 50 and 10 G. For the strong network region, the simulations started with a bipolar distribution of vertical fields with average strength of 200 G. The 5-minute sequence was taken relatively early after the beginning of the simulation.

Each of the simulation runs consist in single precision cubes of dimension $288 \times 100 \times 288$ pixels. The horizontal and vertical extent are respectively 6000 and 1400 kilometers, thus the horizontal mesh-width is about 20.8 km and the vertical step size is 4.86 km, extending from $z = -800$ to $z = 600$ km. $z = 0$ km is the height where $\tau = 1$. The equivalent grid resolution is $0\farcs0287$, implying a spatial resolution of $0\farcs057$ (41.6 km) on the solar surface. The physical parameters provided by the MHD models are summarized in Table 5.1.

[3]All continuum optical depths refer to the opacity at 500 nm

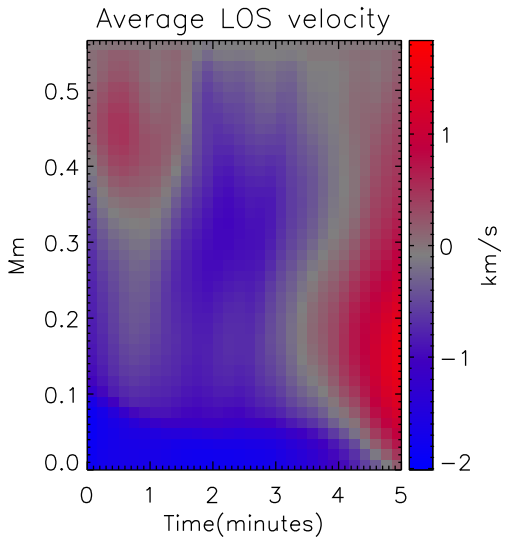

FIGURE 5.1— 2D diagram showing the temporal evolution of the LOS velocity at different heights. It can be seen that there is the presence of an oscillatory pattern in the upper layers.

In the simulation runs, the time-averaged radiation flux density which leaves the box at the top has the solar value $F_{\odot} = 6.3410^{10}$ erg s^{-1} cm^{-2}. One has to keep in mind that the behavior of the models resulting from the simulations are strongly influenced by the limited box extensions. As a consequence, although acoustic oscillations emerge naturally in the simulations, they populate a rather small wavenumber space and their amplitudes are unrealistically large, implying that the simulations cannot be used to predict the magnitude of oscillation-induced line-shifts in the real Sun (as is the 5-min oscillations)[4]. In Fig. 5.1 we represent a 2D map of the variation of the LOS velocity with height (Y-axis) and time (X-axis). The visible oscillation of the flow velocity in high layers ($\sim$400 km) has an approximated time period of 5 minutes. Notice that typical photospheric lines are almost no sensitive to perturbations in the LOS velocity at that heights.

5.3 Spectral synthesis

In order to synthesize the Stokes profiles that emerge from the MHD simulations we have to solve the RTE for polarized light. This process has been carried

[4]Solar oscillations shift the Stokes profiles back and forth, therefore they have a direct impact on the design of solar instrumentation, especially on filter-based magnetographs which scan a spectral line at limited, fixed wavelength positions. This issue will be investigated in greater detail in Chapter 9.

out using SIR. The spectral synthesis process is accomplished in two steps: first, the input model atmospheres needed by SIR are built from the MHD simulations; and secondly the RTE is solved.

5.3.1 Extracting the atmospheric parameters

The atmospheric parameters needed to synthesize the Stokes profiles are the temperature (T), electron pressure (P_e), line of sight velocity ($v_{\rm LOS}$), magnetic field strength, inclination and azimuth (B, γ and χ) as well as the optical depth (τ). To derive them from the MHD model we have to carry out the following computations. Firstly, B, γ and χ are calculated as follows:

$$B = \sqrt{B_x^2 + B_y^2 + B_z^2}\sqrt{4\pi}, \tag{5.1}$$

$$\gamma = \arccos \frac{B_y\sqrt{\pi}}{B}, \tag{5.2}$$

$$\chi = \arctan \frac{B_z}{B_x}, \tag{5.3}$$

where γ and χ range from 0 to 180°, and from 0 to 360° respectively, and the magnetic field B and its components $B_{x,y,z}$ are in G. The LOS velocity is extracted from the y-component of the momentum density

$$v_{\rm LOS} = \frac{\rho_{m_y}}{\rho}. \tag{5.4}$$

The electron pressure and optical depth are inferred from the temperature, gas pressure (P_g), and density (ρ). To this end we construct geometric height scale, 14 km of step size, and solve the Saha and Boltzmann equations. The electron pressures and optical depths are different for each pixel. The calculations have been carried out assuming $\log\tau = -4.9$ as a boundary condition at the top of the computational domain ($z = 600$ km). This value has been taken from the Harward-Smithsonian Reference Atmosphere (Gingerich et al. 1971).

5.3.2 Interpolating the atmospheres

Figure 5.2 (left) shows a map of the temperature values closer to the $\tau = 1$ optical depth, corresponding to the first snapshot of the simulations run with $\langle B\rangle = 140$ G. The effects of the non-evenly spaced $\log\tau$ scale are clearly seen as a non-uniform spatial distribution, exhibiting very strong differences from pixel to pixel, like a contour lines pattern. In order to correct this effect the various atmospheric model parameters are interpolated through the whole

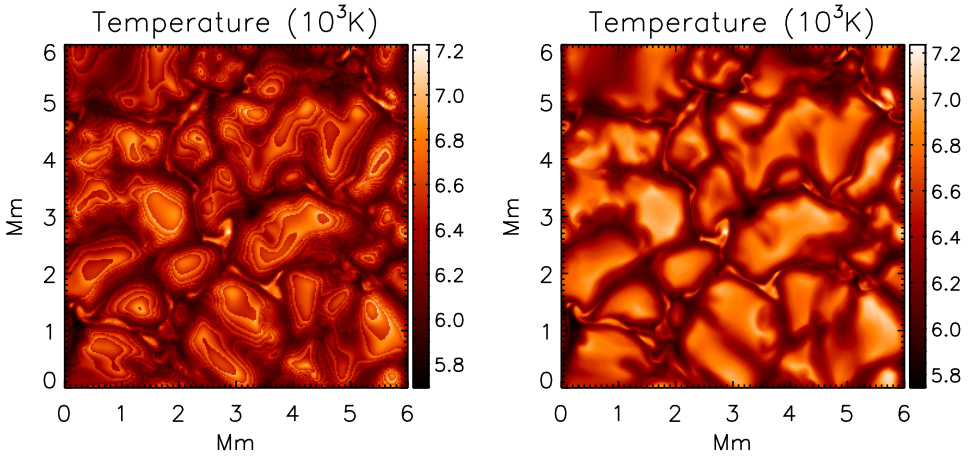

FIGURE 5.2:— Maps of temperature at the nearest value of the level $\tau = 1$ for one data cube without interpolating the model atmosphere (*left*) and the models properly interpolated (*right*). The effect of the non-evenly spaced $\lg \tau$ scale is clearly seen along the map. The data correspond to the $\langle B \rangle = 140$ Gauss simulation run.

atmosphere. We have used a second order polynomial interpolation for all atmospheric quantities. Also, we have let the depth grid vary from $\log \tau = -4$ to 2, with a step size of $\Delta \log \tau = 0.05$. This depth range encompasses the atmospheric heights at which the most commonly used photospheric lines are sensitive.

Figure 5.3 shows an example of vertical stratifications for several of the model parameters (black). Overplotted are the results from the interpolation (red). Similar results are obtained for other pixels. The right panel of Fig. 5.2 shows the temperature map from the interpolated atmospheres. Obviously, the effect of the non-evenly spaced grid has disappeared.

Figure 5.4 shows maps of the field strengths, inclinations, azimuths and velocities found in the simulation run with $\langle B \rangle = 140$ G at $\tau = 1$. In the LOS velocity map the granulation pattern can be clearly seen. The granules exhibit negative velocities while the intergranules show positive velocities. In the intergranular lanes there are small scale structures as well. Some of these structures exhibit velocities of up to 6 $\mathrm{km\,s^{-1}}$.

The magnetic field strength map shows that the field tends to concentrate within the intergranular lanes, reaching values of 2500 G in some locations. The granules harbor weak fields that occasionally reach 300 G. The inclination map shows that the fields are mostly vertical in intergranular regions, and tend to be horizontal in granules. The azimuth map shows granular-sized structures

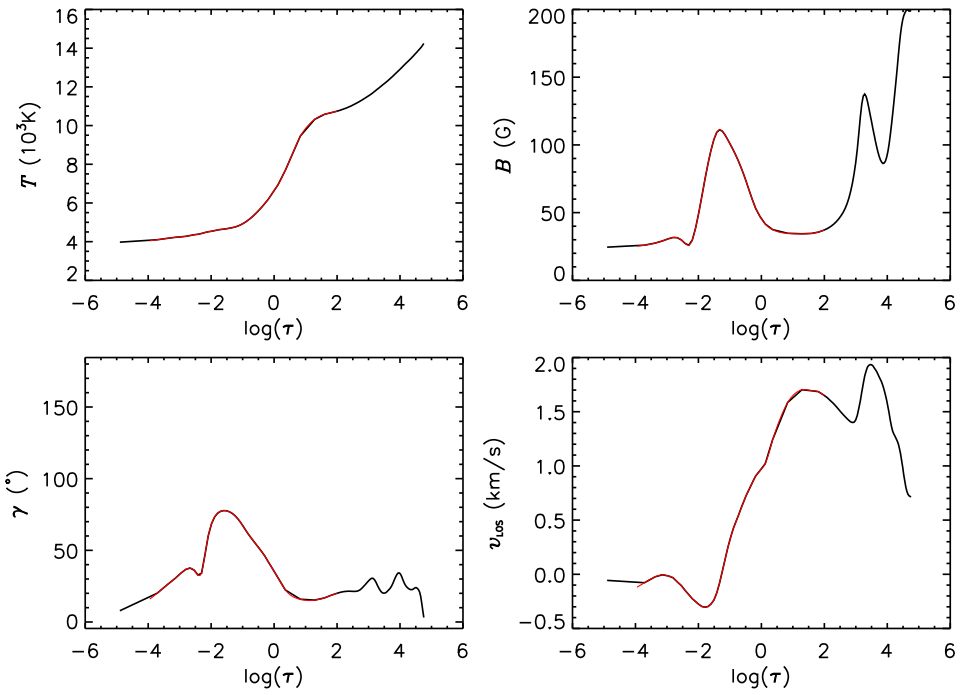

FIGURE 5.3:— Example of stratifications resulting from the simulations. This pixel correspond to a granule. The interpolated atmosphere (red) coincides almost exactly with the non-interpolated one (black). The interpolated model extends from $\log\tau = 2$ to $\log\tau = -4$.

(1″-2″).

For a more quantitative description of the fields present in the simulations, Fig 5.5 shows the field strength and inclination Probability Density Functions (PDFs)[5] for the three simulation runs at optical depth $\log\tau = -1$. The PDFs indicate that most of pixels have magnetic field strengths of the order of hecto Gauss (hG). The PDFs are stepper as we go to smaller flux densities.

The PDFs of the field strength increases rapidly toward weaker fields. For the $\langle B\rangle = 140$ G case the distribution peaks at about 20 G. The inclination PDFs show few magnetic fields purely vertical oriented while there is a larger occurrence of horizontal fields. The $\langle B\rangle = 140$ G run was seeded with mixed-polarity vertical fields, therefore the distribution is rather symmetric about $\gamma = 90°$. The $\langle B\rangle = 10$ and 50 G simulations were initialized with unipolar vertical fields, hence the asymmetric distribution.

[5]The PDF is defined in such a way that $P(B)dB$ is the probability of finding a magnetic field B in interval $[B, B + dB]$, and it has total integral unity, $\int_0^\infty P(B)dB = 1$.

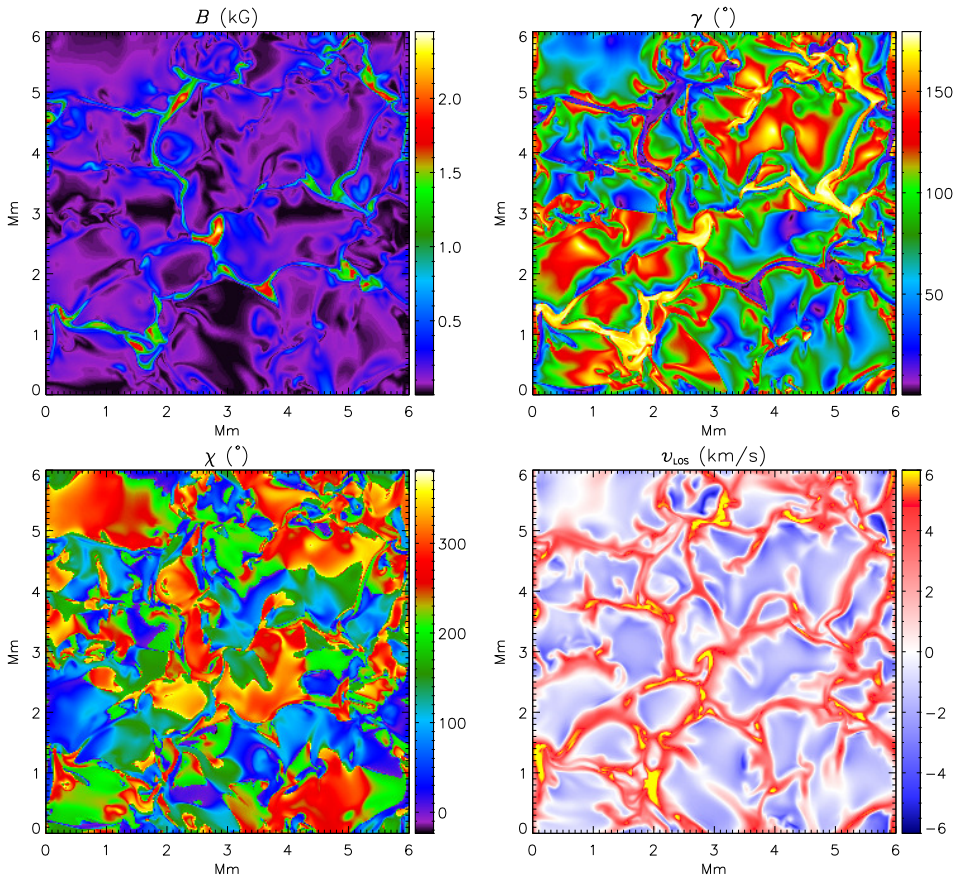

FIGURE 5.4:— Magnetic field strength, inclination and azimuth, and LOS velocity maps from the simulation run corresponding to $\langle B \rangle = 140$ G and corresponding to $\tau = 1$.

5.3.3 Spectral lines and synthesis

Once we have build up the model atmospheres for each of the 288×288 pixels and for all the snapshots we use them as input models for SIR. The spectral synthesis have been carried out for several lines[6] located in the 525.0, 630.2 and 617.3 nm regions (see Table 5.2).

The wavelength sampling has been set to 1 pm except for the 630.2 nm spectral region, which has been sampled at 113 wavelength positions in steps of 2.15 pm. This region contains the two Fe I lines at 630.15 and 630.25 nm. They are the lines observed by the spectropolarimeter aboard *Hinode* (for details, see

[6]The 525.0 nm spectral region includes a wide variety of line transitions in order to evaluate the effects of the secondary transmission peaks of the IMaX étalon (see Chapter 9).

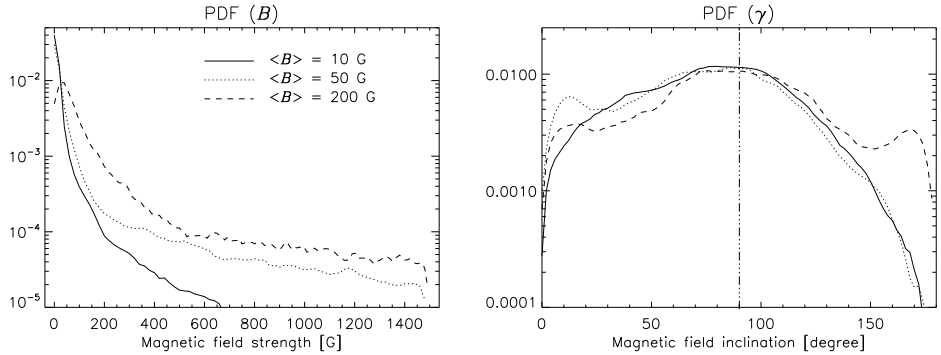

FIGURE 5.5:— Magnetic field strength (left), and field inclination (right) probability density functions from the magneto-convection simulations for $\langle B \rangle = 10$ (solid), 50 (dotted) and 140 G (dashed), taken at optical depth $\log \tau = -1$

Tsuneta 2008). In the case of the 525.0 nm region, the wavelength range extends 1 nm. The atomic parameters used for the synthesis are given in Table 5.2. The $\log(gf)$ values have been taken from the VALD database (Piskunov et al. 1995; Barklem et al. 2000) except for Fe I 630.25 nm (Borrero et al. 2002). The collisional broadening coefficients α and σ due to neutral hydrogen atoms have been evaluated following the procedure proposed by Anstee & O'Mara (1995) and Barklem et al. (1998, 2000). The abundances have been taken from Thevenin (1989). The computation of the Stokes profiles for a single spectral line from a snapshot takes about 12 hours in a 3 Ghz single-processor workstation.

In the synthesis process we have not included broadening due to macro- or micro- turbulent velocity fields. Turbulent fields have been extensively used to artificially broaden the spectral lines with the only purpose of fitting the observed line widths. The simulations are of sufficiently high resolution to describe the smallest scale plasma motions. They also reproduce larger scale motions, as the convective velocity fields. This broad range of plasma motions make it unnecessary the use of macro- or microturbulent velocity fields in a 3D analysis. Asplund et al. (2000) showed that in the case of observations in the absence of the atmospheric seeing the convective flow velocities, in addition to other well known processes like the thermal or collisional line broadening, are sufficient to explain the observed broadening of photospheric spectral lines.

TABLE 5.2:— Atomic parameters for the synthesized lines. λ stands for the central (laboratory) wavelength of the transition, χ_{low} is the excitation potential of the lower transition level of the line in eV, $\log_{10}(gf)$ stands for the multiplicity of the lower level of the transition times the oscillator strength of the line, α and σ (units of Bohr's radius, a_o)are the collisional broadening parameters from the collisional quantum theory of Anstee, Barklem and O'Mara, and finally $g_{\rm eff}$ stands for the effective Landé factor of selected lines.

ION	λ (nm)	χ_{low}	$\log_{10}(gf)$	TRANSITION	α	σ	$g_{\rm eff}$
Ti I	524.65500	0.836	-2.695	$5F_4 - 5D_3$	-	-	-
Cr II	524.67680	3.714	-2.466	$4P_{0.5} - 4P_{1.5}$	-	-	-
Fe I	524.70504	0.087	-4.946	$5D_2 - 7D_3$	-	-	-
Ti I	524.72890	2.103	-0.727	$5F_3 - 5F_2$	-	-	-
Cr I	524.75660	0.961	-1.640	$5D_0 - 5P_1$	-	-	-
Co I	524.79110	1.785	-2.070	$4P_{0.5} - 4D_{0.5}$	-	-	-
Ni I	524.83720	3.941	-2.426	$3G_3 - 3F_2$	-	-	-
Ti I	524.83830	1.879	-1.818	$3G_4 - 3F_4$	-	-	-
V I	524.90730	2.365	-2.067	$2F_{3.5} - 2H_{4.5}$	-	-	-
Fe I	524.91054	4.473	-1.480	$3G_3 - 3F_3$	-	-	-
Cr II	524.94370	3.758	-2.489	$4P_{1.5} - 6D_{2.5}$	-	-	-
Nd II	524.95760	0.976	0.094	$4F_{8.5} - 6D_{7.5}$	-	-	-
Co I	525.00000	4.175	0.320	$4G_{2.5} - 4H_{3.5}$	-	-	-
Fe I	525.02080	0.121	-4.938	$5D_0 - 7D_1$	0.253	207.070	3.0
Fe I	525.06450	2.198	-2.047	$5P_2 - 5P_3$	0.268	343.720	1.5
Ti I	525.09210	0.826	-2.363	$5F_3 - 5D_2$	-	-	-
Ti I	525.14780	0.818	-2.541	$5F_2 - 5D_1$	-	-	-
Fe I	525.19659	3.573	-1.990	$1H_5 - 1H_6$	-	-	-
Ti I	525.21000	0.048	-2.448	$3F_4 - 3F_3$	-	-	-
Fe I	525.30300	2.279	-3.940	$3P_2 - 5P_1$	-	-	-
Fe I	525.32400	3.635	-3.179	$3D_1 - 5F_1$	-	-	-
Fe I	525.34617	3.283	-1.573	$5D_1 - 5D_1$	-	-	-
Fe I	525.33100	4.320	-3.896	$5G_6 - 5H_5$	-	-	-
Co I	525.46470	3.971	-1.249	$4D_{3.5} - 4D_{3.5}$	-	-	-
Fe I	525.49554	0.110	-4.764	$5D_1 - 7D_2$	-	-	-
Cr I	525.51330	3.464	-0.386	$7P_4 - 7D_5$	-	-	-
Mn I	525.53260	3.133	-0.763	$4G_{5.5} - 4F_{4.5}$	-	-	-
Nd II	525.55060	0.205	-0.697	$4F_{4.5} - 6D_{4.5}$	-	-	-
Fe I	630.15012	3.654	-0.75	$5P_2 - 5D_2$	0.243	840.477	1.667
Fe I	630.24936	3.686	-1.236	$5P_1 - 5D_0$	0.240	856.772	2.5
Fe I	617.33356	2.223	-2.879	$5P_1 - 5D_0$	0.266	281.000	2.5

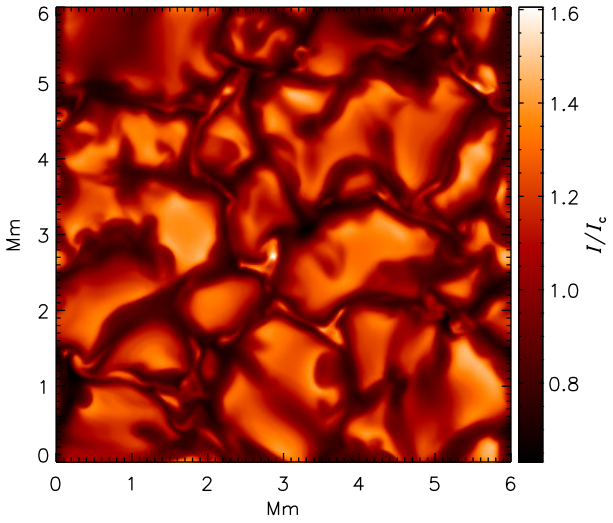

FIGURE 5.6:— Continuum intensity image at 525.0 nm.

5.3.4 Synthesis results

In this section we examine basic properties of the simulated region and make a comparison of the synthetic profiles with real observations. This provides us with information about the suitability of the MHD simulations.

Continuum contrast

Figure 5.6 shows the continuum intensity map at 525.0 nm for a single snapshot of the $\langle B \rangle = 140$ G run. Not surprisingly, it is rather similar to the temperature map shown in Fig. 5.2. In the continuum map the granular and intergranular regions can be clearly seen. The rms intensity contrast[7] is 17.9 %. It is greater than current values obtained from ground solar observations. The contrast measured from speckle reconstructed G-band images (Uitenbroek, Tritschler, & Rimmele 2007) does not surpass 15%. The only difference between the simulated images and real observations is that the latter are affected by atmospheric distortions and optical degradations while the former are not.

[7]The intensity contrast is evaluated as the standard deviation of the image divided by its mean value

Results for the different spectral lines

In order to check whether the synthesized Stokes profiles reproduce real solar observations, we have compared the (temporally and spatially averaged) Stokes I profile observed with the solar Fourier Transform Spectrograph (FTS) atlas of Brault & Neckel (1987) and Neckel (1999), which has minor instrumental broadening effects.

Figure 5.7 shows the comparison between the FTS for the quiet Sun and the averaged Stokes I for each of the synthesized spectral regions. The mean profiles have been taken from the $\langle B \rangle = 140$ G simulation run, since it allows for temporal averages (30 snapshots representing 5 minutes of evolution). The averaged profiles have been shifted in wavelength to correct for the solar gravitational redshift (611 $\mathrm{m\,s^{-1}}$). A minor correction to the wavelength shift has been allowed to improve the fits. The spectral resolution of the FTS ($\lambda/\Delta\lambda = 520\,000$) has also been taken into account. The Figure shows that the Doppler widths of the averaged profiles resemble the FTS. The intensity difference (bottom panel from Fig. 5.7) does not exceed 3%. The differences are not symmetric around the line core position, which indicate the presence of line asymmetries in the FTS, the averaged I profile, or both.

To carry out the comparison the FTS and the synthetic I profiles have been normalized to unity. However, the continuum intensities of the synthetic I profiles are 2.15, 2.93 and 4.02% higher for the 630.1, 617.3 and 525.0 nm spectral regions, respectively. This difference may be due to the finite temporal and spatial dimensions of the simulation box (Khomenko et al. 2005) which prevent, for instance, the generation of realistic 5-min solar oscillations. These oscillations induce weak variations on the continuum intensity.

A brighter continuum level indicates that the mean effective temperature[8] of the simulations is larger than the real one (Holweger 1969). Finally, note that the uncertainties on the atomic parameters used to synthesize the spectral lines modify the shape of the lines, but not the continuum level.

Figure 5.8 represents the temperature profile averaged over all pixels in the 140 G snapshot. In the same plot we have drawn the temperature stratification of the HSRA model atmosphere[9]. The temperature from the simulated data is 225 K hotter in deep layers ($\log\tau = 1$) and slightly cooler at higher layers, being $\Delta T = -50$ K at $\log\tau = -1$. On the top of the photosphere, the simulations are again hotter ($\Delta T \simeq 100$ K). As we mentioned before, the continuum intensities

[8]The mean effective temperature is defined as the mean temperature of the solar photosphere at the Rosseland optical depth, $\tau_R = 2/3$.

[9]SIR normalizes the spectra to the continuum intensity obtained from the HSRA model atmosphere at the given spectral range

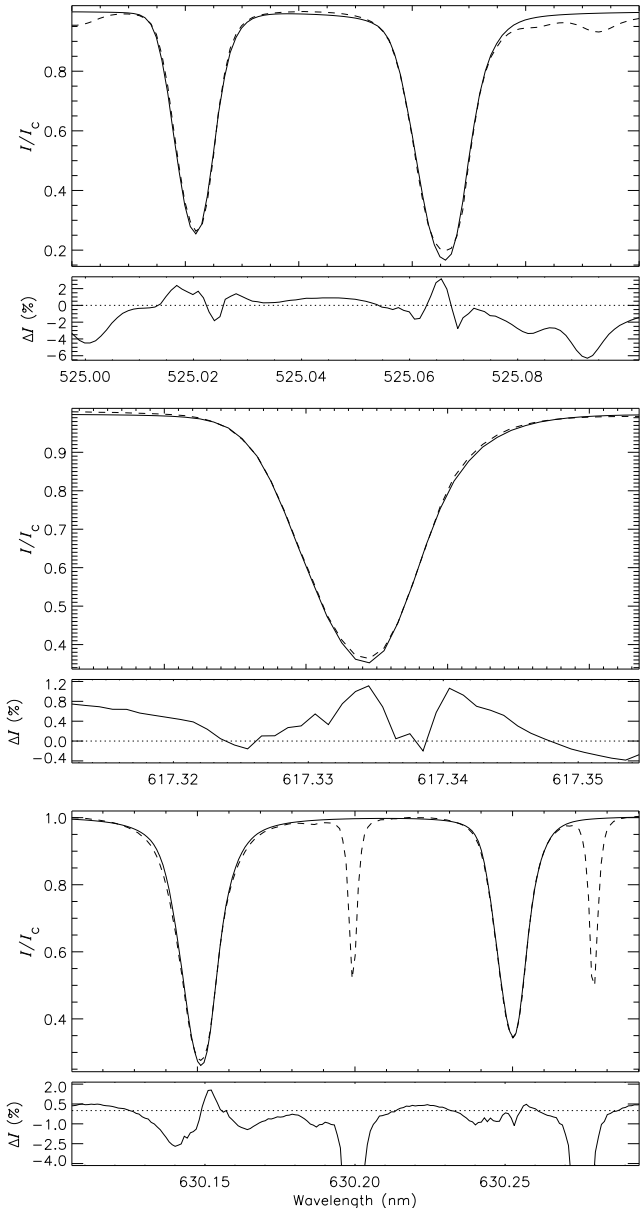

FIGURE 5.7:— *From top to bottom*: FTS intensity profile (*solid*) compared with the mean profiles from the simulation run with $\langle B \rangle = 140$ G (*dashed*), for the Fe I lines at 525.0, 617.3 and 630.15 nm, respectively. At the bottom of each panel we represent the intensity differences (FTS - simulation) in percent.

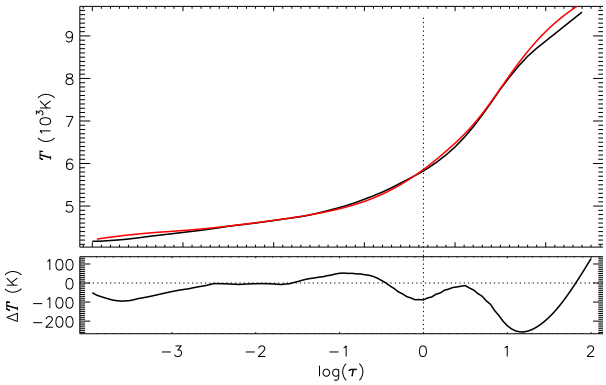

FIGURE 5.8— Mean temperature profile over all pixels (*red*) and temperature profile from the HSRA model atmosphere (*black*). At the bottom we represent the temperature differences (HSRA - simulation) in K.

of the Stokes I profiles are larger than the ones of the FTS atlas. The reason is the temperature difference at the photospheric layers at about $\log\tau = 0$ where the intensity of the continuum comes from. There, the simulated data is about 90 K hotter than the HSRA model atmosphere.

Khomenko et al. (2005) and Sheylag et al. (2007) found that the averaged I profiles from the simulations fit the continuum of the FTS. Contrary to our results, they found differences of 10% in the core of the Fe I lines at 630.5 nm.

In summary, despite slight differences between the FTS and the averaged I profiles, the simulations resemble quite satisfactorily the observations, yielding intensity differences smaller than 3%. Therefore, the MHD models seem appropriate to simulate realistic Stokes profiles.

5.4 ME inversion of the Stokes profiles

To determine the vector magnetic field and the LOS velocity, we apply a ME inversion to the two Fe I spectral lines at 630 nm simultaneously[10] using the MILOS code (see Chapter 4). The Stokes profiles are taken from a single snapshot of the $\langle B\rangle = 140$ G simulation run. No noise is added to the Stokes profiles. Hereafter all results will refer to this specific spectral line and this simulation run.

We assume a single one-component model atmosphere. Given the very high spatial resolution of the simulations we do not consider broadening of the spectra by macroturbulent velocities, although it is implicitly contained in the

[10]The Fe I pair of lines at 630 nm can be inverted simultaneously because they belong to the same multiplet. This implies that no more parameters are needed for the ME model (Lites et al. 1988), besides the ratio of oscillator strengths of the two lines that is indeed well known from atomic physics. Note that this shortening only applies to ME inversion. Codes whose assumptions are less restrictive (e.g., SIR) can simultaneously invert several lines.

thermodynamic parameters of the ME atmosphere. A total of 9 free parameters are determined: the thermodynamic parameters, S_0, S_1, η_0, $\Delta\lambda_D$ and a; the magnetic field strength, inclination and azimuth B, γ and χ; and the line-of-sight velocity, v_{LOS}. The filling factor is unity, i.e., the whole pixel is occupied by the magnetic atmosphere.

Finally, we allowed a maximum of 200 iterations, using the same guess model for all inverted pixels. The initial model was $S_0 = 0.2$, $S_1 = 0.8$, $\eta_0 = 6.5$, $B = 200$ (G), $\gamma = 20°$, $\chi = 20°$, $\Delta\lambda_D = 30$ mÅ, $v_{LOS} = 0.25$ (km s^{-1}) and $a = 0.03$.

5.5 Understanding the ME inferences

ME inversions provide a single value for the LOS velocity and for the magnetic field strength, inclination and azimuth. However, the analyzed spectral lines are sensitive to a broad range of optical depths. The variations of the physical properties of the atmosphere with height are encoded in the shape of spectral lines. For instance, the wing of the lines carry information from deeper layers and the core tells us about the physical properties of higher layers. Thus, the asymmetries in the profile shapes give information about vertical gradients. However, a ME model is unable to produce asymmetric profiles. Under these conditions the successfulness of the ME inversions may be questionable. Are the ME inversions appropriate for analyzing real observations?

Figure 5.9 represents the magnetic field strength, inclination, azimuth and LOS velocity stratifications of three pixels, (a), (b) and (c). In the same figure we represent the corresponding Stokes I, Q, U, and V profiles. The result of the ME fit is over plotted in red. Case (a) shows symmetric polarization profiles, in (b) the profiles are rather asymmetric and (c) shows three-lobed V profiles and anomalous linear polarization profiles. Also, (a) represents a strong field case and (b) and (c) weak fields. In the three cases the atmospheric quantities show large variations with optical depth.

The ME fit is good in (a) and worse in (b) and (c). Clearly, as the asymmetry level increases, the ME model has more difficulties in reproducing the profiles. The differences are clearly visible in Stokes Q, U and V. They are more difficult to notice for Stokes I.

The ME models retrieved from the inversion are represented on the left panels of Fig. 5.9 (red lines). The figure demonstrates that ME inversions result in height-independent parameters which can be interpreted as RF-weighted averages of the real stratifications (Westendorp Plaza et al. 1998). However, it is difficult to confirm this fact by simply looking at the parameter stratifications.

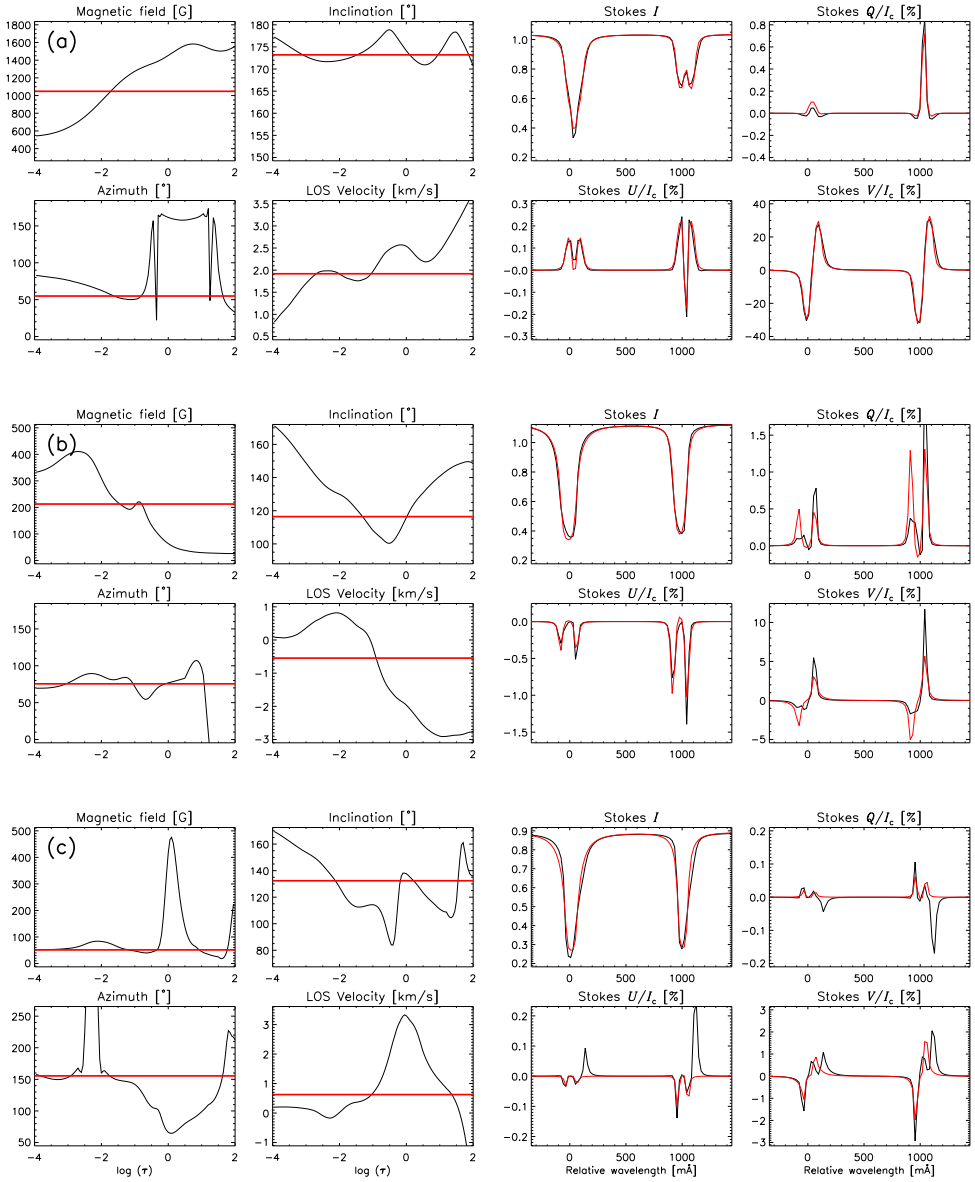

FIGURE 5.9:— Examples of MHD atmospheres and simulated profiles (black) and ME fits (red). *Left panels*: stratifications of the magnetic field strength, inclination and azimuth, and LOS velocity. The red horizontal lines indicate the ME inversion result. *Right panels*: Stokes I, Q, U and V profiles synthesized from the MHD simulations with no noise (black) and ME fit to the profiles (red). Cases (a), (b) and (c) correspond to pixel locations (x,y)=(84,52), (139,124), and (80,83), respectively.

To get an insight into the aforementioned issue, let us make a detailed analysis of case (c) from Fig. 5.9. This case represents a pixel whose ME fit is not satisfactory. The analysis of the stratifications show that the profile arises from an atmosphere that has a sharp discontinuity in field strength and in LOS velocity. Notice that a visual inspection of the Stokes V profile signatures readily provide information from the different atmospheric layers (see Khomenko et al. 2005; Ploner at al. 2001). Surprisingly, the ME model resulting from the inversion seem to account only for the weaker "component" of the atmosphere. How is this possible?

The ME inversion algorithm uses all wavelength samples along the profile to provide a fit. As mentioned before, different wavelength positions across the line sample different atmospheric layers. Thus, the ME inversion is forced to return average parameters along the LOS in order to fit the whole line profile reasonably well without any bias toward better fits in the line core or in the line wings. Figure 5.9 explicitly shows that inversion based on ME model atmospheres do not provide information about the vertical variation of the atmospheric parameters.

Figure 5.9 demonstrates that the ME model parameters coincide with the real stratifications at specific optical depths. Sometimes this occurs at various depths. We can determine the optical depths at which the inferred ME parameter coincide with, or is closer to, the stratifications. This allow us to determine the effective "height of formation" of the ME parameters.

Maps of optical depths have been calculated taking the depth locations of the nearest stratification values to the inferred ME parameter. The computation of the optical depths has been limited to the range $\log\tau = 0$ to -2.5. This range of optical depths include the vast majority of layers to which the Fe I lines are sensitive. If more than one value of the MHD stratification coincide with the corresponding ME parameter we take the one located at deeper optical depths. The optical depth location of the minimum (or maximum) of the MHD stratification values is taken if the ME parameter is smaller (or larger) than all stratification values.

Figure 5.10 shows the results for the magnetic field strength and the LOS velocity. For convenience the figure also displays a map of the continuum intensity and the field strength as retrieved from the inversion. Different colors indicated different atmospheric layers. There are clear differences between the two optical depths maps: In the granular centers the predominant color in the LOS velocity map is green ($\log\tau \sim -0.7, -1.2$), with the size of the patches being comparable to the granules; In the field strength map, smaller patches (green and red, i.e., $\log\tau \sim -0.3, -0.7$) are seen above granules. The intergranular lanes show small-scale structures (blue, $\log\tau \sim -1.3, -1.7$) in both

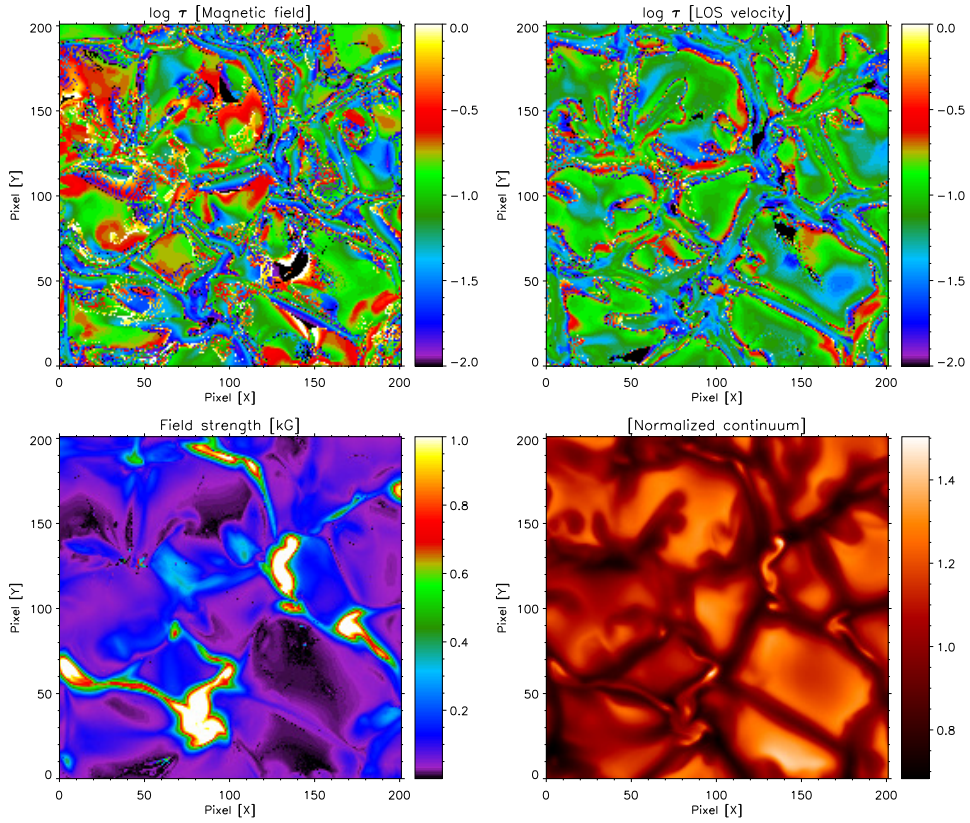

FIGURE 5.10:— Maps showing the optical depths at which the inferred ME parameter coincides with the real stratifications for the magnetic field strength and LOS velocity (*top left* and *right*, respectively). *Bottom* panels represent the magnetic field strength retrieved in the ME inversion and the normalized continuum intensity, *left* and *right* respectively.

maps. Note that the stronger the field, the higher the optical depth at which the ME parameter coincides with the real stratification. As we go from the granule centers towards the intergranular lane in the LOS velocity map, ME results corresponds to deeper layers (green turns into red). Nevertheless, sharp discontinuities are seen since the intergranular lanes tend to be blue. Note that the heights at which these spectral lines are sensitive to perturbations on the magnetic field and the LOS velocity go from $\log \tau \sim 0$ to -2.5.

Both maps exhibit differences from pixel to pixel, which are more noticeable for the field strength. The noise in the two panels is due to stratifications with many jumps in the MHD simulations.

In conclusion, as expected, ME inversions provide results that cannot be

assigned to a constant optical depth layer, as shown by the differences from pixel to pixel. Also, as follows from the comparison of the two optical depth maps, the heights to which the ME parameters refer change depending on the physical parameter (as predicted by del Toro Iniesta & Ruiz Cobo 1996; Sánchez Almeida, Ruiz Cobo, & del Toro Iniesta 1996; and Westendorp Plaza at al. 1998). For the Fe I 630.2 nm lines, we find a mean optical depth $\log\tau = -1$ and -1.1 for the LOS velocity and the field strength, respectively. This includes granular and intergranular regions. The rms is of about 0.4 and 0.5.

*From theoretical point of view, it is possible to determine the "height of formation of a ME measurement". This concept was introduced by Sánchez Almeida et al. (1996) and is based on generalized response functions (Ruiz Cobo and del Toro Iniesta 1994). Analytically, the height of formation of a measurement (τ_f) is

$$\log(\tau_f) = \frac{\int_{\lambda_i}\int_0^\infty R_x(\tau,\lambda)\log(\tau)d\tau d\lambda}{\int_{\lambda_i}\int_0^\infty R_x(\tau,\lambda)d\tau d\lambda}, \tag{5.5}$$

where $R_x(\tau,\lambda)$ stands for the generalized RF with respect to the parameter x. In the equation, i stands for the number of wavelength samples and Stokes profiles. This expression coincides with the barycenter of the generalized RF and has been used by del Toro Iniesta et al. (1994), Westendorp Plaza et al. (1998), Carroll, & Staude (2001), Khomenko et al. (2005) and Bellot Rubio, Schlichenmaier, & Tritschler (2006).

In practical applications, the concept of generalized RF is of little use, since the physical conditions of the solar atmosphere are not known (in fact, the goal of any inversion is to determine them). Note also that the stratifications resulting from the MHD simulations are highly non-linear, which would not lead to accurate theoretical predictions. As such, they differ significantly from the simple cases considered by Sánchez Almeida et al. (1996).

All previous considerations make the concept of hight of formation of a measurement meaningless. Therefore, the best choice to determine the uncertainties when interpreting real measurements with ME model atmospheres is to compare the results from the inversion with the physical quantities from a single optical depth layer. This layer is referred as the reference model.

5.6 Inversion results

In this section we make a qualitative and a quantitative comparison between the ME inversion results and the real stratifications of the atmospheric param-

eters. The comparison is done with the MHD model parameters at $\log\tau = -1$, hereafter refereed to as the "reference model".

Figure 5.11 shows maps for the magnetic field strength, inclination and azimuth, and the LOS velocity. The left panels correspond to the reference model while the right panels depict the parameters retrieved from the ME inversion. To better visualize the details we only show a small area of about 9 Mm^2.

At first glance, one notices the strong resemblance between the reference parameters and the results of the inversion. If we look in greater detail, we see that the shape of the different structures outlined by the model parameters are better reproduced in the magnetic field strength and inclination maps than in the LOS velocity and azimuth maps. There are some places where the inversion yields bad results for the inclination and azimuth. These areas show weak polarization signals. In general one can say that the ME inversion is able to determine the magnetic field vector satisfactorily. Even magnetic structures showing field strengths as low as 100 G are recovered. The differences seem to be larger at the intergranular lanes rather than in the granule centers for the case of the LOS velocity.

Figure 5.12 shows the atmospheric parameters at $\log\tau = -1$ form the MHD simulations vs the ME parameters inferred from the fit. These scatter plots include all the pixels (as mentioned in Sect. 5.4 noise has not been added to the profiles) and allow us to estimate the uncertainties that can be expected from the use of the ME approximation.

As can be seen, the scatter is larger for the magnetic field inclination than for the field strength and LOS velocity. For the azimuth the scatter is high. The mean values[11] (blue dots) show that the magnetic field strength is really close to the reference model values from 0 to 500 G. For larger fields the retrieved values are slightly below those of the reference model, although the deviation is always smaller than ∼300 G. The rms fluctuations of the strength (red) show deviations smaller than ∼150 G for the whole range of strengths. The inclination rms is smaller than 10° for vertical fields, and reaches 25° for inclined fields.

The LOS velocity panel shows that the retrieved velocity is by some 200-300 $\mathrm{m\,s}^{-1}$ below the reference velocities for receding flows (intergranular lanes). The rms values are smaller than 500 $\mathrm{m\,s}^{-1}$ in the full velocity range.

The scatter shown by the different panels of Fig. 5.12 originates from a combination of the use of a ME model atmosphere to explain the observations

[11]The averaged values have been calculated by taking equal bins along the X-axis of size 28 G, 3° and 115 $\mathrm{m\,s}^{-1}$, depending on the physical quantity.

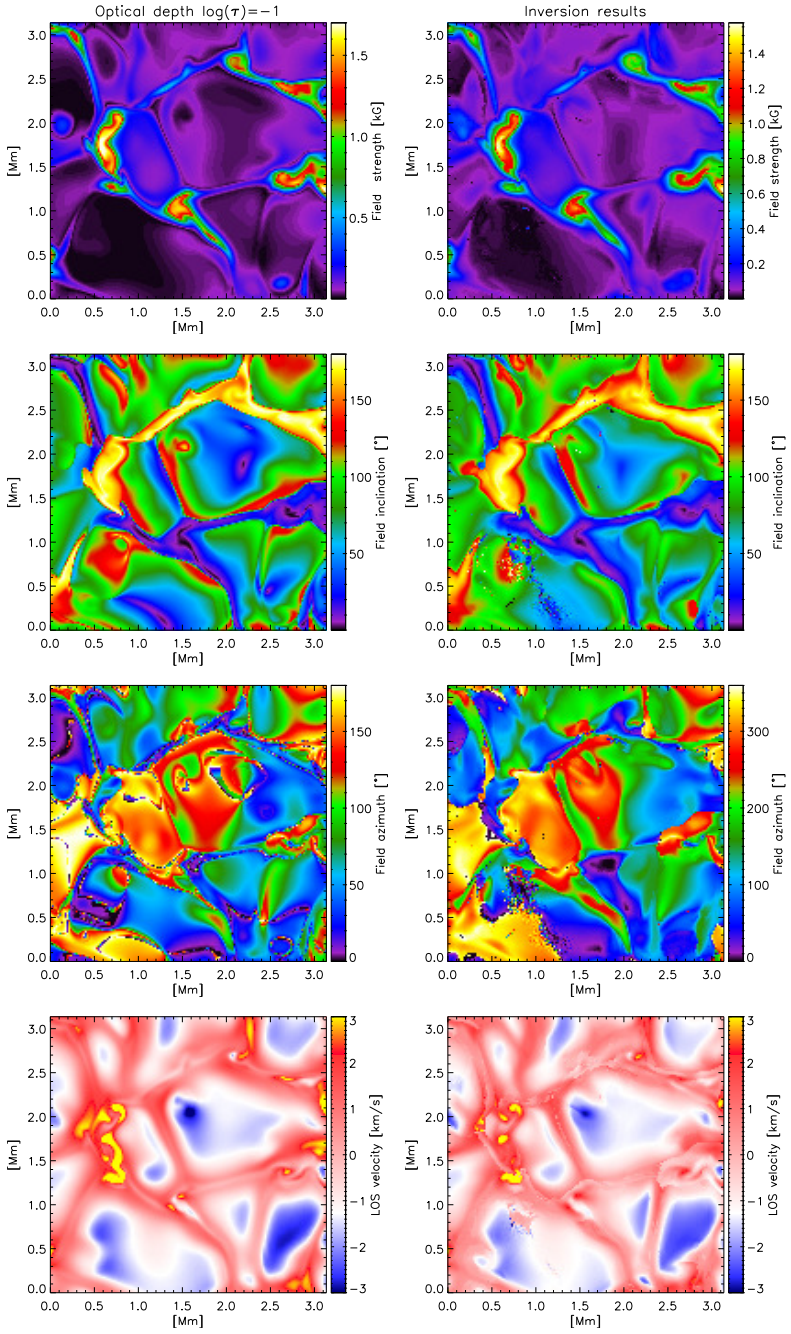

FIGURE 5.11:— From top to bottom: magnetic field strength, inclination and azimuth, and LOS velocity. Left represents the layer from the $\langle B \rangle = 140$ G simulation run at $\log \tau = -1$. Right shows the result of the ME inversion of the Fe I lines at 630.2 nm.

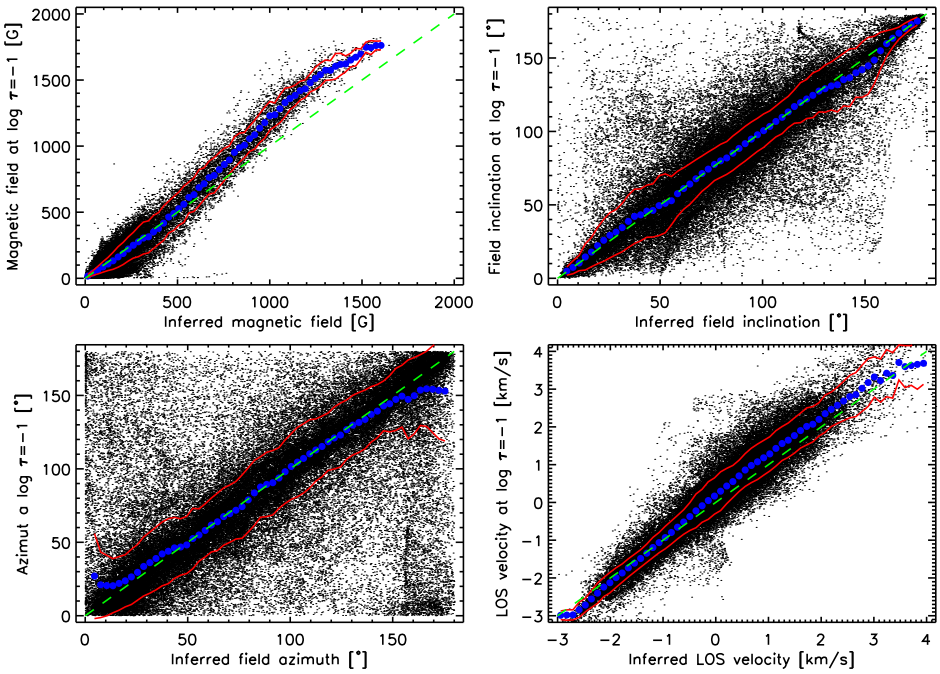

FIGURE 5.12:— Scatter plot of the magnetic field strength, inclination, azimuth and LOS velocity from the simulations at $\log\tau = -1$ vs the ME model parameters inferred from the inversion. The green dashed lines represent one-to-one correspondences. The blue dots represents the average mean values over very small, evenly-spaced intervals along the X-axis. The red line represents the rms fluctuations of the ME parameters.

and the pixel-to-pixel variations of the height of formation of the ME parameters, as explained in the previous section. The deviation of the mean values in the field strength from a one-to-one correspondence with the MHD field strengths can easily be understood by looking at the top panel of Fig. 5.10. We have choosen the atmospheric layer at $\log\tau = -1$ as a reference. For those spatial locations at which the optical depth value assigned to the inferred ME parameter is smaller that the optical depth of the reference layer, the resulting field strength will "apparently" be underestimated. These spatial locations are associated with strong field concentrations. In the MHD models the field lines spread out with height, therefore we retrieve weaker fields.

The previous discussion explain the deviations from the one-to-one correspondence of the ME inferences. We simply associate these deviations to the pixel-to-pixel variations of the height of formations. Therefore, the important quantity to keep in mind is the rms fluctuation of the ME parameters. This

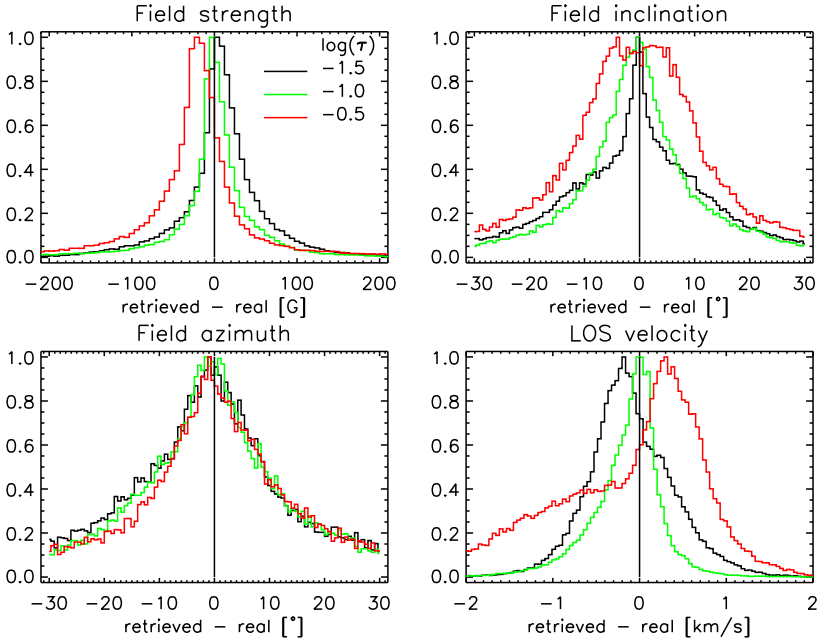

FIGURE 5.13:— Normalized histograms of the differences between the inferred ME model parameters and the real ones taken at different optical depths.

quantity provide us with the statistical deviations of the ME inferences from the real stratifications.

Depending on the optical depth assigned to the reference model the mean and rms of the various physical quantities change. To illustrate this, Fig. 5.13 represents histograms of the differences between the inferred parameters and the reference model taken at different optical depths ($\log\tau = -0.5, -1, -1.5$, coded in black, red and blue, respectively).

For the magnetic field strength, the histogram corresponding to $\log\tau = -1$ peaks at around zero. It shifts towards negative values when the inversion results are compared with deeper layers (fields are underestimated on average) and towards positive values when the comparison is made with higher layers (over-estimating the fields). The full width at half maximum (FWHM) is about 30 G for $\log\tau = -1$ an increases to $\sim$45 and $\sim$50 G for $\log\tau = -1.5$ and -0.5, respectively. These effects are less pronounced for the field inclination. In this case the peak of the histograms are around zero and the FWHM varies from 6° at $\log\tau = -1.5$ to $\sim$13° and $\sim$23° for $\log\tau = -1$ and -0.5. The larger scatter originate from the extended wings of the distribution. The azimuth histogram seem not to vary when comparing with different optical depths. In this case,

the FWHM is about 20°.

The histograms of the LOS velocity differences show larger variations. The one corresponding to $\log\tau = -1$ has the smaller FWHM ($\sim 500\ \mathrm{m\,s^{-1}}$). It also shows a long tail towards negative values which corresponds to pixels located in the intergranular lanes. The asymmetry of the histograms around the location of the maximum peak change dramatically when we compare the results of the inversion with different atmospheric layers. For instance, if the reference is taken at $\log\tau = -0.5$ the histogram is a clear combination of two different distributions, one representing granular centers (higher and narrower) and other one representing intergranular lanes (smaller in amplitude and broader). This explicitly shows the variations of the mean and the rms of the ME inferences with respect the height of the reference model.

5.6.1 Summary and conclusions

In this Chapter we have described basic properties of the MHD simulations. With the model atmospheres of the simulations we have synthesized the Stokes profiles emerging from three different spectral regions at 525.0, 630.2, and 617.3 nm. The comparison of the synthetic profiles with real observations of the quiet Sun (as represented by the FTS atlas) has proved that the simulations describe quite satisfactorily the physical conditions of the solar photosphere, although the MHD models are slightly hotter that the solar photosphere.

After synthesizing the Stokes profiles, the applicability of ME inversions to high spatial resolution observation has been tested. We have considered the case of the Fe I pair of lines at 630.2 nm. The analysis of the profiles by means of ME inversions has allowed us to characterize the uncertainties that can be expected from the ME approximation. For this reason, the synthetic profiles have not been degraded by noise, instrumental effects, or spatial resolution.

The main limitation of ME inversions is that they provide atmospheric quantities that are constant with height, whereas the MHD atmospheres feature physical properties that change with height. This limitation means that ME models are unable to reproduce spectral line asymmetries. Also, the ME inferences cannot be assigned to single atmospheric layers. Depending on the physical conditions of the atmosphere the inferred ME parameters sample different ranges of optical depths. This makes the interpretation of ME inferences difficult.

However, from the statistical analysis of the ME inversions vs the reference model we can conclude that they provide reasonable estimates of the physical quantities at $\log\tau = -1$. In particular they provide inferences with rms erros smaller than 30 G for the magnetic field strength, 6° and 20° for the field

inclination and azimuth and $500\mathrm{m\,s^{-1}}$ for the LOS velocity. These values are taken from the FWHM of the histograms of the differences between the inferred ME parameters and the real ones. We caution that when considering the inversion results for individual pixels the errors may be rather large, even when the best-fit ME profiles satisfactorily reproduce the observed ones (cf. field strength in case (a) from Fig. 5.9).

It is important to remark that the errors associated with the ME approximation dominate against those originated from the intrinsic noise of the observations (photon noise). We have analyzed photon noise errors (Chapter 3 and 4) and the results indicate that they are significantly smaller than the ones obtained in the present analysis. Therefore, we can conclude that for typical observations systematic errors dominate the photon noise errors. Note however that noise also prevents polarimetric signals from being detectable, point that we have been excluded from the current analysis.

Thus, the analysis presented in this Chapter is not complete because we have ignored important instrumental effects such as photon noise and image degradation by telescope diffraction or atmospheric seeing. These effects introduce additional uncertainties in the determination of solar magnetic fields.

In the next Chapter we go one step further by simulating a real observation with all the instrumental effects involved. We consider the case of the spectropolarimeter aboard *Hinode*, since it provides the highest spatial resolution currently achievable.

6

Simulating and analyzing Hinode spectropolarimetric observations

In the preceding Chapter we have demonstrated that ME inversions are able to determine the magnetic field vector and the LOS velocity from simulated Stokes profiles that are unaffected by the measurement. In this Chapter we study a more realistic scenario in which the profiles are degraded by the instrument: we simulate high-spatial resolution observations of the spectropolarimeter aboard the *Hinode* satellite using model atmospheres from MHD calculations, and then we invert them with MILOS. This allows us to assess the performance of ME inversions of high-spatial resolution observations of the quiet Sun.

6.1 Introduction

The spectropolarimeter (SP; Lites et al. 2001a,b; Tarbell et al. 2008) of the Solar Optical Telescope (SOT; Tsuneta et al. 2008; Suematsu et al. 2007; Shimizu et al. 2007; Ichimoto et al. 2007) aboard *Hinode* (Kosugi et al. 2007) is able to provide nearly diffraction-limited observations of the solar photosphere, with a spatial resolution of $0\farcs32$. The instrument measures the Stokes profiles of the Fe I pair of lines at 630.2 nm with high spectral resolution and polarimetric sensitivity (S/N = 1000).

Here we investigate whether reliable magnetic field strengths and field inclinations can be derived from *Hinode*/SP observations. To this aim we make use of MHD simulations of quiet-Sun regions to synthesize the Stokes profiles of the

Fe I 630.2 nm lines. The profiles are degraded to the nearly diffraction-limited resolution of $0\farcs32$ achieved by *Hinode*/SP. Then, we add noise to the Stokes profiles and infer the various atmospheric parameters by means of ME inversions. The comparison of the inferred values with the real ones will provide us with an estimation of the uncertainties in field strength, field inclination, and magnetic flux to be expected from the analysis of *Hinode* data.

To date, only Khomenko et al. (2007a,b) have examined the diagnostic potential of high spatial resolution observations in the absence of atmospheric seeing. Among other topics, they investigated the capabilities of the Fe I pair of lines at 630.2 nm for quiet Sun internetwork (IN) field studies.

A complete analysis of the capabilities of these two lines for IN fields determination is of interest in view of the results of Martínez González et al. (2006). These authors argued that the Fe I 630.2 nm lines do not carry enough information to uniquely determine the magnetic field strength at $1''$. Moreover, they suggested that inversions of IN Stokes profiles results seem to be biased toward strong fields. Therefore, there are clear needs to examine whether or not it is possible to derive the field strength distribution of IN regions from very high spatial resolution polarimetric observations in the visible, as those carried out by the *Hinode*/SP.

The Chapter is structured as follows: first, we describe the MHD simulations and how we have degraded them to match the spatial resolution and pixel size of *Hinode*/SP. The effects of the degradation of the Stokes vector is discussed in some detail. Then, we explain the strategy used to invert the simulated profiles, introducing the concept of local stray light. At the end of the Chapter we discuss the inversion results and carry out a comparison with the real model quantities.

6.2 MHD simulations and spectral synthesis

We use three snapshots from the radiative MHD simulations of Vögler et al. (2005) to describe the solar photosphere in the more realistic way possible. They correspond to simulation runs with mean flux $\langle B \rangle = 10$, 50 and 140 G. Figure 6.1 shows the corresponding PDFs for the magnetic field strength and inclination taken at optical depth $\log \tau = -2$. As can be seen, most of the magnetic fields have strengths of the order of hG. Note also that horizontal fields are very common. We then synthesize the Stokes spectra of the two Fe I lines using SIR. The lines are sampled at 113 wavelength positions in steps of 2.15 pm, following the *Hinode*/SP normal map mode (for details, see Shimizu 2004). For details of the MHD simulations and the synthesis of the Stokes

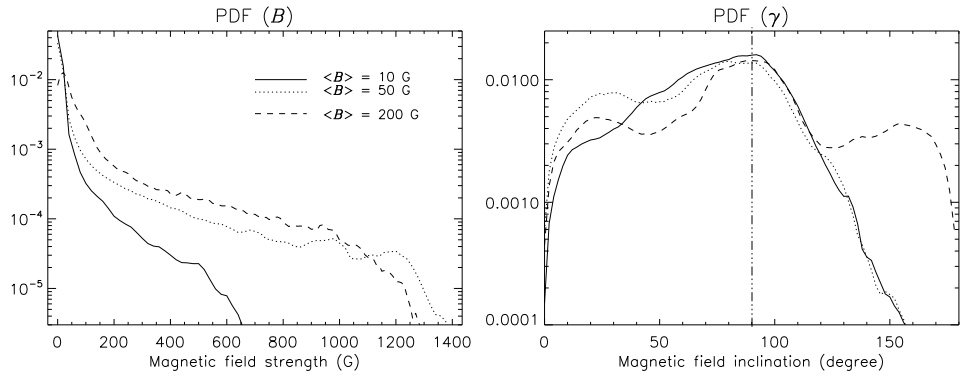

FIGURE 6.1:— Magnetic field strength (*left*), and field inclination (*right*) probability density functions in the magneto-convection simulations with $\langle B \rangle = 10$ (*solid*), 50 (*dotted*) and 140 Gauss (*dashed*), taken at optical depth $\log \tau = -2$.

profiles the reader is referred to Chapter 5.

The sampling interval in the simulations is $0\farcs0287$, which implies a spatial resolution of $0\farcs057$ (41.6 km). Thus, the synthetic Stokes profiles derived from the MHD snapshots have to be degraded to match the *Hinode*/SP resolution.

6.3 Instrumental degradation of the simulated data

In this section we describe the alterations that the instrument introduces in the "observed" Stokes profiles. This includes the effects of the optical system, i.e, the telescope, the spectrograph, and the detector. All of them modify the observations to a larger or smaller extent, degrading their original resolution and image contrast. We do not include the influence of the terrestrial atmosphere since we concentrate on high spatial resolution data taken from space. Simulating a solar observation is critical because the optical system employed to observe the Sun prevents it from being recorded at optimum quality.

6.3.1 Spatial degradation: basics

Let be $I_o(x, y)$ the true intensity distribution coming from the solar surface. This distribution is distorted by the optical system according to

$$I(x, y) = I_o(x, y) * \mathrm{PSF}(x, y) + n(x, y), \tag{6.1}$$

where $I(x, y)$ is the observed image, $\mathrm{PSF}(x, y)$ denotes the Point Spread Function of the optical system, and $n(x, y)$ stands for the noise (photon noise due to

the detector). The symbol $*$ stands for convolution. We can write this equation in the Fourier domain as

$$\hat{I}(x,y) = \hat{I}_o(x,y) \cdot \mathrm{OTF}(s_x, s_y) + \hat{n}(x,y), \tag{6.2}$$

where the Optical Transfer Function (OTF) is the Fourier transform of the PSF and represents the spatial frequency response of the optical system. The Modulation Transfer Function (MTF) is the modulus of the OTF. The symbol $\hat{}$ stands for the Fourier transform. The MTF includes all the effects of the optical system, i.e., the possible aberrations associated with the telescope (polishing errors, defocus, etc), the transfer optics, the spectrograph or filtergraph (e.g. the amplitude and phase shifts of an étalon or the limited spectral resolution of the spectrograph), and finally the detector.

The effective spatial resolution of the telescope corresponds to the cut-off frequency of the first term of the MTF (diffraction limit). To first order, the PSF can be considered rotationally symmetric in the X-Y plane. In this case, if we consider that only telescope diffraction contributes to the PSF it can be shown that

$$\mathrm{PSF}(r) = \frac{1}{\pi}\left[J_1(\frac{D\pi}{\lambda r})/r\right]^2 \tag{6.3}$$

(Born and Wolf 1970), where J_1 is the order 1 Bessel function of the first kind (Airy diffraction pattern), r the angular distance from the center of the PSF in the image plane, λ the working wavelength, D the telescope's aperture. The first zero of Eq. (6.3) occurs at $r_{\min} = 1.22\lambda/\mathrm{D}$. This expression is known as the Rayleigh criterion. Thus, the resolving power of the telescope is given by the diameter of the telescope and the working wavelength. In practice, it is preferable to define the diffraction limit as $r_{\mathrm{cut}} = \lambda/\mathrm{D}$, i.e., the highest detectable angular frequency in arcsec (first minimum of the MTF). It is 1.02 times the FWHM of the central component of the Airy diffraction pattern.

6.3.2 Modeling the *Hinode*/SOT+SP MTF

To model the combined MTF of the *Hinode* Solar Optical Telescope and the espectropolarimeter we need a set of parameters describing the optical system. They are summarized in Table 6.1. In particular, we include the following effects in the MTF:

- the limited spatial resolution of the telescope, i.e., the diffraction limited telescope which cut off high frequencies while allowing low and mid frequencies to be transmitted,

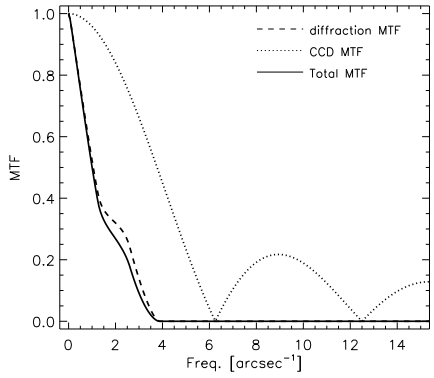

FIGURE 6.2— MTF of the *Hinode*/SOT detector (dotted line), diffraction limited MTF (dashed line), and combination of both effects (solid line).

- the central obscuration of the entrance pupil (caused by the secondary mirror), which affects the intermediate frequencies,

- the pixilation of the detector (detector footprint MTF)[1], which introduces an extra lost of contrast, and spatial sampling.

The diffraction limited spatial resolution of *Hinode* SOT is $\sim 0\farcs26$ (cut-off frequency of the first term of the MTF), but the final spatial resolution of $\sim 0\farcs32$ of the SP is determined by the detector pixel size ($0\farcs16 \times 0\farcs16$). When the detector sampling is larger than the spatial resolution provided by the telescope, the highest spatial frequencies transmitted by the optics are lost. This effect is known as aliasing.

Figure 6.2 shows the MTFs describing the filtering of spectral components induced by telescope diffraction and pixilation effects in the CCD. Note the modification of the effective MTF caused by the central obscuration of the entrance pupil. The cut-off frequency ($f_{\rm cut} = {\rm D}/\lambda$) stands for the spatial resolution limit of the image while the shape of the MTF affects the overall image contrast. The plot also shows that the shape of the MTF is only slightly modified by the detector MTF.

6.3.3 Spectral smearing

The finite spectral resolution of the *Hinode*/SOT affects the Stokes profiles through convolution:

$$\mathbf{I}_{\rm obs} = \mathbf{I} * F(\lambda), \tag{6.4}$$

[1]It represents the loss of contrast of the image due to the integration of signal in each of the CCD pixels of the camera

TABLE 6.1:— Basic optical parameters of *Hinode*/SOT and SP.

APERTURE	0.5 m	
WORKING WAVELENGTH	630 nm	
SPATIAL RESOLUTION	$\sim 0\farcs26$	$\sim$190 km
CENTRAL OBSCURATION	34.4%	
CCD PIXEL SIZE	$0\farcs16 \times 0\farcs16$	

where $F(\lambda)$ stands for a scalar smearing profile and $\mathbf{I}_{\rm obs}$ is the observed Stokes vector. This spectral smearing produces well known effects in the Stokes spectra: it broadens the polarization profiles and reduces their amplitudes. In general, the smearing reduces the quality of the observations and diminishes the sensitivity of spectral lines to the atmospheric quantities (see Chapter 2).

The effect of the finite resolving power of the spectrograph has to be included in the image degradation process. In our case, we use a Gaussian function of a given FWHM to represent the smearing profile. Note that, in this case, the limited resolution of the spectrograph produces the same effects as a macro-turbulent velocity field.

6.3.4 Degradation of the data

Santiago Vargas and José Antonio Bonet, from the Instituto de Astrofísica de Canarias, have developed a code that is able to simulate the degradation of an image (real object) caused by an instrument. To this end the code needs several input parameters: the aperture of the telescope, the working wavelength, the size of the primary mirror, the central obscuration of the telescope and the CCD pixel size (spatial sampling). Finally, the user has to specify the dimensions of the real object, in pixels, as well as the sampling interval, in arcsec.

The spatial degradation we perform includes the most important terms, but is not complete because other effects are difficult to model. For instance, we do not consider the polishing quality of the primary mirror (which affects high frequencies of the MTF), the spider legs supporting the secondary mirror, or stray light by scattering in any optical device. A more detailed theoretical calculation of the *Hinode*/SOT+SP MTF has been carried out by Danilovic et al. (2008). They included the effects of the spider legs and SP defocus. Both contributions affect the continuum images by reducing their contrast by $\sim$1% at most, depending on the defocus of the SP. The spatial resolution remains unaltered, though. For an empirical determination of the PSF of *Hinode*/SOT in combination with the Broadband Filter Imager (BFI) see Wedemeyer-Böhm (2008).

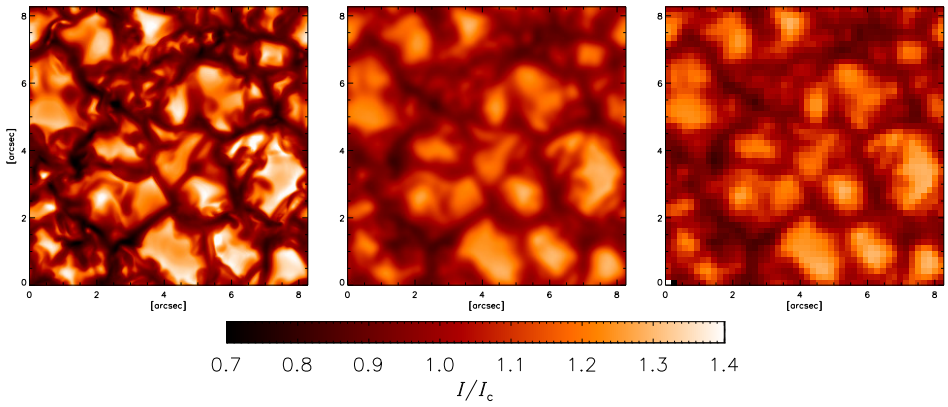

FIGURE 6.3:— *Left*: Original continuum intensity maps for the simulation snapshot with average unsigned flux of 10 Mx cm^{-2}. *Middle*: same, but for the data spatially degraded considering telescope diffraction. *Right*: same after degradation by CCD pixel size. Color scales are the same in the two maps. The contrast varies from 13.7% in the original image to ∼8.5% in the spatially degraded ones.

The spatial degradation is applied to monocromatic images, i.e., we have spatially degraded a total of 112×4 images, corresponding to the number of wavelength samples times the Stokes parameters. Once each of the images has been degraded to account for telescope diffraction[2], we take into account the sampling of the detector, i.e., the 112×4 images are rebined to match the *Hinode*/SP CCD pixel size of 0.″16. Actually, the spatial sampling of the rebined images corresponds to 0.″172. The reason is the following: the step size of the MHD simulations is 0.″0287. A pixel size of 0.″16 corresponds to 5.6 pixels in the original data. To avoid interpolations between pixels, we assume a final spatial sampling of 0.″172, i.e., 6 pixels from the original resolution, which leaves us with monochromatic images of 48×48 pixels.

Once the spatial degradation has been applied to the data, we account for the spectral smearing of the *Hinode* spectrograph. To this end all four Stokes profiles from the 48×48 pixel fo the FOV are convolved with a Gaussian of 25 mÅ FWHM. Finally, noise at the level of $10^{-3}\,I_c$ is added to the profiles to simulate the detector photon noise.

[2]Since no confusion is possible, we hereafter refer to the spatial degradation as telescope diffraction and CCD pixel size.

6.3.5 Effects of telescope diffraction and spectral smearing

Figure 6.3 shows continuum intensity maps for the original data, and for the degraded data with and without CCD pixilation, corresponding to $\langle B \rangle = 10$ G. The instrument causes two main effects: a reduction of the rms contrast from 13.7% to 8.5%, and a worse spatial resolution, as can be seen from the pixilation due to the CCD in the degraded image. Intergranular fine-scale structures are apparently lost when degrading the image. The rms intensity contrast of the granulation, the internetwork, is about 7.5% on real *Hinode*/SP observations, slightly lower than in the spatially degraded data. As shown by Danilovic et al. (2008), the spider legs of the secondary mirror decreases the rms contrast an additional ∼0.2%. The difference between the contrast in real data and the spatially degraded simulations can be ascribed to second-order optical aberrations, including SP defocus which may reduce the contrast by 1%. The focal plane package of SOT is not achromatic, and therefore some amount of defocus occurs in the SP when the BFI or NFI are focused.

Figure 6.4 compares the average Stokes I profiles from the spatially degraded data ($\langle B \rangle = 10$ G) and the NSO Fourier Transform Spectrometer Atlas of the quiet Sun (top panel). Both spectra are very similar, with only small differences in the line core and wings of Fe I 630.1 nm. The lack of a temporal average excludes, for instance, the effect of the 5-min oscillation in the simulated profile. This might explain part of the observed differences.

The bottom panels of Fig. 6.4 show the distribution of the Stokes V and $L = \sqrt{Q^2 + U^2}$ amplitudes of the spatially and spectrally degraded profiles for the three simulation snapshots used in this Chapter. Clearly, the amplitude of the polarization signals increases as the mean flux density of the snapshot increases.

Telescope diffraction modifies the shape of the Stokes profiles. Figure 6.5 shows an example in an intergranular lane, before and after the spatial degradation of the image. The profile shapes change dramatically after the degradation: Stokes I is broader and shifted towards the blue; Stokes Q, U, and V are smaller in amplitude and smoother; finally, the profiles show less asymmetries. The comparison of the profiles has been done before binning the images to the final pixel size of 0.″16 and without considering the finite resolving power of the spectrograph.

Diffraction affects each pixel differently depending on its neighboring pixels. This makes it difficult to characterize how the degradation caused by the telescope changes the Stokes profiles. To get some insight we analyze the total circular polarization, TCP $= \int |V(\lambda)|/I_c d\lambda$, and total linear polarization, TLP $= \int (Q^2(\lambda) + U^2(\lambda))^{1/2}/I_c d\lambda$, signals. Figure 6.6 shows the TCP and the

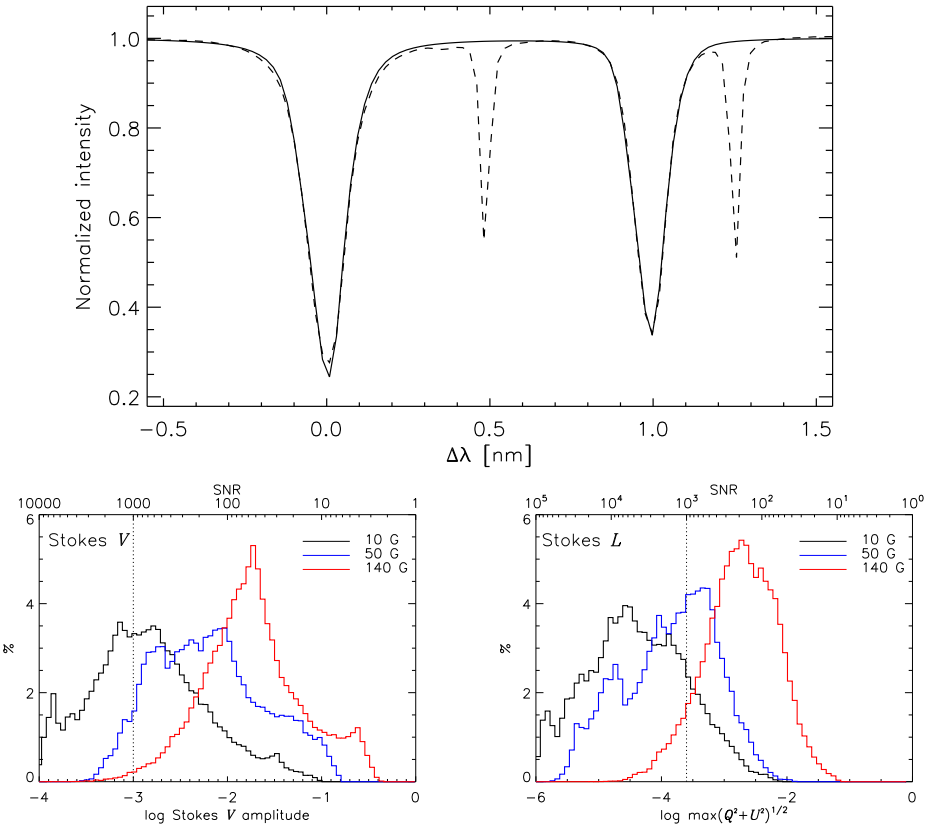

FIGURE 6.4:— *Top*: Comparison between the average Stokes I profiles from the spatially degraded data (solid) and the FTS spectral atlas (dashed). Both continua are normalized to unity. *Bottom*: Distribution of the Stokes V and $L = \sqrt{Q^2 + U^2}$ amplitude in the spatially and spectrally degraded images corresponding to the simulation runs of $\langle B \rangle$ = 10, 50 and 140 G. Vertical, dotted lines indicate S/N = 1000.

TLP maps for the original and degraded data rebinned to the *Hinode*/SP CCD pixel size of 0.″16. The pixilation is clearly visible in the four panels of the figure. The color scales are the same in the various panels to emphasize the differences in contrast that occur. The top panels show the images as we would record them with an ideal telescope of 50 cm allowing all spatial frequencies to be identically transmitted, while the bottom panels show the real effects of telescope diffraction.

Diffraction makes polarization signals to appear "blurred" in the degraded image. It also substantially diminishes the contrast due to the weakening of the polarization signals. The spatial degradation acts in the same direction

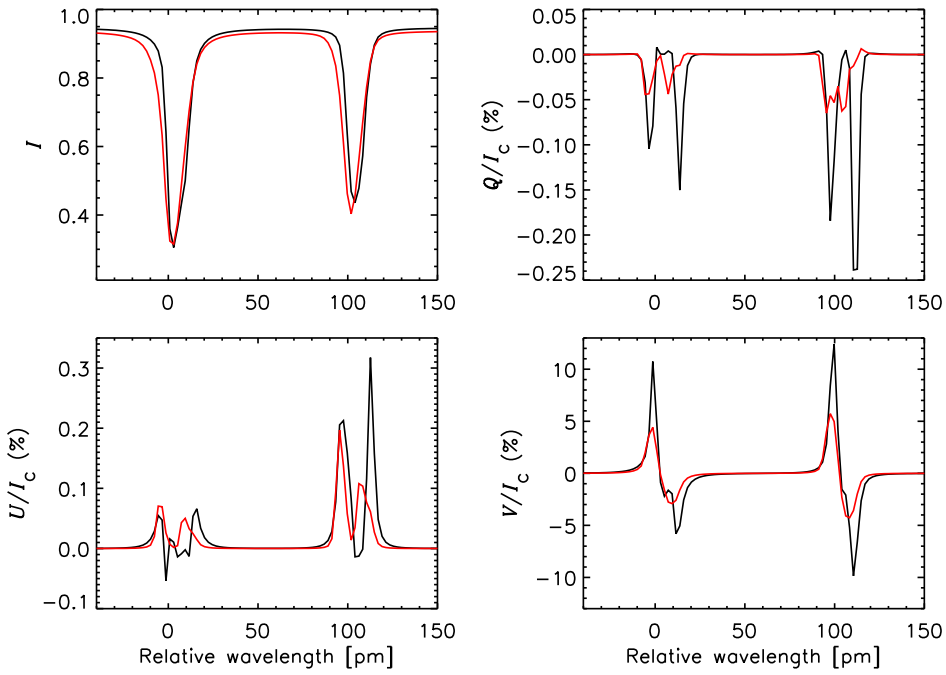

FIGURE 6.5:— Stokes I, Q, U and V profiles corresponding to the pixel x=87 y=170 of the simulation run with $\langle B \rangle = 10$ G before and after image degradation (black and red lines, respectively). The image has not been rebinned to the pixel size of $0\farcs16$, in order to make a direct comparison.

for both the TCP and TLP signals. It is also clear that small-scale structures (higher frequencies) seen on the TCP and TLP original maps disappear after the image object has passed through the telescope: the MTF of the telescope behaves as a *low-pass* filter. Finally, notice that the effect of diffraction on the polarization is the same as that of a magnetic filling factor: in both cases the polarization signals are smaller in amplitude.

The distributions of Stokes V and $L = \sqrt{Q^2 + U^2}$ amplitudes in the original and degraded maps provide more quantitative information about the effects of telescope diffraction and CCD pixel size. In Fig. 6.7 we show histograms corresponding to the simulation run with $\langle B \rangle = 10$ G. Noise has not been considered in this analysis. The histograms of V and L are asymmetric, with a steep tail toward large and small amplitude values, respectively. They have a clear maximum, which in the case of Stokes V is located at about -2.6 and -3 dex for the original and degraded images, respectively.

The distributions of Stokes V amplitudes reflects the effects of diffraction:

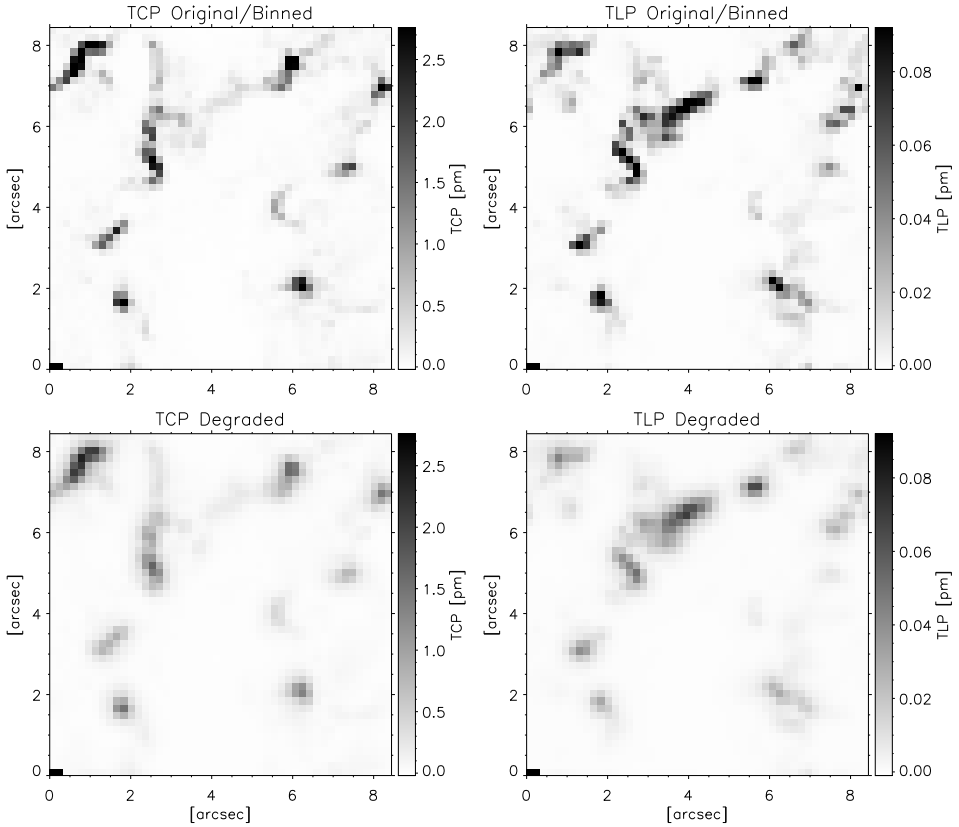

FIGURE 6.6:— Total circular polarization signal (TCP) and total linear polarization signal (TLP), as we would record it on the *Hinode*/SP CCD without the effects of telescope diffraction, i.e., the binned original image, and with the changes due to telescope diffraction (bottom panels).

first, the histogram shape is modified, i.e., the large Stokes V amplitudes region is less populated while the weaker amplitudes are more numerous, and secondly it shifts as a whole towards smaller amplitude values. The effects on L are slightly different. The distribution of Stokes L after diffraction is narrower. The largest/weakest Stokes L amplitudes are less populated while the frequency of intermediate amplitudes increases. The position of the histogram peak does not change.

The PSF of the telescope distributes part of the polarization signal of a pixel to nearby ones. For point sources the effect of diffraction is easily understood as a "bloom" (Lites et al. 1999) of the polarization signals: the pixel spreads out its signal to the immediate non-magnetic, vicinity generating a kind of artificial

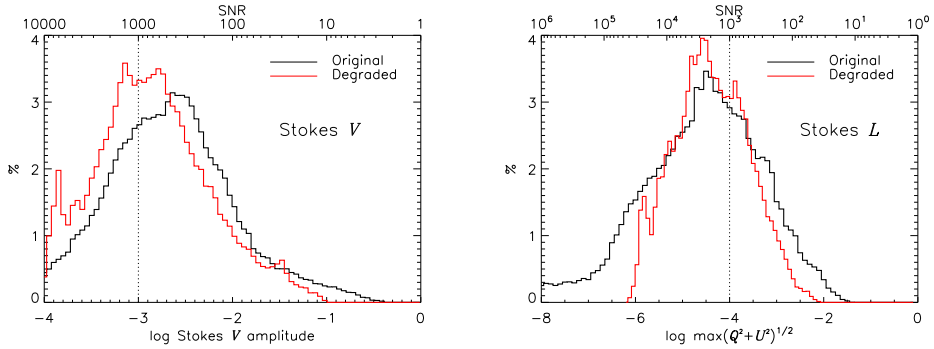

FIGURE 6.7:— Distribution of the Stokes V and $L = \sqrt{Q^2 + U^2}$ amplitudes in the original (black) and degraded (red) images. The Stokes profiles have been taken from the simulation run having $\langle B \rangle = 10$ G.

canopy. In general, polarization signals are not isolated therefore all pixels will spread their signal out. Although in general, pixels with the strong polarization signals will tend to loose their signals and those with weaker signals will take that from their immediate vicinity, all pixels contaminate each other and the final result depend on the particular distribution of pixel signals and naturally, on the PSF of the telescope.

Overplotted to Figs. 6.4 and 6.7 is a vertical, dotted lines indicating S/N=1000 which corresponds to the typical noise level of *Hinode*/SP. Stokes V (or L) signals with amplitudes below these thresholds are hard to detect. The position of the maximum of the non-degraded Stokes V histogram lies close to the S/N=1000 boundary while the maximum of Stokes L is always below. This implies that a non-negligible number of pixels exhibit circular and linear polarization signals that are below the detection limit already in the original MHD simulations. The fraction of such pixels increases when the image is spatially degraded. The amount of Stokes V signals above the noise level decreases ∼12%. In the analysis we have included the contribution of the limited spectral resolution of *Hinode*/SP. It shifts the histograms as a whole toward smaller amplitude values. For a FWHM of 25 mÅ however, the shifts are small.

6.4 Inversion

As we have shown, diffraction alters the shapes of the Stokes profiles, mixing information from nearby pixels. Is it possible to infer the magnetic field vector under these conditions? In this section we aim at understanding how telescope

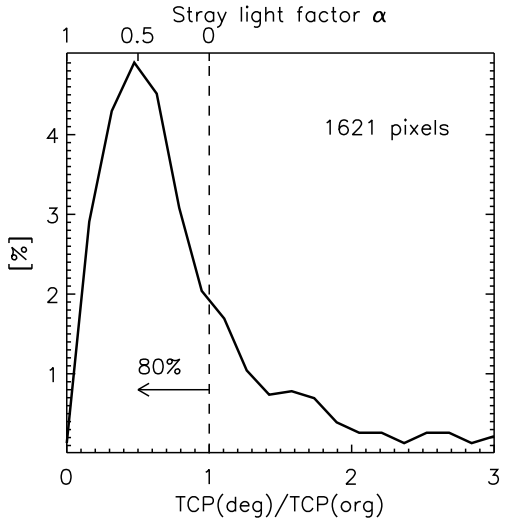

FIGURE 6.8— Histogram representing the ratio of total circular polarization signal in the degraded image with respect to that in the original image, for the simulation run with $\langle B \rangle = 10$ G. The upper X-axis indicates the equivalent stray-light contamination factor.

diffraction hampers the inversion of *Hinode*/SP measurements. In other words, we want to examine how the degradation of the data by telescope diffraction affects the inference of the various physical quantities.

We derive the magnetic field vector from the simulated profiles using the MILOS code. As we have discussed in Chapter 5, inversion techniques based on ME atmospheres represent the best option to interpret the measurements if one is not interested in vertical gradients of the physical quantities. They are simple and often provide reasonable averages of the atmospheric parameters over the line formation region (e.g. Westendorp Plaza et al. 2001; Bellot Rubio 2006).

6.4.1 Modeling the telescope diffraction

Before entering into the inversion details, we explain a possible way to take into account the effects of telescope diffraction. Figure 6.8 displays the ratio of total circular polarization signal in the degraded snapshot with respect to that in the original snapshot for the simulation run with $\langle B \rangle = 10$ G. Only pixels whose Stokes Q, U, or V amplitudes remain above $4.5 \times 10^{-3}\, I_c$ after the spatial degradation are considered here, since the others are below the noise level. This leaves us with 1621 pixels. In line with the results of Sec. 6.3.5, the histogram indicates that the circular polarization is smaller in the degraded image: 80% of the pixels show weaker signals. The decrease in polarization signal is not due to cancellation of opposite polarity fluxes (since mixed polarities are not present in the snapshot at very small spatial scales), but is truly the result of

diffraction.

If one does not account for the reduction in polarization signals related to telescope diffraction, the inversion would systematically fail. In pixels where the magnetic field is intrinsically weak, the field strength is determined mainly from the Stokes V amplitude. In this case, if we do not correct the effects of diffraction, then the inversion code will yield smaller field strengths.

For this reason we use a stray/scattered-light contamination factor in the inversion of the Stokes profiles even if there is no atmospheric seeing affecting the SP observations. A reduction in polarization signals also occur when only a fraction of the pixel is occupied by a weak magnetic field. In this case, the stray-light contamination factor acts as the filling factor of a non magnetic component (the stray-light profile) occupying the rest of the resolution element. There is no way to distinguish between the two cases.

Since telescope diffraction mixes light from nearby pixels, not from pixels far away, a local stray-light profile must be considered. This differs from typical strategies for the stray-light evaluation. In our case, the stray light profile is evaluated individually for each pixel by averaging the Stokes I profiles within a box $1''$-wide centered on the pixel. Notice that the FWHM of the *Hinode*/SP MTF (Fig. 6.3, top panel) is about 1 arcsec.

This treatment of telescope diffraction is simplistic because we use an *unpolarized*[3] stray-light contamination, while it is clear that diffraction also mixes the polarization signals. In Fig. 6.8 it can be seen that 20% of the pixels show larger polarization signals after degradation. For those pixels the adopted strategy of a stray/scattered-light for the inversion is not appropriate because a stray-light factor can only reduce the polarization signals. However, as we will see below, this new strategy represents a significant improvement over conventional treatments in which a single global stray-light profile is employed to invert the observed spectra.

The differences between simulated *Hinode*/SP observations analyzed with a global and a local stray-light profile are illustrated in Fig. 6.9 for a single pixel. The best fit using a global stray-light contamination cannot simultaneously explain the intensity and polarization spectra because the stray-light profile has a different shape than that needed to account for the observed Stokes I profile. The problem disappears when a local stray-light profile is used, improving the determination of the intrinsic field strength.

[3]By unpolarized stray light we mean that the Stokes Q, U and V parameters are identically zero. Note that when averaging the Stokes I profiles in the neighborhood of a pixel we are including the polarization signatures present in Stokes I.

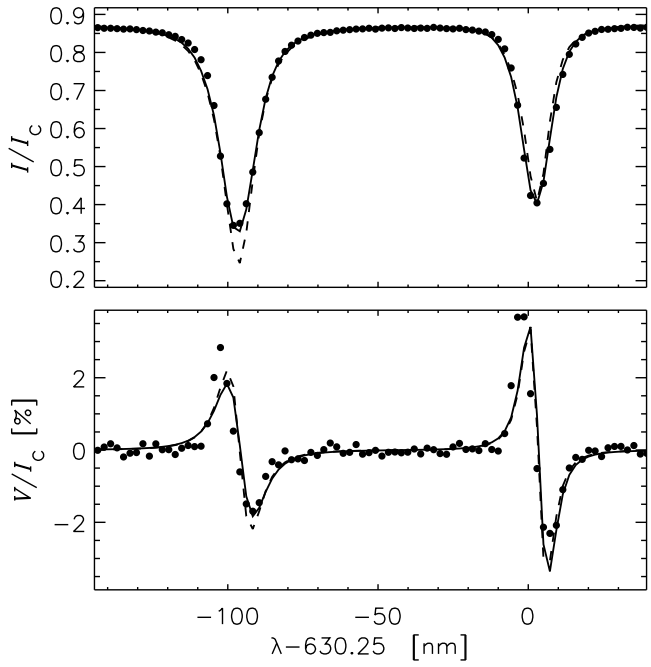

FIGURE 6.9:— Observed (*dots*) and best-fit Stokes I and V profiles from simulated *Hinode*/SP observations using a global (*dashed*) and a local (*solid*) stray-light profile in the inversion. The stray-light factor are 15% and 55%, respectively. The local stray light inversion results in a significantly better fit to the intensity profile.

6.4.2 Inversion strategy

To determine the atmospheric parameters from the simulated *Hinode*/SP observations we apply the ME inversion to the Fe I 630.15 nm and Fe I 630.25 nm lines simultaneously. A total of 9 free parameters are retrieved (S_0, S_1, η_0, $\Delta\lambda_D$, a, B, γ, χ, and v_{LOS}). We do not allow for additional broadening of the profiles by macroturbulence. In all inversions we use the same initial guess model, allowing a maximum of 300 iterations. The initial guess model is: S_0=0.02, S_1=1, η_0=4.9, $\Delta\lambda_D$=29 mÅ, a=0.45, B=100 G, γ=45°, χ=45°, v_{LOS}=0.1 km s^{-1}, and $\alpha = 10\%$.

Three different inversions are performed to derive the atmospheric parameters. All of them use a simple one-component model, i.e., *a laterally homogeneous magnetic atmosphere occupying the whole resolution element*. We first invert the profiles in the absence of noise, and then with noise added at the level of $10^{-3}\, I_c$. In the last inversion, the noisy profiles are fitted considering

non-zero stray-light contaminations factors. The last two inversions allow us to study the improvement brought about by the use of a stray light profile to account for telescope diffraction. The inversion is applied to the three snapshots with $\langle B \rangle = 10$, 50 and 140 G (see Sect. 6.2).

6.5 Results

Figure 6.10 shows the vector magnetic field (strength, inclination, and azimuth) retrieved from the inversions of the Stokes profiles. The first row displays a cut at optical depth $\log \tau = -2$ of the simulation snapshot with average flux density of 10 Mx cm^{-2}. The second and third rows contain the results of the ME inversions of the degraded profiles in the absence of noise and the specific case of a S/N of 1000, respectively. Finally, the fourth row shows the atmospheric parameters derived from the noisy profiles accounting for telescope diffraction. White regions represent pixels which have not been inverted because of their small polarization signals (we only consider pixels whose Stokes Q, U or V amplitudes exceed three times the noise level).

Over the granules, the magnetic field is very weak and the polarization signals are buried in the noise for the most part. These pixels represent $\sim$55% of the total area (white regions in Fig. 6.10). The stronger fields concentrate in intergranular regions. In those regions, the magnetic structures inferred from the inversion have bigger sizes than the real ones, i.e., they appear "blurred". This is caused by the degradation of the images due to telescope diffraction and CCD pixel size as explained in Sec. 6.3.5. The field inclination and azimuth structures resulting from the inversion are blurred as well. The azimuth values are rather uncertain because of the tiny linear polarization signals produced by the weak fields of the simulations.

Figure 6.11 is a close up of small features observed in intergranular regions. When we consider that the polarization signal is produced by a single magnetic component within the resolution element and no telescope diffraction is corrected, the inferred field strengths are smaller than those in the model, so the field is underestimated (middle panels of Fig. 6.11). If one accounts for the effects of telescope diffraction via a stray-light factor, the inferred fields become stronger (right panels), but also noisier due to the increased number of free parameters. Note that each *Hinode*/SP pixel of $0\farcs16 \times 0\farcs16$ corresponds to 36 pixels in the simulation, hence they usually contain a broad distribution of magnetic field strengths.

To analyze these results in a more quantitative way we calculate the mean and rms values of the errors. We define the error as the difference between

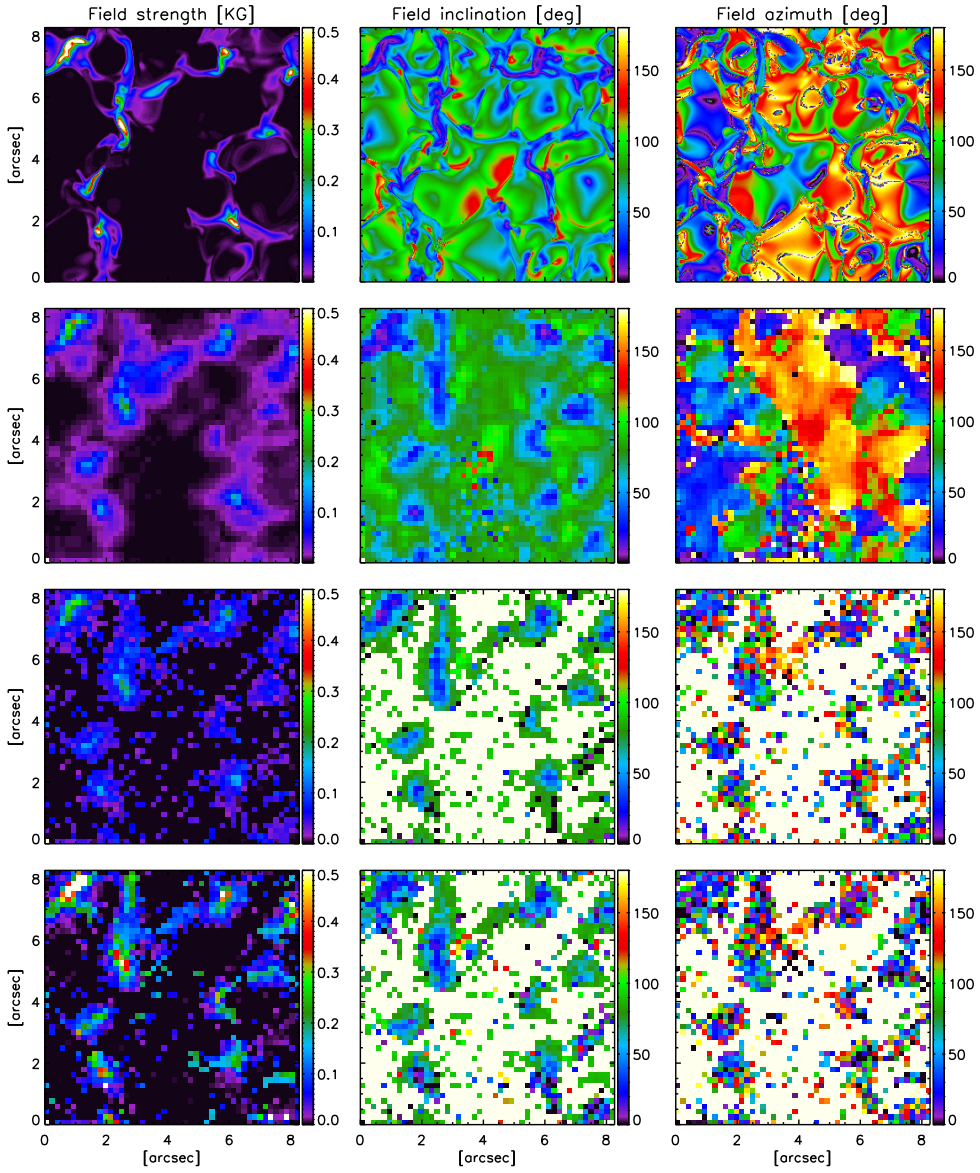

FIGURE 6.10:— *First row*: Cuts at optical depth $\log\tau = -2$ of the model atmospheres provided by the MHD simulation with averaged unsigned flux of 10 Mx cm^{-2}. *Second row*: Maps of the physical quantities retrieved from the ME inversion of the profiles with no noise. *Third row*: Maps retrieved from the ME inversion of the profiles with S/N of 1000 and no stray-light correction for. *Fourth row:* Same as before, but accounting for stray light. From left to right: magnetic field strength, inclination, and azimuth.

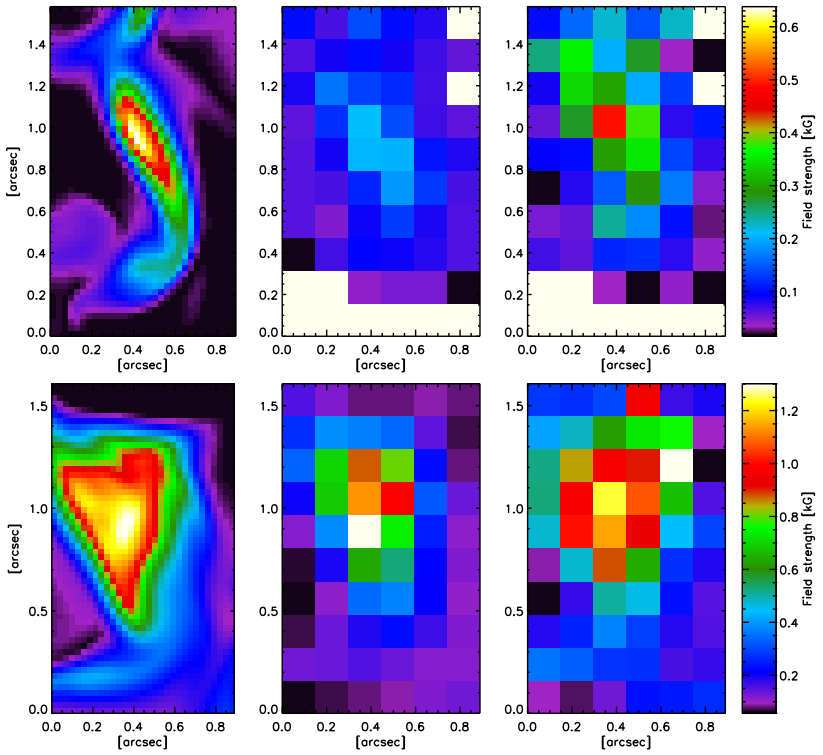

FIGURE 6.11:— *Left:* Field strengths at $\log\tau = -2$ in the MHD simulations with 10 Mx cm^{-2} (top) and 50 Mx cm^{-2} (bottom). *Middle*: Field strengths derived from the ME inversion of the spatially degraded Stokes profiles with S/N 1000 and no stray light contamination. *Right*: Field strengths from the ME inversion correcting for telescope diffraction.

the inferred and the real parameters at optical depth $\log\tau = -2$. This optical depth has been chosen by comparing the inversion results with the MHD simulations at different heights. It is indeed the one yielding smaller rms errors for the inferred model quantities. Since one pixel of the degraded data corresponds to 36 pixels in the simulations, we compare each inverted pixel with the mean of the corresponding 36 pixels in the original map. By comparing the retrieved atmospheric quantities with the real ones at a fixed optical depth we are including all possible sources of error in the analysis, i.e., the inability of the ME solution to fit asymmetric profiles, the degradation of the images, and photon noise.

Figure 6.12 shows the mean and rms errors of the field strength resulting from the inversion without accounting for telescope diffraction (top left panel). It is clear that fields above ∼100 G are underestimated. The results are similar

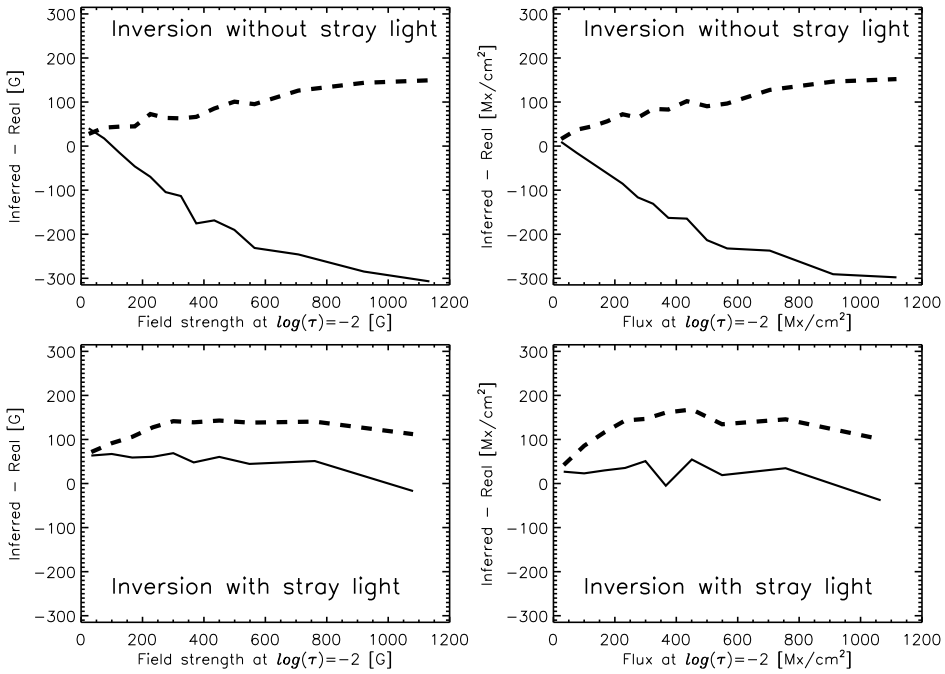

FIGURE 6.12:— *Top:* Mean (solid) and rms (dashed) errors of the field strength (left) and flux (right) derived from the inversion of the profiles with S/N=1000 assuming a single magnetic atmosphere and no stray light contamination. *Bottom:* Same as before but accounting for stray-light contamination.

for the magnetic flux density (top right panel). The inversion considering stray-light contamination as a means to correct for telescope diffraction yields much better inferences, as can be seen in the bottom panels of Fig. 6.12. The field strength and flux are slightly overestimated for weak fields, but the rms errors do not exceed 150 G in any case.

Figure 6.13 shows the mean and rms of the errors for the field inclination resulting from the inversion with and without stray light contamination (right and left panels, respectively). Interestingly, the mean and rms are larger when we correct the effects for telescope diffraction. In particular, rms values remain well below $\sim 22^\circ$ for fields as weak as 200 G, and they increase linearly as we go towards weaker fields. The mean values are of about $\sim 4^\circ$, at the most.

Figure 6.14 shows the distribution of stray light factors derived from the inversion of the simulated profiles with noise at the level of S/N=1000. The histogram is rather symmetric and has a clear maximum at $\alpha = 0.55$. Overplotted is the ratio of total circular polarization signal in the degraded image with

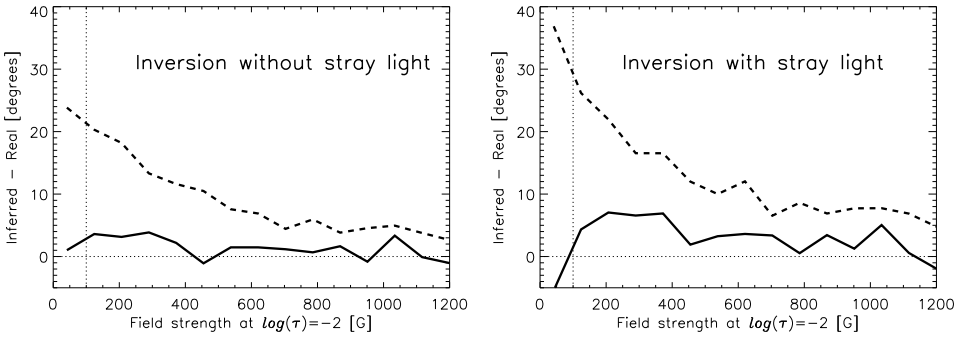

FIGURE 6.13:— *Left:* Mean (solid) and rms (dashed) errors of the field inclination derived from the inversion of the profiles with S/N=1000 assuming a single magnetic atmosphere and no stray-light contamination. *Right:* Same as before but accounting for stray-light contamination.

respect to that in the original image (dashed line). The strong resemblance between the two distributions indicates that the stray light factors derived from the inversion actually model the effects of telescope diffraction and CCD pixel size. In other words: the inferred α's do not represent a real magnetic filling factor, but just the degradation of the image caused by the instrument. This is valid under the following conditions:

- a simple one-component model is used in the inversion
- the data have $0\farcs32$ of spatial resolution
- the data are not contaminated by the atmospheric seeing.

6.6 Discussion

ME inversions of the Fe I 630 nm lines at spatial resolutions of $0\farcs32$ (the case of *Hinode*/SP) underestimate the magnetic field strength by some hundred G if no correction for telescope diffraction is made. When stray light is accounted for, ME inversions are able to recover the magnetic field strength and inclination with reasonable accuracy. Specifically, very weak fields, say below 200 G, can never be misinterpreted as stronger fields, say above 500 G. Rms uncertainties for fields weaker than 100 G can be as large as 100% but this certainly does not hamper the important qualitative diagnostic of having truly weak magnetic fields. More accurate, quantitative measurements of very weak fields may need

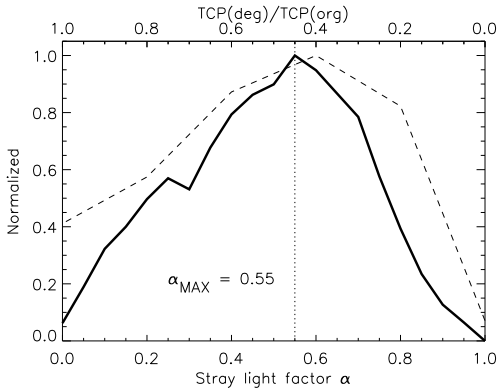

FIGURE 6.14— Normalized histogram of the stray light factor derived from the inversion of the profiles with S/N=1000 (solid line). Overplotted is the histogram representing the ratio of TCP in the degraded image with respect to that in the original image (dashed line). Equivalent units are in the upper X-axis. The dotted vertical line indicates the peak of the stray light factor distribution.

different techniques, but ME features results that are more than good enough to our purposes.

Therefore, we always derive weak fields from the simulated *Hinode*/SP observations where the field in the MHD model is weak. Likewise, strong fields retrieved by the ME inversion actually correspond to strong fields in the MHD model. This is in sharp contrast with the results of Martínez González et al. (2006), whose inversions of IN profiles observed at $\sim 1''$-$1\farcs5$ resolution yield strong or weak fields depending on the initialization. The difference between our results and those of Martínez González et al. is probably due to:

1- Our significantly higher spatial resolution, which makes the polarization signals larger by a factor of $\sim$10 and also narrows the range of field strengths present in the pixel. In fact, higher resolutions can be expected to imply larger filling factors. The increase on the polarization signal reduces the effects of noise on the observed Stokes profiles, as well as makes it visible new signals that were completely buried by the noise.

2- Our model atmosphere is much simpler than those considered by Martínez González et al. (one component vs two-component models) and we do not employ micro- or macro-turbulent velocities. This reduces the degrees of freedom of the solution and the possibility of crosstalk between different atmospheric quantities.

3- The simple description of the thermodynamics provided by the ME model which, contrary to the atmosphere used by Martínez González et al., does not allow the temperature and micro-turbulence to compensate for incorrect magnetic parameters.

To determine the magnetic field strength and magnetic flux we need to account for telescope diffraction. We do it by including a stray-light profile in

the inversion. The results show that the inferences of the field strength and magnetic flux improve when a local stray-light contribution in used. Due to the larger number of free parameters, the field inclinations retrieved from the inversions are more uncertain. In any case, the variation is not dramatic: on average, the error is smaller that $\sim 5^\circ$ and the rms remains below 30° for fields stronger that 100 G. This means that the ME inversion is able to distinguish purely vertical fields from purely horizontal ones, even when Q and U, or V, are below the noise level. The reason is that Stokes I helps determine the inclination of the magnetic field vector.

We caution that these results may only be valid as long as the MHD simulations provide a realistic description of the Sun. The performance of ME inversions could be different if the magnetic field is structured on scales much smaller than $\sim 0\farcs3$. For the moment, however, there is no compelling observational evidence that extremely tiny magnetic elements exist in the quiet solar photosphere.

Finally, it is important to remind that ME inversions are not able to reproduce the asymmetries exhibited by the Stokes profiles used in this analysis. Interestingly, image degradation "helps" the ME inversion algorithm fit the profiles because *degradation smooths out profile asymmetries*. An analysis of the χ^2 values from the inversion of the profiles before and after the degradation shows that the inversion of the degraded profiles yields better χ^2 values. This, however, does not mean smaller uncertainties for the inferred atmospheric parameter. Independently of the fit quality, the ME model is not always able to explain the shapes of the Stokes profiles, especially those exhibiting strong asymmetries. As we have shown throughout previous sections, ME inversions do not account for vertical stratifications, they just provide averaged values of the atmospheric quantities over the line forming region.

6.7 Conclusions

We have used the best MHD simulations currently available to examine the diagnostic potential of the pair of Fe I lines at 630 nm in the case of very high spatial resolution, seeing-free observations, as those provided by the *Hinode*/SP instrument. To this end we have applied a degradation to the original Stokes profiles to simulate the SP and then we have used ME inversions to infer the magnetic field vector.

Telescope diffraction and CCD spatial sampling lead to:

- Reduced image contrast and blurred polarization signals

- Disappearance of the smallest structures
- A mixing of light from nearby pixels: 80% of the pixels show weaker polarization signals
- A smoothing of the asymmetries exhibited by the profiles
- A reduction of the amount of polarization signals detectable above the noise level. As a consequence, the number of pixels showing weak fields decreases against those harboring stronger fields, whose abundance does not change.

The ME inversion results show that the visible lines at 630 nm can be used to study the magnetism of the quiet Sun when the spatial resolution is high. At $0\farcs3$ we obtain for the magnetic field strength uncertainties smaller than 150 G in the whole range of strengths from $\sim$0.1 to 1 kG. The magnetic field inclination is well determined (uncertainties smaller that 20°) for field as weak as 250 G. The azimuth values, however, are rather uncertain because of the very weak linear polarization signals present in the IN. Overall, these results justify the use of the Fe I 630.2 nm line pair by space-borne instruments.

Previous analyses of visible (630.2 nm) and near-infrared (1565 nm) iron lines do not agree on the distribution of field strengths in IN regions, as observed at $\sim1''$. In particular, the visible lines systematically seem to deliver kG field strengths and small filling factors, while the near-infrared lines suggest a predominance of hG fields (see Khomenko 2006, for a recent review). Our analysis suggests that *Hinode*/SP observations should make it possible to determine the real distribution of field strengths in quiet Sun internetwork regions using one-component Milne-Eddington inversions, provided the effects of telescope diffraction are modeled by means of a local, stray-light contamination factor.

In order to shed light on the previously mentioned contradiction, we undertake in the next Chapter a similar analysis but using real *Hinode*/SP observations.

7

Quiet Sun internetwork magnetic fields from the inversion of *Hinode* measurements

In this Chapter we analyze Fe I 630 nm observations of the quiet Sun taken with the spectropolarimeter of the Solar Optical Telescope aboard the *Hinode* satellite. The analysis of the polarization profiles is done by using the inversion strategy presented in Chapter 6, i.e., deriving the physical quantities from a Milne-Eddington inversion after considering a *local*, stray-light contamination to account for the effects of telescope diffraction. With the results of the inversion we compute the PDFs for the field strength, inclination and stray-light factor and compare them with other results. We also analyze the magnetic flux and other polarimetric quantities derived from the Stokes profiles. The influence of noise and initial guess models in the inversion results are also discussed throughout the Chapter.

7.1 Introduction

Since its launch in September 2006, the *Hinode*/SP has been taking high-precision, high-angular resolution measurements of the Fe I lines at 630.2 nm. The angular resolution of about $0\farcs32$ opens exciting possibilities for the analysis of the weak magnetic signals observed in the quiet Sun. It should permit, for instance, a better isolation of the magnetic elements that form the quiet

photosphere, provided they are not organized on scales much smaller than $0\farcs1$. The increased spatial resolution may result in significantly larger polarization signals than those recorded on the ground. This would minimize the influence of noise, which has long been recognized as one of the main problems in the study of quiet Sun magnetic fields (Bellot Rubio & Collados 2003; Martínez González et al. 2006; López Ariste et al. 2006).

The availability of very high angular resolution observations, virtually free from seeing effects, is also important for other reasons. Since the light entering one pixel comes from a much smaller region of the solar surface, the effect of different atmospheres contributing to the intensity and polarization profiles is decreased. This should facilitate the interpretation of the measurements, as relatively simple one-component atmospheres may be sufficient to explain the observations. Stokes inversions of ground-based data are usually performed in terms of two-component atmospheres because the intensity and polarization profiles are not compatible with the signals emerging from a homogeneous magnetic atmosphere, due to the relatively modest angular resolution attained.

Both the smaller influence of noise and the possibility of using simple model atmospheres make high resolution measurements ideal to study the magnetism of the quiet solar photosphere. In Chapter 6 (see also Orozco Suárez et al. 2007) we have investigated the diagnostic potential of the visible Fe I lines at 630.2 nm using radiative magnetoconvection calculations. The main result was that Milne-Eddington (ME) inversions of high-angular resolution Fe I 630.2 nm measurements satisfactorily recover the actual field strengths present in the simulation snapshots provided we minimize the effects of telescope diffraction.

In this Chapter we analyze Fe I 630 nm measurements of the quiet Sun taken by *Hinode*/SP. The data used have also been analyzed by Lites et al. (2007a,b) and Orozco Suárez et al. (2007a,b).

In Sec. 7.2 we present the observational data and analyze some polarimetric quantities derived from the Stokes profiles. Next, the Stokes profiles are inverted in Sec. 7.3 by using the strategy presented in Chapter 6. Various results are presented and discussed from Secs. 7.4 through 7.9. Finally, we summarize the main conclusions in Sec. 7.10.

7.2 Observations

To analyze the magnetism of the quiet Sun we use two different data sets taken at disk center with the *Hinode*/SP. The observation parameters are summarized in Table 7.1. The two sets will be referred to as 1 and 2. To obtain the observation 1, the spectrograph slit (with solar S-N orientation), of width $0.16''$,

TABLE 7.1:— Observational Data. Note that the Obs. area for data set 2 corresponds to space and time (see text).

	DATA SET #1 (NORMAL MAP)	DATA SET #2 (HIGH S/N MAP)
Date	March 10, 2007	March 10, 2007
Time (UT)	11:37:37	00:20:00
Obs. area	$302'' \times 162''$	$302'' \times 0\farcs16$
(Pixels)	1024×2048	1024×727
Exp. time	4.8 s	67.2 s
Stokes V Noise	$1.1 \times 10^{-3}\, I_{\rm QS}$	$3 \times 10^{-4}\, I_{\rm QS}$
Stokes Q/U Noise	$1.2 \times 10^{-3}\, I_{\rm QS}$	$2.9 \times 10^{-4}\, I_{\rm QS}$

was moved across the solar surface in steps of $0\farcs1476$ to measure the four Stokes profiles of the Fe I lines at 630.2 nm with a spectral sampling of 2.15 pm pixel^{-1} and a exposure time of 4.8 s. The spatial coverage of data set 2 was smaller. In this case, the slit was kept fixed at the same spatial location while recording the Stokes spectra with 9.6 s of exposure time. The completion of the map for data set #1 took about 3 hours while the time series of data set #2 was completed in one hour and 51 minutes. The effective exposure time in observation #2 was increased by averaging seven consecutive 9.6 s measurements. This allowed to reach a final exposure time of 67.2 s, which corresponds to a ∼3.74 gain in terms of S/N with respect to data set #1. The *Hinode* correlation tracker makes it possible to perform averages over more than one minute due to the superb image stability it provides (better than $0.01''$ rms; Shimizu et al. 2008). Also, the time evolution of a regular granule (Title et al. 1989). This data set has been analyzed by Lites et al. (2008).

The polarization noise levels are shown in Table 7.1 as well. Note the noise reduction from observation #1 to #2 due to the longer exposure times of the latter. The noise level was obtained by taking the mean value of the standard deviation of the corresponding Stokes profile, continuum wavelengths. Before evaluating the noise levels, the data were corrected for dark current, flat-field, and instrumental cross-talk as explained by Lites et al. (2008). The whole process was done using the IDL routine `sp_prep.pro` of the Solar-Soft package. The Stokes profiles were normalized to the average quiet Sun continuum intensity, $I_{\rm QS}$, evaluated using all pixels from each data set. We will refer to the average quiet Sun continuum as either $I_{\rm QS}$ or $I_{\rm c}$.

7.2.1 Qualitative analysis of the polarimetric signals

Figure 7.1 shows the normalized continuum intensity of data set 1 (hereafter referred to as normal map) for a small subfield of $160'' \times 80''$. The scanned area covers both network and internetwork regions. The high contrast of the granulation, of about 7.5%, testifies the quality of the observations.

Figure 7.2 shows maps of the (signed) total circular polarization and total linear polarization defined as

$$\begin{aligned} V_{\rm TOT} &= \mathrm{sgn}(V_{\rm blue}) \frac{\int |V| \, \mathrm{d}\lambda}{I_{\rm c} \int \mathrm{d}\lambda}, \\ L_{\rm TOT} &= \frac{\int (Q^2 + U^2)^{1/2} \, \mathrm{d}\lambda}{I_{\rm c} \int \mathrm{d}\lambda}, \end{aligned} \tag{7.1}$$

and evaluated in a passband of 21 wavelength samples centered on the line core position of the 630.25 nm spectral line ($\Delta\lambda \simeq 45$ pm).

The visual inspection of these maps reveals a wealth of magnetic signals in the field of view (FOV). In the $V_{\rm TOT}$ map one can easily identify several super-granular cells outlined by the network fields (intense white and black field concentrations). The larger polarization signals correspond to areas where the granulation is distorted. The interior of these super-granular cells, i.e., the internetwork (IN), is not devoid of magnetic signals. At a glimpse many small and less intense signals are detectable. Note that the gray scale for the total polarization map has been clipped at $\pm 0.7\%$ to emphasize the IN. The $L_{\rm TOT}$ map shows a smaller abundance of magnetic features. The different patches, of similar sizes, are scattered across the map. The stronger concentrations (and larger in size) are located in network areas. The map also contains appreciable random noise in addition to the solar features (light-gray background). The nature of these IN fields is a controversial topic (see Khomenko [2006] for a recent review).

The continuum intensity map along with total, circular (absolute valued) and linear polarization maps corresponding to data set 2 (hereafter referred to as high S/N map) are displayed in Fig. 7.3 and 7.4, respectively. The slit crosses through a super-granular cell (as shown by the co-spatial Ca II H broad band images that were recorded simultaneously). The intensity image shows, in the X-axis, the evolution of the granulation (single granules are identified with bright fringes, while intergranular lanes are darker). The maps do not represent a simple snapshot but rather time evolution, although we will use it as if it were (we are not interested in the evolution of the different solar features that are tracked with the slit). The continuum contrast is slightly lower by about 0.2%

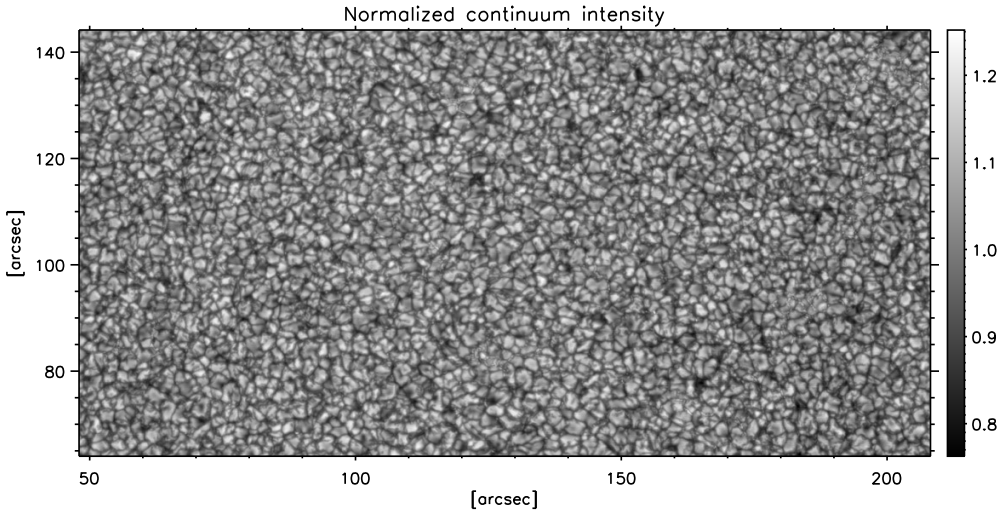

FIGURE 7.1:— Small area of $160'' \times 80''$ showing the normalized continuum intensity of observation 1. The granulation contrast is 7.44%.

than that for the normal map. This is a consequence of the longer exposure times.

The linear polarization signals are more numerous for these data than for the normal map. The reason is the higher S/N, which is significantly better ($\sim$3.5 times) than the S/N level for the normal map. The maps show the time evolution of IN magnetic features. Notice that the mean size of the circular polarization features in the horizontal direction (time) is larger than that for the linear signals. A network patch is identified at around 1/3th of the slit ($Y \sim 60''$) in the maps.

These two data sets complement each other: the normal map scans a large solar area while the high S/N map push the intrinsic noise of the measurements to the minimum achievable with the *Hinode*/SP. A noise level of $3 \times 10^{-4}\, I_{\rm QS}$ at $0''.3$ is comparable to the best S/N levels (close to $10^{-5}\, I_{\rm QS}$) achieved by ground based observations at $1''$ (Martínez Gonzalez et al. 2008).

7.2.2 Noise analysis and selection of IN areas

As shown in the previous section, photon noise is present in real observations and prevents polarimetric signals to be cleanly detectable. It also affects the Stokes profiles hindering the information encoded on their shapes. The inversion of noisy polarization signals may introduce undesirable results in the final analysis. For this reason only pixels showing polarization signals above a rea-

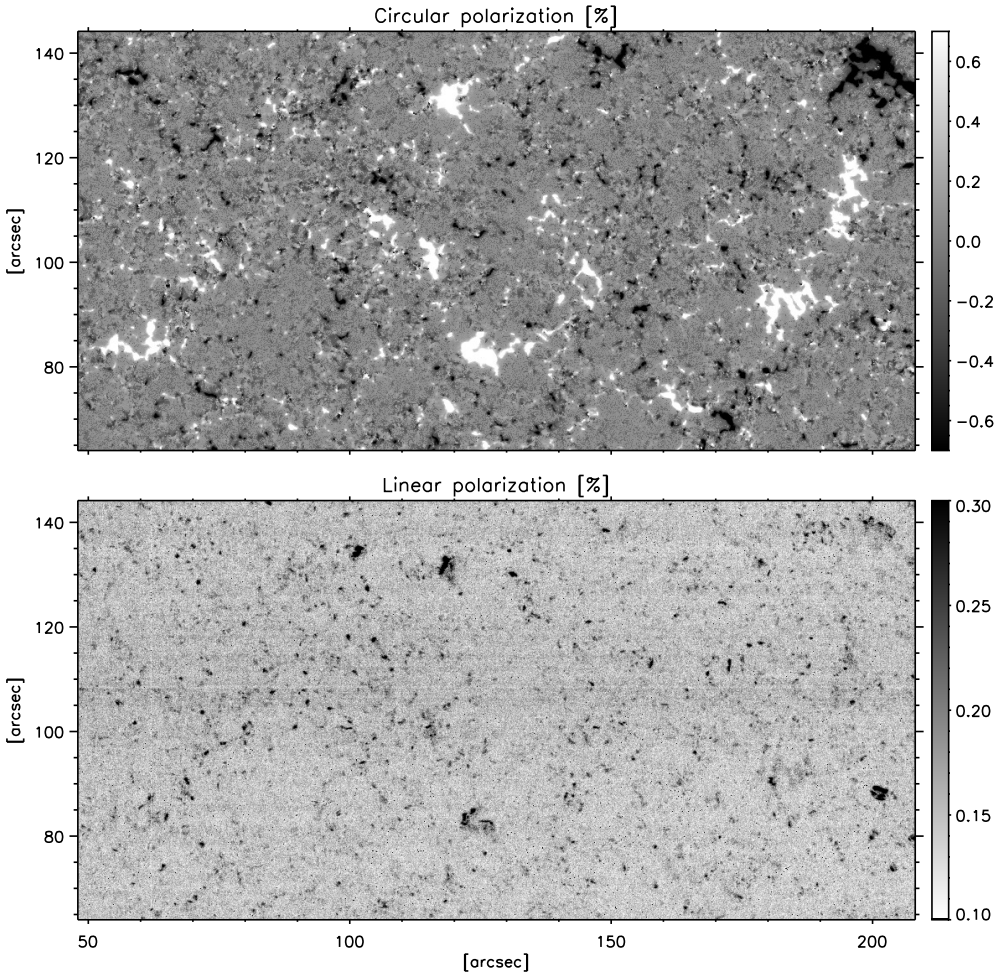

FIGURE 7.2:— Small area of $160'' \times 80''$ showing the total circular polarization signals, $V_{\rm TOT}$, and the total linear polarization signal, $L_{\rm TOT}$ (*top* and *bottom* panels, respectively). Units are in percent. Network and internetwork areas can easily be identified. The circular and linear polarization maps have been clipped at ± 0.7 and 0.3%, respectively.

sonable noise threshold will be analyzed by means of the ME inversion. This should exclude profiles that cannot be inverted reliably.

Figure 7.5 shows the histograms of the absolute valued Stokes V and $L = \sqrt{Q^2 + U^2}$ amplitudes, left and right panels respectively. First notice the large occurrence of weak polarimetric signals. The distributions for the high S/N and normal maps are similar although there exist differences. The histograms for the normal map have maximum peaks located at larger amplitudes than

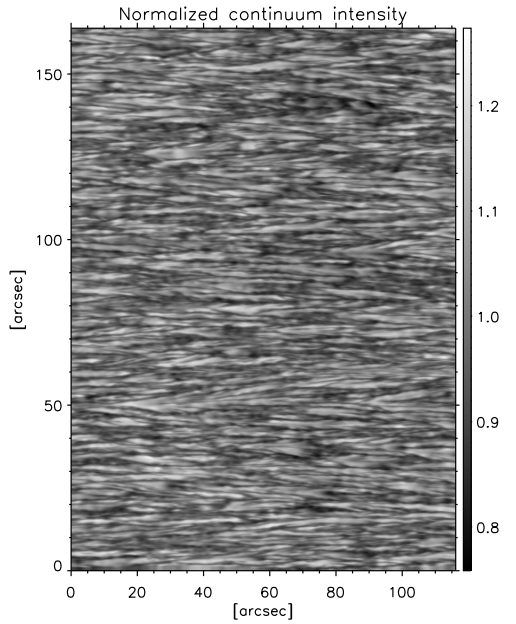

FIGURE 7.3— Normalized continuum intensity of data set 2. The Y-axis represents the slit while the X-axis time in arcsec. The granulation contrast is 7.3%.

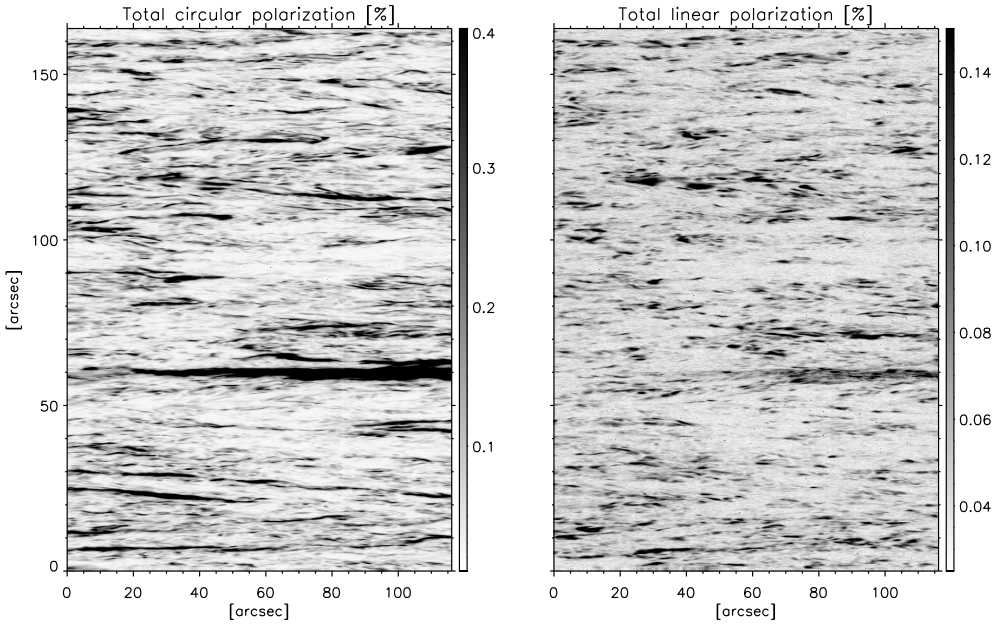

FIGURE 7.4:— Total circular and linear polarization signals, $|V_{\rm TOT}|$ and $L_{\rm TOT}$, *left* and *right*, respectively. The circular and linear polarization maps have been clipped at 0.4 and 0.15 %, respectively.

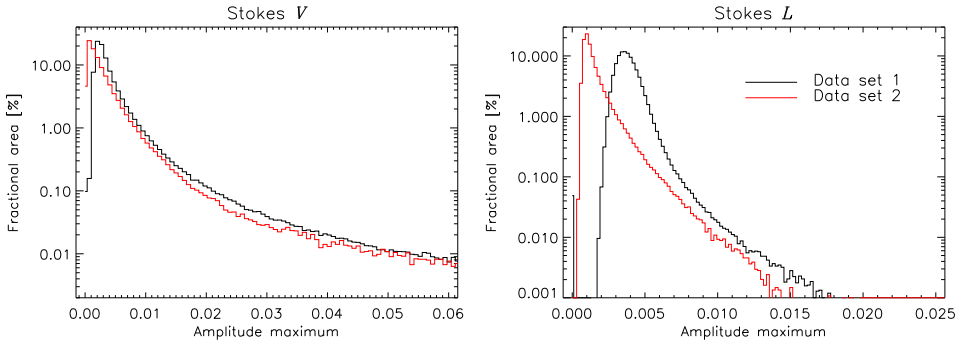

FIGURE 7.5:— Histograms of the absolute valued Stokes V, and Stokes L amplitudes in units of I_c, *left* and *right* panels. *Black* and *red* stand for the normal and high SNR maps respectively.

those peaks from the high S/N map. The difference is greater in the linear polarization histograms. Note as well that the peak locations are close to the noise limit (polarization sensitivity). The peak locations of the Stokes V distributions are at about 3.7 and 8.3 times the corresponding noise levels of the maps. For Stokes L the peaks are at 1 and 3 times the noise level.

As the peaks are close to the polarization sensitivity, it is reasonable to think that photon noise contributes to a larger or smaller extent to generate the maximum of the distributions. Noise may also contribute to the rapid increase of polarimetric signals with decreasing amplitude values. This is less probable to occur for the Stokes V histogram corresponding to the high S/N map. In this case the peak is well above the noise level ($\sim$8 times) which indicates that it may have solar origin. Martínez González et al. (2008) made numerical simulations and proposed that the observed peaks in Stokes V amplitude histograms might be an observational evidence of flux cancellations within the resolution element, for $1''$ data. In our case it is less probable given the higher spatial resolution. The peak may also reflect the "true" distribution of V amplitudes in the IN.

It is important to eliminate from the analysis polarization signals that are highly contaminated by noise. Therefore, we only analyze pixels with Stokes Q, U or V amplitudes larger than 4.5 times their noise levels. This threshold translates into an apparent flux density[1] of 13.4 Mx cm^{-2}. A 35.5 and 74.4%

[1]The term "apparent flux density" refers to the quantity $f\mathbf{B}\cos\gamma$ where f is the fill fraction of the magnetic field (see Keller et al. 1994; Lites et al. 1999). This quantity is the one measured by solar magnetometers whose minimum sensitivity limits depend on the measurement itself, on the instrument and on the angular resolution. In this case the apparent flux density has been calculated by determining the magnetic parameters of a ME atmosphere with vertical fields that produces Stokes V signals at the level of the noise and assuming $f = 1$.

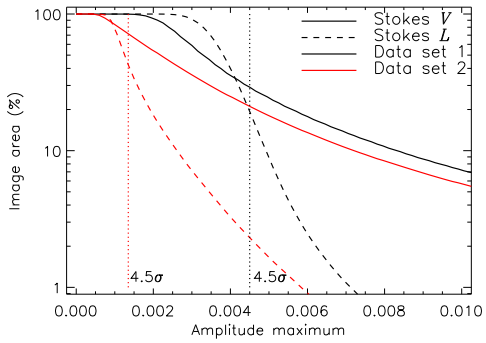

FIGURE 7.6— Cumulative histogram of the absolute valued Stokes V, and Stokes L amplitudes for the two data analyzed in this Chapter. The vertical lines stand for the selected noise thresholds in the normal map and in the high S/N map (see text for further details).

of the pixels fulfill this criteria in the normal and high S/N maps respectively.

Figure 7.6 show the cumulative histograms[2] for the Stokes V and L amplitudes. It shows the dependence of the total image area showing polarization signals above a given noise threshold with respect the amplitude maximum. It is important to notice that the distributions are the same for the two analyzed data sets apart from a normalization constant.

Only 30.7% of the normal map area shows Stokes V signals above the noise threshold. This percentage increases to 71.5% in the high S/N map. These percentages increase rapidly as soon as we make lower the noise threshold condition. The same occurs for the linear polarization signals. In this case the image areas are 24.2 and 42.3% respectively. Noticeably, we estimate that 87.1 and 87.4% of the image and for both sets show Stokes V signals above 3σ (cf. with the 92.6% provided by Martínez González et al. 2008 for visible observations).

Notice that the amount of pixels exhibiting linear polarization signal is always smaller above the noise threshold and the rapid increase of the various percentages as we go toward the left and attributed to the noise.

The selection of IN areas for the normal map has been done manually. In particular, we have selected squared areas in the interior of supergranular cells, avoiding the strong flux concentrations of the network. Figure 7.7 shows the pixels of the image whose Stokes Q, U, or V exceed the noise threshold (white). It also displays the IN selected areas. For the high S/N data we have

The thermodynamic parameters of the model have been fixed to the mean values derived from the inversion of the *Hinode* measurements (see next sections).

[2] A cumulative histogram is a variation of a normal histogram in which the vertical axis provides with the counts of a single bin plus all bins for larger values of the amplitude, i.e., $g(i) = \sum_{k=L}^{i} h(k)$ where $h(k)$ represent a normal histogram and $i = L-1, \ldots, 0$ being L the total number of bins.

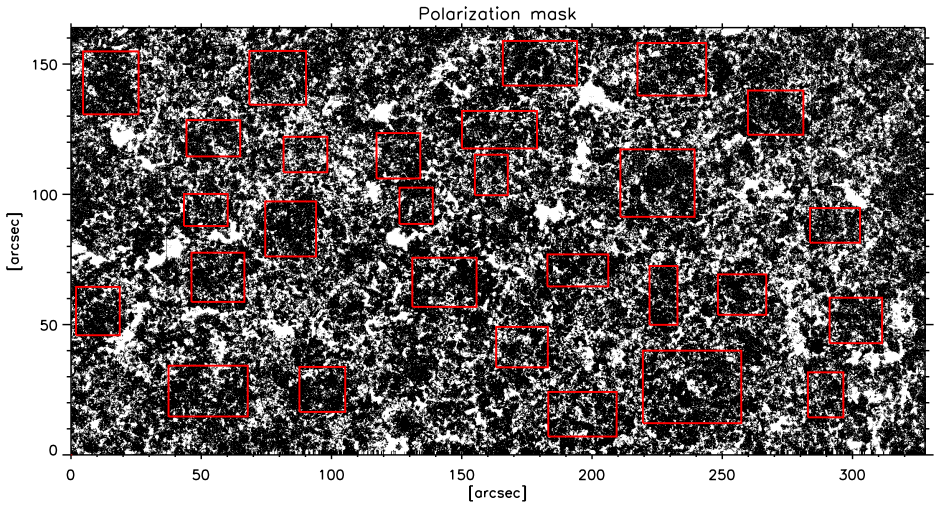

FIGURE 7.7:— Image showing the locations (white) of pixels with any of their polarimetric signals exceeding the noise threshold (4.5σ). The red box indicates the selected IN areas (see text). The map represent the whole orbserved area (normal map).

just remove the strong magnetic feature shown in the polarization maps, see Fig. 7.4.

7.2.3 Wavelength calibration

The absolute wavelength scale for the observed Stokes spectra has been determined using the Stokes I line core position of the two Fe I lines average over quiet Sun areas and using the Fourier Transform Spectrometer atlas as a reference spectrum. It has been separately done for the two data sets.

We first took the averaged Stokes I profile over all the observed area exhibiting negligible polarization signals (bellow 5 times the noise levels). Then the line core of the two Fe I lines were fitted with a Gaussian in order to determine the pixel position (spectral direction) of the absolute minimum of the two lines with sub-pixel accuracy. The same was done for the FTS. Then, to determine a wavelength calibration constant and spectral sampling, a line-fit was performed. To remove the gravitational redshift we simply subtract the corresponding wavelength shift. The results are the same for the two data sets and are in agreement with the ones used by Lites et al. (2007a,b). In particular the wavelength shift was 630.08921 nm and the sampling 2.148 pm pixel^{-1}.

7.3 Inversion of the data

7.3.1 Inversion strategy

To analyze *Hinode*/SP observations of quiet sun regions we use the approach described in Chapter 6, i.e., a least-squares inversion technique based on ME atmospheres (MILOS code) with simple one-component, laterally homogeneous models and a local stray-light contamination factor to correct for the reduction of the polarization signals due to diffraction. As a first approximation, we evaluate the stray-light profile individually for each pixel as the average of the Stokes I profiles observed in a box $1''$-wide centered on the pixel. The inversion is performed with only 10 free parameters: the three components of the magnetic field (strength B, inclination γ, and azimuth χ), the line-of-sight velocity ($v_{\rm LOS}$), the two parameters describing the linear dependence of the source function on optical depth (S_0 and S_1), the line strength (η_0), the Doppler width ($\Delta\lambda_{\rm D}$), the damping parameter (a), and the stray-light factor (α). The number of iterations was 300. No broadening by macroturbulence needs to be considered. Broadening by microturbulent velocities should effectively be accounted for by the Doppler width parameter. The inversion is applied to the Fe I 630.15 and 630.25 nm lines simultaneously, using a Gaussian of 2.5 pm FWHM to account for the spectral resolving power of the SP. As shown in Sec. 7.2.2, we only analyze pixels with Stokes Q, U or V amplitudes larger than 4.5 times their noise levels.

The evaluation of the local stray-light profile is different for the high S/N map. In this case we cannot make the two dimensional averages. Therefore, we take the stray light as the average Stokes I profile along $1''$ of the SP slit and centered on the pixel. With this approximation we avoid using data taken at times longer than a minute but we also introduce larger uncertainties on the inferences as the stray light may not appropriately account for diffraction.

In the following sections we show the results from the inversion of the two maps. But before commenting on the different results, we perform several tests to check the performance of the ME inversions when applied to real *Hinode*/SP data. We make such analysis in view of the results from Martínez González et al. (2006) who demonstrated that the Fe I 630.2 nm lines may not provide enough binding information to determine the field strength and the stray-light factor unambiguously under particular analysis conditions. We will see that the Stokes I profile plays an important role in the determination of the stray-light contamination.

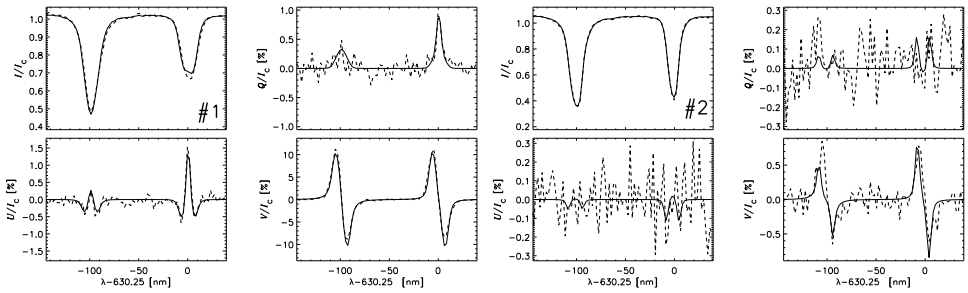

FIGURE 7.8:— Observed (*dashed*) and best-fit (*solid*) Stokes profiles emerging from network pixels #1 (*left*) and #2 (*right*). The field strengths and the stray-light factors retrieved from the inversion are 1334 and 237 G, and 61 and 71%, respectively. The specific locations of the pixels are indicated on the maps of Appendix B.

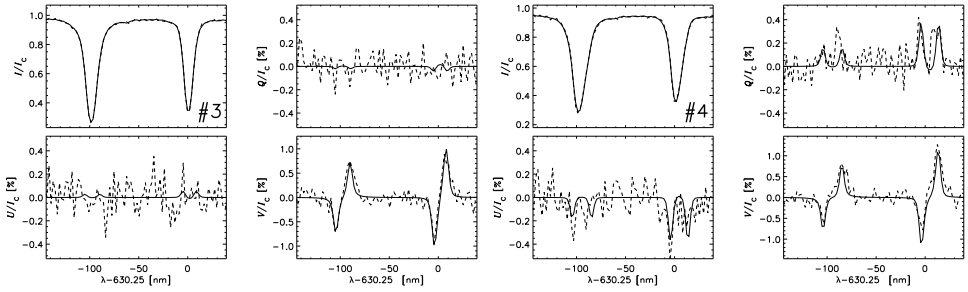

FIGURE 7.9:— Same as Fig. 7.8 but for Stokes profiles emerging from the internetwork. The field strength and the stray-light factor are 247 and 380 G for pixel #3 (*left*) and 88 and 85% for pixel #4 (*right*), respectively.

7.3.2 Profile fits

Figure 7.8 displays sample fits for individual pixels belonging to the network from the normal map. Pixel #1 (*left*) represents a typical network element at the center of strong flux concentrations, whereas pixel #2 (*right*) comes from the edge of a network patch. For both pixels the fits to Stokes V are not very successful due to the asymmetries of the profiles. Note that ME profiles are *symmetric* by definition. The inversion returns a field strength of 1334 G, a field inclination of 19°, and a field azimuth of 136°, with a stray-light factor of 61%, for pixel #1, and a field strength, inclination, and azimuth of 237 G, 69°, and 160° with a stray-light factor of 71%, for pixel #2.

Figure 7.9 displays sample profiles as well, but in this case for two pixels belonging to the IN of the normal map. The observed Stokes V amplitudes

exceed ∼10 and ∼13 times the noise level, respectively. In contrast to the profiles coming from the network, Fe I 630.15 nm shows significantly smaller Stokes V amplitudes than Fe I 630.25 nm, suggesting weak fields. The inversion indeed confirms this point, retrieving field strengths, inclinations and azimuths of 247 G, 141° and 248° for pixel #3 (*left*) and 380 G, 115° and 164° for pixel #4 (*right*).[3] The stray-light contamination factor is 88% and 85%, respectively.

Overall, the quality of the fits is remarkably good keeping in mind the limitations of the ME approximation and the fact that only one-component atmospheres are used.

7.3.3 Invariance against the initial guess model

Different initial guess models may lead to different results, which has raised concerns about the uniqueness of the model atmospheres derived from quiet Sun inversions of Fe I 630.15 and 630.25 nm (Martínez González et al. 2006a,b). For the inversion of both data sets we have employed the same initial guess model: $S_0 = 0.02$, $S_1 = 1$, $\eta_0 = 7.2$, $a = 0.78$, $\Delta\lambda_D = 29$ mÅ, $v_{LOS} = 0.1$ km/s, $B = 100$ G, $\gamma = 30°$, $\chi = 30°$, and $\alpha = 10\%$.

How do the results change when a strong-field rather than a weak-field initialization is used? To investigate this issue we have inverted a small IN area of $32\farcs2 \times 32\farcs2$ adopting different initialization for the magnetic field strength. In particular we have carried out four inversions with initial field strengths of 100, 500, 1000, and 1500 G.

Figure 7.10 shows an histogram of the differences between the field strengths, inclinations and azimuths resulting from the 100 and 1500 G initializations. This plot demonstrates that the solutions do not depend on the initial magnetic field strength. Even the azimuth show variations smaller than 1° (notice that the azimuth angle is usually the parameter with worst uncertainties just because it is only inferred from Stokes Q and U, which are, in general, more affected by the noise). Finally, Figure 7.11 shows the differences between the stray-light factors obtained from the 100 and 1500 G initialization.

Another indication that the results are largely independent of the initial guess is provided by the fact that the percentage of pixels which gets substantially better fits is small: only 3.1% for the 500 G initialization, 4.7% for the 1000 G initialization, and 4.3% for the 1500 G initialization. Here, "substantially" better fits mean that the final χ^2 value is at least 50% smaller than the one obtained with 100 G.

[3] The azimuth values are less reliable when the Stokes U and Q signals approach the noise level, as in pixel #2 (Fig. 7.8) or pixel #3 (Fig. 7.9).

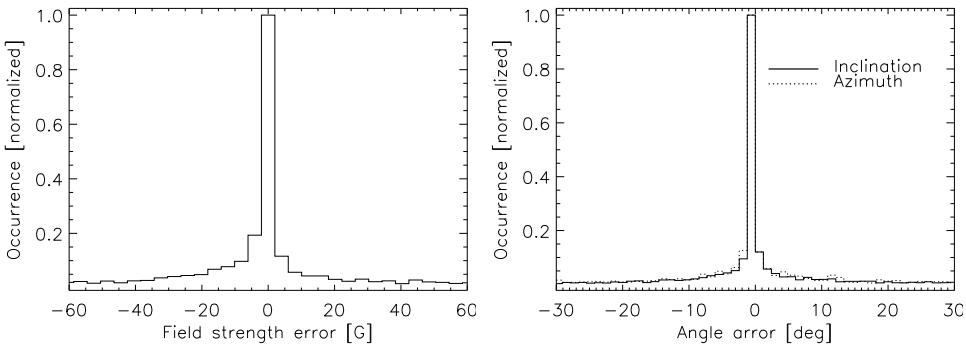

FIGURE 7.10:— Histogram of the difference between the field strength (*left*), inclination and azimuth (*right*) values inferred with two different initializations, 100 and 1500 G.

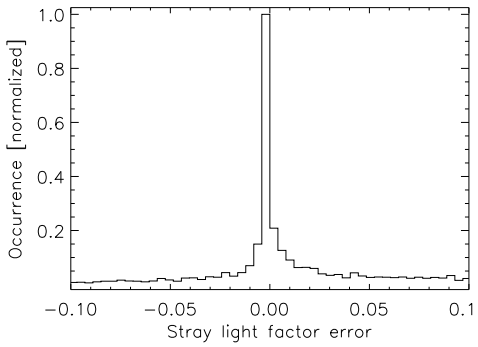

FIGURE 7.11— Histogram of the difference between the stray-light factor values inferred with two different initializations, 100 and 1500 G.

In conclusion, even if there are unavoidable differences between the results of different initializations, their magnitude is so small that the field strength, inclination, azimuth and stray-light factor distributions remain essentially the same. This is in sharp contrast with the inversions of ground-based measurements of the Fe I 630.2 nm lines described by Martínez González et al. (2006a). Additional information on the robustness of inversion codes can be found in e.g. del Toro Iniesta & Ruiz Cobo (1996), Westendorp Plaza et al. (1998), and Bellot Rubio (2006).

7.3.4 Convergence analysis

The tests presented in Sect 7.3.3 demonstrate that the ME inversions are capable of disentangling the effects of the various atmospheric parameters. In particular, they successfully distinguish between the stray-light factor and the

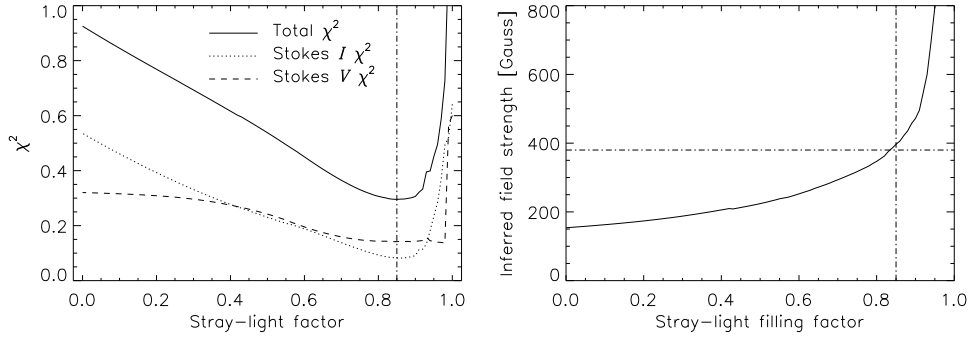

FIGURE 7.12:— *Left*: χ^2 values of the best-fit profiles resulting from the inversion of pixel #4 (as observed by *Hinode*) with fixed, erroneous stray-light factors. The solid,dotted and dashed lines stand for the total, Stokes I and V χ^2, respectively. The vertical line represents the "true" stray-light factor. *Right*: retrieved magnetic field strength for each fixed value of the stray-light factor. The dash-dotted line indicate the best-fit solution.

magnetic field strength, the inclination, and even the azimuth. How is this achieved in the weak field regime that applies in most of the IN pixels?

To answer this question, let us assume that the ME models derived from the inversions of Sect. 7.3 are the "true" solution. We have repeated the inversion of the profiles observed by *Hinode* fixing the stray-light factor to erroneous values. 101 different stray-light factors, from $\alpha = 0$ to 1, have been considered. The other parameters for the initial guess model are the same as those described in Sect. 7.3.3 (except for the the stray-light factor, which is fixed to a wrong value).

To analyze the inversion results we evaluate the χ^2 function. This is basically the same as looking to the profiles, but mathematically. To see the "differences" between the synthetic and the observed Stokes I and V profiles, we have also evaluated the merit function separately for Stokes I and V.

In Fig. 7.12 (left panel) we represent the χ^2 values of the 101 fits against the corresponding fixed stray-light factors, for the particular case of pixel #4 in Fig. 7.9 (the results for other pixels are equivalent). The solid line displays the total χ^2, whereas the dotted and dashed lines indicate the χ^2 values for Stokes I and V, respectively. The vertical line represents the "true" solution. Note that χ^2 is dimensionless and that its absolute value is irrelevant to the inversion code.

This analysis has been carried out over 12 different pixels, taken from network and internetwork areas. For simplicity, we have shown the results only for pixel #4.

This plot gives a clear explanation of what is happening. When the stray-light factor is fixed to erroneous values, the fits worsen and the total χ^2 increases. The variation of the total merit function is large enough to be detectable by the inversion algorithm. Remarkably, the Stokes I and V merit functions behave quite differently. The Stokes V χ^2 values around $\alpha = 0.8$ are very similar. This implies that different stray-light contaminations produce equally good fits to Stokes V. In other words: many compatible solutions, characterized by different stray-light factors and correspondingly different field strengths, exist for Stokes V. However, the range of acceptable stray-light contaminations is strongly limited by Stokes I. This is reflected in the rapid increase of the Stokes I merit function away from the correct stray-light factor. The conclusion is the following: for the most part, the inversion algorithm uses the information encoded in Stokes I to determine the stray-light contamination. Thus, the often forgotten Stokes I also plays an essential role in the process of finding the absolute minimum of the total merit function.

In the same figure (right panel) we represent the retrieved magnetic field strength for each fixed value of the stray-light factor. The vertical and horizontal lines represent the real solution. We see that the magnetic field strength varies smoothly from some 100 G when there is no stray-light contamination ($\alpha = 0$) to more that 1 kG when $\alpha = 1$. However, the merit function increases rapidly in the region of large stray-light contaminations (0.9-1.0), which makes it impossible to retrieve kG fields from this particular example.

Figure 7.13 shows the corresponding best fit profiles for 5 fixed stray-light factors. Note that is is difficult to visually determine which fit is better against the others. However, there are small differences. For instance, there are differences on the wings and core of Stokes I. Also, Stokes Q, U and V shows differences in the splitting of the different lobes.

For this example we can conclude that the inversion algorithm does its work properly, just using the information contained in the Stokes profiles. However, this particular case corresponds to a Stokes profile exhibiting little linear polarization signals. This may introduce some doubts to the analysis just because the inversion uses the full Stokes vector. Part of the IN Stokes profiles do not exhibit linear polarization signals, therefore, in order to make these analysis more consistent we have analyzed two additional Stokes profiles (pixels #5 and #6) showing negligible linear polarization signals. In Fig. 7.14 we show two stokes profiles (top panels) belonging to IN regions and with very weak circular polarization signals and no Stokes Q and U. Over-plotted are the best-fit profiles. Notice that the best-fit profiles show clear Stokes Q and U, they would be buried by the noise though.

The bottom panels represent the corresponding χ^2 values of the 101 fits

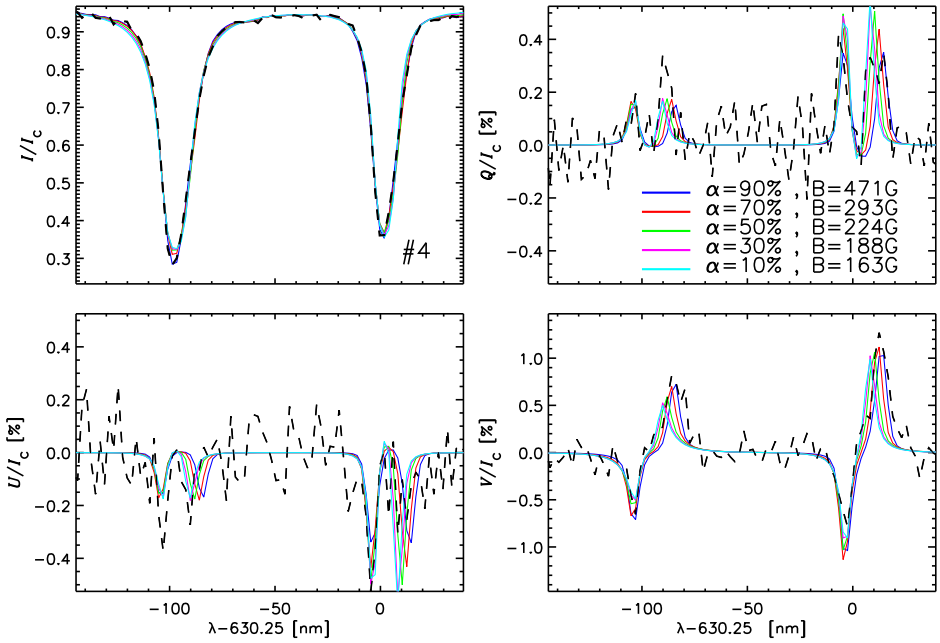

FIGURE 7.13:— Best-fit profiles resulting from the inversion of pixel #4 with fixed, erroneous stray-light factors. Different line colors stand for different values for the stray-light factor. It is difficult to visually see which corresponds to the best fit (actually approx. blue profile).

against the corresponding fixed stray-light factors (as previously explained for pixel #4). The analysis of pixel #5 just confirm the results from #4. The inversion algorithm finds the best solution with the help of the χ^2, i.e., using Stokes I and V simultaneously: there is no linear polarization.

Profile #6 is a very particular case. In this case the circular polarization signal is 7 times larger than the noise, very close to the threshold limit used for the analysis of the *Hinode* data. Very interestingly, this profile is not fully explained with a ME inversion and local stray light. The reason is that there are "two" different models that might explain Stokes I and V separately. Let us explain this in greater detail.

The Stokes I χ^2 has a clear minimum. Also, the Stokes V χ^2 has a clear one. The location of these two minima correspond to different values of the stray-light factor. For instance the Stokes I χ^2 has its minimum located at about ~ 0.7 while it for Stokes V is close to $\alpha = 1$. This indicate that the model is not able to explain Stokes I and V separately (there are two best

solutions for the χ^2). As the ME model has to explain both Stokes profiles simultaneously, the inversion takes a kind of compromise between the Stokes I and V best-fits. In practice, it can be written than $\chi^2_{\rm Total} \sim \chi^2_I/\sigma_I + \chi^2_V\sigma_V$. So depending on the weight of Stokes I and V, the inversion will be favoring the best-fit to one of them. In our case we have weighted both profiles equally, therefore, the best fit finds an α value that is somewhere between 0.7 and 1.

As a final comment we want to point out that Stokes Q and U do also contribute to the inversion. The Stokes[4] Q/U χ^2 (dashed-dotted line from bottom right panel) is almost constant for all stray-light factor values. This indicates that independently of Stokes I and V, the differences between the Stokes Q and U and the best fit profiles are always below noise levels. We should mention that this does not mean Q or U do not contribute to the inversion, they just act as boundary values for the inclination and azimuth. As soon as the field takes wrong inclination or azimuth values, the Q/U χ^2 would increase, indicating wrong convergence.

The analysis of the remaining 9 pixels lead to the same results as for the first case explained in this section. These tests have also been carried out varying the initialization of the magnetic field strength (100, 800 and 1500 G). In all the cases the results turn out to be the same.

In addition, there are a number of arguments that strongly support that ME inversions successfully separate the stray-light factor from the field strength when applied to high angular resolution observations:

1- In internetwork regions we obtain weak fields from the *Hinode*/SP measurements, much in the same way as we got them from the MHD simulations with average unsigned flux density of 10 Mx cm^{-2} (see Chapter 6), and contrary to ground-based observations of these visible lines (see next sections).

2- The inversions do not depend on the initial guess adopted for the magnetic field strength. If the code were unable to disentangle the stray-light factor and the magnetic field strength, the histograms of Figs.7.10 and 7.11 would be certainly worse.

3- Our results are in agreement with those of Lites et al. (2007a,b), using the same data (see discussion).

Finally we would like to point out that these tests have been carried out with pixels belonging to the normal map. As the high S/N map provided polarization profiles that are less affected by photon noise we find it unnecessary to repeat the tests given that noise is the main source of uncertainty in the analysis.

[4]we use Q/U because the results is representative for both Stokes profiles. The one which is drawn has been calculated from Stokes Q.

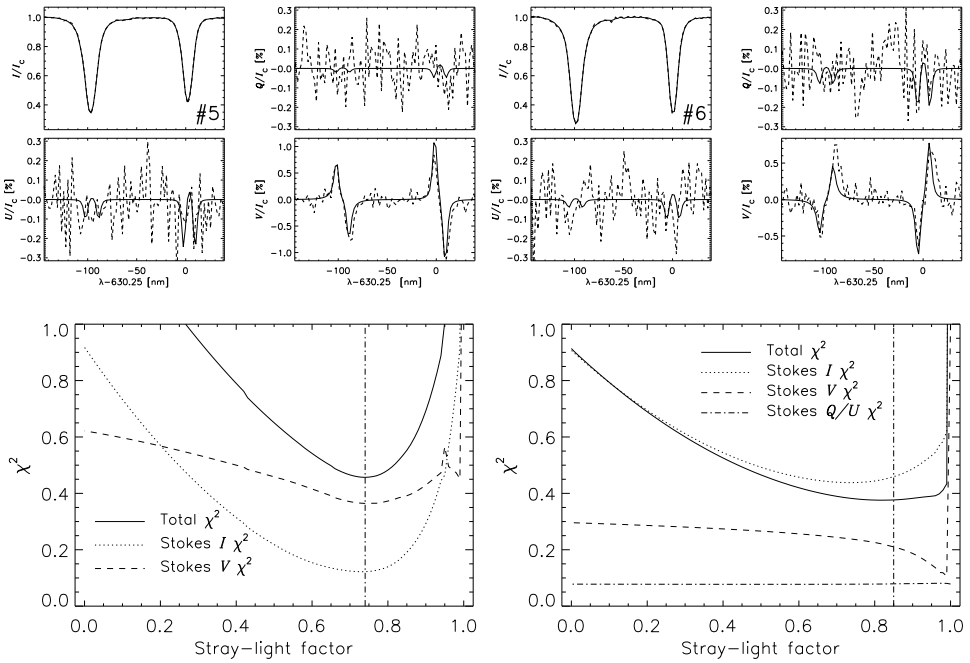

FIGURE 7.14:— *Top*: Observed (*dashed*) and best-fit (*solid*) Stokes profiles emerging from network pixels #5 (*left*) and #6 (*right*). The field strengths, inclinations and the stray-light factors retrieved from the inversion are 185 and 219 G, 126 and 105°, and 73 and 84%, respectively. *Bottom*: χ^2 values of the best-fit profiles resulting from the inversion of pixel #5 (left) and #6 (right) with fixed, erroneous stray-light factors. The solid,dotted and dashed lines stand for the total, Stokes I, V and Q/U χ^2, respectively. The vertical line represents the "true" stray-light factors.

7.3.5 Qualitative results

The maps of the retrieved field strength, inclination, azimuth, stray-light factor, and LOS velocity are shown in Appendix B for the normal map and for the high S/N map. Black regions represent pixels which have not been analyzed because of their small signals. In the field strength map two different regions can be identified: the network, characterized by strong fields (above 1 kG), and the IN, with much weaker fields and slightly larger stray-light factors. Supergranular cells are clearly outlined by the network fields. The inclination map shows that network flux concentrations exhibit nearly vertical fields in their interiors and more inclined fields toward the edges, suggesting the presence of magnetic canopies. By contrast, IN fields are rather horizontal.

The results from the inversion of the high S/N map are also shown in

Appendix B. These maps show a richer amount of magnetic features. The magnetic field strengths are of the order of hG and horizontally oriented. The stray-light factor values are of the same order than those from the normal map. The azimuth is much better recovered due to the noise.

Figure 7.15 represents a zoom over a $7\farcs4 \times 7\farcs4$ IN area (white box in the images from Appendix B) and display continuum intensities, magnetic field strengths, field inclinations, azimuths, stray-light factors and total polarization signals, $P = \sqrt{Q^2 + U^2 + V^2}/I_{\rm QS}$. In the field strength map one can see that most of the fields are weak. The stronger concentrations are located in intergranular lanes (the contours outline the granulation). Interestingly, we find ubiquitous weak fields over granules. The map showing the total polarization just confirms this finding. Note also that the fields are more horizontal in granular regions than elsewhere. The azimuth map shows small patches of $\sim 1''$. Finally, the map of stray-light factors show values between 70 and 90%, and no conspicuous variations for granule center to intergranular regions.

The intrinsic magnetic field of network patches lie between 1200 and 1700 G (See Solanki 1992 for a extended review) and the field lines tend to be vertically oriented (Sánchez Almeida, & Martínez Pillet 1994; Martínez Pillet, Lites & Skumanich 1997). Figure 7.16 shows the results of the inversion of a network element found in the normal map. The retrieved field inclinations of this particular network element are close to the LOS at the center of the network patch and the retrieved magnetic flux (2×10^{18}) is compatible with earlier observational estimates of $\sim 10^{18} - 10^{19}$ Mx (e.g. Schrijver et al. 1997a,1997b).

Notice that the total polarization signal is well correlated with the magnetic field strength. Also, the total polarization map clearly shows the "bloom" (Lites 2002) of the signal due to the PSF of the telescope as described in Chapter 6. As a consequence, a canopy like structure is seen surrounding the network magnetic element, which is strongly associated with the abnormal granulation as well. In this case the canopy may be interpreted as a virtual surface that separates two different physical environments along the LOS, one magnetic (upper layers) and one non-magnetic (bottom layers). However, this canopy-like structure is partially due to telescope diffraction. The size of the canopy is reduced in the magnetic field strength map as a consequence of the use of the stray-light factor. Also, the field strength map seem to be noisier than the total polarization map as a consequence of the additional free parameter. The obtained stray-light factors are of the order of 60-80%, slightly smaller than for IN areas. Note the small-scale structures in form of $0\farcs5$-$1''$ parches in the stray-light factor map and in the azimuth map.

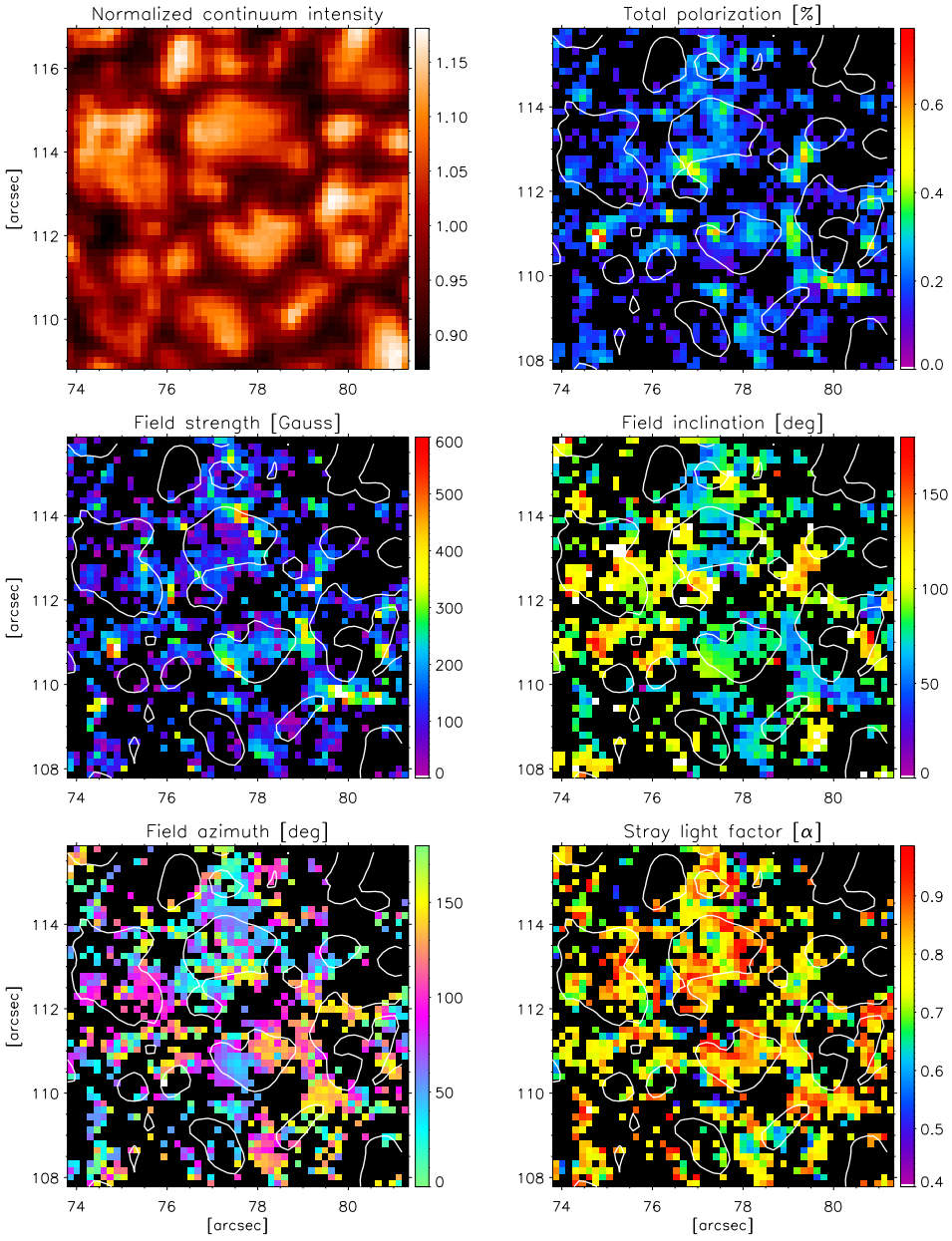

FIGURE 7.15:— Small IN area of $7.4'' \times 7.4''$ (white box in the maps shown in Appendix B). The different panels display continuum intensities, total polarization signals, $\int (Q^2 + U^2 + V^2)^{1/2}\, \mathrm{d}\lambda / I_\mathrm{c}^\mathrm{QS}$, magnetic field strengths, field inclinations, field azimuth, and stray-light factors. Contour lines represent regions with continuum intensities $I_\mathrm{c}/I_\mathrm{c}^\mathrm{QS} > 1.05$. The field strength color bar has been clipped at 600 G (*white*).

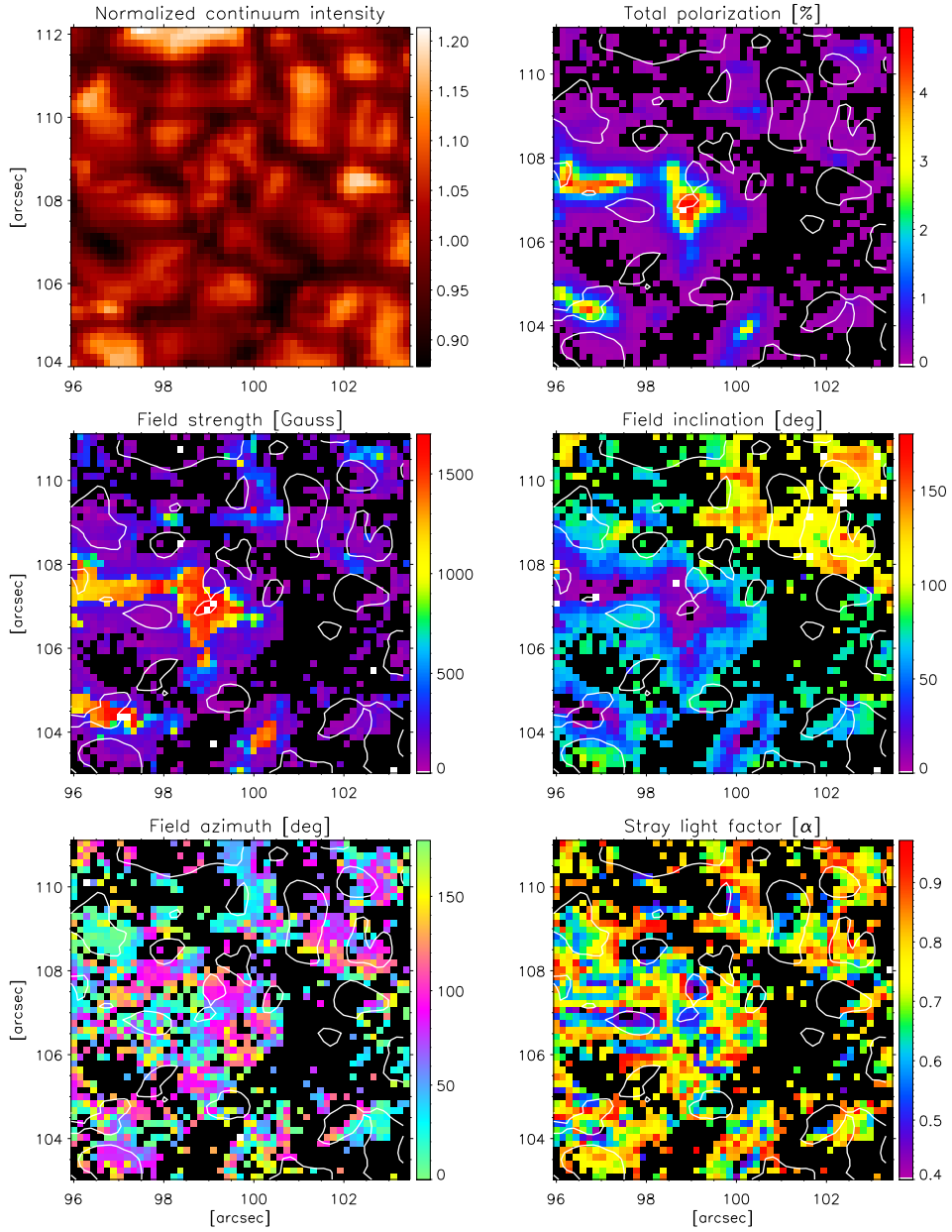

FIGURE 7.16:— Same as Fig.7.15 but for a network area (red box in the maps shown in Appendix B). In this case the field strength color bar has been clipped at 1700 G.

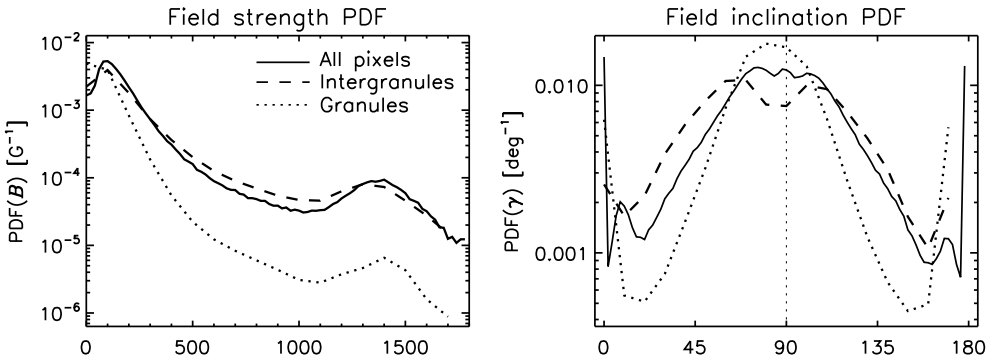

FIGURE 7.17:— Magnetic field strength (*left*) and inclination (*right*) probability density functions. In the upper panels, the solid, dashed, and dotted lines stand for all pixels in the FOV, intergranular lanes, and granules.

7.4 Distribution of intrinsic field strengths and inclinations

A common way to characterize the distributions of field strengths is through the so-called Probability Density Function (PDF). It represents the probability of finding a magnetic field strength B in the interval $(B, B + dB]$ and has total integral unity, $\int_0^\infty P(B)dB = 1$.

To date, different analyses of IN areas using the pair Fe I at 630.2 nm of lines reveal PDFs with maximum peaks at kG fields (Socas Navarro, & Sánchez Almeida 2003, Domínguez Cerdeña et al. 2003; Sánchez Almeida al. 2003; Lites, & Sócas Navarro 2004; Domínguez Cerdeña et al. 2006, and Martínez Gonzalez et al. 2008). Only few analysis have delivered field strengths in the hG region (see e.g., Rezaei et al. 2007) with these spectral lines. The distribution of IN field inclinations has only been studied by Lites et al. (1996) and Khomenko et al. (2003), though. We contribute to shed light to these results with the analysis of the *Hinode*/SP data. Figure 7.17 shows the total PDF for the magnetic field strength (*left*) and field inclination (*right*) resulting form the ME inversion of ∼650 000 pixels belonging to the normal map.

Contrary to most of the results previously published, the peak of the total PDF for the field strength is located at about 90 G. The curve decreases rapidly toward stronger fields: at around 1 kG it reaches a minimum and then shows a small hump centered at about 1.4 kG. Strong fields (B >1 kG) are found in only 4.5% of the pixels, the majority of which correspond to network areas. It is important to emphasize that the PDF does not increase monotonically from 90 G to 0 G. This suggests that the inversions are not biased by noise, and

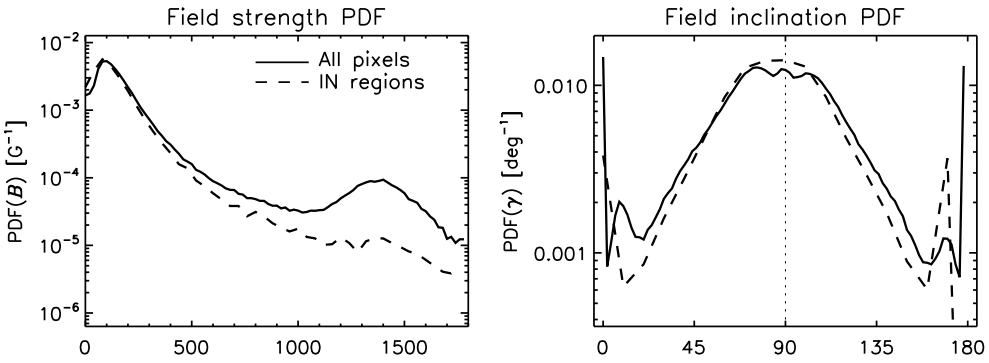

FIGURE 7.18:— Same as Fig 7.17 but the solid and dashed lines represent all pixels in the FOV and IN regions, respectively.

that the peak at 90 G is likely solar in origin. Note that we have analyzed only pixels whose polarization signals where above 4.5 times their noise levels. The peak may also represent cancellation of magnetic flux at spatial scales smaller than 0.″32 (Martínez González et al. 2008).

In the figure we have also represented the PDFs for granules and intergranular lanes, dotted and dashed lines respectively. The separation between granular and intergranular regions has been performed using the continuum intensity and the retrieved LOS velocity from the inversion. In particular we define granular (intergranular) regions as those areas whose pixels show larger (lower) continuum intensity values than the mean intensity of the full map and also show blue- (red-) shifted velocities.

The distribution of field strengths is steeper in granules as compared with intergranular lanes, i.e., strong fields are much less abundant in granular regions. Noticeable is the large fraction of very inclined ($\sim$90°) fields in granules. Although inclined fields are also common in downdrafts, the field lines tend to be more horizontal over convective upflows (right panel of Fig. 7.17). The rapid increase of the PDF near 0° and 180°, however, indicates that vertical fields also exist in granules (see Chapter 8).

Figure 7.18 displays the distribution of field strengths and inclinations, for the full FOV and for IN regions, given as probability density functions (PDFs). IN areas have been selected manually in the interior of supergranular cells, avoiding the strong flux concentrations of the network (see Sect. 7.2.2). In the IN, the field strength distribution reaches a maximum near 90 G and decreases toward larger fields (left panel of Fig. 7.18). This demonstrates that the IN basically consists of hG flux concentrations. In addition, the fields tend to be horizontally oriented as shown by the PDF(γ) for the IN (right panel of

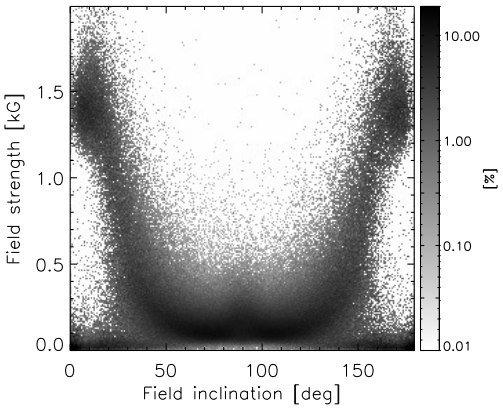

FIGURE 7.19— Inferred magnetic field strength versus the inclination of the field.

Fig. 7.18) and in agreement with the finding of Lites et al. (1996) and Martínez González et al. (2007).

There are different humps in the PDFs(γ). In particular, we find humps at $\gamma \sim 10$ and $\sim 170°$, and at $\gamma \sim 70$ and $\sim 110°$. The reason may be that it is not possible to determine purely vertical or horizontal fields when the field is weak (see e.g. Sec.$\tilde{3}$.5 from Khomenko et al. 2003). For vertical fields, the inversion algorithm tries to fit the noise of Stokes Q and U, for horizontal ones, it tries to fit the noise of Stokes V. In both cases the inversion would yield wrong field inclination. However, we find purely vertical and horizontal fields in the IN. How is this possible? The reason is in Stokes I. The sensitivity of Stokes I to perturbations on the field inclination is greater than that residing in Stokes V, or Q and U, in the weak-field regime (see Chapter 4). Therefore Stokes I plays an important role in the determination of correct field inclinations. Lites (2002), by means of numerical tests, allready demonstrated that the ME inversion do infer the correct inclinations for weak fields although with larger uncertainties.

The results for the magnetic field strength are in agreement with Keller et al. (1994) who also found weak fields in the internetwork using the Fe I 525.0 nm lines, although at a lower spatial resolution and without inclination information. They also agree with the infrared results (Lin 1995: Lin & Rimmele 1999; Khomenko et al. 2003) and with the simultaneous inversion of visible and infrared lines (Martínez González et al. 2008).

Finally, Fig. 7.19 represents the retrieved field strength values against the inclination of the field. As pointed out by Martínez González et al. (2008) there is a clear tendency of strong fields to be vertically oriented (network fields). Magnetic fields weaker than ∼500 G tend to have orientations between 30 and

150°. There also find weak fields with all posible orientations. Interestingly, there are no magnetic fields stronger than ∼500 G in the range of inclinations from 50 to 130°.

7.5 Effects of noise on the PDFs

The polarization signals in the internetwork are typically smaller than those in active regions. As a result, they are more affected by noise. This may make the determination of vector magnetic fields less reliable. To minimize the influence of noise we have analyzed only Stokes profiles whose polarization signals exceed a given threshold above the noise level σ. The inversions presented so far correspond to pixels whose Q, U or V signals are larger than 4.5 σ. This should increase the robustness of the results because we do not include too noisy profiles in the analysis. Our experience with simulations and real observations tells us that ME inversions provide reliable results in the quiet Sun under these conditions.

To evaluate the effect of noise in more detail we have calculated the field strength and inclination PDF of IN regions for four different thresholds: 1.2, 4.5, 7.5, and 10 σ. Figure 7.20 displays the results. Note that the 1.5 σ PDFs correspond to the inversion on the high S/N map, hence the different shape. These observations have a S/N about 3.7 times larger than that of the normal map. The polarization threshold of 4.5 times the noise level in the high S/N map is equivalent to a threshold of 1.2 times the noise level of the normal map.

As the threshold level increases, the peak of the PDF decreases in amplitude, shifts toward stronger fields, and becomes broader. Thus, the larger the threshold, the smaller the percentage of weak fields detected. Since weak fields are usually associated with weak polarization signals for fully resolved magnetic structures, this is exactly what one would expect just because the weak polarization signals are excluded from the analysis. The important result is that, independently of the polarization threshold used, the amount of strong fields remains unchanged. Even for very high polarization thresholds, the field strength PDFs are dominated by weak fields, so they cannot be the result of noise in the profiles. Also remarkable is the fact that the peak location of the field strength PDF for 1.5 σ does not change. This indicates that the peak has a solar origin. This also indicates that noise is not producing an artificial excess of weak fields. Finally notice the increase of very weak magnetic fields for the high S/N map.

Interestingly, the field strength PDF for 1.5 σ shows that the distribution increases monotonically toward smaller fields, just after the hump of the dis-

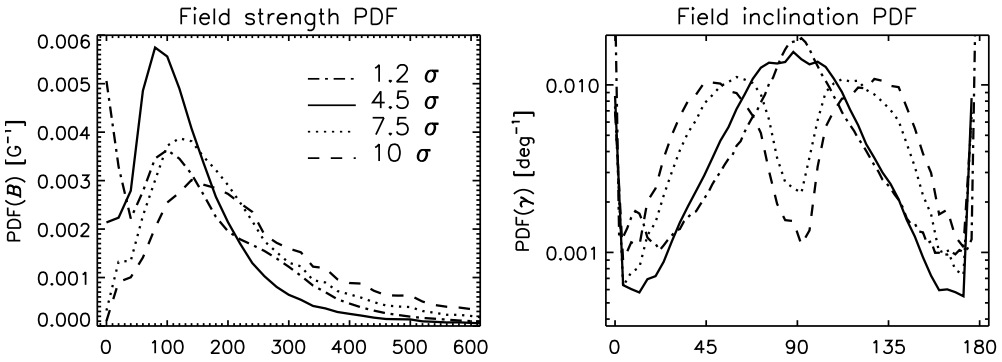

FIGURE 7.20:— Magnetic field strength and inclination probability density functions for IN regions. The different line styles stand for different threshold levels in the analysis. Pixels whose Stokes Q, U or V amplitudes do not exceed these levels are rejected.

tribution. This may indicate that there are two different mechanism of field generation in the quiet Sun.

The PDFs(γ) also provide clear evidences of that the IN is full of horizontally oriented fields. Note that for large noise thresholds (10 and 7 σ) the PDFs show two clear humps located between 45 and 65° and the occurrence of purely horizontal fields is small. As we reduce the noise threshold, the different humps disappear and the PDF values at 90° increases considerably, loosing completely the humps with the high S/N map case. The reason is that the inclination of the field is determined from the four Stokes profiles but for high thresholds, only Stokes I and V are available, yielding larger uncertainties in the inclination. Notice that the occurrence of horizontal fields is similar than for vertical ones in the 10 σ case. This could also indicate that the weakest signals are those from the more horizontal fields.

7.6 Distribution of stray-light factors

Current ground-based spectropolarimetric observations at 1″-1.″5 are not sufficient to spatially resolve the magnetic field structures present in IN areas. This relative lack of spatial resolution is largely responsible for the different field strength distributions found from the analysis of visible and infrared (IR) lines. The most recent analyses of visible and IR lines by means of inversion techniques have estimated magnetic filling factors of about 1-2% and 0.5-1%, respectively for both spectral regions (Martínez González et al. 2008).

In Figure 7.21 we show the PDF of the stray-light factor for the full FOV

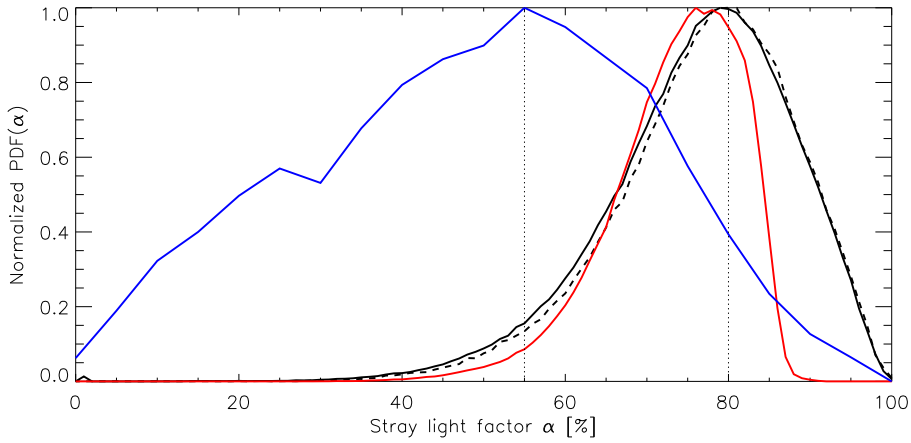

FIGURE 7.21:— PDF of the stray light-factor corresponding to the normal map (black) and to the high S/N map (red). Solid and dashed lines represent the full FOV and IN regions, respectively. Overplotted is the histogram representing the stray-light factors derived from the inversion of simulated Stokes profiles. The dotted vertical lines indicates the peak of the stray-light factor distributions.

and IN regions from the normal map and for IN regions of the high S/N map (black and red lines respectively). The PDFs for the normal map peak at $\alpha \sim 80\%$ while the PDF for the high S/N map peaks at about 75%. There are clear differences on the width of the PDFs corresponding to the two data sets.

According to the discussion in Sect. 7.3 (see also Chapter 6), the stray-light factor corrects for the effects of diffraction in the polarization signals, but it might also represent magnetic filling factors smaller than 1. In this case the stray-light factor would be representing the fill fraction α of a non-magnetic component in the pixel. The rest of the pixel is then occupied by the magnetic component, whose filling factor is given by $f = 1 - \alpha$. If one accepts this alternative interpretation, then the fractional area of the resolution element occupied by magnetic fields would be small, showing a peak at $f \sim 20\%$. This value is considerably greater than tipical filling factors inferred from the graund at $1''$.

In the same figure we have represented the PDF of stray-light factors (blue) derived from the inversion of Stokes profiles that arise from MHD simulations (see Chapter 6 for details). Note that the PDF has a maximum at around 55%. This indicate that the stray-light factor of $\sim 80\%$ derived from the inversion of real data might actually represent the combination of: (i) the reduction of the polarimetric signals due to the action of the telescope (diffraction) and, (ii) a

real filling factor due to still insufficient angular resolution.

If this is the case, a 55% of the stray-light factor can be attributed to diffraction. The rest 25% represents the $1 - f$ factor. In summary, if we neglegt diffraction, the "effective" magnetic filling factor (per pixel) would be $f \sim 45\%$ in the quiet Sun.

Errors in the stray-light determination would immediately lead to different field strengths and/or inclinations because most of the observed signals are formed in the weak-field regime. However, as we have shown in Sect. 7.3.4, the high-spatial resolution allowed by the *Hinode*/SP makes it possible to distinguish between field strength and stray-light factor unambiguously, even under weak field conditions. After these comments, we caution that different interpretations of the same problem are possible. Therefore, further work should be carried out to investigate the exact meaning of the stray-light factors inferred from ME inversions of *Hinode*/SP measurements.

Finally, the filling factor of $f = (1 - \alpha) = 20\%$ derived in our analysis is in full agreement with the, in average, 23% inferred by Lites et al. (2008) with the same data. He used the MERLIN[5] code (Lites et al. 2007a) to determine the magnetic field strength and the stray-light factor. The stray-light profile was determined by averaging the Stokes I profiles of those points with very weak polarization signals. They also found the optimal wavelength shift of the stray-light profile.

7.7 Comparison with MHD simulations

Figure 7.22 compares the PDFs of IN regions of the normal map (black) with those calculated from the magneto-convection simulations of Vögler et al. (2005), for three snapshots with mean unsigned flux densities of 10, 50 and 140 Mx cm^{-2} (color coded lines).

The simulation run that better match the slope of the IN PDF(B) corresponds to the $\langle B \rangle = 10$ G at around optical depth $\log \tau_5 = -2$. However, this distribution of fields does not reproduce the hump on the PDF at around 90 G. The distribution from the simulations increases monotonically towards 0 G while the IN PDF has a clear maximum. As we have discussed in previous sections, this hump is of solar origin. Only the PDF corresponding to the $\langle B \rangle = 140$ G simulation run has a clear hump, but in this case the slope is completely different.

The field inclination PDFs appear to be rather different, by contrast. In the simulations the distributions are much flatter. These simulation runs in with

[5]Milne-Eddington gRid Linear Inversion Network

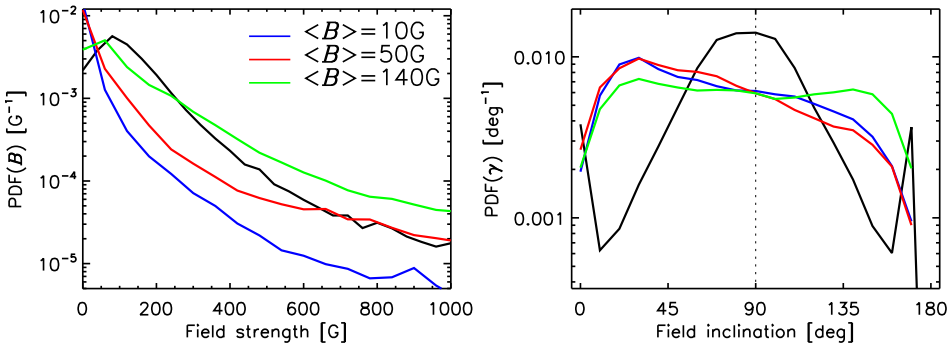

FIGURE 7.22:— Magnetic field strength and inclination probability density functions for IN regions and from the magneto convection simulations for $\langle B \rangle = 10$, 50 and 140 Gauss, taken at optical depth $\log \tau = -2$

an imposed (initial) net vertical flux do not show a dominance of horizontal fields (Shüssler & Vögler, 2008) as it seems to be the case in the IN of the quiet Sun.

In order to make the PDF(B) available for the community we have fit the PDF(B) of the IN in the range 1-8 hG to a lognormal function

$$f(B) = (\pi^{1/2}\sigma B)^{-1} \exp[-(\ln B - \ln B_0)^2/\sigma^2 \tag{7.2}$$

which describes satisfactorily the PDF with $B_0 = 36.7$ G and $\sigma = 1.2$.

7.8 The magnetic flux density in the IN

The determination of the (unsigned) averaged flux density of quiet Sun IN regions has been pursued by many authors. It ranges from the 6-9 Mx cm^{-2} reported by, e.g., Sánchez Almeida et al. (2003); Khomenko et al. (2003), to the 21 Mx cm^{-2} found by Domínguez Cerdeña et al. (2003). Other studies using simultaneous observations of visible and infrared lines, gives 11-15 Mx cm^{-2} (Khomenko et al. 2005a). An upper limit to the flux density seem to be $\sim$50 Mx cm^{-2} (e.g., Lin & Rimmele 1999; Faurobert et al. 2001).

There is a large disparity between the average flux densities provided in the literature and the reason is that the results are biased by the angular resolution of the observations and also by the different techniques of analysis that are used.

The *(net) magnetic flux* through a portion (resolution element) of the solar surface is defined as:

$$\Phi = \mathbf{BS}, \tag{7.3}$$

where $\mathbf{B} = f(x, y, x)$ is the magnetic field vector, $\mathbf{S} = \hat{n}S$ is the surface crossed by the magnetic field lines, and $\hat{n}$ the unit vector perpendicular to the solar surface. Averaging over the pixel surface $A_{\rm px}$ we obtain the *magnetic flux density* $\phi = \Phi/A_{\rm px}$, expressed in Mx/cm^2. If the field element occupies a fraction f of the resolution element, $S/A_{\rm px} = f$, then

$$\Phi = f A_{\rm px} B \cos\gamma \tag{7.4}$$

and

$$\phi = f B \cos\gamma = f B_{\rm long} \tag{7.5}$$

where B is the field strength and $B_{\rm long}$ refers to the longitudinal (vertical to the surface) component of the field. γ stands for the Zenith angle. The mean *net* magnetic flux density is $\overline{\phi}_{\rm n} = \sum_{i=1}^{N} \phi_i/N$ and the *unsigned*, magnetic flux density $\overline{\phi} = \sum_{i=1}^{N} |\phi_i|/N$ where N is the total number of pixels and ϕ_i is the flux density for each pixel i. Some athors also compute the so-called unsigned transverse flux density $\overline{\phi}_{\perp} = \sum_{i=1}^{N} |f_i^{1/2} B_i \sin\gamma_i|/N$. We would like to stress that this quantity is physically meaningless. Finally, we also compute the mean intrinsic field strength[6] as $\langle B \rangle = \sum_{i=1}^{N} f_i B_i/N$ and measured in G/cm^2.

Table 7.2 shows the different flux estimates for the normal map and for the high S/N map[7]. Before discussing the different flux values we should take into consideration two things: first that the different fluxes have been computed assigning zero fluxes to pixels which were not inverted (those whose Stokes Q, U or V maximum (unsigned) amplitudes were below 4.5 σ); second that we have assumed that $f = 1 - \alpha$. Therefore, we are considering that the stray-light factor reflects the filling factor for the magnetic field. We know that it is actually a combination of two things, i.e., the effects of diffraction and the fraction of the resolution element occupied by the magnetic feature. It is important to remark that the fill fraction f of the magnetic field explicitly appears in ϕ because of the integration of the flux per unit of resolution area. On the contrary, the quantity α aims at accounting for the dilution of the polarimetric signals due to diffraction. Therefore, the stray-light factor has no relationship with the area of integration. For practical application, it is not possible to separate stray-light from filling factor. The reason is that both affect in a similar way to the polarization signals. However, the stray-light factor should not be considered for the evaluation of ϕ. As a conclusion of the two previous comments, the different flux estimates presented in Table 7.2 represent *lower limits*.

[6] In Orozco Suárez et al. (2007) we determined the quantity "mean unsigned apparent flux

TABLE 7.2:— Estimated flux values of the FOV and IN regions corresponding to the normal map and to the high S/N map. Columns are the *unsigned*, magnetic flux and transversal flux densities, $\overline{\phi}$ and $\overline{\phi}_\perp$, and the net flux $\overline{\phi}_\mathrm{n}$ in units Mx cm^{-2}, and the mean magnetic field strength $\langle B \rangle$ in units of G cm^{-2}

		$\overline{\phi}$	$\overline{\phi}_\perp$	$\overline{\phi}_\mathrm{n}$	$\langle B \rangle$
Normal map	FOV	9.58	23.49	1.7	16.74
	IN	3.41	15.2	-0.1	8.46
High S/N map	FOV	22.57	68.93	2.20	48.17
	IN	7.78	49.87	-0.58	29.18

As already pointed out by Lites et al. (2008a,b), the results indicate a large occurrence of horizontal fields in IN regions. They also give support to the "seething" horizontal features found by Harvey et al. (2007).

The flux values that we have estimated for the normal map are below those reported by Lites et al. (2008a,b)[8] which are $B^L_\mathrm{app} \simeq 11$ and $B^T_\mathrm{app} \simeq 60$ Mx cm^{-2}. The reason is in the higher noise threshold condition the polarimetric signals have to fulfill in order to be included on the analysis. Therefore, we obtain smaller flux values. However, the ratio between the longitudinal and transverse flux is about $r \sim 4.5$, very close to the factor $r = 5$ found by Lites et al. (2008a,b).

The longitudinal and transverse flux values increase with increasing S/N. In fact, the transverse flux obtained from the inversion of the high S/N data is very close to the 64 Mx cm^{-2} obtained by Lites et al. (2008a) using similar ME inversions but with a completely different code (MERLIN). In addition, we have found that for these data $r = 6.4$.

As a final comment, we want to discuss again the physical meaning of the stray-light factor α. As shown in Sect. 7.6 the stray-light factor distribution shows a peak located at about 80%. As explained before, the stray-light factor represents a combination of two different effects: firstly the effects of diffraction and secondly the real fill fraction of the magnetic field. Let us assume that the real stray-light factor is of about 55% for *Hinode*/SP observations. In this case the equivalent fill fractions of the magnetic field would be larger, $f \simeq 45\%$. The same occurs for the longitudinal and transverse flux densities. If we do not remove the effects of diffraction in the evaluation of the different flux densities, the longitudinal flux is underestimated by a factor of ~ 2.5. This factor is

density" when we really meant the mean intrinsic field strength per unit area.

[7]We also include the meaningless transverse flux density for comparison purposes with other authors.

[8]They used a different terminology, i.e., $B^L_\mathrm{app} \propto \phi$ and $B^T_\mathrm{app} \propto \phi_\perp$, see Lites et al. (1999).

of about ∼1.5 for the transverse flux because it scales with $\sqrt{f}$. Moreover, the ratio between the longitudinal and transverse flux densities would become smaller.

Steiner et al. (2008), using MHD simulations, have argued that the ratio between the longitudinal and transverse flux should increase when applying a PSF to the original data because of apparent flux cancellation within each finite resolution element. This is exactly what happens if we consider that the stray-light factor represents a real filling factor, but the higher ratio is mainly due to the dilution of the polarimetric signals due to the PSF and not to cancellation of flux within the resolution element. The contribution to r of the later depends mainly on the spatial scales of the magnetic features.

7.9 Discussion

Up to now, the analysis of IN fields have been controversial. Visible lines seemed to deliver mostly kG fields while IR lines yielded hG fields. To explain these conflicting results, it has been argued that visible and IR lines sample different magnetic structures in the resolution element (Socas-Navarro 2003 & Sánchez Almeida & Socas Navarro). Also, Bellot Rubio & Collados (2003) suggested that noise may be responsible for the different magnetic field distributions resulting from visible and infrared lines, and highly recommend to improve the S/N of the measurements. Even more recently, Martínez González, Collados, & Ruiz Cobo (2006) have shown that the Fe I 630.2 nm lines are not adequate to obtain reliable field strengths from IN regions at 1″ spatial resolution. Given these concerns, other authors have explored new ways to derive IN fields (e.g., Asensio Ramos et al. 2006, López Ariste et al. 2006, Trujillo Bueno et al. 2004).

The polarimetric sensitivity of the Hinode/SP data is almost 10 times larger than ground-based observations at 1″. The results here presented suggest that, most probably, previous analyses where strongly biased by the spatial resolution and the atmospheric seeing. Al least, our tests suggest that the results from the ME inversion of *Hinode*/SP data are neither biased by the initialization of the algorithm nor by the intrinsic noise of the observations.

Thus, the *Hinode*/SP measurements indicate that most IN fields are weak. This is in agreement with the picture derived from the more magnetically sensitive Fe I lines at 1565 nm (Lin 1995; Lin & Rimele 1999; Collados 2001; Khomenko et al. 2003; Martínez González et al. 2006b; Domínguez Cerdeña et al. 2006). Keller et al. (1994) also found weak fields in the internetwork using the Fe I 525.0 nm lines, although at a lower spatial resolution and without inclination information.

Our results confirm the findings by analyzing the Mn I 553 nm (López Ariste et al. 2006), which indicate that the IN is dominated by fields bellow 600 G. They also partially agree with the analysis of the near-infrared Mn I located at 1526.2 nm (Asensio Ramos et al. 2007). They found a Gaussian shaped PDF(B) located at around 250-350 G.

If we analyze separately granules and intergranular lanes, we agree in the presence of hG fields above granules with different authors but not in the granular lanes. However, we find a large occurrence of horizontal fields. The scenario of an IN filled by nearly horizontal hG fields is compatible with the large trasverse magnetic fluxes found in the IN by Lites et al. (2007a,b) and Martínez González et al. (2007). This clear dominance of horizontal magnetic fields may be generated by the action of a near-surface turbulent dynamo (Abbett 2007; Shüssler & Vögler 2008).

Interestingly, the slope of the field strength distribution in the IN is similar to that obtained from magnetoconvection simulations of comparable mean flux density. The observed field inclinations, however, turn out to be significantly larger than those predicted by the simulations.

Measurements based on the Hanle effect (Trujillo Bueno, Shchukina, & Asensio Ramos 2004) suggest that the IN is filled by nearly horizontal fields of about 60 G, which is surprisingly close to the PDF maximum field strengths in our analysis. The increased resolution may not cancel magnetic structures of opposite polarity allowing the determination of very weak fields by means of the Zeeman effect. The results support the idea of an IN filled by turbulent fields which originate and dissipate following the granular motion. We also found an averaged net flux of 1.71 Mx cm^{-2}.

7.10 Conclusions

In this Chapter we have applied the Milne-Eddington inversion strategy described in Chapter 6 to the high spatial resolution spectropolarimetric measurements of the quiet Sun performed by *Hinode*.

The inversion strategy has been applied to a quiet Sun raster scan and to a time sequence of $\sim$2 hours with very high S/N, both taken with the *Hinode* SP. We have demonstrated that noise does not significantly affect the results of ME inversions, provided a sufficiently large polarization threshold is used to invert the Stokes profiles. A threshold around 4.5 times the noise level seems to yield correct inferences. In addition, we have shown that the results do not depend on the initial magnetic field strength of the model, because the information contained in the Stokes profiles observed at the resolution of *Hinode* is sufficent

to disentangle the various model parameters.

The inferred PDFs of the magnetic field strength indicate that internetwork regions are mainly formed by hG field concentrations with large stray-light factors, contrary to what is obtained from the same lines at $1''$. This is the first time that Fe I 630 nm observations confirm the weak IN fields indicated by near-infrared measurements, which may definitely close the discrepancy between the results derived from both spectral regions. They show that quiet Sun internetwork regions consist mainly of hG fields with stray-light contaminations of about 0.8. Taking into account the weakening of the polarization signals due to telescope diffraction, these large stray-light factors might also be interpreted as magnetic filling factors of the order of 0.45. The preliminary analysis presented here confirms the picture of weak internetwork fields derived from ground-based measurements in the near infrared (see, e.g., Collados 2001).

We still do not know the origin of the ubiquitous horizontal IN fields. In the next Chapter we analyze time series of *Hinode*/SP measurements in order to study more in detail plausible mechanisms contributing to the current distribution of IN fields.

8

Magnetic field emergence in the quiet Sun

The previous Chapter was dedicated to the analysis of quiet Sun's magnetic fields. To that end we used high spatial resolution spectropolarimetric data recorded with the *Hinode* satellite. In this chapter we explore the benefits of high-cadence time series of spectropolarimetric measurements taken with the same instrument. The advantage of using *Hinode*/SP time series data is utilized although at the cost of introducing constrains to the measurements, as smaller fields of view or larger noise levels.

8.1 Introduction

The analysis of spectropolarimetric measurements taken with the spectropolarimeter aboard *Hinode* indicates that the internetwork harbors a substantial amount of magnetic flux, being the intrinsic magnetic fields predominantly *weak* and tending to be horizontally oriented. We have now a good understanding of the properties of such fields, but their origin remain largely unknown.

There have been different theoretical approaches intended to explain the origin of quiet Sun photospheric magnetic fields. Cattaneo (1999) suggested that the action of a local dynamo at the solar surface may generate a considerable amount of magnetic flux. But the questions of how these fields appear on the solar photosphere and whether or not a local dynamo operates are still open.

A way to seek for the origin of the fields is to perform spectropolarimetric observations at high temporal cadence. This would allow to observe the evolution of individual magnetic features, therefore gaining additional information about their dynamics and the magnetism itself.

At present, the *Hinode* spectropolarimeter is the most suitable instrument to perform high-cadence time series of spectropolarimetric measurements in the quiet Sun. It provides very high spatial resolution data in the absence of atmospheric seeing. The absence of the Earth's atmosphere permits recording long time series of data with constant effective spatial resolution. This allows the magnetic features to be studied in greater detail although at the cost of smaller fields of view and/or larger noise levels in the polarization spectra.

There have been attempts to characterize the quiet Sun magnetic fields by analyzing high-cadence time series. Lites et al. (1996) employed the Advance Stokes Polarimeter (ASP) to record time sequences of maps in quiet Sun regions with spatial resolutions not better than $\sim 1''$. From them, they reported on the existence of small-scale ($1''$-$2''$) magnetic features typically lasting $\sim$5 minutes and predominantly horizontal. Their findings have been recently confirmed by Martínez González et al. (2007) using time series taken with the Tenerife Infrared Polarimeter (Collados 1999) installed at the Vacuum Tower Telescope (Teide Observatory, Tenerife). They presented convincing evidence of low-lying loops connecting opposite-polarity flux concentrations in the solar internetwork. Figure 8.1 shows a pictorical view of such loops connecting different magnetic patches at the solar surface (courtesy of M. J. Martínez González).

Analysis of magnetograph data with moderate spatial resolution have significantly contributed to this topic as well. de Pontieu (2002) used the Swedish Vacuum Solar Telescope to record high-spatial resolutions longitudinal magnetograms of the quiet Sun. His observations showed flux concentrations emerging in the internetwork and disappearing in about 10-15 minutes with no evidence for flux cancellation, i.e., he did not find opposite-polarity magnetic features at the location of the emergences. The observations were taken away from disk center, so there is a possible connection with the small-scale magnetic loops discovered by Lites et al. (1996) and confirmed by Martínez González et al. (2007). More recently, Lamb et al. (2007) employed MDI longitudinal magnetograms with a spatial resolution of $1\farcs2$, to analyze the emergence of small-scale magnetic features that seem to be apparently of unipolar flux.

As previously mentioned, improvements in the spatial resolution of spectropolarimetric measurements and the ability of taking high cadence maps will provide new insights to understand the emergence, evolution and disappearance of small-scale magnetic flux concentrations over quiet Sun regions. Indeed, Centeno et al. (2007) and Ishikawa et al. (2007) have made use of the *Hinode*/SP

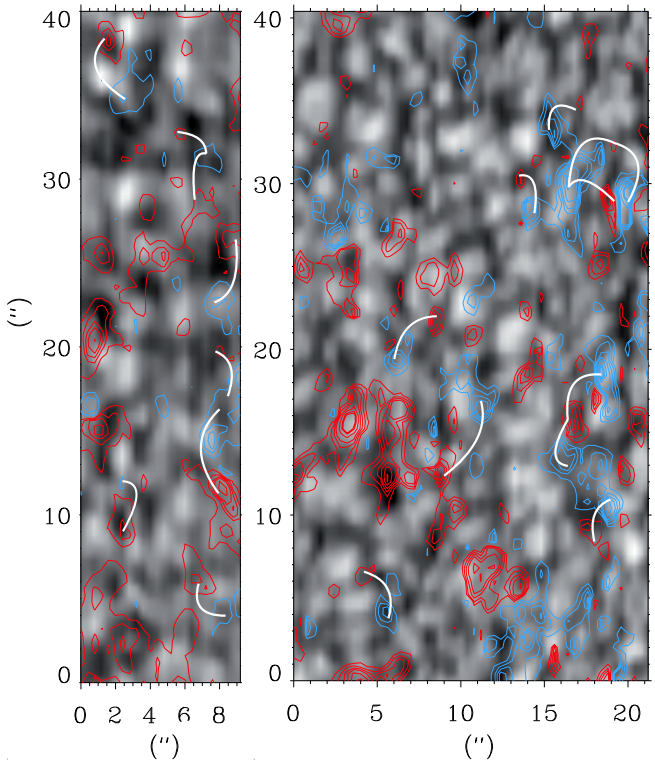

FIGURE 8.1:— Pictorial view of low-lying magnetic loops in quiet Sun regions. Red and blue contours represent fields of opposite sign. The loops are indicated with white lines. The data were recorded with the TIP instrument at the VTT (see text for details). Cortesy of M. J. Martínez González.

capabilities to confirm the existence of very small-scale magnetic loops in quiet Sun areas and plage regions, respectively.

In this Chapter we concentrate on the analysis of long-time series of *Hinode*/SP raster scan maps taken over quiet Sun regions. The idea is to analyze the evolution of the emergence events that are found in the data. The Chapter is structured as follows: we first describe the observations and then we perform a qualitative analysis of the emergence events. Then, we evaluate line parameters from the observed Stokes profiles. At the end we discuss the possible origin of the emergence phenomena and present several physical scenarios.

8.2 Observations

The data under analysis consist of three sequences of narrow raster scans performed with the spectropolarimeter aboard *Hinode* at disk center. As we have shown in Chapter 7, the SP measures the Stokes profiles of the two Fe I lines at 630.2 nm. The advantage of the *Hinode*/SP over current magnetographs is that, although it cannot achieve their very high cadences, we get the four Stokes profiles of the two lines with a spectral sampling of 2.15 pm pixel^{-1}. This, together with a spatial sampling of about 0.″16 and high polarimetric sensitivities, makes the SP data ideal to analyze the evolution of photospheric emergence events.

The parameters of each of the observing run can be found in Table 8.1. Two of them scanned a narrow internetwork solar area with a cadence of about 2 minutes and signal-to-noise ratios of about 1000. A third one was obtained by scanning a smaller quiet sun area with shorter integration times, therefore gaining in temporal resolution but at the expense of lower signal-to-noise ratios. In addition, to monitor the conditions of the chromosphere, filtergrams in the Ca II H line core were acquired with the *Hinode* Broadband Filter Imager (BFI; Tsuneta et al. 2008). Only for one of the data sets we have Dopplergrams and magnetograms taken in the chromospheric Mg b I line at 517.2 nm. Dopplergrams are determined from the simple ratio of the difference of blue and red wing intensities divided by their sum. The blue/red images are taken at a distance of 11.2 pm from line center. The magnetograms are taken at the same wavelength distance. This observing run belongs to the *Hinode* Operation Plan (HOP) 14, entitled "Canary Islands Campaign".

Figure 8.2 shows G band and Ca II H images corresponding to the data set #1. In the same figure, the area scanned by the spectropolarimeter is outlined by the red box. The slit is parallel to the Y-axis and the SP scans from left towards right. The zero position along the slit is on the left-bottom corner. The green box indicates the position of event A at $\Delta t = 8$ min (see next section). The Ca II H filtergram shows that the SP slit is placed in an internetwork region, far from network areas (brighter regions near the top and bottom of the FOV). Only the top of the slit observes part of a network. We center the analysis only on IN areas.

The SP data have been corrected for dark current, flat-field, and instrumental cross-talk using standard routines included in the SolarSoft package. The absolute wavelength scale for the observed Stokes spectra has been determined by comparing the line core positions of Fe I 630.1 and 630.2 nm, averaged over quiet Sun areas, with the Fourier Transform Spectrometer atlas. This is done for each of the observing runs. To remove the gravitational redshift we simply

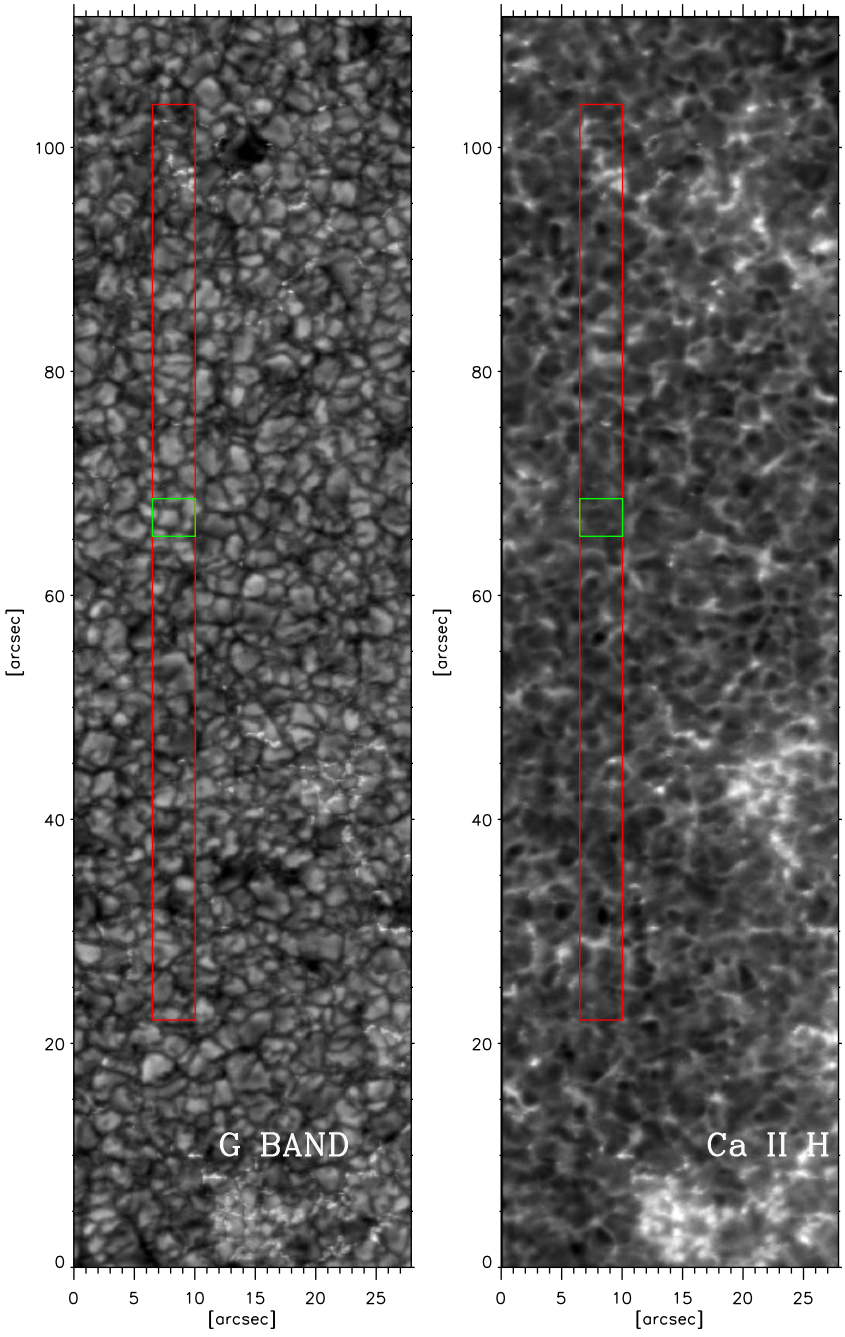

FIGURE 8.2:— Left: *G*-band. Right: Ca II H. Red, dashed line box shows the area scanned with the SP on data set #1. The green box shows the position of emergence event A (see text for details). The FoV is $93\farcs5 \times 28\farcs1$. North is up and West is right.

TABLE 8.1:— Basic parameters for the three observing runs. The first three columns specify the data set and the initial date and time (UT). The fourth column stands for the total duration of the run. The fifth and sixth columns are the number of slit positions in a scan and the corresponding slit integration time. The second row block stands for: the estimated noise levels for V, Q, and U in units of $10^{-3}\,I_{\rm c}$, the field-of-view (FoV), and the cadence. The three last columns indicate the available additional data with their temporal resolution and pixel sizes.

DATA SET	DATE (2007)	TIME	DURATION	SLITS	EXP. TIME
1.....	Feb. 11	11:07:08	4:33h	25	4.8s
2.....	Mar. 10	00:17:03	5:30h	25	4.8s
3.....	Oct. 6	08:01:07	1:59h	18	1.6s
NOISE V - Q/U	FOV	CAD.[a]	BFI DATA	CAD.	PIXEL SIZE
1.1 - 1.2	$4'' \times 81\farcs9$	∼123s	Ca II H	64s	$0\farcs054$
1.1 - 1.2	$4'' \times 81\farcs9$	∼123s	Ca II H	35.5s	$0\farcs108$
1.7 - 1.8	$2\farcs9 \times 41\farcs0$	∼34s	Ca II H/Mg I	32/35s	$0\farcs054/0\farcs08$

[a]Notice that the temporal cadence does not coincide with the number of slit scans × the exposure time. There is an extra time needed to move the slit back from the last scan to the position of the first one.

subtract the corresponding wavelength shift of 615 m s^{-1}. For further details see Sec. 7.2. The calibration algorithm applied to the filtergrams removed cosmic rays, hot pixels, and dark current.

The SP maps, BFI filtergrams, and NFI magnetograms have been aligned as follows: to align the Ca II H filtergrams with the SP data we have compared the G-band images recorded with the BFI against the intensity continuum images made from the SP raster scans. The corresponding X and Y offsets to the images have been calculated by using Fourier cross-correlation techniques with sub-pixel accuracy. To remove the additional image shift among the G-band and the Ca II H images, a correction to the computed offsets is applied. The offsets among the G-band and the Ca II H can be found in Shimizu et al. (2007). The Mg I magnetograms have been aligned with the SP by comparing them with a magnetogram constructed by using the SP Stokes V profiles.

8.3 Emergence processes on the quiet Sun

From the visual analysis of the evolution of continuum maps together with the circular and linear polarization maps (Figs. 8.3 and 8.4), we have found several emergence events in which the appearance and disappearance of magnetic flux is clear. Among them we pay attention to

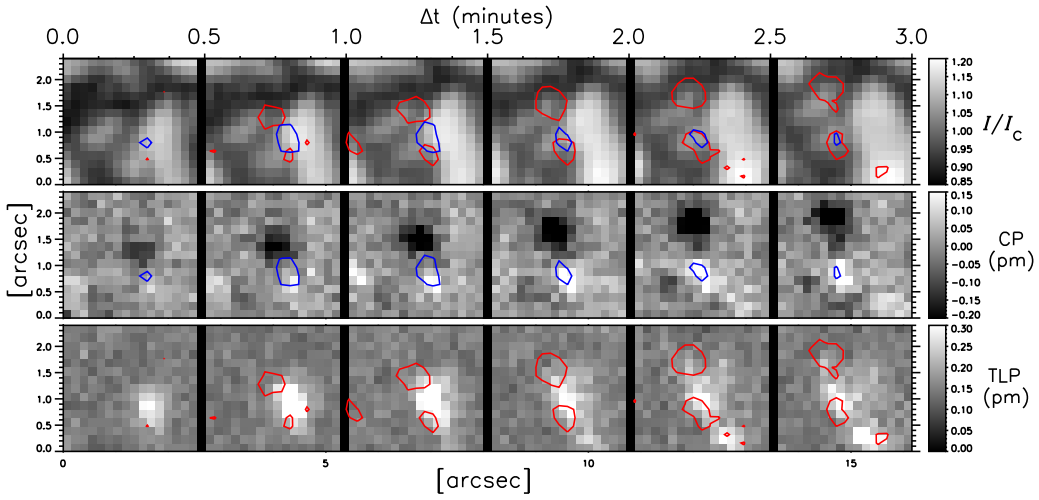

FIGURE 8.3:— Time evolution of the emergence of a magnetic loop observed on September 25, 2007. The cadence was ∼30 s and the maps covered a FOV of 2.″56 × 2.″4. *From top to bottom:* normalized continuum intensity, and circular (CP) and linear (TLP) polarization signals. The red/blue contours enclose areas with CP/TLP signals larger than 0.12 pm. $\Delta t = 0$ min corresponds to 15:15:33 UT.

1.– the emergence of small-scale magnetic loops

2.– and the emergence and disappearance of what seem to be a new form of small-scale magnetic flux phenomenon in the quiet Sun, in which unipolar magnetic flux patches appear above granular cells and with apparently vertical orientation.

Lets us show an example of each of the two types. Figure 8.3 shows the first of them, i.e., the emergence of a small magnetic loop. Displayed are the continuum intensity, and circular and linear polarization signals (from top to bottom, respectively). The Y-axis represents the image of the Sun through the slit, while the X-axis the scan direction and hence the time.

The emergence of magnetic loops in the photosphere is observed as horizontal fields above granules and foot-points of opposite polarity rooted in the adjacent intergranular lanes. In this example, the loop starts being visible from the beginning and rises with time (the linear polarization signal patch grows accordingly, blue contours). The foot-points of the loop, each of different polarity (red contours), appear at t=0.5 min and separate as the flux emerges (during the temporal range shown). The linear magnetic signal patch starts to became smaller 1.5 minutes later. This indicates that the apex of the loop continue

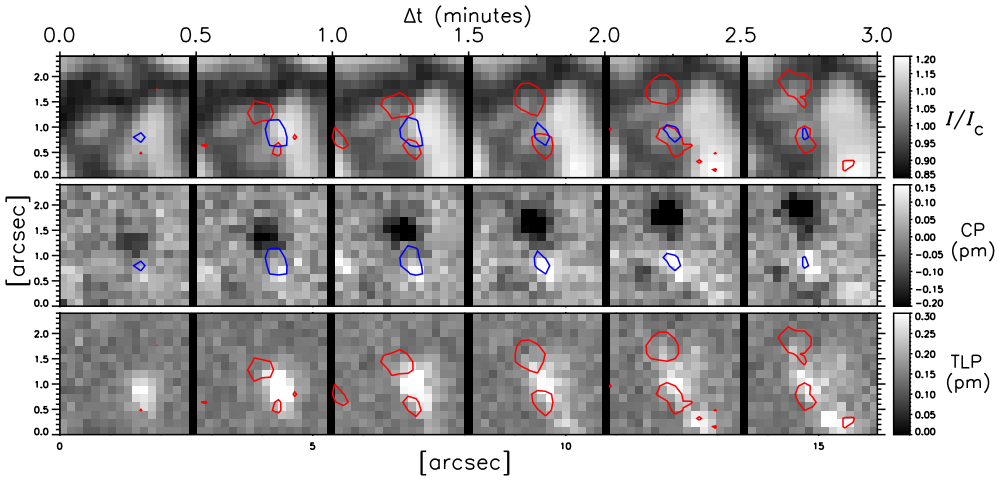

FIGURE 8.4:— Time evolution of the emergence of a magnetic loop observed on September 25, 2007. The cadence was ∼30 s and the maps covered a FOV of 2.″56 × 2.″4. *From top to bottom:* normalized continuum intensity, and circular (CP) and linear (TLP) polarization signals. The red/blue contours enclose areas with CP/TLP signals larger than 0.12 pm. $\Delta t = 0$ min corresponds to 15:15:33 UT.

rising, leaving the photospheric layers where the two Fe I lines are sensitive to magnetic perturbations.

This emergence event is nothing but the observational evidence of the rise of small magnetic loops from lower photospheric layers towards upper ones. This emergence loop is similar to those reported by Ishikawa et al. (2007) in plage regions and Centeno et al. (2007) in quiet Sun areas, using similar *Hinode*/SP time series. The frequency of appearance of these loops seems to be much higher than ever thought (Martínez González and Bellot Rubio, in preparation).

Figure 8.4 shows an example of the second type of emergence events listed. The observations clearly show circular polarization signals that appear above granular convection cells and disappears soon afterwards.

These photospheric magnetic events differ from the emergence of magnetic loops in that there is no linear polarization signal associated with the magnetic features. Contrary to the behavior exhibited by the magnetic loops, it is the circular polarization signal which appears above the granular cells. Therefore, they are different phenomenon. We identify these events as vertical and unipolar flux emergences above convective cells. The appearance of unipolar flux concentrations in the quiet Sun have been reported by de Pontieu (2002) and Lamb et al. (2007) at a much lower spatial resolution. It is thus very difficult to establish as association between their reported appearances and ours. To

our knowledge this is the first time that the appearance of vertical magnetic structures on granules has been observed. From now on, we will concentrate on the analysis of these vertical-field emergence events.

8.4 Statistical analysis of the emergence processes

We have detected a total of 9 emergence events on a surface area of 655 arcsec^2 in about 5 hours, and another 4 events on a surface area of 118 arcsec^2 in $\sim$2 hours (Table 8.1). It is not a large occurrence in comparison with the few tens emergence of small-scale magnetic loops that we have detected in the data. In this section we analyze several properties of these emergence events. We will pay special attention to five representative examples that will be named as events A, B, C, D and E.

To carry out a qualitative analysis of each of the events we have evaluated various emergence properties: the spatial position of the emergence along the slit; the initial and final time of the event as well as the total duration; the maximum size of the flux concentration in arcsec^2; the maximum spatially average unsigned longitudinal magnetic flux density; the maximum magnetic flux; and the maximum blue shifted zero-crossing velocity. In addition to these and for the selected representative examples we have evaluated several Stokes profile parameters to analyze their temporal evolution: the circular polarization signal, the total linear polarization signal, and the LOS velocity.

The LOS velocity was evaluated from the Stokes V zero-crossing wavelengths for pixels whose Stokes V amplitude signal exceeded 4 times the corresponding noise levels. The circular polarization (CP) maps have been calculated by integrating the blue lobe of the Fe I line at 630.25 nm, i.e.

$$\mathrm{CP} = \int_{\lambda'-\lambda_a}^{\lambda'-\lambda_b} \frac{V(\lambda)}{I_\mathrm{c}} d\lambda, \tag{8.1}$$

where λ' is the wavelength position where the blue peak of Stokes V reaches its maximum. λ_a and λ_b are the limits for the wavelength integration range, being $\lambda_b - \lambda_a = 23.6$ pm. In the same way, the total linear polarization signal (TLP) is computed as

$$\mathrm{TLP} = \int_{\lambda_0-\lambda_a}^{\lambda_0-\lambda_b} \frac{[Q^2(\lambda) + U^2(\lambda)]^{1/2}}{I_\mathrm{c}} \mathrm{d}\lambda, \tag{8.2}$$

where λ_0 is the central wavelength of the Fe I 630.25 nm line and λ_a and λ_b are wavelength integration limits with $\lambda_b - \lambda_a = 62.4$ pm. The integration ranges for the CP and the TLP have been selected as narrow as possible to minimize the contribution of noise. The CP and the TLP are measured in pm.

To calculate the longitudinal magnetic flux for each individual pixel we use the standard magnetograph formula (see, e.g. Landi degl'Innocenti 1992) based on the weak-field approximation

$$V(\lambda) = -\phi\, C \frac{dI(\lambda)}{d\lambda}, \tag{8.3}$$

where $\phi = fB\cos\gamma$ is the longitudinal magnetic flux density; $C = k\lambda_0^2\bar{g}$, the classical calibration constant used for magnetographs, $\bar{g}$ is the effective Landé factor, λ_0 the central wavelength of the line, and $k = 4.67 \times 10^{-13}$ [Å^{-1} G^{-1}]. ϕ is measured in units of Mx cm^{-2}.

To determine ϕ we need the Stokes I and V profiles. In particular we use all the wavelength samples along the spectral line. Therefore, Eq. (8.3) can be solved analitically using linear least-squares. Hence, the solution can be cast (Dominguez Cerdeña et al. 2003)

$$\phi = \frac{\sum_i V(\lambda_i)\left(\dfrac{dI(\lambda)}{d\lambda}\right)_i}{C\sum_i \left(\dfrac{dI(\lambda)}{d\lambda}\right)_i^2} \tag{8.4}$$

where $i = 1 \ldots n$ refers to the number of wavelength samples n. The derivative of Stokes I is evaluated numerically. The SP provides more wavelength samples than classical magnetographs. Using the whole line profile we reduce the effect of noise in the determination of the flux density.

The magnetic flux is measured in Mx, and is given by $\Phi = \phi \times A$, where $A \approx 116^2$ km^2 stands for the area sampled by a single pixel on the solar surface. The spatially average unsigned flux density is given by $\overline{\phi} = \sum_i |\phi_i|/N$, where N is the number of pixels, i. Finally, the total unsigned, flux is $\Phi_{\rm T} = NA\sum_i |\phi_i|$.

Table 8.2 summarizes the different properties for the emergence events. Unless otherwise indicated, the various quantities are calculated for pixels whose CP$>$ 0.15 pm, which is approximately 6 σ.

The size of the events varies from 1.6 to 6.72 arcsec^2, although it depends on the CP threshold used to define the extent of the flux concentration. They are smaller than the hosting convection cells. The average time in which the magnetic flux patch emerges and vanishes is about 13 min. The mean magnetic flux density is $\sim$30 Mx cm^{-2}, and the flux do not surpass the $1.5{\times}10^{18}$ Mx, with a mean flux of $\sim 5{\times}10^{17}$ Mx.

TABLE 8.2:— First column identifies each of the events. Next column shows the corresponding data set from table 8.1. The position of the emergence along the slit, the initial and final time of the emergence in UT, as well as the total duration, the maximum size of the emergence, the maximum average, unsigned longitudinal magnetic flux and unsigned flux densities, and the maximum blue shifted zero-crossing velocity, are shown on subsequent columns. The initial time are taken from the first slit scan of the snap showing CP larger than 0.15 pm.

EVENT (ID)	DATA SET	SLIT [pixel]	t_i	t_f	ΔT [m]	SIZE [$''^2$]	$\overline{\phi}$ [Mx/cm^2]	Φ_T [10^{17}Mx]	v_{LOS} [km/s]
1 (A)	1	280	11:09:23	11:33:04	23.7	6.72	52.9	13.1	2.7
2 (C)	1	127	15:00:59	15:09:38	8.4	5.12	39.7	5.7	4.0
3 (D1)	1	260	11:07:08	11:35:15	28.1	6.72	28.2	7.3	3.0
(D2)	1	266	11:13:35	11:30:55	17.3	2.88	29.5	5.0	$\sim$2.5
4[a]	1	122	11:11:25	11:24:25	13.0	4.16	23.5	3.4	$\sim$1.9
5	1	360	12:07:43	12:20:43	13.0	4.16	33.2	6.5	$\sim$3.5
6	1	85	13:14:51	13:25:41	10.8	3.52	26.5	4.4	2.1
7 (B)	2	82	00:56:01	01:09:00	13.0	5.12	27.6	4.7	2.1
8	2	195	03:21:04	03:27:34	6.5	2.56	27.0	3.6	1.5
9	2	251	01:09:00	01:22:00	13.0	4.16	31.5	4.1	2.4
10 (E1)	3[b]	148	08:53:37	09:08:32	14.9	4.48	34.0	7.6	2.4
11 (E2)	3[b]	144	08:48:50	08:56:00	7.2	1.60	24.7	1.9	3.4
12	3[b]	191	09:40:46	09:43:46	3.0	1.60	18.0	1.3	1.9
13	3[b]	189	09:43:46	09:51:31	7.8	6.08	26.8	7.9	2.7
MEAN	-	-	-	-	13.1	4.21	30.2	5.5	-

a:– The various physical quantities have been evaluated for pixels whose CP exceeds 0.08.
b:– Same as *a* but for pixels with CP$>$ 0.12.

For comparison, the emerging unipolar flux concentrations found by de Pontieu (2002), shows magnetic fluxes of about 5×10^{17} Mx and flux densities of $\sim$200 Mx cm^{-2}. The sizes of the emerging patches are about 1.5 arcsec^2, similar to those presented in Table 8.2. Note that it is difficult to perform an objective comparison of the fluxes since the instrumental sensitivities as well as the angular resolutions and the method of analysis are different.

The flux values shown in Table 8.2 are close to the average of $\sim 10^{16} - 10^{17}$ found in internetwork areas (e.g., Socas-Navarro and Sánchez Almeida 2002), and far from network flux values $\sim 10^{19}$ (e.g., Schrijver et al. 1997). The mean magnetic flux density of $\sim$30 Mx cm^{-2} is, approximately, equivalent to field strengths of 150-300 G, if we assume filling factors of 20-10% for typical internetwork field concentrations (see Chapter 7 of this thesis). In any case, we caution that these field strengths are merely rough estimates. To derive accurate values for the field strength showed by these kind of emergence processes an analysis based on inversion techniques is mandatory.

8.5 Qualitative analysis

The events marked with capital letters in Table 8.2 are studied in more detail in what follows. Figures 8.5 through 8.9 show the corresponding time sequences. Each of the figures is structured as follows: the first row shows the continuum intensity at 630 nm normalized to the averaged continuum intensity of the corresponding raster scans. Maps of the circular polarization signal (CP) and of the total linear polarization signal (TLP) are displayed in the second and third rows, respectively. The fourth row shows Ca II filtergrams, and the last row depicts LOS velocities evaluated from the Stokes V zero-crossing wavelengths. In addition, Mg I magnetograms are shown in the sixth row only for event E. As in Fig. 8.3, the Y-axis represents the image of the Sun through the slit, while the X-axis the scan direction and time.

To track magnetic flux emergences we have overplotted contour lines enclosing areas where the circular and linear polarization signal are larger than 0.15 pm (red and blue respectively). In case of event E the contours were taken at 0.12 pm. White areas in the velocity maps represent pixels with polarization signals smaller than 0.4 I_c.

We note that the cadence of the Ca II H filtergrams and Mg I magnetograms is larger than that for the SP maps. Therefore only a few of them are represented. In particular, we display those whose observation time is closer to that corresponding to the central slit position for each map. Hence, only half of the total number of maps is available. The maps not shown have been visually inspected to look for transient brightenings (Ca II H) and polarization signals (Mg b I), though. Also, to increase the S/N, the chromospheric filtergrams have been spatially rebined to match the SP pixel size of $0\farcs16$.

8.5.1 Event A

For this event (Fig. 8.5) the circular polarization maps show a unipolar flux concentration (white patch) barely visible at $\Delta t = 0$ min. It grows both in size and in strength, reaching the maximum size and circular polarization signals 8 min later. At that point, the flux concentration looks roundish and occupies an area of $\sim 4 \times 4$ pixels (some 200 000 km^2; red contours), which corresponds approximately to one third of the granular cell surface. The granule is defined to be the region where the continuum intensity is at least 1.05 times brighter than the average quiet Sun. At $\Delta t = 16$ min the signal starts to fade away. At $\Delta t = 24$ min (not shown), the circular polarization signal has vanished completely. No clear negative polarity signal are detected in the area of interest during the whole sequence. The continuum intensity maps demonstrate that

the magnetic flux appears in an existing granule and persists there for 20 min while the granule evolves. Interestingly, the flux concentration does not seem to be disturbed by the granular flows: it remains co-spatial with the brightest part of the granule until $\Delta t = 16$ min and never gets advected to the adjacent intergranular lanes.

There is no detectable linear polarization signal associated with this event. Only the last two maps show traces of linear polarization when the circular polarization signal is almost absent. The observed linear polarization patch lies close to the flux concentration (less than $1''$ up and right), but we believe it is not related to its disappearance.

The emergence is characterized by blueshifted velocities already from the initial stages. At $\Delta t = 10$ min we observe the stronger upflows of about -2.5 km s^{-1}. We do not detect any Ca II H brightness enhancement strictly associated to the emergence event. The brightenings apparent at $\Delta t = 2$ and 20 min seem to be too far from the magnetic feature.

The LOS velocity (last row in figure) has been evaluated from the zero-crossing wavelengths of the Stokes V profiles whose amplitude values exceed 4 times the noise levels. Pixels which do not fulfill this criterion are represented in white. From $\Delta t = 10$ to 22 min a greenish patch can be seen in the velocity panel which closely resemble the shape of the granular cell. A careful look at the data reveals that the area occupied by the granule shows rather noisy Stokes V signals that slightly surpass the selected thresholds. This magnetic signal may represent a background magnetic field component. Given the weaknesses of the signals we cannot determine the orientation of the field.

8.5.2 Event B

This second event (Fig. 8.6) differs slightly from the previous one. It appears at $\Delta t = 2$ min and has a shorter duration. The maximum spatial size of the magnetic patch is similar to that of event A. However, it occupies about half of the granule at $\Delta t = 6$ min, and almost the whole granule 4 min later. The circular polarization signal is maximum at $\Delta t = 14$ min. As before, there is no evidence for horizontal magnetic fields since no linear polarization is detected.

The emerging flux interacts differently with the plasma: as shown by the continuum intensity maps, the granule starts to diminish in size at $\Delta t = 10$ min, disappearing completely four minutes later, while the flux concentration still persists. Thus, our observation suggests that the magnetic field somehow contributed to the granular disruption. Throughout the sequence, the flux concentration appears to be decoupled from the advection flow (e.g., it moves towards the center of the granule between $\Delta t = 6$ min and $\Delta t = 10$ min).

Similarly to the first case, blueshifts are observed right from the beginning of the process. From $\Delta t = 16$ min on, weak downflows are detected instead, corresponding to the granule disappearance. The largest upflows of $-2.2\ \mathrm{km\,s^{-1}}$ are comparable with those of event A. The Ca II H filtergrams show no significant brightenings associated with the process.

8.5.3 Event C

In Fig. 8.7 we show the third emergence process. In this case the magnetic feature becomes visible at $\Delta t = 2$ min and disappears at $\Delta t = 10$ min. In contrast with events A and B, the magnetic patch elongates at $\Delta t = 6$ min, just after it reaches its maximum spatial size. Two minutes later the magnetic patch become much smaller. From $\Delta t = 10$ to 12 min the existing magnetic signals above the granule is not very well spatially correlated with their precursors. In this event the granule in which the flux emerges, modifies its shape with time. There is no evidence of interaction between the granule and the magnetic patch.

The circular polarization signal is maximum at $\Delta t = 4$ min. Notice that there is no detectable linear polarization signals until $\Delta t = 10$ min. The signal pertains to a small magnetic loop which appear near the circular polarization signal patch and in the same granular cell. The linear polarization patch lies above a granule and it is slightly elongated. At the opposing edges of the magnetic patch there exist opposite polarity magnetic features corresponding to the foot-points of the magnetic loop. They are rooted at intergranular lanes (cf. Fig. 8.3).

This emergence event shows the strongest blueshift at $\Delta t = 4$ min, reaching $-4\ \mathrm{km\,s^{-1}}$, and it is the shortest in time. In the rest of the frames weak upflows are detected. Again, there is no significant brightenings in the Ca II H line associated with the process.

8.5.4 Event D

This emergence event (Fig. 8.8) is the longest in duration we have found in the three temporal sequences. It differs from the others in that two magnetic features of opposite polarity appear at different times in the same granule. They are identify as events D1 and D2 in Table 8.2. There is no evidence of connection between the two magnetic patches, although the fact that they have appeared in the same granular cell showing opposing polarities suggest that the may be correlated.

The magnetic patch of positive polarity (*white*) become visible in the circular polarization map at $\Delta t = 0$ min. It changes its spatial size with increasing

time, reaching the maximum size and circular polarization at $\Delta t = 8$ min. At this point a second patch, smaller in size and of opposite polarity, emerges within the same granule at a distance of $1''$. Then the white patch starts to fade progressively from $\Delta t = 8$ to 24 min. At $\Delta t = 26$ min it disappears completely. The black patch preserves its size and polarization signal value. At $\Delta t = 16$ min it starts to fade as well and disappears 4 min earlier that the white one. The distance between both magnetic patches does not change. At $\Delta t = 6$ min the size of the magnetic patches occupy a small fraction of the hosting granule. The granule evolves and changes it shape during the process. At $\Delta t = 12$ it clearly separates in two, dividing the two magnetic signals. Between $\Delta t = 16$ and 20 min seems to be distorted, maybe due to the action of the harbored magnetic features, and finally disappears at $\Delta t = 22$. As shown by the continuum intensity, the white magnetic patch seems to appear at the granular edge, $\Delta t = 0$ min, and move towards the granular center with time. Finally, notice that the white patch ended in an intergralular lane at $\Delta t = 24$.

There exist some linear polarization signals from $\Delta t = 0$ to 14 min. It is not localized between the opposite polarity patches. At $\Delta t = 4$ and 12 min we find the largest linear polarization patches. They coincide with the emergence of positive polarity (white). The white circular polarization patch seems not to change with the appearance of the linear polarization signals. It may indicate a bending on the flux tubes at that times.

The emergence event shows the strongest blueshift at $\Delta t = 4$ min, reaching -3 km s^{-1}. Given the strong asymmetries of the Stokes profiles in this case (see Sec. 8.6) the velocities are less reliable. We do not know what happens in the early stages of the emergence due to a lack of data. Finally, the Ca II H line shows no significant brightenings associated with the emerging flux.

8.5.5 Event E

Figures 8.9 and 8.10 show the time evolution of an emergence event (E1) with a cadence of ∼30 s. It occurs close to an existing strong magnetic signal, located in an intergranular lane. The faster cadence achieved by these observations allows us to carry out a deeper analysis of the emergence process although at the expense of lower signal-to-noise ratios. The process starts above a granular cell at $\Delta t = 5$ min where the circular polarization signal is larger than 0.12 pm (red contours). From $\Delta t = 0$ to 4.5 min, there is diffuse circular polarization over the granule (In order not to misidentify the emergence with the adjacent magnetic patches the position of the starting point of the emergence as well as the point where it emerges at $\Delta t = 5$ min are indicated with green arrows in the circular polarization signal maps) 12.5 min later, the magnetic signal

is weakened and starts to diminish. From $\Delta t = 13.5$ to 14.5 min the granule center shows sparse polarization signal until it fades below the noise level.

No opposite-polarity signals are associated with the emerging flux during the whole sequence. From $\Delta t = 4$ to 6 min we find a non-negligible amount of linear polarization signal (blue contours). It appears at the edge of the granular cell, relatively close to the emerging flux patch, but not related to it. The circular polarization signal occupies a significant area of the granular cell surface and appears at its very center. The granular cell evolves normally with time, without being distorted by the magnetic flux.

In line with the previous cases, the emerging flux shows blueshifted velocities already from the initial stages, reaching a maximum (~ -2.4 km s^{-1}) at $t =$ 8 min. With a cadence of ∼30 s, the photospheric 5-min oscillations are clearly seen in the velocity maps.

In the same time sequence we detect another magnetic flux emergence (E2). It is smaller in spatial size than the previous one, persisting for a shorter time. The emerging flux is observed for the first time at $\Delta t = 1$ min (see yellow arrow) and disappears at $\Delta t = 7$ min. There is no relationship between events E1 and E2.

8.5.6 Relation with the chromosphere

Data set #3 (see Table 8.1) differs from the other two: first, it has higher cadence; secondly, the chromosphere can be better examined because Mg I magnetograms are available, besides the Ca II H filter images. Therefore, we can look for any chromospheric change that may be related to the emergence events E1 and E2.

As for the other four events, no chromospheric brightening is detected in the Ca II H filtergrams. This indicates that there is no energy transfer from the photosphere to higher layers. But which is more surprisingly is that no magnetic signal is visible in the Mg I magnetograms. The qualitative analysis of the emergence indicates that the field lines are vertically oriented and above granules. Therefore, the absence of signal in the Mg I magnetograms indicates that there is no connection between this emergence event and the chromosphere. As a result, the field lines that emerge vertically through the granule have to bend at some point. The last entails a change on the polarity of the field lines.

In contrast to these emergence events, the rise of magnetic loops from low photospheric layers to higher ones is clearly visible in the Mg I magnetograms. In particular, some time after the emergence of the loop, the two foot-points of the loop, which have opposite magnetic signals, are seen as two magnetic patches on the chromospheric magnetograms that separate with increasing time

(Martínez González et al. in preparation). This finding indicates that the loop reaches the chromosphere. However, we do not find any evidence that the vertical magnetic flux emerging in granules reaches the chromosphere. This limits these kind of events to be *essentially photospheric*.

In summary, all five events show the same behavior: a magnetic flux concentration that *appears* just at the center of a granule and some minutes later vanishes, interacting or not with the plasma flow. All of the examples examined do not show linear polarization signals at the locations of the emergence, which points in a very preliminary way to a vertical configuration of the field lines.

8.6 Observed properties from the Stokes I and V profiles

In this section we perform an inspection of the Stokes profiles in order to provide constraints to the physical mechanism behind the emergence of vertical magnetic flux through convective cells. As we have shown, there is no linear polarization signals associated with these events. Hence, we focus on the Stokes I and V profiles pertaining to each of the emergence processes, paying special attention to their shapes and any intrinsic peculiarity. We also analyze the temporal evolution of the emergence process by means of changes in the Stokes I and V shapes.

8.6.1 Profile shapes and spatial distribution

The visual inspection of the Stokes V profiles associated with each of the emergences subjected to analysis reveals distinctive properties that lead us to classify them in four classes. They are far from *normal*. By *normal* we mean profiles showing two lobes of opposite sign, an asymmetric shape, and a well defined zero-crossing point. In Fig 8.11 we show four example profiles, each of one representing each of the classes, from I to IV. The various profiles have been taken from event A at $\Delta t = 10$ min and are of positive polarity as the emerging flux. Similar Stokes profiles are found in all the events analyzed in this Chapter. Profiles of negative polarity are also found, in e.g., events E1 and E2.

Class I profiles are characterized by their asymmetric shape. These profiles can be found all around the emerging magnetic patch although they are more frequent at the the center. They have positive area and amplitude asymmetries ($\delta A > 0$, $\delta a > 0$), independently of the polarity of the flux. Class II stands for one-lobed profiles, i.e., profiles whose asymmetry is strong enough to suppress one of the two lobes of normal Stokes V profiles. Profiles belonging to this

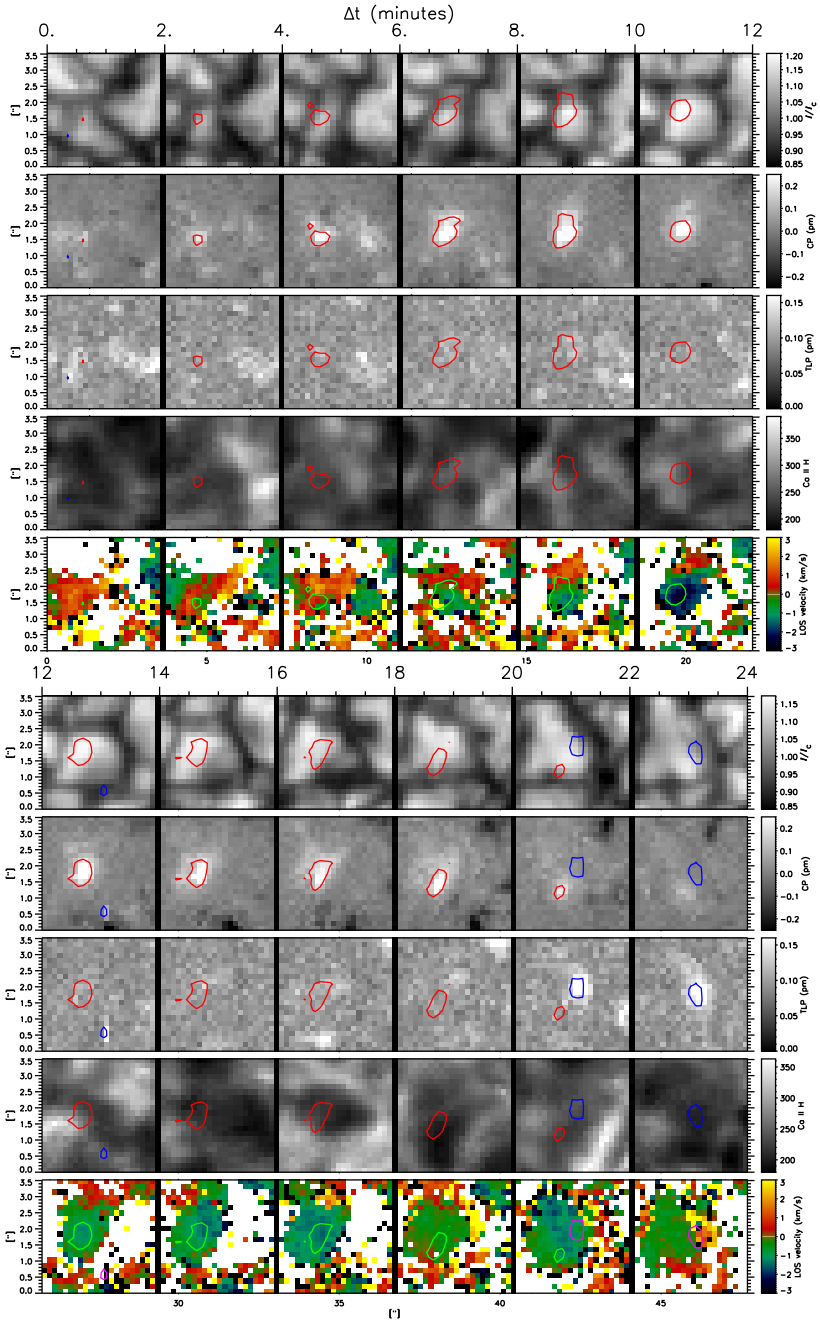

FIGURE 8.5:— Temporal evolution of a flux emergence process (event A) observed on February 11, 2007. The cadence is 123 s and the maps cover a FOV of $3\farcs5 \times 3\farcs5$. *From top to bottom:* normalized continuum intensity, circular and total linear polarization signals, Ca II H line core intensity, and LOS velocity evaluated from the Stokes V zero-crossing wavelengths. Negative velocities indicate blueshifts. The red contours enclose areas with CP signals larger than 0.15 pm. Blue contours enclose areas with TLP larger than 0.15 pm. White areas represent pixels not included in the analysis. $\Delta t = 0$ min corresponds to 11:09:23 UT.

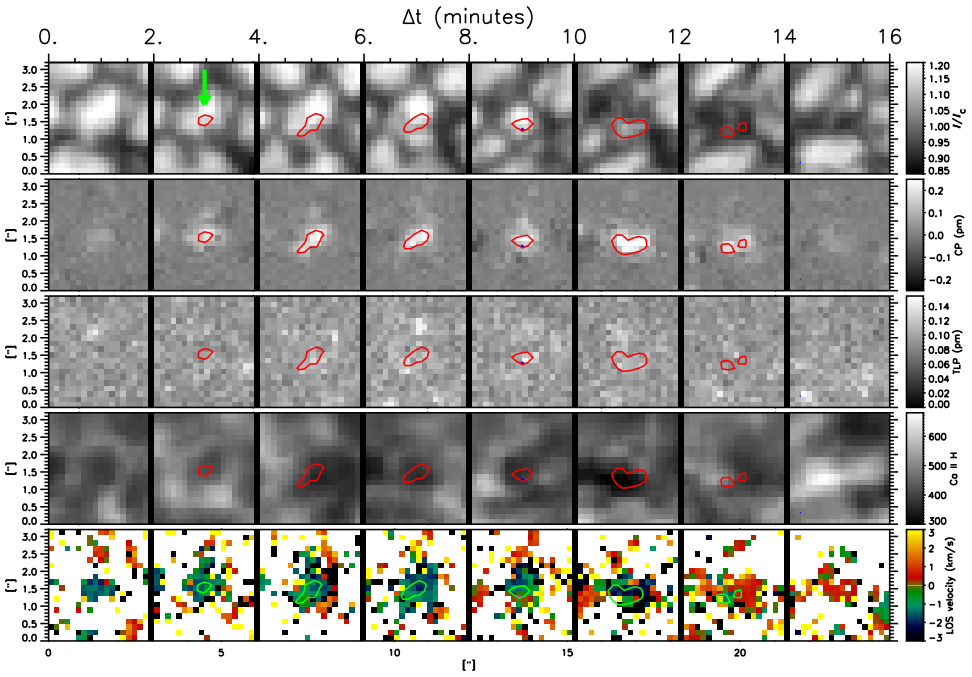

FIGURE 8.6:— Emergence process (event B) observed on March 10, 2007. The panels show the same quantities as those of Fig. 8.5. Green arrows indicate the starting position of the emergence. $\Delta t = 0$ corresponds to 00:54 UT.

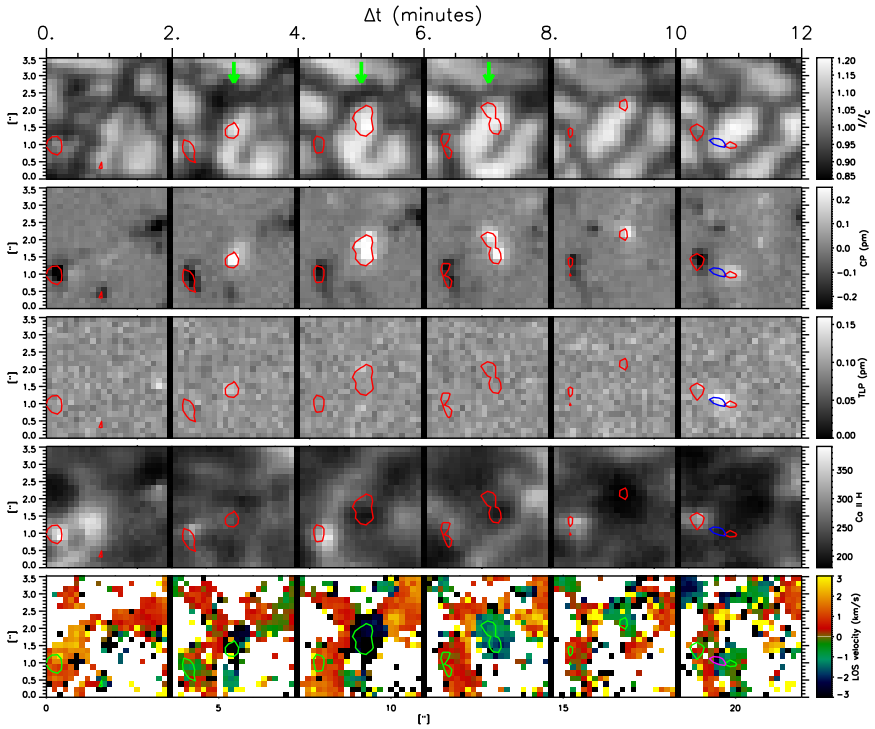

FIGURE 8.7:— Emergence process (event C) observed on February 11, 2007. The panels show the same quantities as those of Fig. 8.5. $\Delta t = 0$ corresponds to 14:58 UT. Green arrows indicate the position of the emergence event in order not to mislead it with the neighboring magnetic signals.

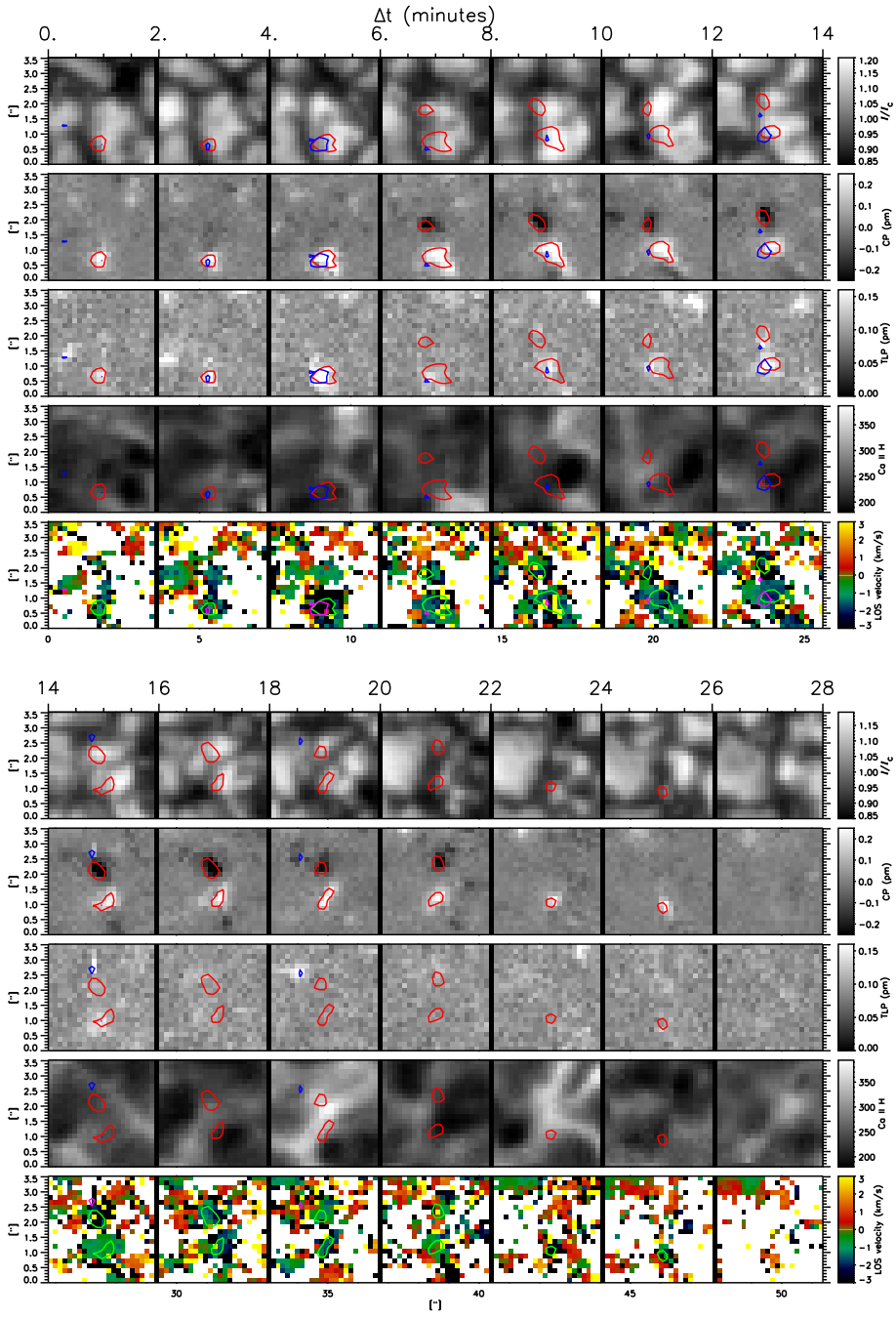

FIGURE 8.8:— Emergence process (event D) observed on February 11, 2007. The panels show the same quantities as those of Fig. 8.5. $\Delta t = 0$ corresponds to 11:07 UT. In this particular case we have an emergence process with opposite polarities. It is also noticeable the linear polarization signal appearing at $\Delta t = 4$ min.

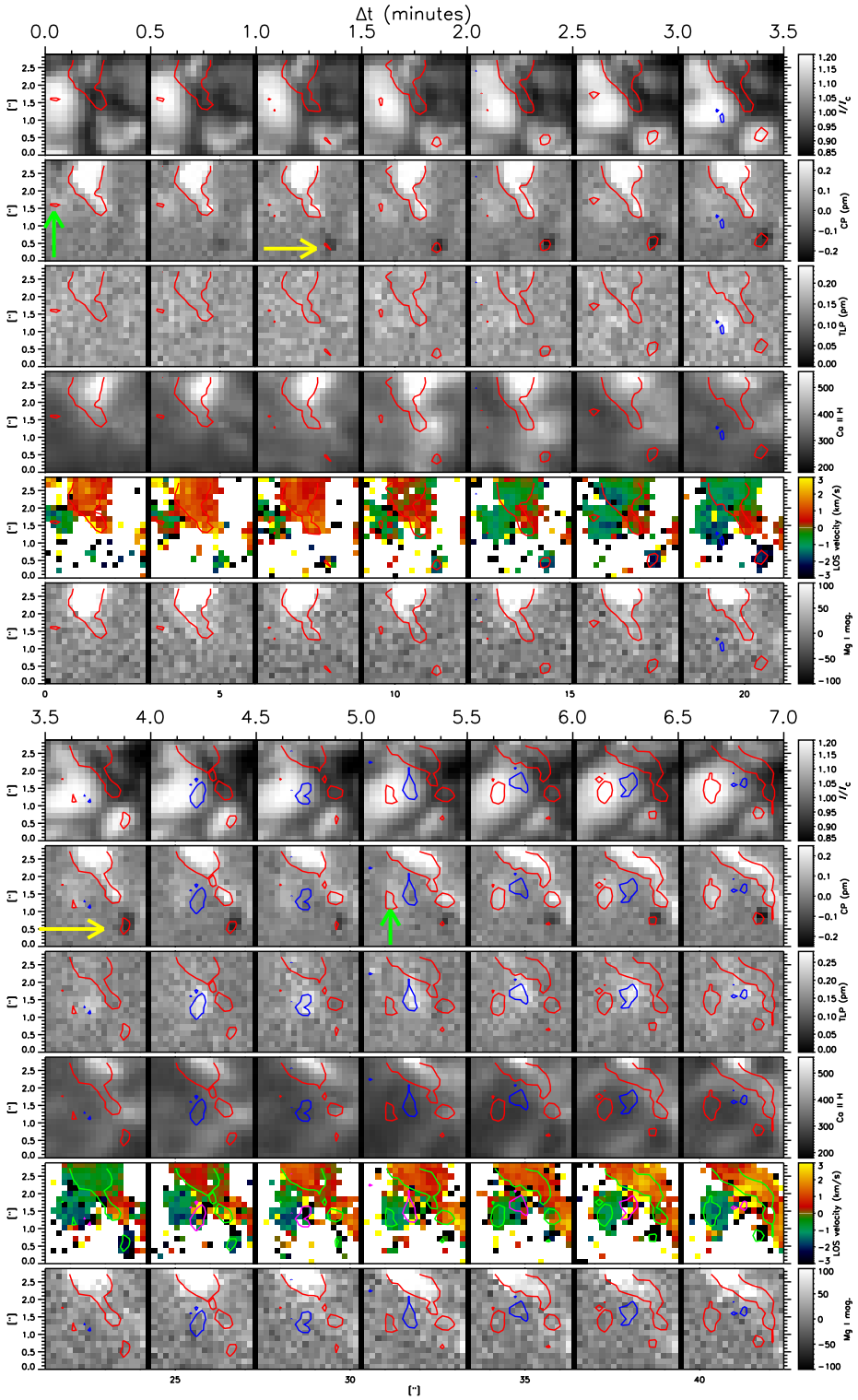

FIGURE 8.9:— Emergence process (event E) observed on October 6, 2007. This plot represents the first half of the event. The cadence of the SP maps is 34 s and cover a FOV of $4\farcs0 \times 2\farcs88$. The five first rows show the same quantities as Fig. 8.5. The last row shows a magnetogram taken in the Mg I 517.2 nm line. $\Delta t = 0$ corresponds to 8:47:38 UT.

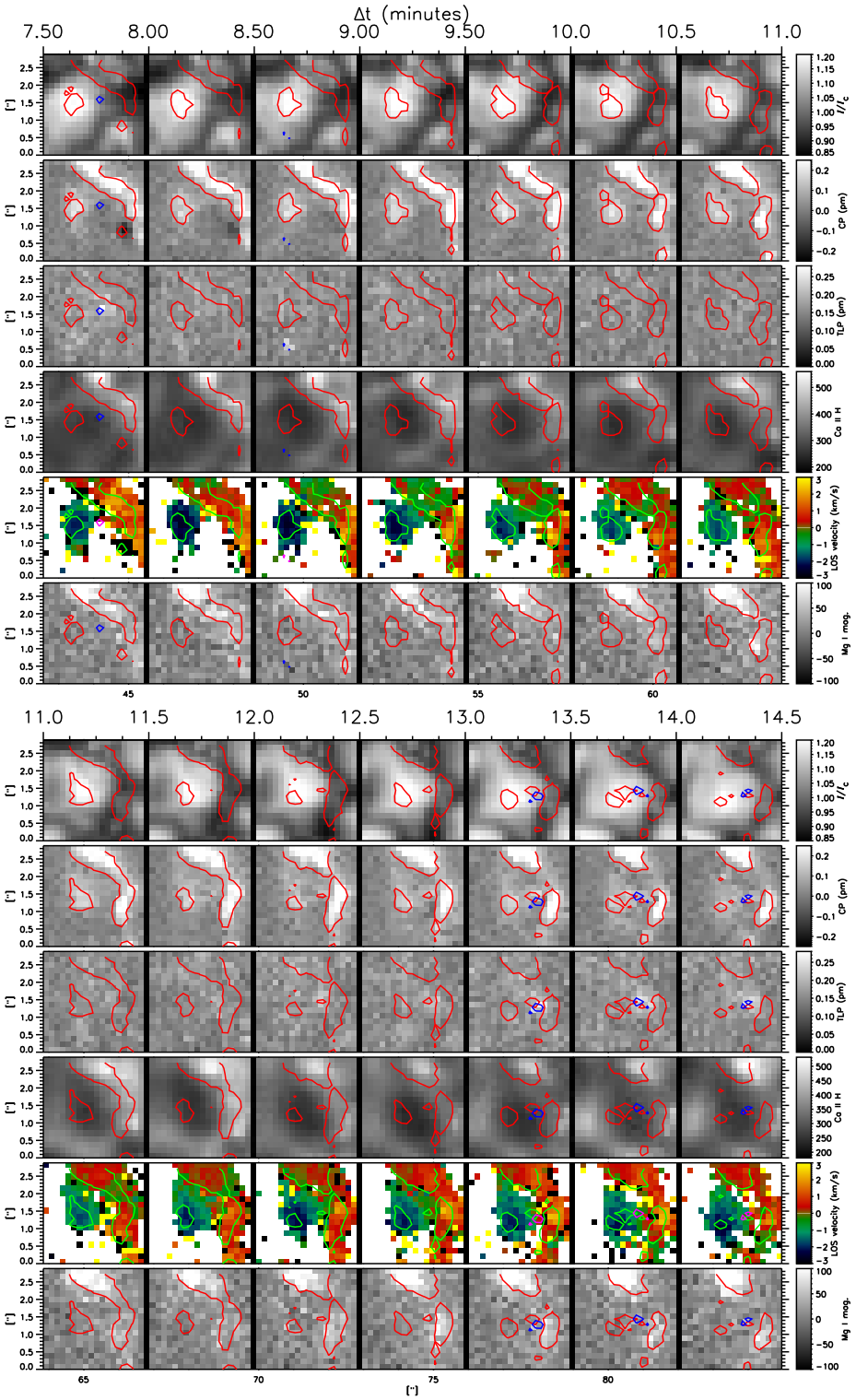

FIGURE 8.10:— Continuation of the emergence process (event E) of Fig. 8.9

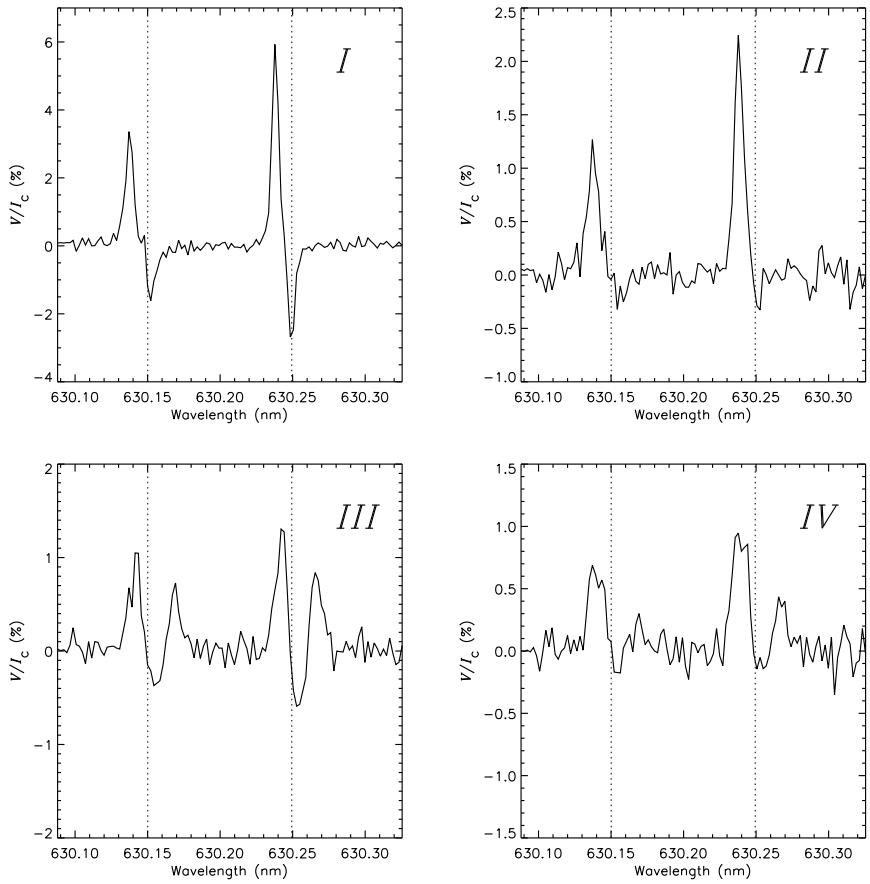

FIGURE 8.11:— Different classes of Stokes V profiles, from classes I to IV, that are found in the emergence event A. They exemplify the kind of profiles that are associated to these events. The vertical dashed lines represent the reference wavelengths of the 630.15 and 630.25 nm spectral lines.

class show δA and δa close to one. Classes I and II profiles are found in all emergence events presented in Sect. 8.4.

Class III contains V profiles showing three lobes, e.g., two positive and one negative (bottom left panel). Class IV comprises profiles with two lobes of the same sign. These two classes of profiles are less frequent and occur in the vicinity of the emerging patch, closer to the granular edges. Classes II and IV may be understood as extreme cases of classes I and III, in which, profiles have lost one of their lobes.

These unusual shapes provide additional information about the vertical

stratification of the atmospheric parameters, although their analysis and interpretation is arduous. They cannot be the result of atmospheric seeing (spaceborne observations) or instrumental effects (e.g., telescope diffraction which mixes the signal from pixels to each other). The strong asymmetries of classes I and II require large gradients of atmospheric parameters, at least on the velocity (Illing et al. 1975; Auer & Heasley 1978). These gradients should be more prominent for class II profiles. Several mechanisms may cause such strong gradients. For instance, they can be originated by canopy or magnetopause-like environments, i.e, at least two different media are present along the line of sight, each of them showing different magnetic and/or dynamic properties (e.g., a magnetic atmosphere and a field-free one). Such a configuration introduces strong discontinuities along the LOS, hence producing asymmetries on the Stokes profiles.

Class I and II profiles have been detected earlier in ground based observations of quiet solar regions at $1''$ (e.g., Sigwarth et al. 1999). Attempts to find the physical mechanisms responsible for such strong asymmetries have been made by Grossmann-Doerth et al. (2000) and Ploner et al. (2001).

The superposition of two Stokes V profiles, with positive area asymmetry and of opposite polarity, emerging from two distinct atmospheres within the same pixel may explain classes III and IV. In Fig 8.11 we have indicated the central wavelength of each spectral line with vertical, dotted lines. Notice that, for classes III and IV, there seems to be a strong, red-shifted component of opposite polarity. The very existence of classes III and IV indicates that magnetic fields of opposite polarity coexist within the same pixel. These kind of profiles can be also generated with particular magnetic field configurations (Steiner 2000). In particular, they can be generated by a single magnetic component which orientation and velocity changes dramatically with height. We will discuss a number of possible physical scenarios behind these profiles in Sect. 8.7.

To provide a clearer view of how the Stokes V profiles are spatially distributed in Fig. 8.12 we display a set of 5×5 ($0\farcs8 \times 0\farcs8$) profiles corresponding to event B at $\Delta t = 10$ min. The central profile corresponds to the spatial location where the magnetic flux is maximum. Note that it does not coincide with the position of maximum continuum intensity. Each profile represents a single $0\farcs16 \times 0\farcs16$ pixel.

As previously mentioned, profile classes I and II are seen at the center and at the edges of the granule, whereas profile classes III and IV occur only at the edges. The amplitude of the Stokes V profiles is larger at the center and diminishes as the edges are approached. Hence, the circular polarization signals concentrates close to the center of the granular cell. We have found

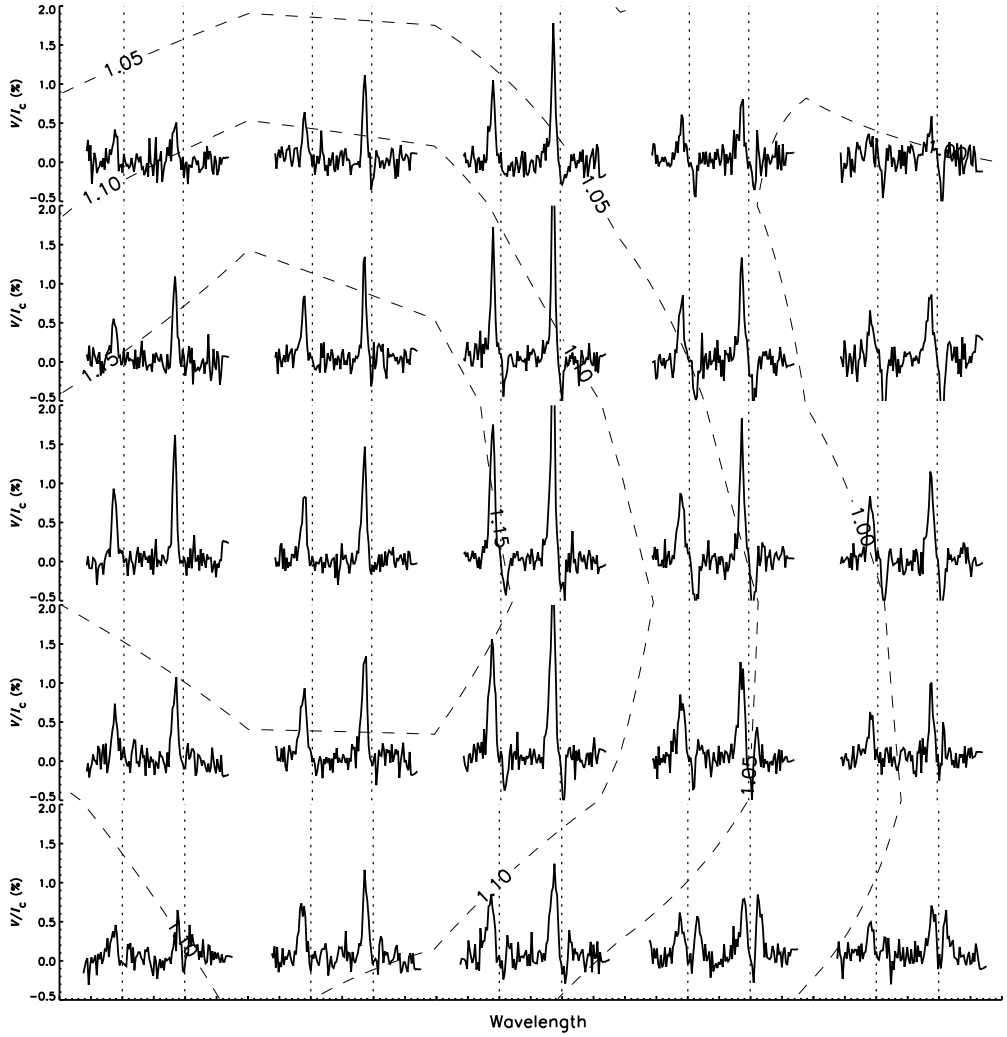

FIGURE 8.12:— Set of Stokes V profiles of Fe I 630.15 and 630.25 nm lines observed at the center of the flux concentration of event B at $\Delta t = 10$ min. The central profile corresponds to the pixel showing the largest circular polarization signal. Dotted, vertical lines represents the central wavelengths of the two lines. Overplotted are the contour lines of the continuum intensity (dashed lines). The four classes of profiles described on the text are clearly distinguishable (cf. Fig. 8.11).

that about 20% of the Stokes V profiles are of classes III and IV, for event D. The percentage is smaller for events A, C and D. We did not find such profiles

in emergence event E.

It is interesting to note how the Stokes V profiles change from class I to III as we move diagonally from the center of the emergence patch toward the bottom, right-most profile. Suppose that these three-lobed profiles originate from two distinct magnetic atmospheres, each harboring magnetic fields of opposite polarity. One possible physical scenario that may favor the formation of class III profiles at the edge of the granule can be the following: as the observations reveal, the profiles at the center of the emerging magnetic patch exhibit clear polarities. Also, there is a clear absence of linear polarization signals. This indicates that the field at the center of the magnetic patch is vertically oriented. If, the field lines become more horizontal as one moves toward the granule edge and, moreover, some of these field lines change their orientation, i.e., the field become of opposite polarity. This introduces a strong discontinuity in the inclination of the field lines along the line of sight. This discontinuities are capable of producing such anomalous Stokes V profiles (cf. crossover effect in sunspots, e.g., Grigorjev and Katz 1972).

To confirm this physical scenario it would be necessary to find linear polarization signals on the various pixels. However, this is not the case. There is a total absence of linear polarization signals. Therefore, inversions are of fundamental importance to obtain information about the inclination of the field lines from Stokes I and V.

8.6.2 Dynamic and magnetic properties

Figure 8.13 displays the temporal evolution of the Stokes I and V profiles for emergence events A and B. As we clearly see, the changes in the profile shapes provide indications for the rising of magnetic flux from lower photospheric layers.

We start with the Stokes profiles corresponding to event A (Fig 8.13, top panels). The profiles have been taken from the center of the magnetic flux concentration, where the magnetic flux is maximum. We represent only Stokes profiles corresponding to $\Delta t = 8$, 10 and 12 minutes (solid, dotted, and dashed lines, respectively). Both Stokes I and V exhibit strong asymmetries at $\Delta t = 8$ min. Notice that the blue wing of Stokes I is significantly blueshifted while the line core remains almost at rest. This suggest the existence of strong upflows in deep atmospheric layers and smaller velocities higher up. The signature of large gradients of atmospheric parameters is even more conspicuous in Stokes V: since the pioneering work by Illing et al. (1975) and Auer & Heasley (1978) it is known that the circular polarization profiles are symmetric unless a velocity gradient is present along the LOS. The asymmetry of Stokes V is extreme in

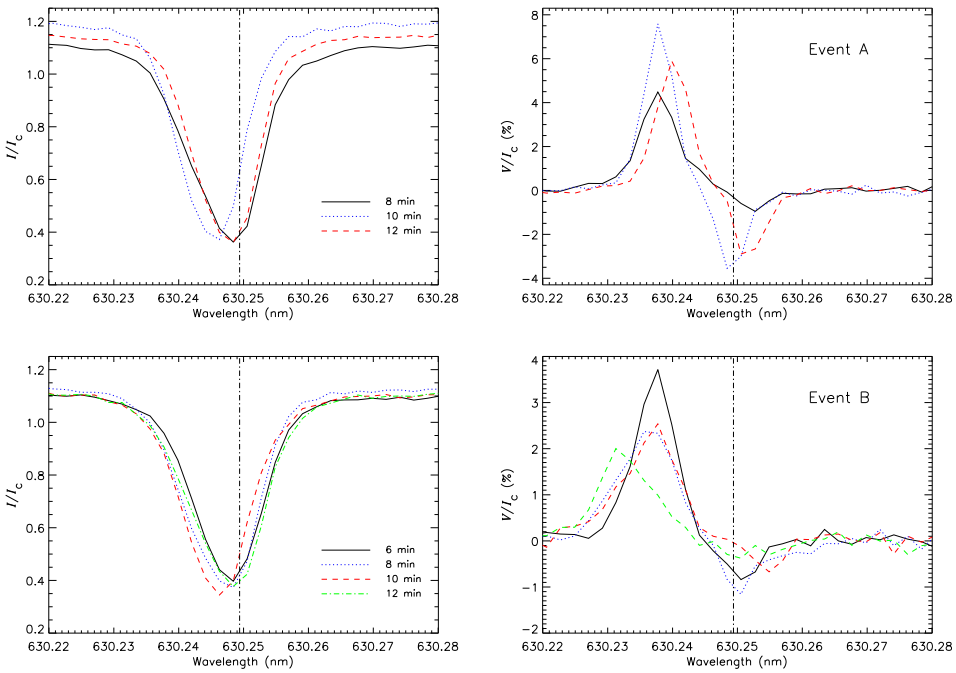

FIGURE 8.13:— Stokes I (*left*) and V (*right*) profiles of Fe I 630.25 nm observed at the center of the flux concentration A (*top*), B (*middle*) and E(*bottom panels*). Different line shapes stand for different times through the time evolution of the emergence. The vertical lines mark the zero point of the velocity scale.

this case, with the red lobe being almost absent. It belongs to class II of Stokes V profiles. Such a degree of asymmetry can only be produced by large velocity *and* magnetic field gradients. At $\Delta t = 10$ min, the whole line is affected by a strong blueshift, but the velocity gradient seems to have decreased significantly since the profiles look more symmetric. At $\Delta t = 12$ min, the gradients are still small and the global velocity shift is reduced. Altogether, this qualitative interpretation of the Stokes I and V profiles suggests that we are witnessing the rise of magnetic fields through the granule, from the bottom of the photosphere to higher layers. Apparently, the field is vertical because we do not detect linear polarization signals.

The time evolution of the Stokes I and V profiles pertaining to event B (bottom panels from Fig. 8.13) follows the same tendencies. In this case, the changes in the profile shapes are smaller, showing weaker blueshifts and polarization signals. However, the asymmetries are more pronounced, indicating stronger gradients of the physical quantities. As for event A, the Stokes I pro-

file stays almost at rest $\Delta t = 6$, and two minutes later the blue wing is slightly blueshifted due to plasma upflows. The flux reaches higher layers at $\Delta t = 10$ min (red, dashed lines). After the plasma has risen Stokes I recovers its initial shape. Stokes V follows the same behavior, although the strong asymmetries make it difficult to compare the profiles. Finally, we do not find any conspicuous property in the profile shapes providing hints as to why the magnetic flux contributes to the disappearance of the granule in the case of event B.

The analysis of the Stokes V profiles of emergence events C and D, led to the same conclusion. However, event E shown a different behavior. Fig. 8.14 shows a set of Stokes I and V profiles corresponding to emergence event E from $\Delta t = 6.5$ to 10 min (solid and dashed lines, respectively). Dotted profiles represent intermediate profiles. We have taken this time range because there is a strong blue shift in the zero crossing velocity as can be seen in Figs. 8.9 and 8.10. The largest blue shift corresponds to $\Delta t = 8$ min. (blue profile). The Stokes V profiles are less asymmetric in this case. There are not clear evidences on the Stokes I or V profile shapes pointing towards the rise of material from lower photospheric layers upwards, regardless the higher temporal cadence. Only to remark that, although the amplitude values of the Stokes V profiles does not vary with time (within the time period ranged by the displayed profiles), the wavelength location of the blue lobe amplitude maximum is blue-shifted while that for the red lobe is not. Also the zero-crossing wavelengths seem to be bluer than that from the minimum of the Stokes I.

Consequently, event E does not show the same physical properties of the other events. This may indicate that event E is a different physical phenomenon. This may also explain why the origin and end of this emergence is not clear. However, it is important to remark that the observations suggest a magnetic field configuration in which the lines are oriented vertically above the granular cell. So there might be different mechanisms able to produce circular polarization signals above granular cells.

8.7 Disscusion

There are clear evidences of magnetic flux rising at the center of the granular cells and with vertical orientation. Both Stokes I and V profiles for four out of five of the events analyzed exhibit strong asymmetries at different times. The significant blueshift of the Stokes I profiles while the line cores remain at rest, suggest strong upflows in deep atmospheric layers and smaller velocities higher up. The signature of large gradients of atmospheric parameters is even more conspicuous in Stokes V. The asymmetry of Stokes V can be extreme, with the

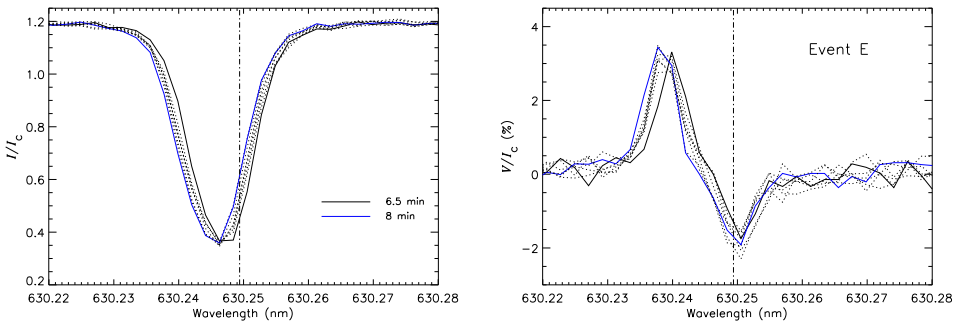

FIGURE 8.14:— Stokes I (*left*) and V (*right*) profiles of Fe I 630.25 nm observed at the center of the flux concentration E. Different line shapes stand for different times through the time evolution of the emergence. The vertical lines mark the zero point of the velocity scale.

red lobe being almost absent. Such a degree of asymmetry can only be produced by large velocity *and* magnetic field gradients. Later on, the whole Stokes profiles are affected by strong blueshifts and the profiles look more symmetric, indicating that the velocity gradients have decreased significantly. At the end, the gradients are small and the global velocity shift is reduced. Altogether, the qualitative interpretation of the Stokes I and V profiles of event A and B suggests that we are witnessing the rise of magnetic fields through the granule, from the bottom of the photosphere to higher layers. Apparently, the field is vertical because we do not detect linear polarization signals.

To the best of our knowledge, this form of small-scale magnetic flux emergence has not been described in the literature. It differs significantly from the emergence processes in granular convection studied by Centeno et al. (2007) and Ishikawa et al. (2007), since we do not detect linear polarization signals or opposite-polarity foot points surrounding them. Clearly, the geometry of the fields is not that of small magnetic loops. Lamb et al. (2007) have described examples of the emergence of unipolar flux, but at a poorer resolution of $1\farcs2$. No association of the flux with granules or intergranules was made in their paper. They suggested that the origin of the unipolar flux appearance is coalescence of pre-existing field lines with the same polarity, which were below the detection limit imposed by the intrinsic noise and the spatial resolution of their observations. While it is not possible for us to rule out the scenario of field-line coalescence, we do not find evidence for diffuse magnetic fields in the emergence sites prior to the events, at the much higher spatial resolution and sensitivity of *Hinode*.

Current magnetoconvection simulations do not seem to explain our obser-

vations either. The simulations of Vögler et al. (2005) do show magnetic fields in granules, but they are much weaker than those reported here, and do not undergo emergence processes. Those granular fields may be the result of recycling of flux initially placed in intergranular lanes, or an effect of enhanced magnetic diffusivities. Cheung et al. (2007), on the other hand, have studied the rise of magnetic flux tubes from the convection zone to the photosphere. Depending on the magnetic flux stored in the tubes, the arrival of magnetic fields at the solar surface has very different observable consequences. For the stronger tubes, a darkening and distortion of the granular convection is expected (and actually observed), while weaker tubes do not modify the brightness of surface granules. In both cases, magnetic fields tend to emerge at the center of granular cells, showing large inclinations to the vertical. The fields are then advected by the horizontal flow towards the intergranular lanes, where they become more vertical and form opposite-polarity patches. Our events do not share these properties.

A hypothetical scenario for the emergence of unipolar vertical magnetic fields would be that granular upflows drag horizontal field lines initially placed in the upper convection zone, carrying them to the photosphere where they would emerge in the granules. However, it is not clear how the horizontal fields may turn into vertical fields. Also, at some point one should observe opposite polarities where the field lines return to the solar surface, but we do not detect them, perhaps as a consequence of still insufficient sensitivity or because they occur outside of the FOV. What is clear is that the scenario of vertical fields emerging in granules faces important conceptual problems.

A radically different interpretation is that the events we have observed do not involve the emergence of new flux, but the "excitation" of already existing, mixed, quasi-isotropic fields (López Ariste et al. 2008). These fields would be largely decoupled from convective motions and hence not affected by them. If the degree of mixing is sufficiently high, the absence of linear polarization cannot be taken as a proof that the field is vertical. This scenario should be investigated more thoroughly, both to demonstrate the existence of such tangled fields and to assess whether they are indeed compatible with the observations presented here.

8.8 Conclusions

In this Chapter we have described different cases for the emergence of apparently unipolar, vertical fields in granular cells. A total of 13 such events occurred during the ∼10 hours covered by the *Hinode* observations. Their

lifetimes are of the order of 15-20 minutes. Their flux values are weak and comparable to typical IN magnetic concentrations. We have qualitatively described five of these events and the underlying physical scenario is still unclear.

In summary, at this stage we cannot offer a clear explanation of the events observed with *Hinode*, but we hope that the report of such processes will stimulate further observational and theoretical work. With this in mind, we plan to perform detailed inversions of the observed profiles in an attempt to derive a consistent picture of the physics behind these processes. Since sensitivity may be an issue, it would also be convenient to carry out additional measurements with the *Hinode* SP, pushing the integration time to a limit.

The characterization of emergence processes at the smallest scales is important to understand the energy balance and origin of quiet Sun magnetic fields. In particular, they may hold the key to determine whether a local dynamo operates in the solar photosphere, as has been suggested on theoretical grounds (Cattaneo 1999). Also, a good knowledge of the ways magnetic fields emerge through the surface may help refine numerical simulations of magneto convection such as those performed by Vögler et al. (2005), Schaffenberger et al. (2006), Stein & Nordlund (2006), and Abbett (2007). If some form of flux emergence is not observed in the simulations, additional ingredients might need to be implemented in current codes.

Finally, the results presented here are neatly different that the horizontal fields found in IN regions (Chapter 7). Also, the *Hinode*/SP is still unable to resolve the different components that may form these magnetic events, provided they are not generated by strong discontinuities on the magnetic field stratification. Therefore, to better understand the nature of the vertical fields above granules, higher spatial resolution as well as better temporal cadences are needed. To this end new instrumentation is being built in order to achieve spatial resolutions of the order of $0\farcs1$, three orders of magnitude larger than current spectropolarimetric data.

9

Retrieval of solar magnetic fields from high-spatial resolution data

For the first time, IMaX[1] will make it possible the observation of the solar photosphere at resolutions of $\sim 0''.1$ ($\sim$80 km), and high temporal cadences and polarimetric sensitivity in the absence of the Earth atmosphere. Unlike current spectropolarimeters, vector magnetographs observe spectral lines at only few wavelength positions. In addition, the spectral resolving power is smaller due to the spectral widths of the tunable filters they utilize. In this Chapter analyze the influence of the limited spectral resolving power, noise, and wavelength sampling on the vector magnetic fields and LOS velocities derived from Milne-Eddington inversions of IMaX measurements. To this end, we simulate an IMaX observation using MHD model to synthesize the Stokes profiles of the photospheric Fe I 525.02 and 525.06 nm lines. Then, the profiles are degraded by telescope diffraction and detector pixel size to a spatial resolution of 80 km on the solar surface.

9.1 Introduction

State-of-the-art vector magnetographs such as HMI, PHI or IMaX, are being designed or has already been built, with the only purpose of observing the Sun photosphere with very high spatial resolving power as well as high polarimetric efficiencies. Attached to different solar telescopes, most of these instruments

[1] A detailed description of the instrument can be found in Chapter 2

are going to be lunched to space, therefore getting rid from perturbations introduced by the Earth atmosphere. Therefore, These instruments will improve the quality of current polarimetric observations. However, they are subjected to broad tunable-filter widths and to a limited wavelength sampling. Consequently, the spectra is degraded and larger errors in the derived physical quantities are expected. The success of these instruments is in how accurately can be derived the physical parameters from their measurements. The information of this new instrumentation will be of vital importance to understand not only the physical processes taking place at the solar photosphere, but also the magnetic coupling of the different atmospheric layers.

In Chapter 6 we demonstrated that it is possible to satisfactorily derive the vector magnetic field and the LOS velocity from spectropolarimetric data at $0\farcs32$. It is reasonable to think that at the increased spatial resolution of $0\farcs1$ we will obtain not similar, but better estimates of the physical quantities. However, as previously mentioned, vector magnetographs provide data with less spectral information. For this reason, in this Chapter we

- explore the errors introduced by the limited spectral resolving power of the instrument
- investigate the drawbacks of the noise for vector-magnetographs
- study the effects of the limited wavelength sampling and position of wavelength samples on the inference of model parameters
- assess the accuracy to which the magnetic field strength, inclination, azimuth and LOS velocity can be obtained from IMaX vector magnetograph data at $0\farcs1$.

9.2 Methodology

To address these questions we have simulated the observational process of IMaX. We followed the steps described in Chapter 5 and 6. Specifically, we first take model atmospheres from MHD simulations. These atmospheres are necessary to generate the observations by synthesizing the Stokes I, Q, U and V profiles. The 525 nm spectral region is synthesized in a wavelength range that extends 1 nm, including the Fe I 525.02 and 525.06 nm spectral lines. The sampling interval were 1 pm. Next, the polarization signals are spatially degraded considering telescope diffraction and detector pixel size. We also degrade the profiles applying a spectral PSF, add noise, and select a few wavelength samples across the line. The extraction of the physical quantities from

TABLE 9.1:— Basic optical parameters of SUNRISE and IMaX.

APPERTURE	100 cm	
WORKING WAVELENGTH	525.02 nm	
SPATIAL RESOLUTION	$\sim 0\farcs1$	$\sim$80 km
CENTRAL OBSCURATION	35.2%	
CCD PIXEL SIZE	$0\farcs05 \times 0\farcs05$	
SMEARING FILTER WIDTH	$\sim$60 mÅ	

the simulated "observations" is done by means of ME inversions. Comparing the retrieved parameters with the real ones we can estimate the uncertainties of the inferences.

In Chapter 5 we determined the errors associated with the ME approximation by analyzing observations in the most favorable case, i.e., in which the instrument measures the Stokes profiles with no noise, very high spectral resolution, and critical wavelength sampling. The conclusion was that they provide averaged values of the physical quantities. We also demonstrate that these errors dominate against those originated from the intrinsic noise of the observations.

In this case, we aim at determining how these ME uncertainties are amplified when applying ME inversions to IMaX data. In particular, we want to examine the effects of the limited spectral resolving power as well as those originated by a limited wavelength sampling across the spectral line. This analysis is of fundamental importance to analyze whether ME inversions represent a good option to interpret IMaX measurements.

We will consider the results of ME inversions of the Stokes profiles degraded by telescope diffraction and with no noise, no spectral PSF, and 61 wavelength samples as *the reference* solution. By comparing this reference with the outcome of ME inversions of the same Stokes profiles affected by noise, limited spectral resolution, and wavelength sampling, we quantify the loss of information induced by the measuring process, avoiding errors due to the ME assumption and telescope diffraction. In Appendix C we have analyzed the reliability of the ME inversion when analyzing synthetic ME profiles affected by different instrumental widths and sampled at only few wavelength samples and different sample point positions. The errors are significantly smaller than the ones associated to the ME approximation to describe real profiles and to the photon noise.

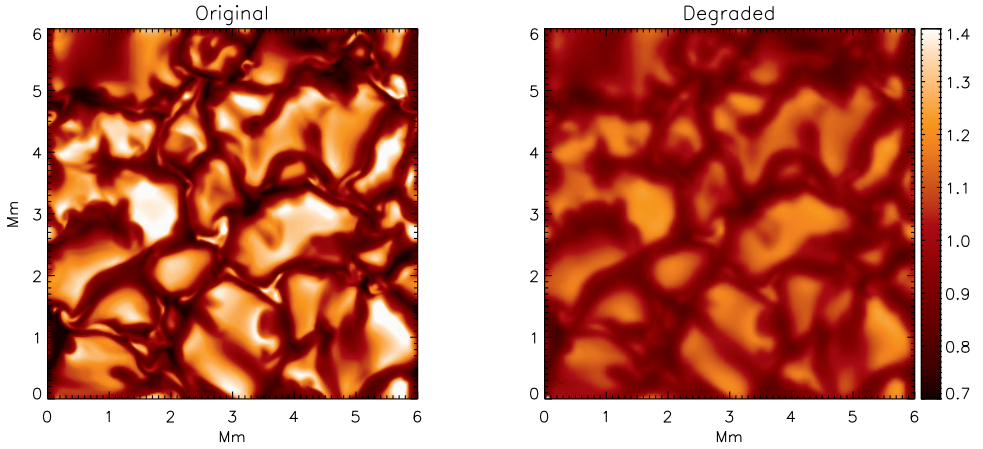

FIGURE 9.1:— Continuum intensity for the non-degraded data (left) and for the spatially degraded data (right) considering telescope diffraction and pixel size.

9.3 Simulating IMaX observations

9.3.1 Spatial degradation

In Chapter 6 we already carried out a spatial degradation by telescope diffraction of a real object. In particular we simulated the spectropolarimeter attached to the *Hinode*/SOT. In this case, the telescope aboard the SUNRISE stratospheric balloon has a diameter twofold the one of the *Hinode* spacecraft. Therefore the spatial resolution is greater and the effects of diffraction on the polarization signals are expected to be smaller. The parameters describing the telescope and the detector are given in Table 9.1. Notice that polarimetric measurements in the absence of atmospheric seeing and with a effective spatial resolution of $\sim 0\farcs1$ has never been obtained.

Figure 9.1 shows maps of the continuum intensity for the original data and for the spatially degraded data corresponding to the simulations with $\langle B \rangle = 140$ G. The contrast due to diffraction and CCD pixel size has decreased by only 4%. The pixel size of the detector is twice the grid resolution of the original MHD model, thus the not readily noticeable binning in the degraded image. Figure 9.2 shows the MTFs of the SUNRISE/IMaX.

The effects of diffraction in the polarization signals have been already analyzed in Chapter 6. In summary, diffraction blurs the data, mixing the light from nearby pixels and diminishing the amplitude of the polarization signals. Consequently, we detect a small amount of magnetic signals, noise become more importantly and also, the smallest-scale structures disappear. For IMaX these

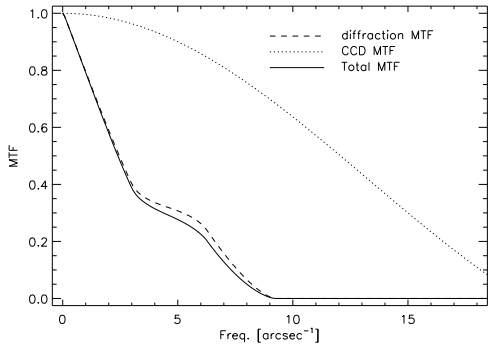

FIGURE 9.2— Dotted line: MTF of the CCD (pixelation effect); dashed line: diffraction limited MTF; and solid line: MTF combining both effects.

effect are less pronounced due to its improved spatial resolution. However, these effect are present. For completeness, Fig. 9.3 displays monochromatic images of Stokes Q, U and V taken at 7 pm from the central wavelength of the Fe I 525.02 nm spectral line and corresponding to $\langle B \rangle = 140$ G. (A) stands for the original images and (B) for the images spatially degraded by telescope diffraction and CCD pixel size. To emphasize details we only represent a small area of the image. The previously mentioned effects are seen on the different maps. For instance, small magnetic structures disappear due to diffraction. We have added noise at the level of $10^{-3} I_c$ in order to see how it affects the weakest signals.

¿Cuanto?

9.3.2 Effects of the smearing filter

IMaX use an étalon whose FWHM corresponds to ~ 6 pm. We will approximate its shape by a Gaussian function. It is known that the finite-width of the étalon affects the Stokes profiles by diminishing their amplitudes and by smoothing the profile shapes through convolution.

A qualitative analysis of the effects of the instrumental filter width on the monochromatic images of Fe I 525.02 nm Stokes Q, U and V profiles taken at 7 pm can be seen in Fig. 9.3. Columns (C) and (D) stand for FWHMs of 6 and 10 pm respectively. The different images show that the smallest-scale magnetic features tend to disappear when we use large filter widths. The consequence is that the spatial resolving power decreases: the larger the smearing filter widths the poorer the spatial resolution. Therefore, the information content on the images is reduced. In addition, the amplitude of the polarimetric signals diminishes. The last is important because it makes the noise more noticeable.

These effects are more pronounced in Stokes Q and U, than in V. The reason is the small amplitudes they exhibit against Stokes V. Notice how noise

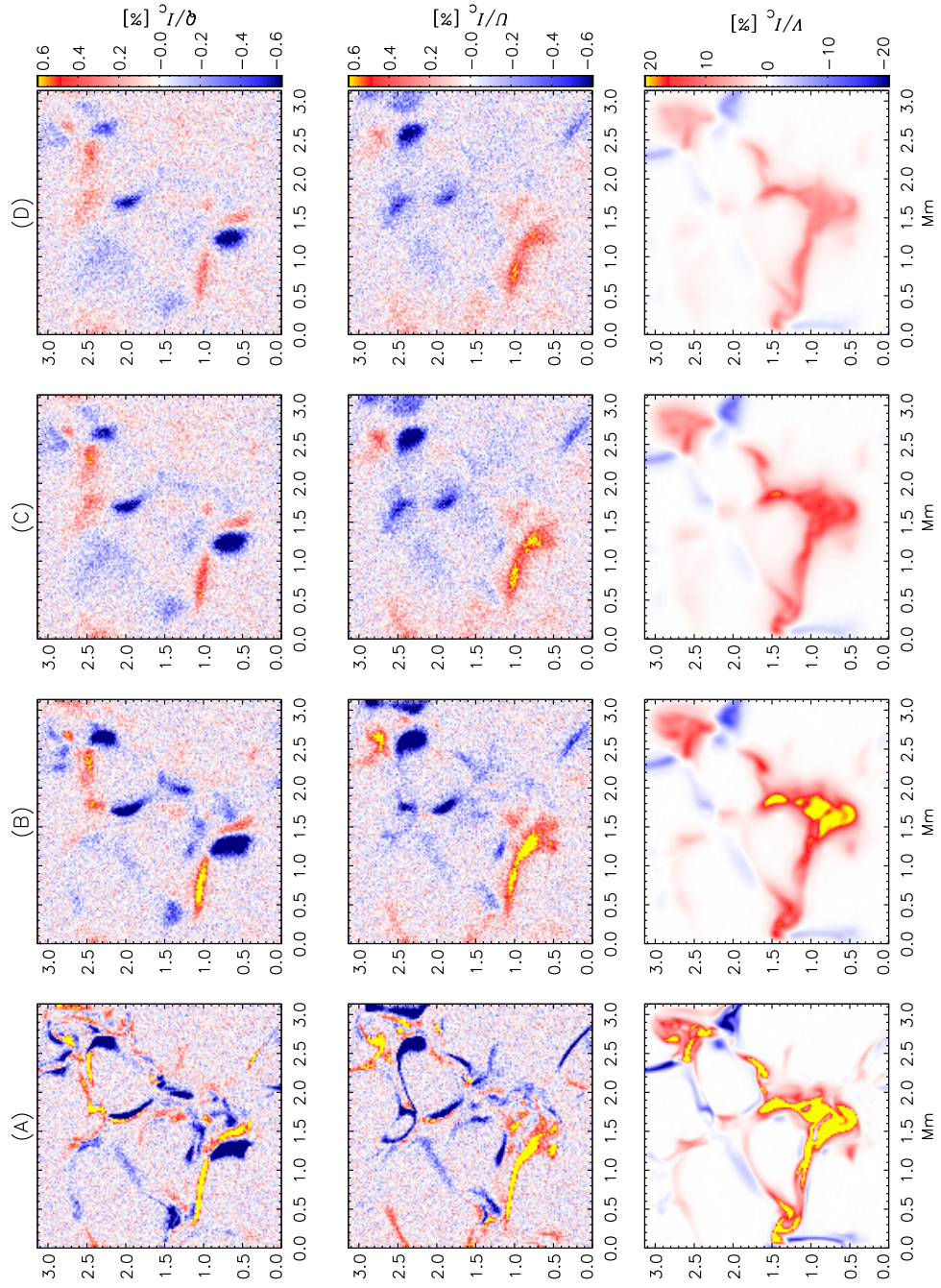

FIGURE 9.3:— Monochromatic images taken at 77 mÅ of the central wavelength of the Fe I 525.02 nm line. From bottom to top: the original data, the spatially degraded data and the data taken into account filter widths of 6 and 10 pm, (A), (B), (C) and (D) respectively. Only a region corresponding to 150×150 pixels is displayed.

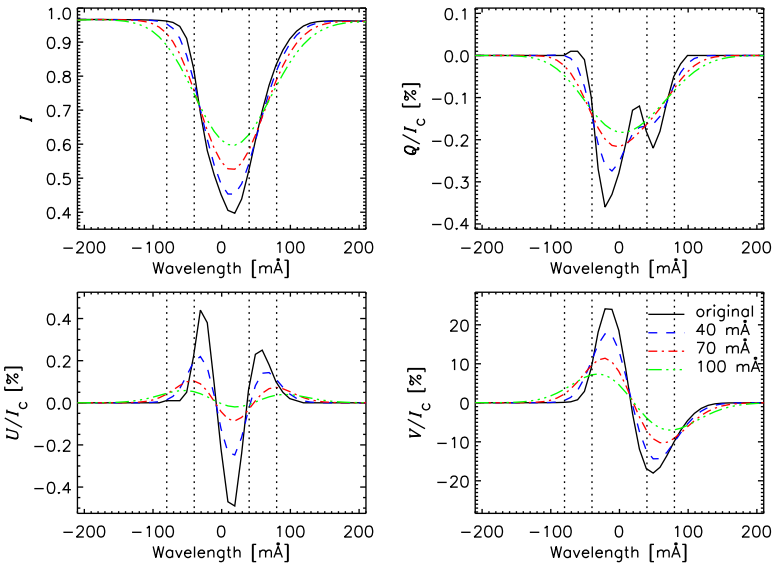

FIGURE 9.4:— Stokes I, Q, U and V profiles of the Fe I 525.02 nm line corresponding to pixel $(x, y) = (94, 214)$ from the spatially degraded image (black) and the same profiles convoluted with three different smearing filter widths, 4, 7 and 10 pm (color coded lines). The pixel corresponds to an intergranular lane. The vertical dotted lines indicate the position of different wavelength samples.

became more appreciable in Stokes Q and U for larger filter widths (columns (C) and (D) from Fig. 9.3).

Figure 9.4 shows the spatially degraded Stokes vector of the Fe I 525.02 nm line corresponding to the pixel $(x, y) = (178, 46)$ and convoluted with different smearing filter widths, 4, 7 and 10 pm (color coded lines). The profile in black corresponds to the spatially degraded profiles. The vertical dotted lines indicate different wavelength samples at [-8,-4,4,8] pm from the central wavelength of the line. The effects of the smearing filter are quite apparent. For instance, the asymmetries of the profiles are smoothed out. Notice that filter widths of 10 pm can originate regular profiles. Notice that the symmetrization of the profiles make it hard the determination of vertical gradients in the model parameters.

At the same time, the amplitude of the polarization signals are lowered significantly, even the signals may be less than half of their original amplitudes, being more dramatic in Stokes Q and U. Notice that the linear polarization profiles would be seen if no smearing is applied to them, they are at the level of $10^{-3} I_c$ for filter widths of 10 pm, therefore buried in noise (for these noise levels).

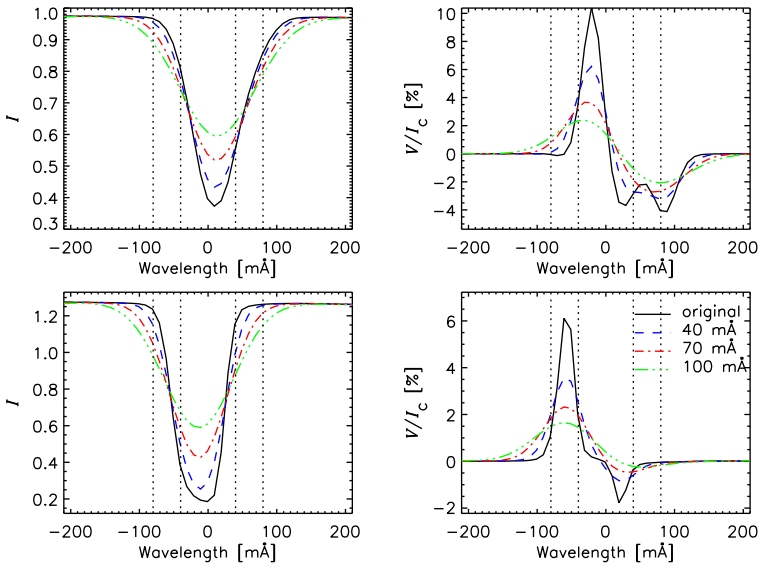

FIGURE 9.5:— Same ar Fig. 9.4 but for oly Stokes I and V corresponding to pixels $(x, y) = (85, 200)$ and $(193, 121)$.

These two effects reduce the information content on the profiles. For instance, the sensitivity to the velocity decreases because the smearing filter broadens the profiles, make them shallower (Cabrera Solana, Bellot Rubio, & del Toro Iniesta 2005). The sensitivity to the magnetic field vector is also reduced (see Chapter 4).

Figure 9.5 shows the effects of the smearing on two pixels: one exhibiting a three lobed Stokes V profile and another one whose Stokes V profile shows a extreme asymmetry (top and bottom panels respectively). In both cases a smearing filter width of 10 pm transform the Stokes V in a regular profile. Even when it shows three lobes.

9.3.3 The effect of noise

As we have explained before, smearing affects in different ways to the Stokes profiles. One of them is that smearing reduces the amplitude of the polarization signals, therefore they are more affected by noise. In this section we aim at quantifying this effect. To this end we analyze the relation between noise and the amplitude of the Stokes profiles.

Fig. 9.6 (left panel) shows, as a function of filter width, the percentage of pixels whose linear polarization $\mathrm{P}(\lambda) = \sqrt{Q^2(\lambda) + U^2(\lambda)}$ amplitude exceed dif-

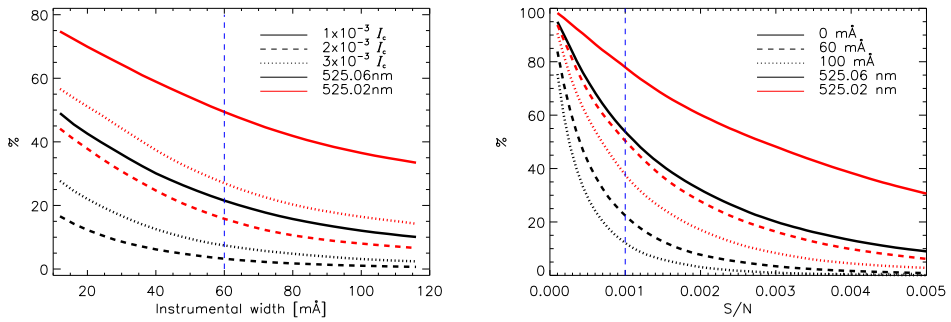

FIGURE 9.6:— Variation of the number of pixels whose Stokes Q or U amplitudes exceed specified noise levels, in percent, as a function of the instrumental filter width and as a function of the signal-to-noise ratio for various filter widths (left and right, respectively).

ferent noise levels (see text insert in the figure). The Fe I 525.02 and 525.06 nm spectral lines are represented in red and black, respectively. Note that the percentage of pixels showing P signals larger than the noise decrease almost linearly with the FWHM of the smearing filter. This figure just shows that the ability to detect linear polarization signals depends on the instrumental profile, for quiet Sun regions.

In the right panel of Fig. 9.6, we represent the percentage of pixels with detectable linear polarization signal against the noise level of the profiles with a fixed filter width of 0, 6 and 10 pm. In this case, and in comparison with the right panel, the amount of linear polarization signal decreases more rapidly with noise than with the width of the smearing profile.

Lets assume that the noise is of $10^{-3}I_c$ and that the filter width of the smearing profile corresponds to 6 pm. This values are indicated with vertical, dashed lines in Fig. 9.6. For the Fe I 525.02 nm spectral line we obtain that $\sim$49% of the pixels show P signals above the noise. For the 525.06 nm line this percentage decreases to $\sim$22%. The figure also shows clear differences between the two lines. The one having larger effective Landé Factor, i.e., $g_{\rm eff} = 3$ for Fe I 525.02 nm, shows larger linear polarization amplitudes. This make it easy to detect linear polarization signals with this spectral line. Of interest, the amount of linear polarization profiles for this line coincides with that of the 525.06 nm line in the absence of smearing filter.

It is also interesting to note that 28% of the pixels are no longer detectable in linear polarization when we apply a filter width of 6 pm. This loss of sensitivity can be compensated by lowering the noise level. For instance, if we are to recover the previous loss of 28% of the pixels, the S/N has to be increased from

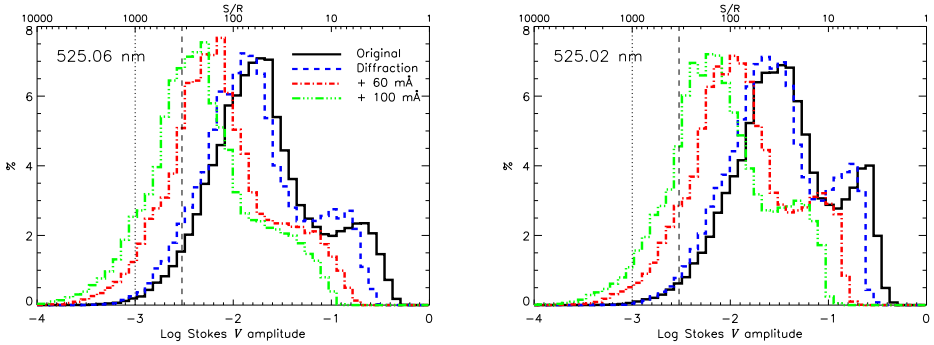

FIGURE 9.7:— Distribution of the Stokes V amplitudes in the original, degraded and degraded images with two different smearing filters. The Stokes profiles have been taken from the simulation run having $\langle B \rangle = 140$ G.

1000 to 2800. This translates into a $\sim$9 factor in exposure time, which may have some unwanted consequences on high spatial resolution observations.

Figure 9.7 shows the distributions of Stokes V amplitudes in the original, spatially degraded maps and taking into account to different smearing filter widths for the Fe I 525.02 and 525.06 nm spectral lines. The histograms show an asymmetric distribution of amplitudes. The effects of diffraction are weak and similar to those explained in Chapter 6. It is very noticeable the effects of the smearing filter against those caused by diffraction. The smearing filter shifts the distribution as a whole toward smaller amplitude values. It also modify the shape of the histogram.

The absolute maximum of the histograms are located at -1.74, -1.63, -2.08, -2.27 dex and at -1.49, -1.41, -1.84, -2.06 dex for the original and spatially degraded image, and the degraded image with two different smearing filter widths, and for the Fe I at 525.06 and 525.02 nm lines, respectively.

Notice that there is a secondary maximum at larger amplitude values for the original and degraded images. These maximum vanish for the 525.06 nm line when applying the smearing filter. The origin of these maximum is in the Zeeman saturation of the lines (Stenflo 1973). In the weak field approximation, the Stokes V amplitude increases linearly with the magnetic field strength until the field reaches a saturation limit. At that point the increase of Stokes V is no longer lineal. This saturation limit occurs when the Zeeman splitting of the line, $\Delta\lambda_{\rm B} \propto \lambda^2 g_{\rm eff} B$, is larger than its Doppler with. From this relationship the Fe I line at 525.02 and 525.06 nm lines saturate at $\sim$ 650 and $\sim$ 1500 G, respectively assuming $\Delta\lambda_{\rm D} = 30$ mÅ. This partially explains the different amplitude size of the secondary maximum. They also depend on the different sensitivity of the

lines to the magnetic field.

A comparison of the histograms for both lines show that the distribution of 525.02 nm Stokes V profiles is located at larger amplitude values, mainly due to larger sensitivity to the magnetic field. The effects of the smearing filter is similar for both lines. As a consequence, the filter width is more critical for the 525.06 nm line just because it exhibit weaker amplitude signals, therefore more affected by noise. In Fig. 9.7 we have represented two different noise levels, 1 and 3 times $10^{-3} I_{\rm c}$, dotted and dashed vertical lines respectively. Below these noise levels the polarimetric signals would not be detectable. Notice that the maximum of the histograms for the 525.06 nm line is closer to these limits than for it neighbor line.

Finally notice that, In order to analyze the effects of the spatial degradation and the smearing filter on the linear and circular polarization signals we have taken the whole Stokes profiles, i.e., the profiles sampled at 61 wavelength positions. IMaX will observe a spectral line at only four wavelength positions, therefore a less amount of pixels showing polarimetric signals is to be expected.

As an example, Figs. 9.4 and 9.5 shows vertical, dotted lines indicating four wavelength samples.

9.3.4 Effects of the secondary peaks of the Fabry-Pérot

Other important effect that we have to take into account when analyzing the Stokes profiles is the effects of the secondary peaks of the Fabry-Pérot on the spectral line. These secondary peaks mixes the spectral information from wavelength range where they are located with the one of the main peak.

In Fig. **??** we represented FTS spectral atlas (black) around the 525.0 nm spectral region and over-plotted was the IMaX transmission filter. The secondary transmission peaks of the Fabry-Pérot are represented by the blue, dashed line. Note that the effects of the secondary peaks is reduced by introducing a pre-filter in the optical path. Although the contribution is expected to be small, it has to be quantify.

Fig. 9.8 shows the FTS atlas of the Fe I lines at 525 nm before and after the convolution with the transmission filter, black and red respectively. We can see how the lines are broader and the residual intensity decreases. In the same plot we represent the difference of the spectral lines convolved with the transmission filter taking into account the secondary peaks of the etalon and without taking them into account. The differences are below 0.6% in the central wavelength of the lines. This percentage is above typical noise levels.

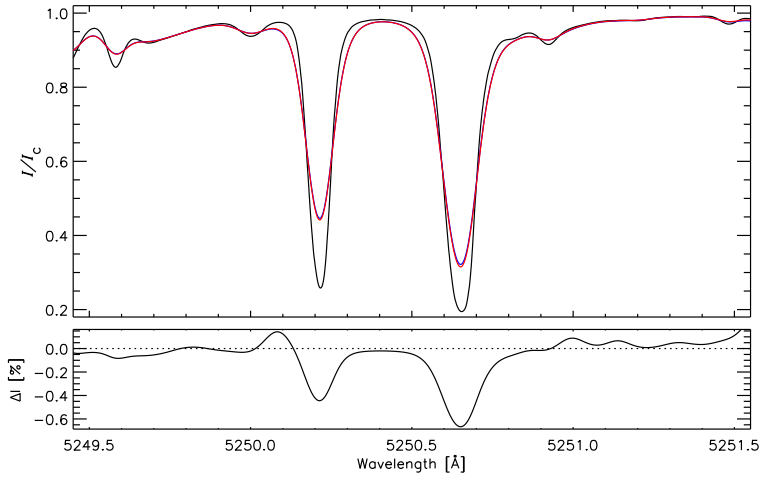

FIGURE 9.8:— FTS atlas after (red) and before (black) being convolved by the instrumental profile (see Fig. **??**). Bottom panel: difference between the profiles convolved taking into account the secondary peaks of the instrumental profile and not.

10

Summary and conclusions

In this thesis, after a brief introduction to radiative transfer theory, we have introduced the concept of Milne-Eddington (ME) response functions (RF) of the radiative transfer equation. We have targeted the Fe I line at 525.06 nm to construct a ME model and to discuss the basic properties of the ME RFs. They are a useful tool to understand the sensitivities of spectral lines to the various model parameters. Using the RFs we have understood the trade-off often found in ME inversion codes. An interesting result is that ME models can disentangle from weak fields and filling factors due to the different sensitivities of the Stokes vector to these parameters. Also, using ME RFs we have proposed a method to select the number of wavelength points and sample positions to be observed by vector magnetographs. Finally, ME RFs can provide with *a-priory* estimations of the affordable errors for different model parameters.

We have introduced on the inversion method techniques that most frequently apply to spectropolarimetric data. A ME inversion code has been developed for the analysis and interpretation of spectropolarimetric observations. In particular the code uses a least-squares Levenberg-Marquardt algorithm. The reliability of the code has been tested.

We have examined the applicability of ME inversion to high spatial resolution observations of the quiet Sun. ME inversions provide atmospheric quantities that are constant with height while real model change along the photosphere. To this end we have employed magnetohydrodynamic (MHD) simulations to generate the Stokes profiles of the Fe I lines at 630.15 and 630.25 nm at very high spatial resolution. After a brief description of the MHD models and synthesis process, we have proved that the synthesized profiles reproduce

the real Sun. The profiles have been analyzed with the ME inversion code in the absence of noise and instrumental effects in order to understand how appropriate is this approach to analyze real profiles. The main conclusions are:

1. ME inversions provide reasonable estimated for the physical quantities at $\log \tau = -1$ being the rms 30 G, 6°, 20° and 500 $\mathrm{m\,s^{-1}}$, for the magnetic field strength, inclination and azimuth, and for the velocity, respectively,

2. individual errors may be rather large, even when the best-fit profile reproduce satisfactorily the Stokes vector,

3. ME inferences cannot be assigned to single atmospheric layers,

4. the errors due to the ME approximation dominate against those due to photon noise.

The IN is believed to store a significant fraction of the total magnetic flux of the solar photosphere. There exist many studies of the IN, but no consensus on the strength of the fields has been reached yet. To shed some light on this issue, we have explored the diagnostic potential of high spatial resolution observations in the absence of atmospheric seeing. We have done this by simulating and analyzing QS measurements of the spectropolarimeter aboard the *Hinode* satellite. To that end we have used the MHD simulations to synthesize the Fe I 630.15 and 630.25 nm spectral lines. Then, we have degraded the polarization maps to account for telescope diffraction and CCD pixilation. The effects of diffraction on the polarization signals have been investigated. The main effects are:

1. the image contrast and the circular, and linear polarization signals are reduced,

2. diffraction mixes polarization signals from the different pixels to nearby ones,

3. the amount of polarization signals detectable above the noise diminishes and the profile asymmetries are smoothed out.

The simulated spectra were analyzed in terms of ME inversions. The results show that it is possible to obtain satisfactory magnetic field strengths and inclinations for fields above 100 G provided we assume a simple one-component model atmospheres filling the resolution element and a local stray/scattered light profile to account for telescope diffraction. The use of a local stray-light contamination factor was found to be essential for retrieving the correct

magnetic field strengths and inclinations, correcting for the main effects of telescope diffraction. Also, we find that the average stray-ligh factor amounts 55% in the degraded simulations. The main conclusion of this analysis is that *ME inversions can be used to analyze the magnetism of the QS.*

We have studied *Hinode* first-light observations of IN regions. In particular we have analyzed a QS raster scan and a time sequence of $\sim$ 2 hours of very high S/N. The qualitative analysis of the Stokes profiles has revealed that the IN is full of polarization signals at the spatial resolution of $0\farcs32$. We have applied the ME inversion accounting for contamination of local stray-light to correct the effects of telescope diffraction in the polarization profiles. We have demonstrated the unicity of ME inversion results against different initialization of the code. We have also demonstrate that the ME inversion is able to disentangle between stray-light factor and field strength, as derived from the analysis of the χ^2.

With the inversion results, we have derived the strength, inclination and stray-light factor distributions of internetwork magnetic fields. The results show that *the internetwork regions consists in hG field concentrations with a average field strength of 90 G and filling factors of about 45%.* This result may definitely close the discrepancies that exist between results with the analysis of visible and IR lines. In addition these fields tent to be horizontally oriented. Finally, we obtain a average flux density of $\sim$ 10 Mx cm^{-2}.

We have analyze high-cadence time series of *Hinode* spectropolarimetric measurements. In the data, *we have discovered a new form of flux emergence in granular cells*, which seems to take vertical magnetic fields from subsurface layers to the photosphere, as shown by the qualitative analysis of 5 emergence events from a total of 13 occurring during 10 hours of *Hinode* observations. They are characterized by weak flux values and duration of 15-20 minutes. The analysis did not provide enough binding information to clarify the underlying physical scenario. These emergence events are different from the emergence of magnetic loops in the IN and constitutes a newly magnetic phenomenon.

We have investigated how well we are able to infer atmospheric parameters from IMaX measurements. To this end we have simulated IMaX observations using the MHD models of the solar photosphere. The analysis comprised three different steps: the synthesis of the Stokes profiles emerging from the simulations, the degradation of the spectra by telescope diffraction, and the interpretation of the profiles using inversion techniques. The latter approach provided fundamental results for IMaX. The inversion is based on the ME approximation and without the contribution of a stray-light contamination factor. In the analysis we have targeted the Fe I lines at 525.02 and 525.06 nm. The main results are:

1. the IMaX transmission filter strongly reduces the amount of detectable polarization signals above the noise and the effective spatial resolution of the images. It also smoothes out the asymmetries of the profiles to a large extent.

2. the Fe I 525.02 nm line is better suited for the determination of the magnetic field vector, while the Fe I 525.06 nm line is for the determination of LOS velocities,

3. IMaX will benefit from the use of the Fe I 525.02 nm line because is shows greater sensitivity to the magnetic field. Therefore it shows larger polarimetric signals and the amount of pixels showing polarization will be less reduced by the action of the instrumental profile,

4. it is possible to determine the magnetic field strength and the plasma velocity from the spectral line sampled at only four wavelength positions plus one point in the nearby continuum. The inclination and azimuth of the field are determined with less accuracy.

5. five wavelength samples at $[\pm 40, \pm 80]$ mÅ from the central wavelength of the line plus a wavelength point in the nearby continuum seem appropriate to sample the Fe I at 525.06 nm spectral line (if we do not consider bulk velocities).

Finally, we would like to point out to the importance of achieving high S/N in the observations in order to minimize the lost of magnetic signals due to the effects of the instrumental filter profile. Also that the use of an additional wavelength sample may improve significantly the quality of the inferences.

A

Explicit formulae for the analytical Response Functions

In Chapter 2.3 (Eq. 2.15) we presented the RTE for polarized light in a plane-parallel atmosphere. We also shown that in a Milne-Eddington (ME) model atmosphere, an analytical solution is found for the RTE (see, e.g. Unno 1956; Rachkovsky 1962, 1967; Landolfi & Landi Degl'Innocenti 1982).

The evaluation of RFs in a ME model atmosphere reduces to the derivatives of the Stokes vector, $\mathbf{I} = (I, Q, U, V)$, with respect to the nine parameters, $(B_0, B_1, \eta_0, B, \gamma, \chi, \Delta\lambda_{\rm D}, v_{\rm LOS}, a)$. In order to easily show such derivatives suppose a generic parameter x. Then,

$$
\begin{aligned}
\frac{\partial I}{\partial x} &= B_1\mu\left(T_1\frac{\partial \eta_I}{\partial x} + \eta_I\frac{\partial T_1}{\partial x} - \Delta^{-1}\eta_I T_1\frac{\partial \Delta}{\partial x}\right)\Delta^{-1}, \qquad \text{(A.1)}\\
\frac{\partial Q}{\partial x} &= -B_1\mu\left(\frac{\partial T_2}{\partial x} + \frac{\partial \rho_Q}{\partial x}\Pi + \rho_Q\frac{\partial \Pi}{\partial x} - \Delta^{-1}\frac{\partial \Delta}{\partial x}[T_2 + \rho_Q\Pi]\right)\Delta^{-1},\\
\frac{\partial U}{\partial x} &= -B_1\mu\left(\frac{\partial T_3}{\partial x} + \frac{\partial \rho_U}{\partial x}\Pi + \rho_U\frac{\partial \Pi}{\partial x} - \Delta^{-1}\frac{\partial \Delta}{\partial x}[T_3 + \rho_U\Pi]\right)\Delta^{-1},\\
\frac{\partial V}{\partial x} &= -B_1\mu\left(\frac{\partial T_4}{\partial x} + \frac{\partial \rho_V}{\partial x}\Pi + \rho_V\frac{\partial \Pi}{\partial x} - \Delta^{-1}\frac{\partial \Delta}{\partial x}[T_4 + \rho_V\Pi]\right)\Delta^{-1},
\end{aligned}
$$

where for simplicity

$$\begin{aligned} T_1 &= \eta_I^2 + \rho_Q^2 + \rho_U^2 + \rho_V^2, \\ T_2 &= \eta_I^2\eta_Q + \eta_I(\eta_V\rho_U - \eta_U\rho_V), \\ T_3 &= \eta_I^2\eta_U + \eta_I(\eta_Q\rho_V - \eta_V\rho_Q), \\ T_4 &= \eta_I^2\eta_V + \eta_I(\eta_U\rho_Q - \eta_Q\rho_U), \\ T_5 &= \eta_I^2 - \eta_Q^2 - \eta_U^2 - \eta_V^2 + \rho_Q^2 + \rho_U^2 + \rho_V^2. \end{aligned} \tag{A.2}$$

Δ and Π are defined in Eqs. (4) and (5), respectively. Their derivatives are thus given by

$$\begin{aligned} \frac{\partial\Delta}{\partial x} &= 2\eta_I\frac{\partial\eta_I}{\partial x}T_5 + \eta_I^2\frac{\partial T_5}{\partial x} - 2\Pi\frac{\partial\Pi}{\partial x}, \\ \frac{\partial\Pi}{\partial x} &= \eta_Q\frac{\partial\rho_Q}{\partial x} + \frac{\partial\eta_Q}{\partial x}\rho_Q + \eta_U\frac{\partial\rho_U}{\partial x} + \frac{\partial\eta_U}{\partial a}\rho_U + \eta_V\frac{\partial\rho_V}{\partial x} + \frac{\partial\eta_V}{\partial x}\rho_V. \end{aligned} \tag{A.3}$$

The derivatives of $T_1, ..., T_5$ are given by

$$\begin{aligned} \frac{\partial T_1}{\partial x} &= 2\left(\eta_I\frac{\partial\eta_I}{\partial x} + \rho_Q\frac{\partial\rho_Q}{\partial x} + \rho_U\frac{\partial\rho_U}{\partial x} + \rho_V\frac{\partial\rho_V}{\partial x}\right), \\ \frac{\partial T_2}{\partial x} &= 2\eta_I\frac{\partial\eta_I}{\partial x}\eta_Q + \eta_I^2\frac{\partial\eta_Q}{\partial x} + \frac{\partial\eta_I}{\partial x}(\eta_V\rho_U - \eta_U\rho_V) + \\ &\quad \eta_I\left(\frac{\partial\eta_V}{\partial x}\rho_U + \eta_V\frac{\partial\rho_U}{\partial x} - \frac{\partial\eta_U}{\partial x}\rho_V - \eta_U\frac{\partial\rho_V}{\partial x}\right), \\ \frac{\partial T_3}{\partial x} &= 2\eta_I\frac{\partial\eta_I}{\partial x}\eta_U + \eta_I^2\frac{\partial\eta_U}{\partial x} + \frac{\partial\eta_I}{\partial x}(\eta_Q\rho_V - \eta_V\rho_Q) + \\ &\quad \eta_I\left(\frac{\partial\eta_Q}{\partial x}\rho_V + \eta_Q\frac{\partial\rho_V}{\partial x} - \frac{\partial\eta_V}{\partial x}\rho_Q - \eta_V\frac{\partial\rho_Q}{\partial x}\right), \\ \frac{\partial T_4}{\partial x} &= 2\eta_I\frac{\partial\eta_I}{\partial x}\eta_V + \eta_I^2\frac{\partial\eta_V}{\partial x} + \frac{\partial\eta_I}{\partial x}(\eta_U\rho_Q - \eta_Q\rho_U) + \\ &\quad \eta_I\left(\frac{\partial\eta_U}{\partial x}\rho_Q + \eta_U\frac{\partial\rho_Q}{\partial x} - \frac{\partial\eta_Q}{\partial x}\rho_U - \eta_Q\frac{\partial\rho_U}{\partial x}\right), \\ \frac{\partial T_5}{\partial x} &= 2\left(\eta_I\frac{\partial\eta_I}{\partial x} - \eta_Q\frac{\partial\eta_Q}{\partial x} - \eta_U\frac{\partial\eta_U}{\partial x} - \eta_V\frac{\partial\eta_V}{\partial x} + \rho_Q\frac{\partial\rho_Q}{\partial x} + \right. \\ &\quad \left.\rho_U\frac{\partial\rho_U}{\partial x} + \rho_V\frac{\partial\rho_V}{\partial x}\right). \end{aligned} \tag{A.4}$$

The derivatives with respect to η_0 can be easily calculated from Eq. (A.2.)

$$\begin{aligned}
\frac{\partial \eta_I}{\partial \eta_0} &= \frac{(\eta_I - 1)}{\eta_0}, \\
\frac{\partial \eta_{Q,U,V}}{\partial \eta_0} &= \frac{\eta_{Q,U,V}}{\eta_0}, \\
\frac{\partial \rho_{Q,U,V}}{\partial \eta_0} &= \frac{\rho_{Q,U,V}}{\eta_0}.
\end{aligned} \tag{A.5}$$

The derivatives with respect to γ and ψ are

$$\begin{aligned}
\frac{\partial \eta_I}{\partial \chi} &= 0, \quad \frac{\partial \eta_V}{\partial \chi} = 0, \quad \frac{\partial \rho_V}{\partial \chi} = 0, \\
\frac{\partial \eta_Q}{\partial \chi} &= -2\eta_Q \tan 2\chi, \\
\frac{\partial \eta_U}{\partial \chi} &= 2\eta_U \cot 2\chi, \\
\frac{\partial \rho_Q}{\partial \chi} &= -2\rho_Q \tan 2\chi, \\
\frac{\partial \rho_U}{\partial \chi} &= 2\rho_U \cot 2\chi, \\
\frac{\partial \eta_I}{\partial \gamma} &= \frac{\eta_0}{2}\left[\phi_p - \frac{\phi_b + \phi_r}{2}\right] \sin 2\gamma, \\
\frac{\partial \eta_Q}{\partial \gamma} &= \frac{\eta_0}{2}\left[\phi_p - \frac{\phi_b + \phi_r}{2}\right] \sin 2\gamma \cos 2\chi, \\
\frac{\partial \eta_U}{\partial \gamma} &= \frac{\eta_0}{2}\left[\phi_p - \frac{\phi_b + \phi_r}{2}\right] \sin 2\gamma \sin 2\chi, \\
\frac{\partial \eta_V}{\partial \gamma} &= -\eta_V \tan \gamma, \\
\frac{\partial \rho_Q}{\partial \gamma} &= \frac{\eta_0}{2}\left[\psi_p - \frac{\psi_b + \psi_r}{2}\right] \sin 2\gamma \cos 2\chi, \\
\frac{\partial \rho_U}{\partial \gamma} &= \frac{\eta_0}{2}\left[\psi_p - \frac{\psi_b + \psi_r}{2}\right] \sin 2\gamma \sin 2\chi, \\
\frac{\partial \rho_V}{\partial \gamma} &= -\rho_V \tan \gamma.
\end{aligned} \tag{A.6}$$

The derivatives with respect to the other parameters imply the derivatives of the absorption and dispersion profiles and these lead us to obtain the derivatives of the Voigt and Voigt-Faraday functions (as defined by Landi degl'Innocenti,

1976):

$$\begin{aligned}
\frac{\partial \phi_j}{\partial x} &= \sum_{M_l - M_u = j} S_{M_l M_u, j} \frac{\partial H(a,\upsilon)}{\partial x}, \\
\frac{\partial \psi_j}{\partial x} &= 2 \sum_{M_l - M_u = j} S_{M_l M_u, j} \frac{\partial F(a,\upsilon)}{\partial x}.
\end{aligned} \tag{A.7}$$

By using the chain rule and the derivatives of $H(a,\upsilon)$ and $F(a,\upsilon)$ with to respect a and υ,

$$\begin{aligned}
\frac{\partial H(a,\upsilon)}{\partial a} &= -2\frac{\partial F(a,\upsilon)}{\partial \upsilon}, \\
\frac{\partial F(a,\upsilon)}{\partial a} &= \frac{1}{2}\frac{\partial H(a,\upsilon)}{\partial \upsilon}, \\
\frac{\partial H(a,\upsilon)}{\partial \upsilon} &= 4aF(a,\upsilon) - 2\upsilon H(a,\upsilon), \\
\frac{\partial F(a,\upsilon)}{\partial \upsilon} &= \frac{1}{\sqrt{\pi}} - aH(a,\upsilon) - 2\upsilon F(a,\upsilon),
\end{aligned} \tag{A.8}$$

we find

$$\begin{aligned}
\frac{\partial H(a,\upsilon), F(a,\upsilon)}{\partial B} &= \frac{\partial H(a,\upsilon), F(a,\upsilon)}{\partial \upsilon}\frac{\Delta\lambda_{i_j}}{\Delta\lambda_\mathrm{D}}\frac{1}{B}, \\
\frac{\partial H(a,\upsilon), F(a,\upsilon)}{\partial \upsilon_\mathrm{LOS}} &= \frac{\partial H(a,\upsilon), F(a,\upsilon)}{\partial \upsilon}\frac{-\lambda_0}{c\Delta\lambda_\mathrm{D}}, \\
\frac{\partial H(a,\upsilon), F(a,\upsilon)}{\partial \Delta\lambda_\mathrm{D}} &= \frac{\partial H(a,\upsilon), F(a,\upsilon)}{\partial \upsilon}\frac{-\upsilon}{\Delta\lambda_\mathrm{D}}.
\end{aligned} \tag{A.9}$$

B

Inversion result maps

This appendix shows the resunting maps from the inversion of the normal map (data set #1) and high SNR map (data set #2) discussed in Chapter 7. The first 5 figures display the magnetic field strengths, inclinations, azimuths, stray-light factors and LOS velocities inferred from the inversion of the normal map. The maps have been rotated 90 degrees conterclockwise in order to fit the page, so the slit scan direction is from bottom to top. Also, we show a small area of $160'' \times 80''$ to see small details. The two boxes over-plotted in the maps outline for the small IN and network areas of $7.4'' \times 7.4''$ shown in Figs. 7.15 and 7.16, white and red boxes, respectively. Arrows indicate the position of the profile fits showed in Sec. 7.3.2 and indicated with numbers. Pixels #1 and #2 belong to the network, while #3 and #4 are representative of IN regions. Black areas correspond to non-inverted pixels. The field strength color bar has been clipped at 1000 G (white). The next five maps display the same ME quantities but corresponding to the inversion of the high SNR map.

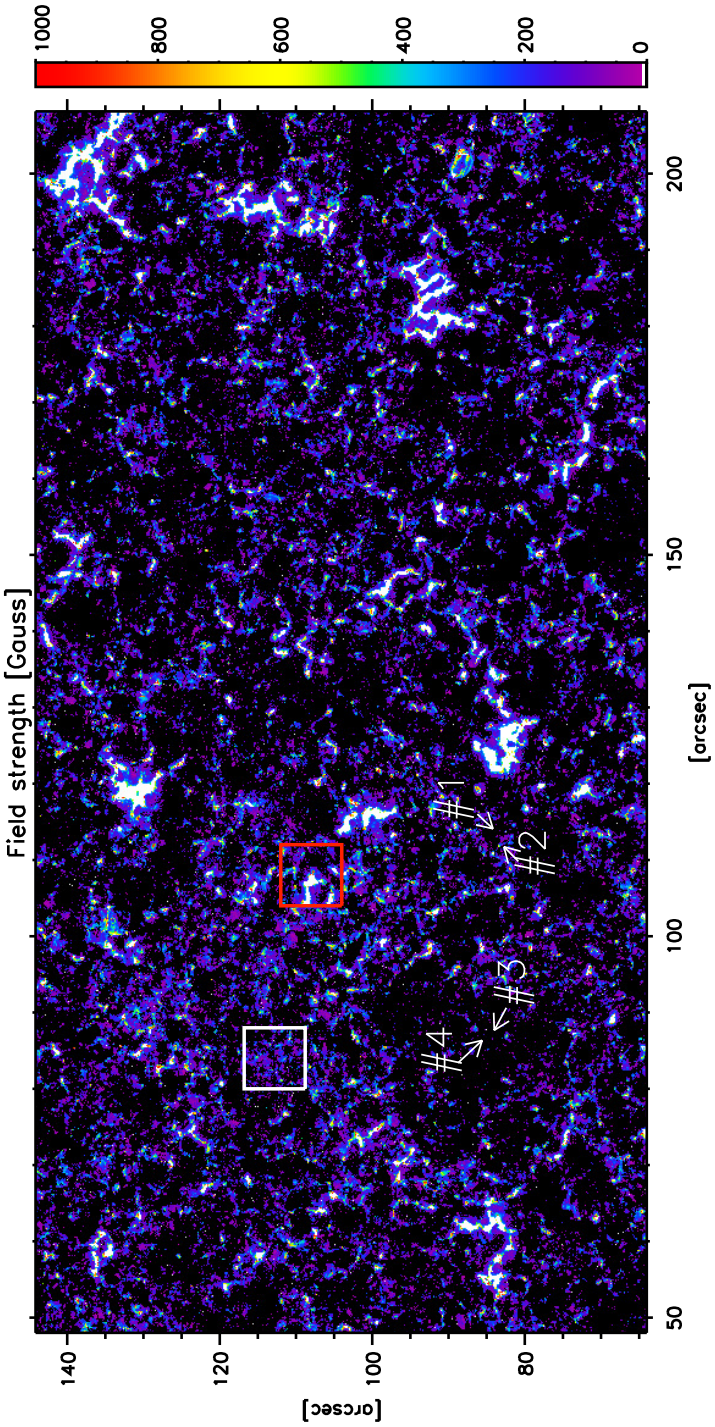
Field strength [Gauss]
1000
800
600
400
200
0
#1
#2
#3
#4
[arcsec]
140
120
100
80
50
100
150
200
[arcsec]

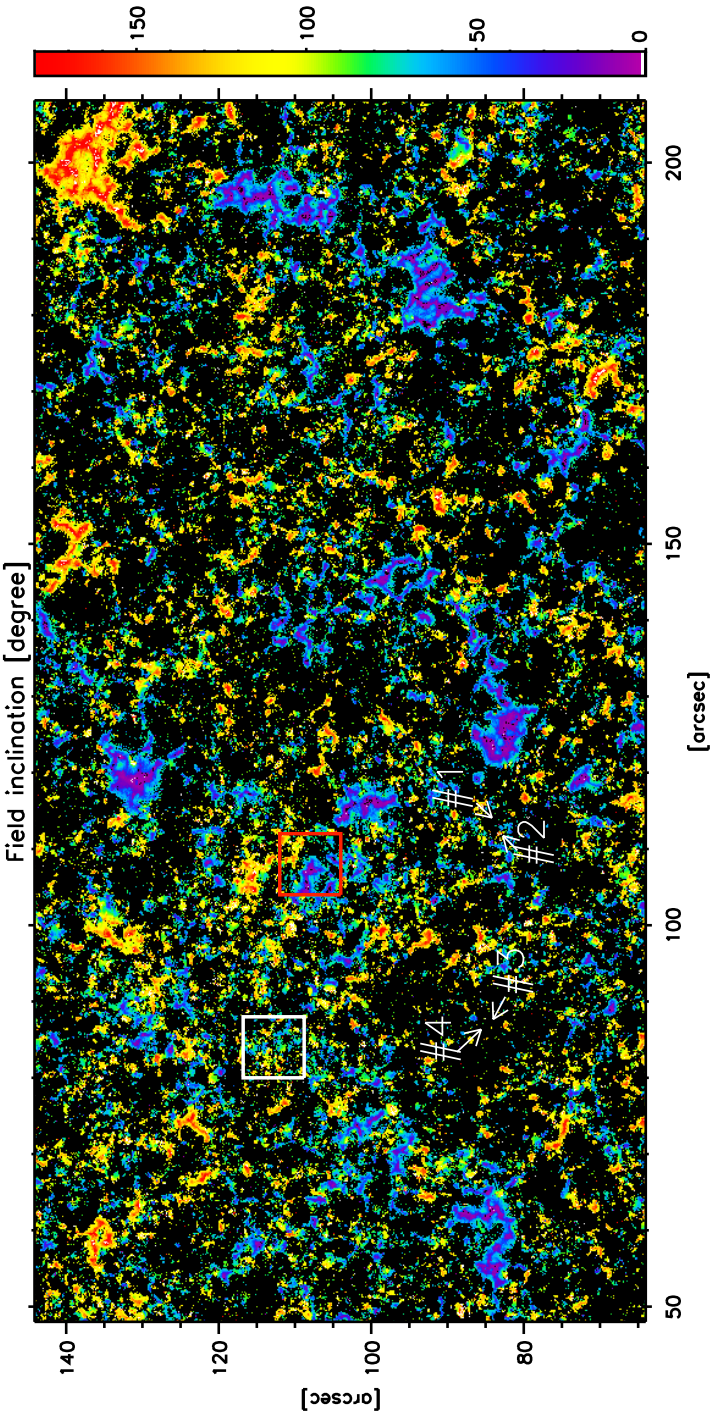
Field inclination [degree]
150
100
50
0
140
120
100
80
[arcsec]
50
100
150
200
[arcsec]
#1
#2
#3
#4

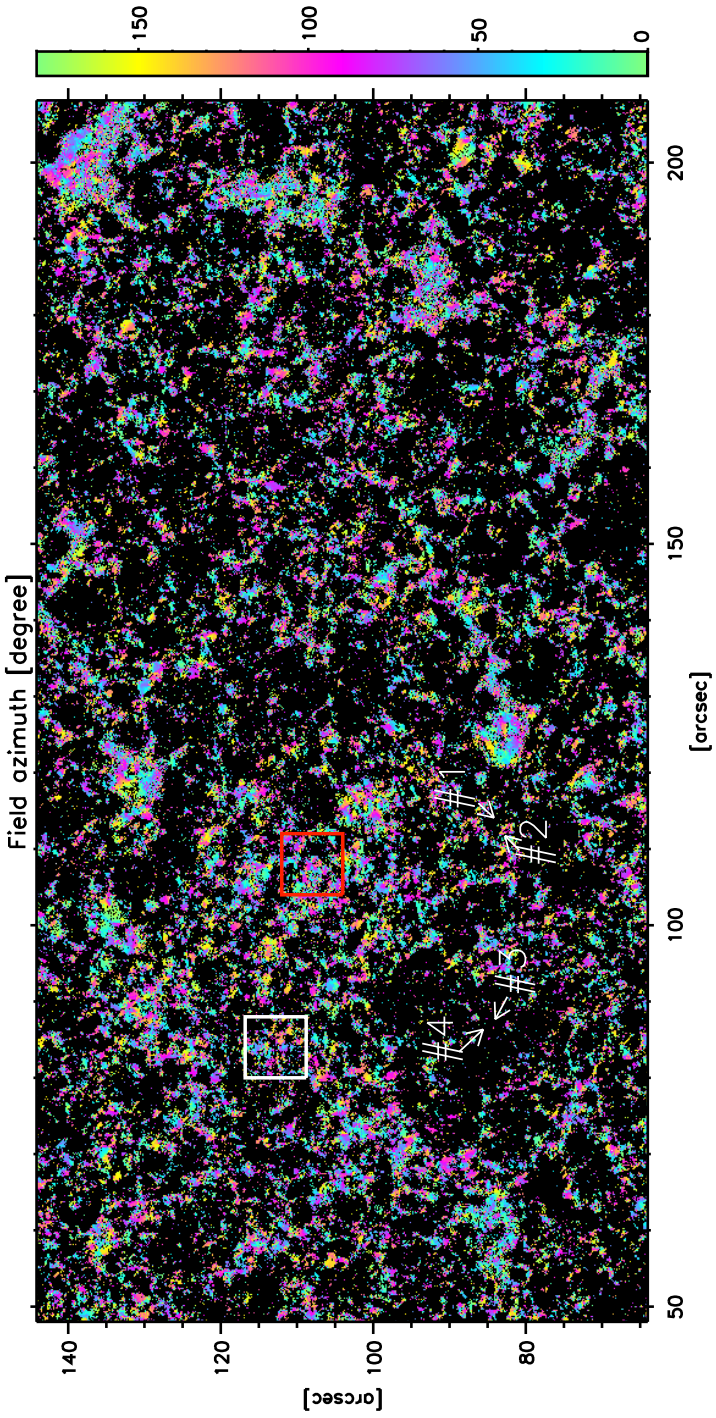
150
100
50
0
Field azimuth [degree]
#1
#2
#3
#4
140
120
100
80
[arcsec]
200
150
100
50
[arcsec]

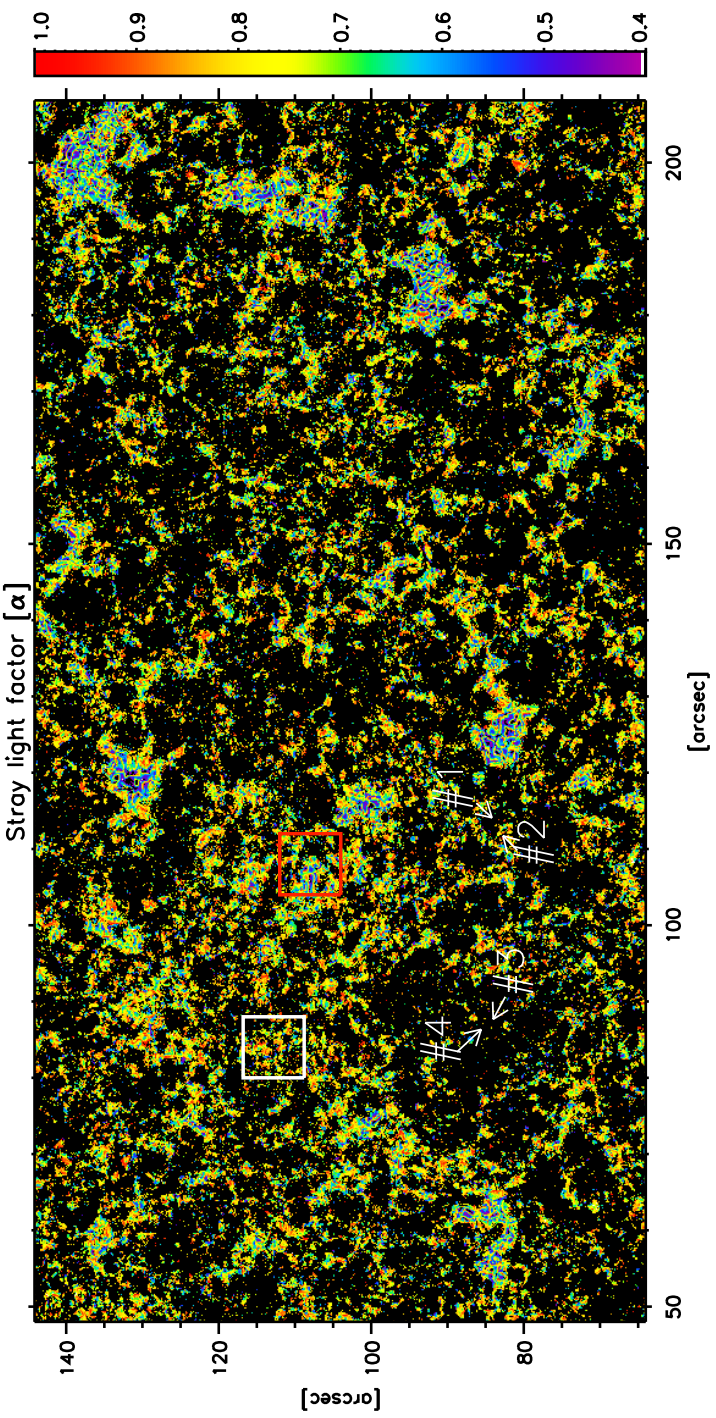
Stray light factor [α]
1.0
0.9
0.8
0.7
0.6
0.5
0.4
#1
#2
#3
#4
50
100
150
200
[arcsec]
80
100
120
140
[arcsec]

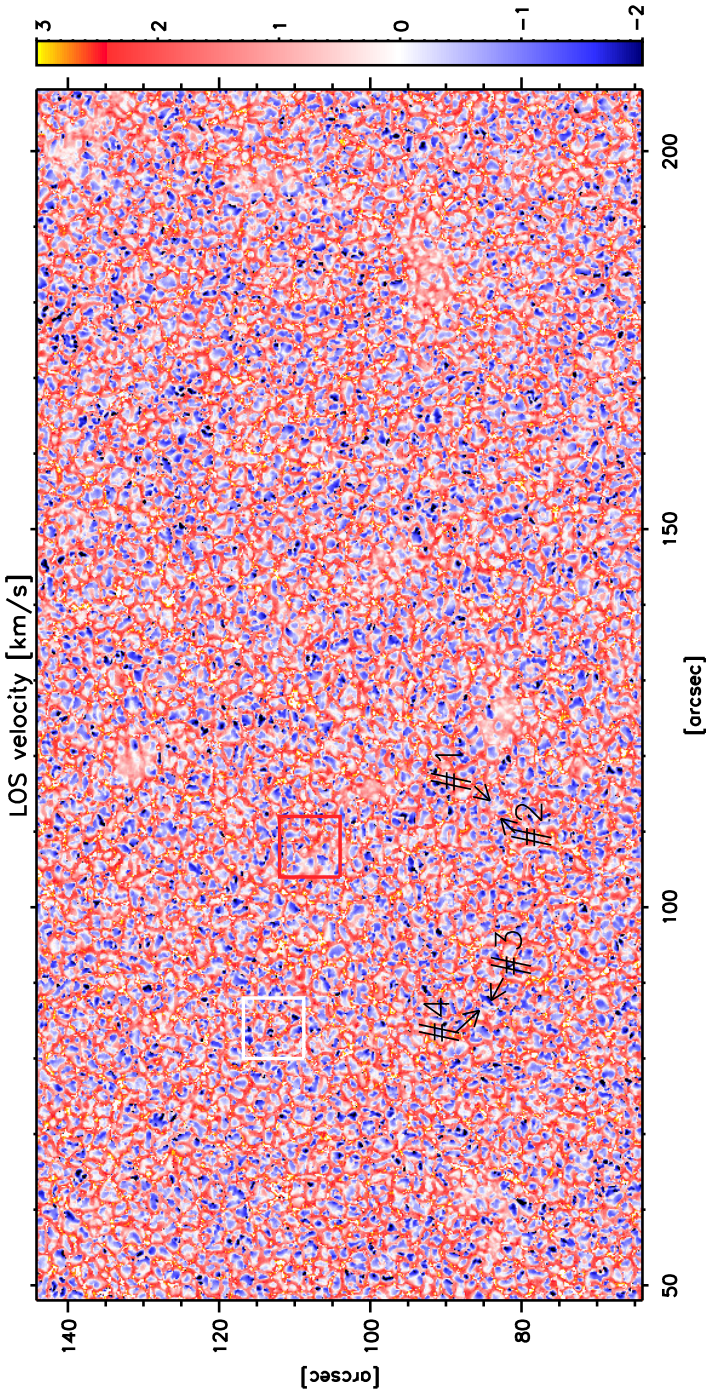
3
2
1
0
−1
−2
LOS velocity [km/s]
#1
#2
#3
#4
140
120
100
80
[arcsec]
200
150
100
50
[arcsec]

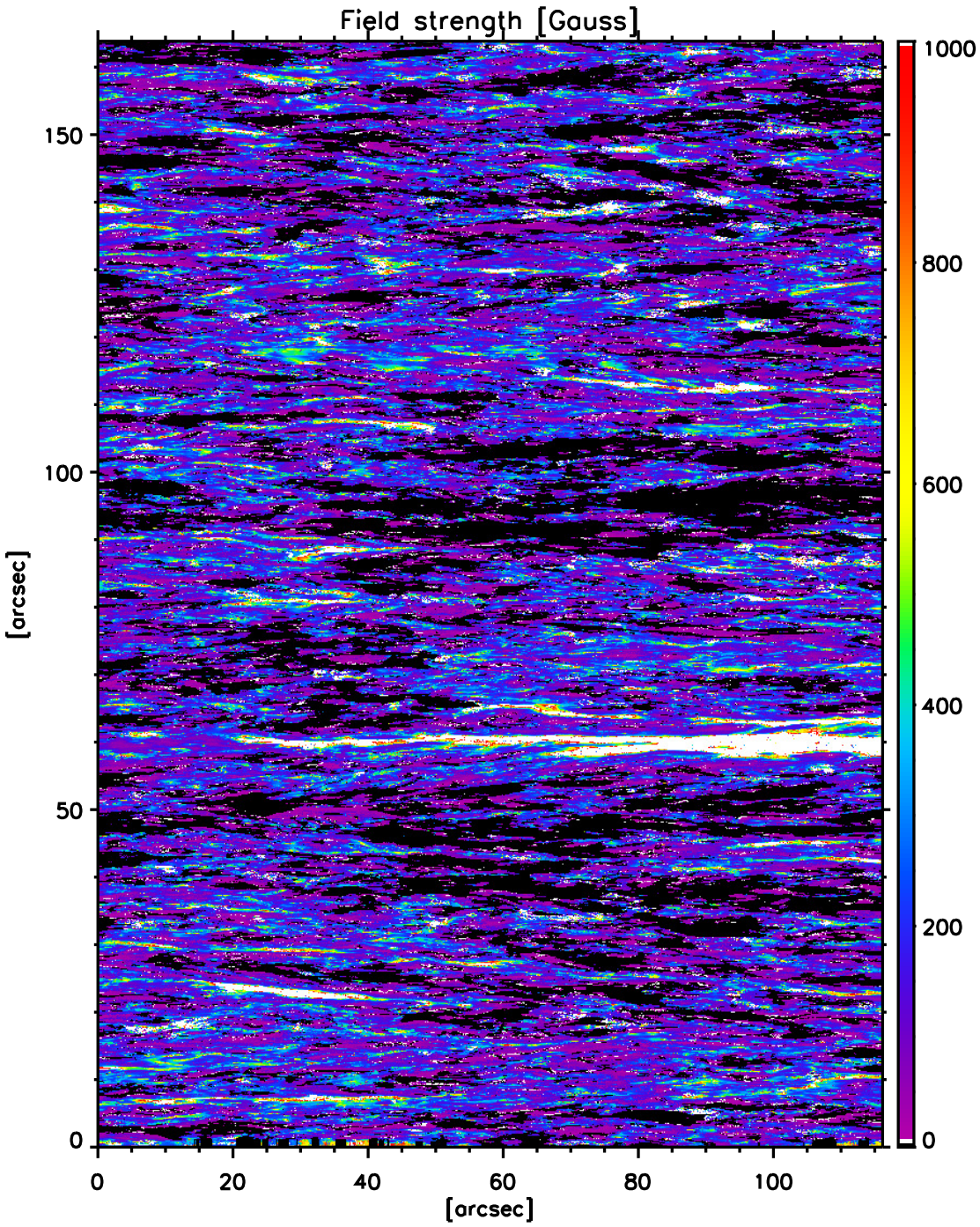
Field strength [Gauss]
1000
800
600
400
200
0
150
100
50
0
[arcsec]
0
20
40
60
80
100
[arcsec]

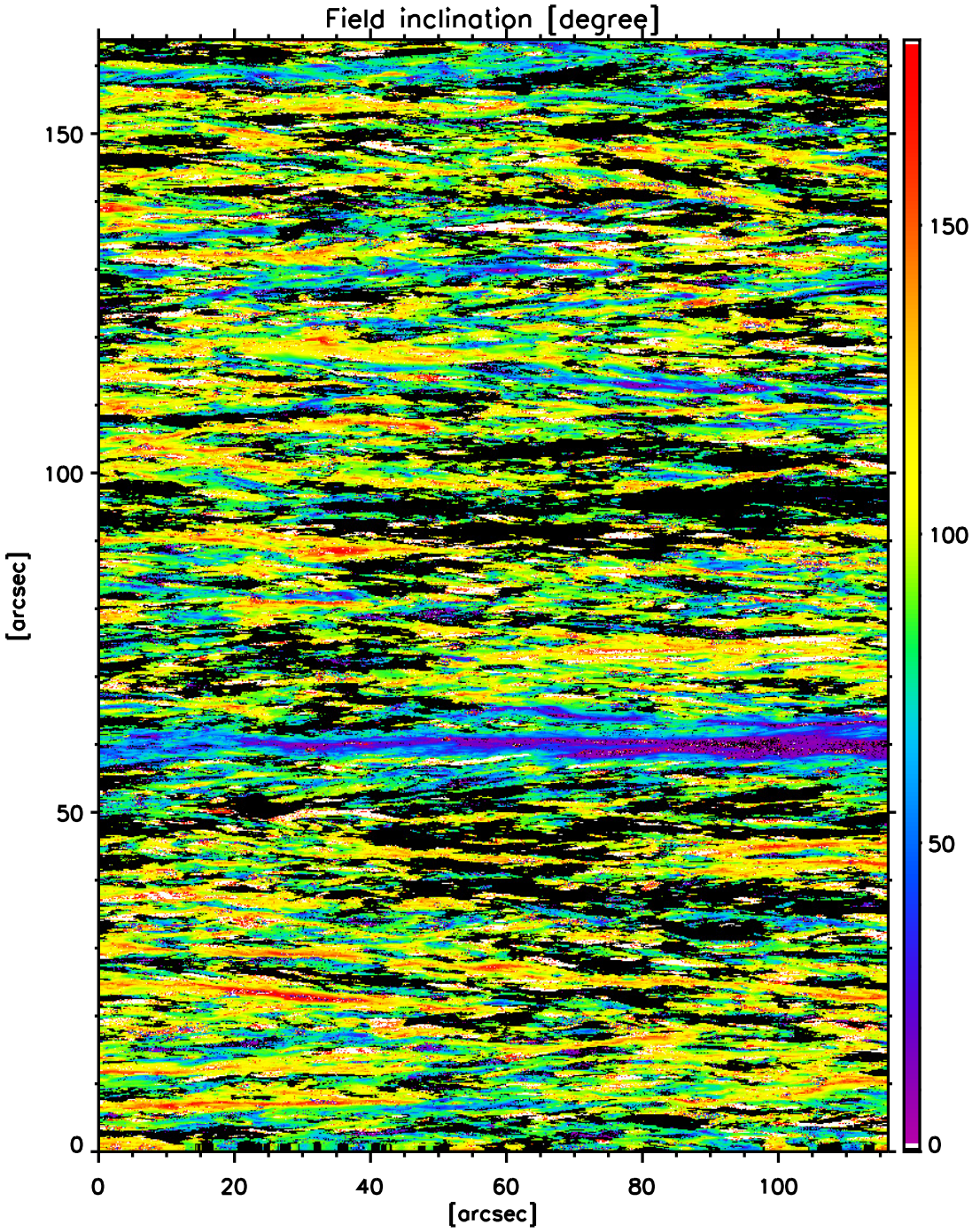
Field inclination [degree]
150
100
50
0
[arcsec]
0
20
40
60
80
100
[arcsec]
150
100
50
0

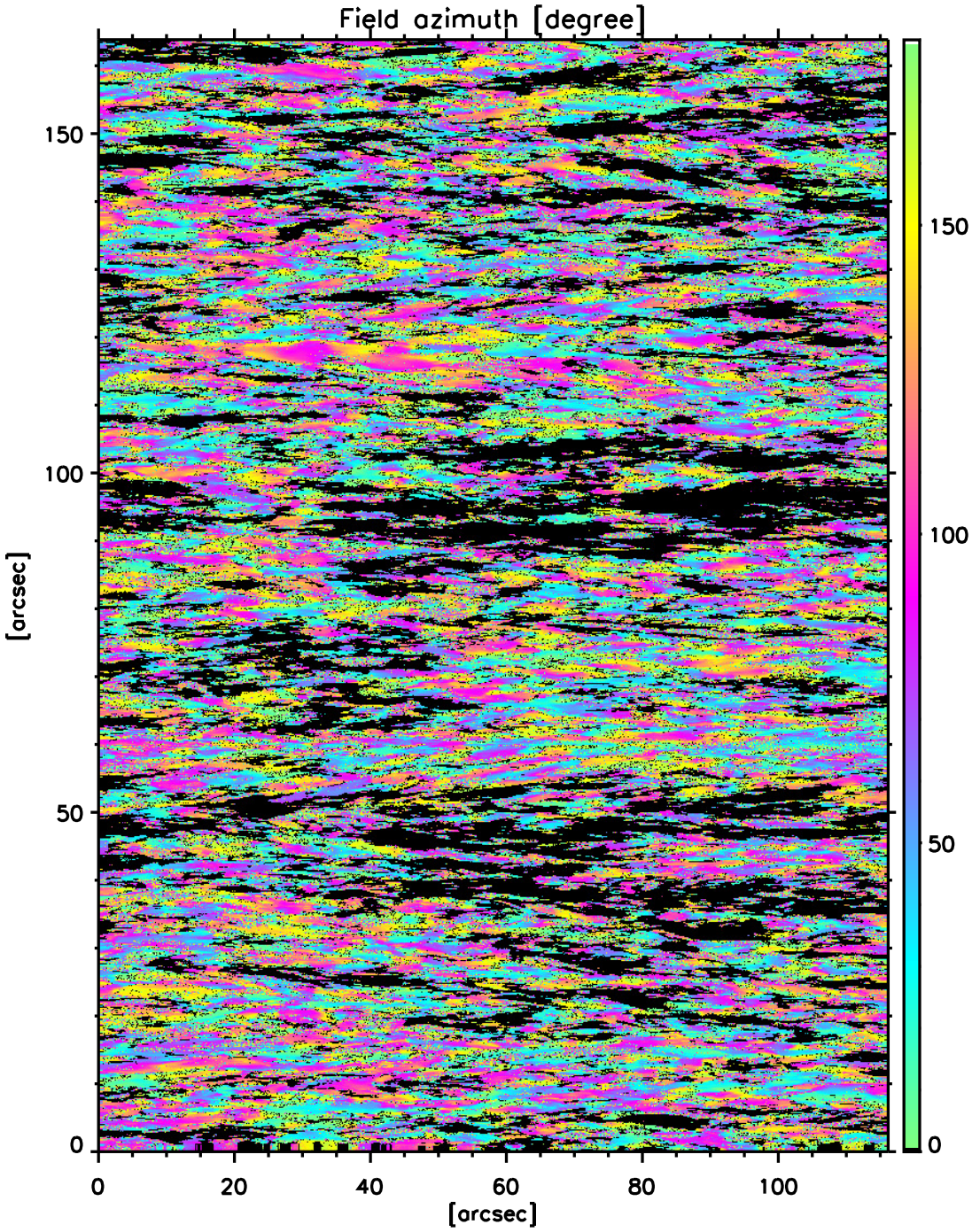
Field azimuth [degree]
150
100
50
0
[arcsec]
0
20
40
60
80
100
[arcsec]
150
100
50
0

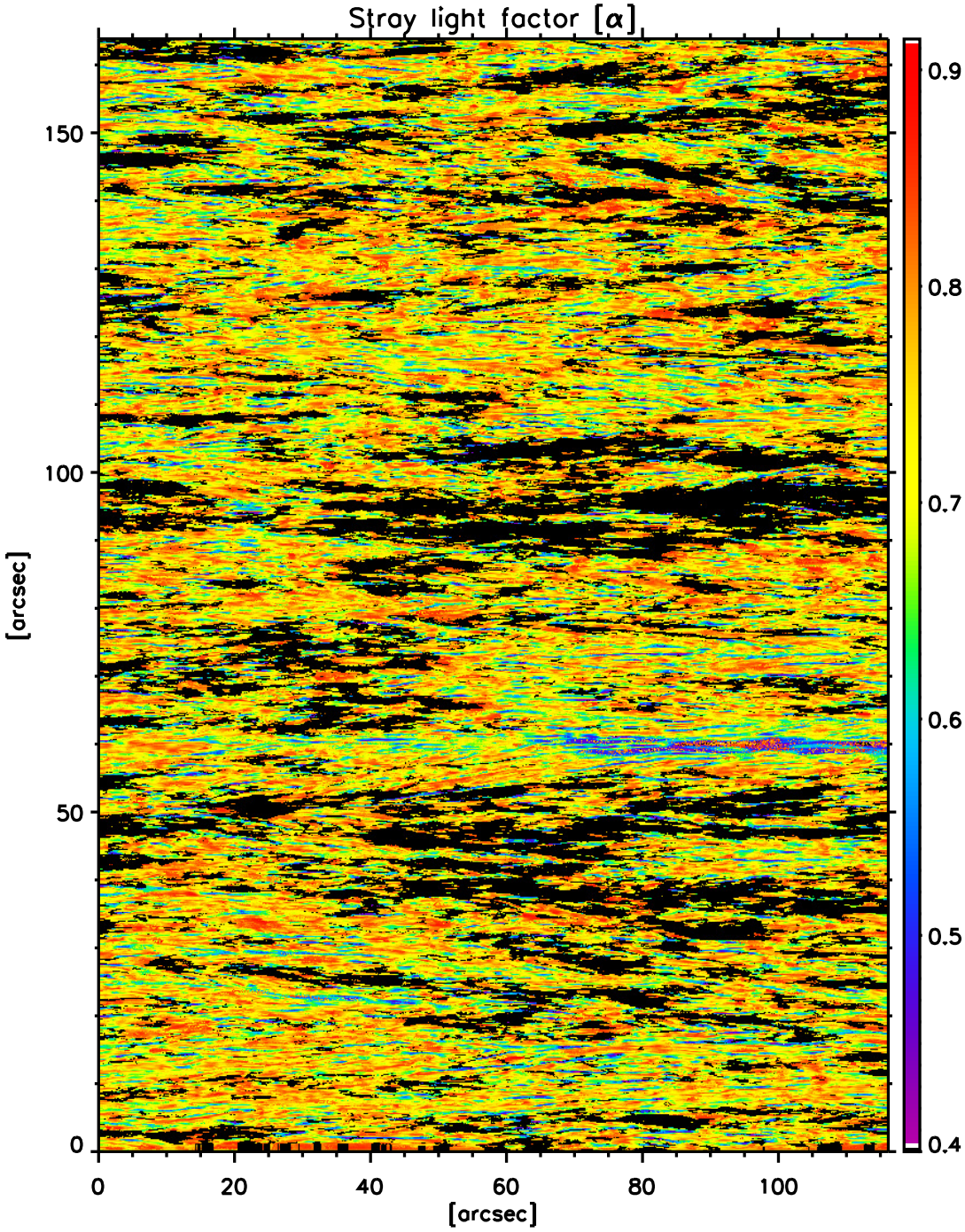
Stray light factor [α]
150
100
50
0
[arcsec]
0
20
40
60
80
100
[arcsec]
0.9
0.8
0.7
0.6
0.5
0.4

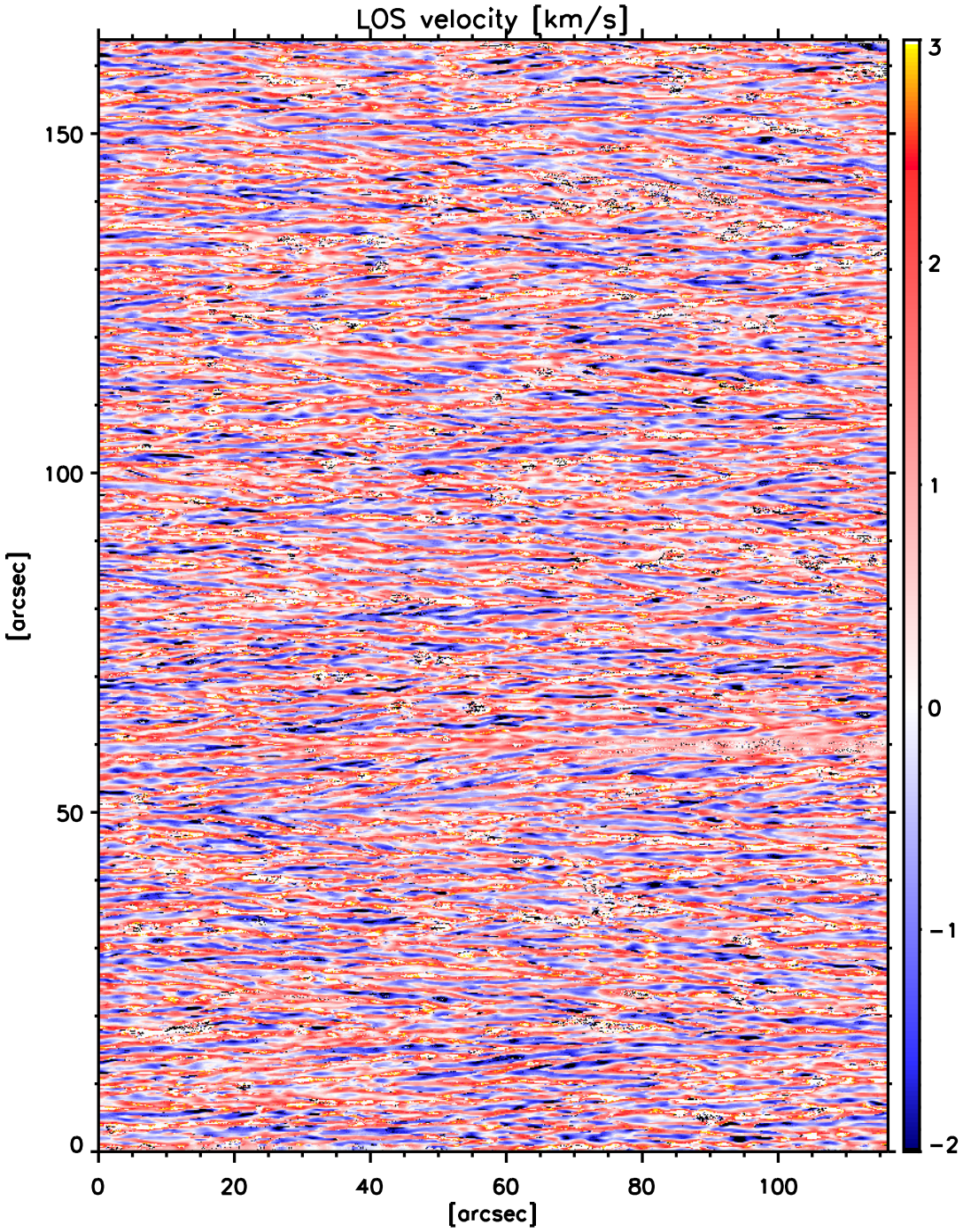
LOS velocity [km/s]
150
100
50
0
[arcsec]
0
20
40
60
80
100
[arcsec]
3
2
1
0
−1
−2

C

Numerical tests

In this Appendix we carry out numerical tests to check the accuracy of the MILOS code to infer the magnetic field vector and the LOS velocity from the Stokes profiles observed by vector magnetographs. In particular we analyze the uncertainties due to the limited spectral resolution, the limited wavelength sampling, and the different position of the wavelength points.

We focus our attention in the Fe I spectral lines at 525.02 and 525.06 nm. These two lines show different sensitivities to the magnetic field, being 1.5 and 3 the corresponding Landé factors. The synthetic profiles are generated using MELANIE.

C.0.5 Reference profiles and initialization of the code

As described in Chapter 4, we use MELANIE to synthesize the Stokes profiles emerging from 10 000 ME model atmospheres with a uniform random distribution of vector magnetic fields (B from 0 to 2500 G, inclination and azimuth from 0 to 180°) and LOS velocities (between -4 and 4 km s^{-1}). The remaining model parameters have been taken from a fit to the FTS atlas. The wavelength sampling has been 0.1 pm, with a total of 100 samples across the spectral line.

All inversions have been carried out under with the following initialization: $\lambda_0 = 10$, maximum number of iterations $k = 300$ (with ϵ_1 small enough to allow the 300 iterations), $S_0 = 0.2$, $S_1 = 0.8$, $\eta_0 = 6.5$, $B = 200$ G, $\gamma = 20°$, $\chi = 20°$, $\Delta\lambda_D = 30$ mÅ, $v_{LOS} = 0.25$ km s^{-1} and $a = 0.03$. Noise of the order of 10^{-3} at the level of Stokes I have been added to the simulated profiles used throughout this Appendix. In what follows we describe in detail each of the

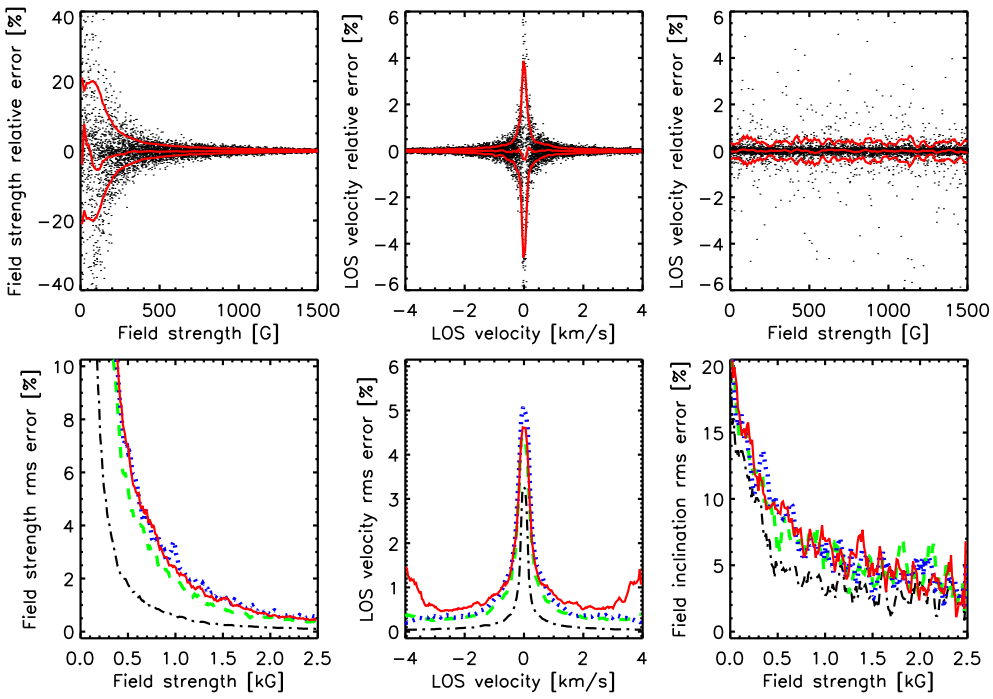

FIGURE C.1:— *Top*: Relative errors for the magnetic field strength, field inclination and LOS velocity from the inversion of five wavelength samples ($[\pm 40, \pm 80]$ mÅ plus a wavelength point in the continuum). The solid lines stand for the corresponding mean and rms values. *Bottom*: rms errors for different parameters. The dash-dotted line corresponds to the full profile inversion, dashed to $[\pm 80, \pm 40, 0]$ mÅ, solid to $[\pm 60, \pm 30]$ mÅ, and dotted to $[\pm 100, \pm 40]$ mÅ.

tests that have been carried out.

C.0.6 Dependence with the wavelength sampling

Here we evaluate the ME uncertainties when inferring physical parameters from the Fe I 525.06 nm spectral line sampled at only few wavelength points and when these samples are taken at different wavelength positions. To this end we have performed three set of inversions: one with the spectral line sampled at five wavelength positions plus a wavelength point in the nearby continuum, and two inversions of the same spectral line sampled at only four wavelength positions plus the continuum. For all inversions the noise was $10^{-3} I_c$. An instrumental filter of 6 pm FWHM has been considered.

The upper panels from Fig. C.1 show the relative errors of the parameters inferred from the inversion of five wavelength samples ($[\pm 40, \pm 80]$ mÅ plus a

wavelength point in the continuum) against the real values. The panels show the individual uncertainties of each of the 10 000 ME inversions. Overploted is the corresponding rms values (red solid line). The bottom panels show the rms values of the relative errors but for the magnetic field strength, its inclination and the LOS velocity from the inversion of the spectral line by taking into account: the full profile (100 wavelength samples), five wavelength samples, $[\pm 80, \pm 40, 0]$, plus a wavelength point in the continuum (green dashed) and two sets of four wavelength sampling (plus continuum) at $[\pm 60, \pm 30]$ and $[\pm 100, \pm 40]$ mÅ (red solid and blue dotted lines, respectively)

The retrieved errors when considering the full profile are almost negligible, being for the magnetic field strength, smaller than 2% for fields larger than $\sim$500 G, or smaller than 0.1% for the LOS velocity. This results are solely due to photon noise and slightly augmented by the 6 pm FWHM filter. The results for the inclination are noisier.

In general, the uncertainties are larger when limiting the number of wavelength samples. The errors in the inferred field strengths are smaller than $\sim$3% for strong fields, $B > 1000$ G. They become larger for weak fields mainly due to the noise, i.e., the weaker the magnetic field strength, the smaller amplitude size of the polarimetric signals (for fields on the weak field regimen and fixed orientation), therefore the Stokes profiles are more affected by noise. For the field inclination (bottom right panel) rms errors of $\sim$5% are to be expected for fields stronger than 1000 G. Note that the inclination is more uncertain for weak fields. The relative errors in the velocity are less than 1% except for velocities close to zero (upper middle panel). Interestingly, the errors in the inferred velocities do not depend on the field strength, as demonstrated by the upper right panel of Fig. C.1. When the velocity is mainly determined by the Stokes I profile, i.e., in the absence of a magnetic field, it is determined from all Stokes parameters likewise, when a magnetic field is present.

Figure C.1 also illustrates the dependence of the errors on the number of wavelength samples and sample points (bottom panels). First, notice the larger errors when decreasing the number of wavelength samples. Secondly, and more interestingly, note that the use of one more wavelength point decreases the rms error of the field strength by less than 1% only, with no clear improvement in the field inclination and LOS velocity. Moreover, there are no significant differences on the field strength and inclination by using different wavelength positions. The error in the LOS velocity, however, increases at high velocity values when the points are less distant (red solid curve). In this case, the wavelength points sample only one wing of the line when large velocities, hence providing lower sensitivity (see Fig. 3.3). Notice that in this case, the spectral shift corresponding to 3 km s^{-1} would be 5.1 pm, large enough to misplace one

of the selected wavelength samples, consequently the Stokes profile is poorer sampled, yielding to large uncertainties.

In all tests, the thermodynamic parameters are not well recovered because of crosstalk problems (Chapt. 3.2.2). This, however, does not imply a poor determination of the magnetic field vector and LOS velocity as our results show. The mean values for the thermodynamic parameters and averaged for all the 10 000 ME inversions were, for the 525.06 nm spectral line and for the tests discussed in this section: $\eta_0 = 7.4 \pm 0.9$, $\Delta\lambda_D = 0.0300 \pm 0.0007$, $a = 0.30 \pm 0.03$, $S_0 = 0.02 \pm 0.02$ and $S_1 = 1.00 \pm 0.02$.

C.0.7 Dependence with the instrumental profile

Here we determine the variation of the uncertainties of the different model parameters with respect the width of the instrumental profile. To this end, the Stokes profiles of the basis are convolved with instrumental profiles of different widths ranging from 4 to 12 pm. The filter profiles are described by a Gaussian function. To amplify the effects of the instrumental profile we have only taken 5 wavelength samples within the spectral line ($[\pm 40, \pm 80]$ mÅ) plus a point in the nearby continuum. The line used for this test is Fe I at 525.02 nm. The inversion procedure is the same as described before.

Figure C.2 displays the variation of the relative rms errors of the magnetic field strength and LOS velocity as a function of the real field strength and velocity values (left panels) and filter width (right panels). The relative errors are small even for widths of 120 mÅ. The rms values for the field strength and LOS velocity slightly increase with increasing filter width. This variation seems not to depend on the magnetic field range (top right panel).

The relative rms errors for the magnetic field inclination and its azimuth are in Fig. C.3. The errors for the field inclination are larger for weaker fields and for vertically oriented fields. In both cases, the error increases due to that the linear polarization signals are smaller in amplitude, therefore more affected by noise. The variation of the rms errors with the filter width and for different ranges of inclination angles is small. Also, the rms for the field azimuth do not vary much for increasing filter widths. In both cases, the relative uncertainties are smaller than 10%.

In summary, the rms of the inferences do not vary significantly with broader filter widths. This indicates that, the uncertainties due to the limited wavelength sampling and noise dominate. We caution that the ME profiles are symmetric ones, therefore the instrumental filter only diminishes the amplitude of the polarization Stokes profiles and smooths out the shape of the Stokes vector. The situation may be much unfavorable when dealing with real profiles, which

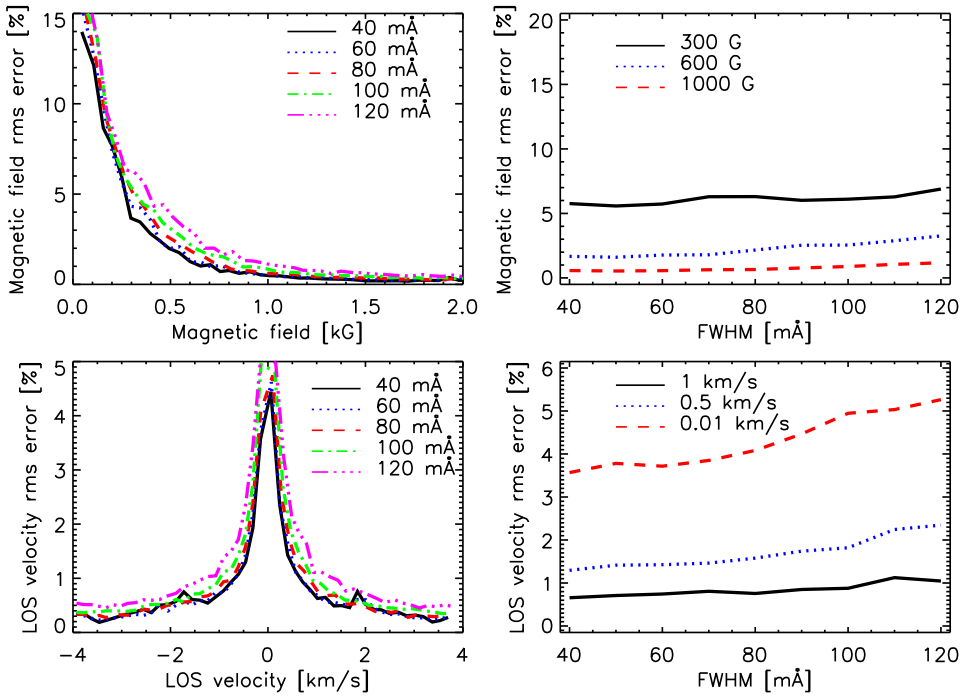

FIGURE C.2:— *Left:* Relative rms errors for the magnetic field strength (top) and for the LOS velocity (bottom) and for different instrumental widths. *Right:* relative rms errors as a function of the FWHM and for pixels having the indicated values of B and $v_{\rm LOS}$. The results correspond to the Fe I at 525.02 nm spectral line sampled at five wavelength,$[\pm 80, \pm 40]$ mÅ, plus a point in the nearby continuum.

exhibit asymmetries.

C.0.8 Influence of the stray light

Throughout previous tests we have assumed that the magnetic field occupies the whole resolution elements, i.e., we have considered magnetic filling factor equal one. However, current measurements of the magnetic field vector on the solar surface indicate that the magnetic field occupies only a fraction of the pixel. The filling factor depends on the spatial resolution and the observed solar feature. Besides, solar instrumentation is not free from scattered light contamination.

Then, suppose that a magnetic atmosphere occupies a fraction f of the resolution element and another one and non-magnetized occupies the rest of the resolution element. Then, if $\mathbf{I}_{\rm m}$ stands for the magnetic component and $\mathbf{I}_{\rm nm}$

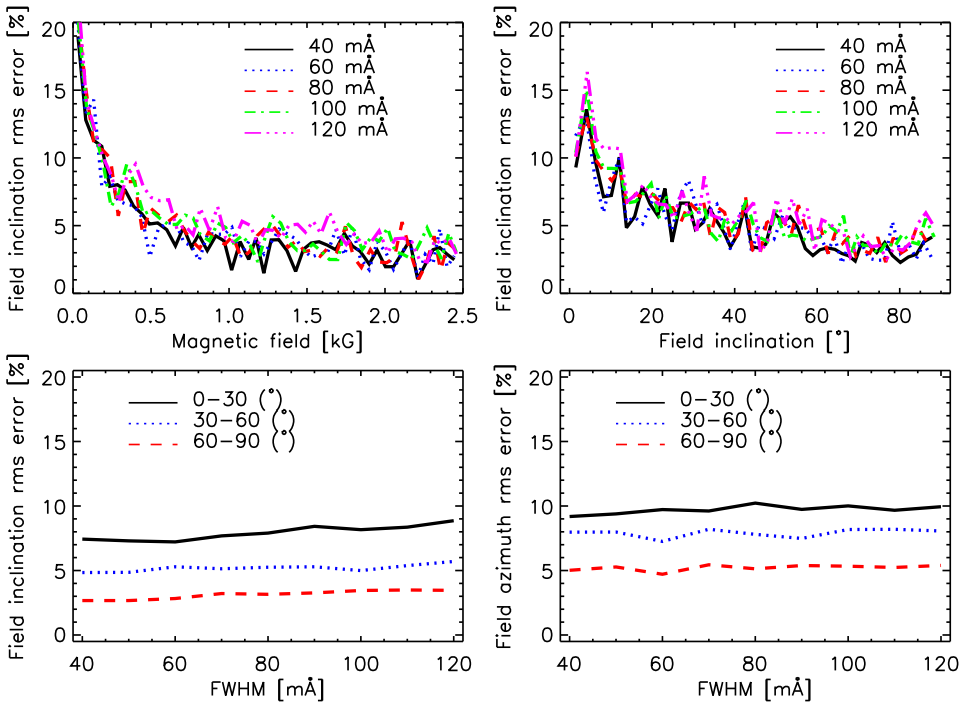

FIGURE C.3:— *Top panels*: Magnetic field inclination relative rms error with respect the magnetic field and its inclination and for different instrumental profile widths.*Bottom panels:* Magnetic field inclination and its azimuth with respect the FWHM of the filter and for pixels having the indicated values of field inclination. As in Fig. C.2 the results correspond to the Fe I at 525.02 nm spectral line sampled at five wavelength,$[\pm 80, \pm 40]$ mÅ, plus a point in the nearby continuum.

is that emerging from the non-magnetized atmosphere, the observed Stokes profile is $\mathbf{I} = (1-f)\mathbf{I}_{\rm m} + f\mathbf{I}_{\rm nm}$. This relation shows that the amplitude of the polarization signals decrease inversely linearly with filling factor. The non-magnetized atmosphere can be considered as stray light contamination which may be known a priory. This section is then aimed at determining the effect of a stray light contamination on the various parameter inferences.

To analyze the influence of stray light we have generated a second reference basis of Stokes profiles (magnetic component) contaminated by a stray-light profile (non-magnetic component). The stray light has been modeled using the same thermodynamic parameters than that used to generate the Stokes profiles. To make it different from the profiles of the basis we have broadened the Stray light by using a macro turbulent velocity of 1 km s^{-1}. We have also fixed the Doppler shift. These two things, together with the presence of a magnetic field

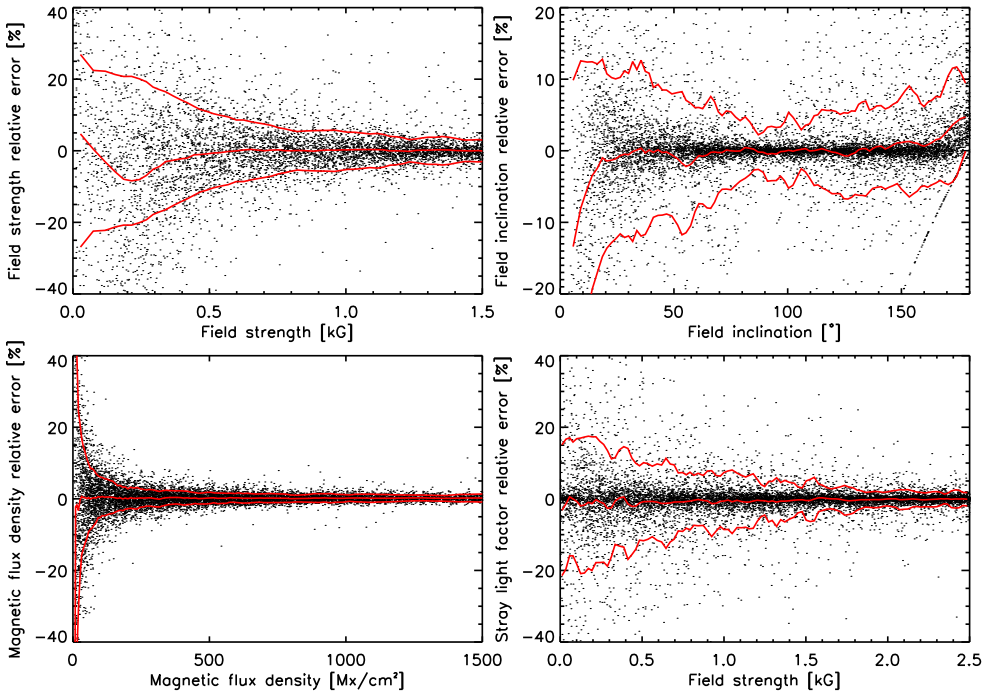

FIGURE C.4:— Individual relative errors for the magnetic field strength, field inclinations, magnetic flux density (absolute valued) and stray light factor, for the Fe I at 525.06 nm spectral line sampled at five wavelength,$[\pm 80, \pm 40]$ mÅ, plus a point in the nearby continuum. The red solid lines stand for the corresponding rms errors.

vector, are the only differences between the non-magnetic component and the magnetic component. There is no recipe to simulate an ideal stray-light profile. In real observations it is usually evaluated by averaging the Stokes I profiles in the surrounding, non-magnetized areas. Therefore, it seems reasonable to consider the stray light as a broader Stokes I profile with fixed Doppler shift. The reference basis have been generated as described in Sec. C.0.5. The filing factor f has been generated with an uniform random distribution varying from $\alpha = 0$ to 0.5.

The inversion procedure is the same as for the previous test. In addition we have the magnetic filling factor f as free parameter. Initially, f have been set to 0.2 and for all inversions. Also, to worsen the situation we have convolved the Stokes profiles with a Gaussian of 6 pm simulating an smearing profile and taken only 5 wavelength samples at $[\pm 40, \pm 80]$ mÅ, plus a wavelength point in the continuum. The spectral line used for this test is the Fe I line 525.06 nm. This situation clearly represent the worst case scenario.

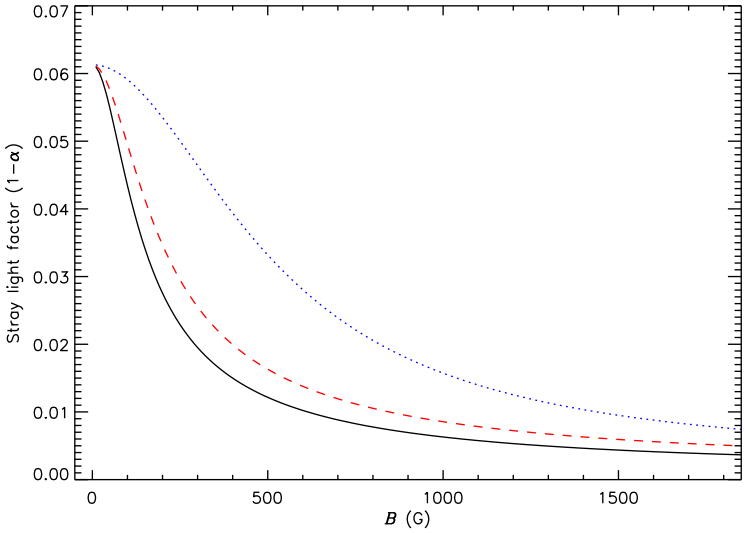

FIGURE C.5:— Minimum detectable Stray light factor as function of the magnetic field strength for three different orientations of the magnetic field vector.

The results are shown in Fig. C.4. The stray light contamination has strong impact on the inferences. The scatter of the individual errors have increased for the magnetic field as well as for the field inclination as compared to the previous tests. The larger scatter is due to the reduced sensitivity of the spectral line by a second component, which worsen the determination of the filling factor. In addition, the polarization Stokes profiles are of smaller amplitude, depending of the f value.

Notice that we are using only 5 wavelength samples along the spectral line. This leaves as with a total of 20 observables. The ME code has to determine 10 free parameters. Also, the spectral line has mid sensitivity to the field strength. However, we obtain that the mean rms errors for the stray light factor ranges from less that 5% for strong fields to ∼20% for weaker fields (bottom right panel). The errors on the magnetic field do not exceed ∼20% for weak fields. For the field inclination, the rms errors are smaller than ∼10%. Interestingly, the rms errors of the magnetic flux density (bottom left panel) are small: *the magnetic flux is always determined with high accuracy*. Note the fluctuation on the rms errors (red solid lines). This indicates worse convergence of the ME code for individual pixels. Finally, the accumulations of points at the bottom right corner for the field inclination panel is due to that the inclination can be nor smaller than 0° neither larger than 180°.

But, can we predict the filling factor uncertainties? The answer is on the linear equations that couple the physical parameters with the polarization profiles, i.e. the ME RFs. They can be used to infer the minimum detectable quantities for the model parameters (see Chap. 3). Let us use Eq. (3.8) to infer the minimum expected errors for the filling factor, f, in this test, i.e., we assume the same model parameters used to generate the profile basis, a filter width of 6 pm and 5 wavelength samples. The results are shown in Fig. C.5. The figure illustrates the variation of the rms value for the filling factor of the non-magnetic component, $\sigma_{(1-f)}$, as a function of the magnetic field strength and for three different inclinations of the field. Clearly, $\sigma_{(1-f)}$ increases as the magnetic field decreases. In average, $\sigma_{(1-f)} \simeq 1\%$ for strong fields of 1500 G, and $\sigma_{(1-f)} \simeq 6\%$ for fields close to 0. The rms values of the test are of $\sim 3-5\%$ for strong fields and $\sim 15-20\%$ in the absence of field. The filling factor ranges from $f = 0$ to 0.5.

C.1 Conclusions

The accuracy of the physical parameters retrieved from ME inversions depends on the observed spectral line, the number of wavelength samples and position of the wavelength points. It also depends on the signal to noise ratio and on the FWHM of the smearing profile. The field strength vector inferences are more affected by these factors than the that for the LOS velocity. For weak fields, the errors are larger.

Four wavelength samples plus the continuum are sufficient to recover the magnetic field vector and LOS velocity with high accuracy ($\sim$1%) when dealing with ME Stokes profiles. The quality of the inferences does not increase much when using 5 wavelength samples. The differences on inclination are not detectable, being the same for all cases. The results slightly depend on the target spectral line.

These results are in agreement with those reported by Graham et al. (2002). In our tests we also take into account the effect of different wavelength points selection. The accuracy of the results is better or at least of the order of those presented for different instruments, i.e, compared to the rms noise of 20 ms^{-1} on the velocity for MDI (Scherrer et al. 1995) or to the 13 ms^{-1} and 10 G on velocity and field strength for HMI (Scherrer & SDO/HMI Team 2002). Also compare with those from Martinez Pillet (2007) for the PHI instrument aboard the Solar Orbiter. The accuracy reported in this case is of 8 m s^{-1} and 7 G on the velocity and longitudinal field strength.

These results are valid and constrained to *symmetric ME Stokes profiles*

and high spatial resolution measurements, where the magnetic field fills the whole resolution elements. The extrapolation of these results to real solar data seems not to be straightforward. We have modeled the effect of the Stray light contamination and the results worse. However, they were the expected ones, as we have confirmed by using a theoretical approach.

Bibliography

Anstee, S. D., & O'Mara, B. J. 1995, MNRAS, 276, 859

Asensio Ramos, A., Martínez González, M. J., & Rubiño-Martín, J. A. 2007, A&A, 476, 959

Asensio Ramos, A., & Trujillo Bueno, J. 2007, The Physics of Chromospheric Plasmas, 368, 163

Asplund, M., Nordlund, Å., Trampedach, R., Allende Prieto, C., & Stein, R. F. 2000, A&A, 359, 729

Barklem, P. S., Anstee, S. D., & O'Mara, B. J. 1998, Publications of the Astronomical Society of Australia, 15, 336

Barklem, P. S., Piskunov, N., & O'Mara, B. J. 2000, A&A Supp.Ser., 142, 467

Barklem, P. S., Piskunov, N., & O'Mara, B. J. 2000, A&AS, 142, 467

Boreman, G. D. 2001, Modulation Transfer Function in Optical and Electro-Optical Systems (Bellingham (SPIE))

Brault J., Neckel H., 1987, Spectral atlas of solar absolute disk-averaged and disk-center intensity from 3290 to 12510Å, available at ftp.hs.uni-hamburg.de/pub/outgoing/FTS-atlas

Cabrera Solana, D., Bellot Rubio, L. R., & del Toro Iniesta, J. C. 2005, A&A, 439, 687

Cattaneo, F. 1999, ApJ, 515, L39

Danilovic, S., Gandorfer, A., Lagg, A., Schüssler, M., Solanki, S. K., Vögler, A., Katsukawa, Y., & Tsuneta, S. 2008, A&A, 484, L17

Gingerich, O., Noyes, R. W., Kalkofen, W., & Cuny, Y. 1971, Sol. Phys., 18, 347

Graham, J. D., López Ariste, A., Socas-Navarro, H., & Tomczyk, S. 2002, Sol. Phys., 208, 211

Grigorjev, V. M., & Katz, J. M. 1972, Sol. Phys., 22, 119

Jones, D. R., Perttunen, C. D., & Stuckman, B. E., 1993, Journal of Optimization Theory and Applications, 79, 157

Kentischer, T. J., Schmidt, W., Sigwarth, M., & Uexkuell, M. V. 1998, A&A, 340, 569

Khomenko, E., & Collados, M. 2007a, ApJ, 659, 1726

Khomenko, E., & Collados, M. 2007b, Memorie della Societa Astronomica Italiana, 78, 166

Khomenko, E. V., Shelyag, S., Solanki, S. K., Vögler, A. 2005, A&A, 442, 1059

Khomenko, E. 2006, Solar MHD Theory and Observations: A High Spatial Resolution Perspective , 354, 63

Kurucz, R. L., Furenlid, I., & Brault, J. T. L. 1984, National Solar Observatory Atlas, Sunspot, New Mexico: National Solar Observatory, 1984,

Landi degl'Innocenti, E. 1976, A&AS, 25, 379

Landi Deglinnocenti, E., & Landi Deglinnocenti, M. 1977, A&A, 56, 111

Landi degl'Innocenti, E. 1992, Solar Observations: Techniques and Interpretation, 71

Landolfi, M., & Degl'Innocenti, E. L. 1982, Sol. Phys., 78, 355

Landi degl'Innocenti, E., & Landolfi, M. 2004, Astrophysics and Space Science Library, 307

Lites, B. W., & Skumanich, A. 1990,ApJ, 348, 747

Marsch, E., Marsden, R., Harrison, R., Wimmer-Schweingruber, R., & Fleck, B. 2005, Advances in Space Research, 36, 1360

Martínez Pillet, V., Collados, M., Sánchez Almeida, J., González, V., Cruz-Lopez, A., Manescau, A., Joven, E., Paez, E., Diaz, J., Feeney, O., and 3 coauthors. 1999, ASP Conf. Ser. 183: High Resolution Solar Physics: Theory, Observations, and Techniques, 183, 264

Martínez Pillet, V., Bonet, Jose A., Collados, Manuel V., Jochum, Lieselotte, Mathew, S., Medina Trujillo, J. L., Ruiz Cobo, B., del Toro Iniesta, Jose Carlos, Lopez Jimenez, A. C., Castillo Lorenzo, J., and 17 coauthors. 2004, Proc. SPIE, 5487, 1152

Mauas, P. J., Avrett, E. H., & Loeser, R. 1988, ApJ, 330, 1008

Mein, P. 1971, Sol. Phys., 20, 3

J. Meiron, "Damped Least-Squares Method for Automatic Lens Design," J. Opt. Soc. Am. 55, 1105- (1965)

Neckel H., 1999, Solar Physics 184, 421

Orozco Suárez, D., & del Toro Iniesta, J. C. 2007, A&A, 462, 1137

Orozco Suárez, D., Bellot Rubio, L. R., & del Toro Iniesta, J. C. 2007, ApJ, 662, L31

Orozco Suárez, D., et al. 2007, ApJ, 670, L61

Orozco Suárez, D., et al. 2007, PASJ, 59, 837

Orozco Suárez, D., Bellot Rubio, L. R., del Toro Iniesta, J. C., & Tsuneta, S. 2008, A&A, 481, L33

Piskunov, N. E., Kupka, F., Ryabchikova, T. A., Weiss, W. W., & Jeffery, C. S. 1995, A&A Supp.Ser., 112, 525

Press, W. H., Teukolsky, S. A., Vetterling, W. T., & Flannery, B. P. 1992, Cambridge: University Press, —c1992, 2nd ed.,

Rachkovsky, D. N. 1962, Izv. Krymskoi Astrofiz. Obs., 27, 148

Rachkovsky, D. N. 1967, Izv. Krymskoi Astrofiz. Obs., 37, 56

Ruiz Cobo, B., & del Toro Iniesta, J. C. 1992, ApJ, 398, 375

Ruiz Cobo, B., & del Toro Iniesta, J. C. 1994, A&A, 283, 129

Sanchez Almeida, J., & Martinez Pillet, V. 1994, ApJ, 424, 1014

Scherrer, P. H., et al. 1995, Sol. Phys., 162, 129

Scherrer, P. H., & SDO/HMI Team 2002, Bulletin of the American Astronomical Society, 34, 735

Schrijver, C. J., Title, A. M., Hagenaar, H. J., & Shine, R. A. 1997, Sol. Phys., 175, 329

Schrijver, C. J., Title, A. M., van Ballegooijen, A. A., Hagenaar, H. J., & Shine, R. A. 1997, ApJ, 487, 424

Schüssler, M., Shelyag, S., Berdyugina, S., Vögler, A., & Solanki, S.K. 2003, ApJ, 597, L173

Skumanich, A., & Lites, B. W. 1987, ApJ, 322, 473

Socas-Navarro, H., López Ariste, A., & Lites, B. W. 2001, ApJ, 553, 949

Stenflo, J. O. 1973, Sol. Phys., 32, 41

Stenflo, J. O., Solanki, S., Harvey, J. W., & Brault, J. W. 1984, A&A, 131, 333

Stix, M. 2004, The sun : an introduction, 2nd ed., by Michael Stix. Astronomy and astrophysics library, Berlin: Springer, 2004. ISBN: 3540207414

Thevenin, F. 1989, A&A Supp.Ser., 77, 137

del Toro Iniesta, J. C. 2003, Introduction to Spectropolarimetry. Cambridge, UK: Cambridge University Press

del Toro Iniesta, J. C., & Ruiz Cobo, B. 1996, Sol. Phys., 164, 169

Unno, W. 1956, PASJ, 8, 108

Vögler, A. 2003, PhD Thesis, University of Göttingen, Germany, http:77webdoc.sub.gwdg.de/diss/2004/voegler

Vögler, A., Shelyag, S., Schüssler, M., Cattaneo, F., Emonet, T., & Linde, T. 2005, A&A, 429, 335

Westendorp Plaza, C., del Toro Iniesta, J. C., Ruiz Cobo, B., Martinez Pillet, V., Lites, B. W., & Skumanich, A. 1998, ApJ, 494, 453